DISS. ETH Nr. 17378

Evolution of ore-forming fluids at the porphyry to epithermal transition: the Famatina Cu-Mo-Au district (NW Argentina)

A dissertation submitted to the
ETH ZURICH

for the degree of
Doctor of Natural Sciences

presented by
CLAUDIA PUDACK

Dipl.-Geol., Freiberg University of Mining and Technology, Germany

born 29.10.1973
citizen of Germany

accepted on the recommendation of

Prof. Dr. Christoph A. Heinrich	ETH Zurich	examiner
Prof. Dr. Werner Halter	ETH Zurich	co-examiner
Prof. Dr. Thomas Pettke	University of Bern	co-examiner
Prof. Dr. Jamie Wilkinson	Imperial College London	co-examiner

Zurich 2007

Dimidium facti
qui coepit habet;
sapere aude;
incipe!

Quintus Horatius Flaccus
(December 8, 65 BC – November 27, 8 BC)
Book I, epistle ii, line 40

ACKNOWLEDGEMENTS

TABLE OF CONTENTS

1 ABSTRACT

The spatial and temporal relationship between deep-seated porphyry systems and shallow high-sulfidation epithermal ore deposits has been discussed by many authors. Despite the demonstrable association in space and time, there has been much debate on the processes by which the two deposit types are related to each other. In an effort to provide insights into possible genetic links between porphyry and epithermal styles of mineralization, the present study investigated high-sulfidation epithermal Cu-Au veins in proximity to a porphyry Cu-Mo-Au system at Famatina, NW Argentina. Here, glacial erosion has uncovered the upper parts of the porphyry system in valleys, whereas numerous high-sulfidation epithermal Cu-Au veins are preserved along an adjacent ridge. The epithermal veins crosscut, but also grade downwards into quartz-sericite-pyrite (QSP) veins, which postdate the potassic alteration associated with the more deeply eroded porphyry system. These field observations indicate that the transitional QSP veins may represent linking channelways for the ore-forming fluids generating the high-sulfidation epithermal deposit.

The distinct metallogeny and accessibility of the Famatina mining district provide a unique opportunity to explore the evolution of the ore-forming fluids from the deep porphyry setting to the shallow high-sulfidation epithermal environment. The chemical and physical evolution of the magmatic to hydrothermal processes has been reconstructed with a quantitative fluid inclusion study. Fluid inclusion petrography, microthermometry, and single inclusion microanalysis by LA-ICP-MS are combined to determine the evolution of pressure, temperature, and ore metal concentrations in the fluids. Furthermore, cathodoluminescence (CL) microscopy is used to constrain the successive stages of quartz formation and the entrapment sequence of the fluid inclusion populations. The combined data reveal a complex but systematic crystallization history and provide new insight into the mechanisms of metal transport and ore mineral precipitation in both systems.

The distribution of fluid inclusion types in space and time is documented based on previously reported observations of the igneous geology, alteration geochemistry, and vein chronology at Famatina. Petrographic investigations and fluid inclusion data from the porphyry system indicate that a single-phase intermediate-density fluid

directly exsolved from a crystallizing magma at pressures and temperatures above 800 bars and 600°C. This high-temperature fluid is recorded in quartz phenocrysts and early veins, which formed within the consolidating portions of the parent intrusion under lithostatic conditions, at depths greater than 1.7 km. The fluid is of low- to intermediate salinity (3-19 wt% $NaCl_{equiv}$) and contains on average 0.15 wt% Cu and no detectable Au (<1 ppm).

Cooling and decompression of this input fluid occurs in the subsequent stages of stockwork mineralization, leading to phase separation by condensation of a small fraction of hypersaline brine (~12%) from large volumes of low-salinity vapor (~88% by mass). The dominant low-density vapor phase is preferentially enriched in Cu (0.19 wt%) and Au (2.0 ppm) relative to its main salt components, and probably plays a major role already in the formation of the porphyry Cu-Mo-Au mineralization. Successive boiling assemblages indicate several episodes of phase separation related to local pressure and temperature fluctuations, between 300 and 800 bars and 450 and 700°C, respectively. These changes in the physical properties cause potassic alteration but no saturation in Cu and Au, as recorded by continually high ore metal concentrations in the fluid inclusions. Precipitation of Cu-Fe sulfides occurs in the late stage of the porphyry system, between 350 and 250°C, and is synchronous with a transition from potassic to sericitic alteration. However, ore metal deposition is subeconomic at present times, probably due to incomplete focusing of the ore-forming fluids through three (or more) spatially separated exit points. The late hydrothermal stage of the porphyry system is characterized by contraction of the vapor phase to a low-temperature (250°C) liquid-like fluid of low- to intermediate salinity (2-13 wt% $NaCl_{equiv}$), which appears to be closely associated with sericitic alteration assemblages.

Fluid inclusion evidence suggests that the transitional quartz-sericite-pyrite (QSP) stage is dominated by aqueous fluids of low salinity (~ 5 wt% $NaCl_{equiv}$), which occur at temperatures between 360 and 325°C. These liquids are the primary metal-transporting agents responsible for the formation of the high-sulfidation epithermal Cu-Au veins at La Mejicana and contain up to 0.55 wt% Cu and 17.4 ppm Au. They are interpreted to originate from greater depth, either as a single-phase magmatic fluid of intermediate density or, more likely, as a vapor phase that condensed out some Fe-rich brine and then cooled and contracted at elevated pressure. This

interpretation is supported by inadequately low Au and relatively higher Fe concentrations in the intermediate-density fluids recorded in the porphyry system.

Attempts to relate fluid inclusion characteristics to the high-sulfidation epithermal stage of mineralization have not been fully successful. Limited data indicate that aqueous inclusions of low salinity (1.5 wt% $NaCl_{equiv}$) and low temperature (230°C) trapped at the end of QSP quartz formation reflect the transition to the main Cu-Au mineralization in the epithermal ore deposit. Compositional differences observed between these liquids and earlier aqueous inclusions are consistent with a 4-fold dilution of the ore-bearing fluids. This hypothesis is supported by very low pressures of 9 to 20 bars, indicating formation under hydrostatic conditions, which permitted incursion of ambient meteoric water. Some low-temperature liquid inclusions exhibit very high Cu concentrations (0.29 wt%), possibly indicating local re-dissolution of previously deposited sulfide ore. Here, fluids became increasingly acid due to physical separation from wall-rock silicates, e.g., in vein centers or at the transition from sericitic to advanced argillic alteration. Another possible explanation is that these inclusions represent a new and more acid fluid pulse of low temperature, introducing the main stage of high-sulfidation epithermal ore deposition.

The apparent coexistence of vapor-rich and aqueous fluid inclusions observed in some of the high-sulfidation epithermal veins may be the result of low-pressure fluid boiling at 9 bars and 175°C. This is consistent with the shallow depth at which deposition of the epithermal ore metals takes place. However, no clear boiling assemblages have been observed. Therefore, it is concluded that high-sulfidation epithermal ore deposition mainly occurs upon cooling and mixing with ambient meteoric water near the paleosurface.

The data are consistent with recent thermodynamic studies indicating that Au and other ore-forming metals are transported as stable bisulfide complexes in the vapor phase from the deep porphyry setting to the site of epithermal ore formation at shallower crustal levels (Heinrich et al., 2004).

2 ZUSAMMENFASSUNG

Porphyrische und epithermale Erzlagerstätten stehen in engem Zusammenhang mit plattentektonischen Aktivitäten und weisen zahlreiche Merkmale auf, die auf eine räumliche und zeitliche Beziehung schliessen lassen. Trotz dieser nachweislichen Assoziation in Raum und Zeit, wird bis heute ein genetischer Zusammenhang der Bildungsprozesse in Frage gestellt. In der vorliegenden Studie wird diese These anhand von gut charakterisierten Flüssigkeitseinschlussgruppen in benachbarten Systemen porphyrischer und epithermaler Vererzung in Famatina (NW Argentinien) getestet. Hier ermöglichen hervorragende Aufschlussverhältnisse eine hinreichende Beprobung beider, normalerweise übereinander liegender Vorkommen. Zudem lassen sich zahlreiche Quarz-Serizit-Pyrit-Adern aushalten, die aufgrund ihrer strukturellen Merkmale als ein Übergangsstadium vom tiefen porphyrischen zum oberflächennahen epithermalen System interpretiert werden.

Die idealen Verhältnisse im Untersuchungsgebiet ermöglichen es, die genaue Abfolge der erzbildenden Prozesse zu rekonstruieren und quantitativ, mittels Mikrothermometrie und LA-ICP-MS, zu bestimmen. Darüber hinaus wurde SEM-CL eingesetzt, um die verschiedenen Generationen der Quartzbildung und der zugehörigen Flüssigkeitseinschlüsse zu erkennen. Die Resultate der vorliegenden Arbeit lassen auf eine komplexe aber systematische Entwicklungsgeschichte schliessen, die in früheren Studien nicht erkannt wurde.

Die Untersuchung des porphyrischen Systems ergab, dass das frühe hydrothermale Stadium von einem einphasigen Fluid mittlerer Dichte geprägt ist, das direkt aus einem tiefer liegenden Magma bei hohen Drücken (>800 bar) und Temperaturen (>600°C) entmischt wurde. Dieses heisse, einphasige Fluid weist trotz geringer Salinitäten (3-19 wt% NaCl äquivalent) hohe durchschnittliche Cu-Konzentrationen von 0.15 wt% auf. Die entsprechenden Au-Gehalte liegen jedoch unterhalb der Nachweisgrenze. Abkühlung und Druckentlastung des Ausgangsfluides führen zur Entmischung einer geringen Menge flüssigkeitsreicher Brine (~12%) von einer dominanten Gasphase (~88%). Die quantitative Analyse der Gasphase ergab hohe Konzentrationen an Cu (0.19 wt%) und Au (2.0 ppm). Sie wird daher als Hauptträger der porphyrischen Erzmetalle interpretiert. Weitere Druck- und Temperaturabnahme führte zur Ausfällung potassischer Alterationsminerale bei gleichbleibend hohen

Metallkonzentrationen in den zugehörigen Flüssigkeitseinschlüssen. Die Ausfällung von Cu-Fe-Sulfiden zwischen 350 und 250°C erfolgte zu einem späteren Zeitpunkt und scheint an die serizitische Alteration des Wirtsgesteins gebunden zu sein. Die Metallkonzentrationen variieren stark zwischen den verschiedenen porphyrischen Intrusivkörpern und sind von geringem wirtschaftlichen Wert. Das späte Stadium des porphyrischen Systems ist durch die Kontraktion der niedrig-salinaren Gasphase zu einem dichteren, wässrigen Fluid gekennzeichnet.

Petrographisch vergleichbare wässrige Fluide dominieren in den QSP-Adern und haben hohe Homogenisierungstemperaturen von 325 bis 360°C, mittlere Salinitäten von 5 wt% NaCl äquivalent und sehr hohe Metallkonzentrationen (bis zu 0.55 wt% Cu und 0.6-12.9 ppm Au). Die erzreichen Lösungen stammen aus grösserer Tiefe und repräsentieren entweder ein einphasiges Fluid mittlerer Dichte oder eine Gasphase, die durch Phasenseparation von einer geringen Menge Brine entmischt wurde. Eine wesentliche Voraussetzung für die Komplexierung und den Transport von Metallen in die oberflächennahen Regionen der epithermalen Vererzung ist die Konzentration an Schwefel im Ausgangsfluid. Es ist daher wahrscheinlicher, dass die Fe-arme aber vermutlich Schwefel-reiche Gasphase die Quelle der erzreichen Lösungen darstellt.

QSP-Adern durchschlagen die quarzreichen Adern des Porphyrs und werden ihrerseits von den darüber liegenden epithermalen Adern geschnitten oder gehen darin über. Sie bilden somit wahrscheinlich Wegsamkeiten für die erzführenden Fluide des epithermalen Systems. Diese Interpretation wird durch späte Flüssigkeitseinschlüsse in den QSP-Adern unterstützt, die in ihren petrographischen und mikrothermometrischen Eigenschaften mit den wenigen primären Einschlüssen der epithermalen Adern vergleichbar sind. Ein Vergleich der gering temperierten (230°C) und niedrig-salinaren (1.5 wt% NaCl äquivalent) Fluide mit den frühen erz-reichen Lösungen ergab, dass die Bildung der späten Phase auf eine 4-fache Beimischung meteorischer Wässer zurückzuführen sein könnte. Dennoch weisen einige späte Flüssigkeitseinschlüsse sehr hohe Cu-Konzentrationen auf (0.29 wt%). Diese lassen sich zum einen auf die Wiederauflösung bereits ausgeschiedener Kupfererze zurückführen. Eine weitere Interpretationsmöglichkeit ist die Einführung eines neuen, aggressiveren Fluidpulses von geringerer Temperatur, der die eigentliche Erzausfällung im epithermalen System einleitet.

Die auffällige Koexistenz von gasreichen und wässrigen Einschlüssen in den Mineralen der epithermalen Adern liesse sich durch eine späte Entmischung dieser Phasen bei sehr niedrigen Drücken (9 bar) und Temperaturen um 175°C erklären. Diese These wird jedoch nicht durch klare „boiling assemblages" unterstützt. Es ist daher anzunehmen, dass die Abkühlung und Verdünnung der erzreichen Lösungen durch Beimischung meteorischer Wässer die Hauptursache für die Bildung der epithermalen Vererzung ist.

Die hier dargestellten Ergebnisse stimmen mit thermodynamischen Modellen überein, die den Transport von Cu und Au aus grosser Tiefe in die oberflächennahen Regionen der epithermalen Erzbildung untersucht haben.

3   INTRODUCTION AND AIM OF THE STUDY

3.1   Introduction

High-temperature porphyry Cu-(Mo-Au) deposits and high-sulfidation epithermal Cu-Au-(Ag-As) deposits are mainly associated with subduction-related, calc-alkaline magmatism at convergent plate margins (Figure 3.1; Hedenquist and Lowenstern, 1994). The two deposit types are geologically distinct, but show a close spatial and temporal relationship (Sillitoe, 1983; Arribas et al., 1995; Hedenquist et al., 1998). This association of the two deposit types implies a physical and chemical link between the ore-forming fluid processes and indeed, has been suggested by a number of different authors (e.g., Sillitoe, 1973; Sillitoe, 1983; Hedenquist and Lowenstern, 1994; Gammons and Williams-Jones, 1997; Heinrich et al., 2004).
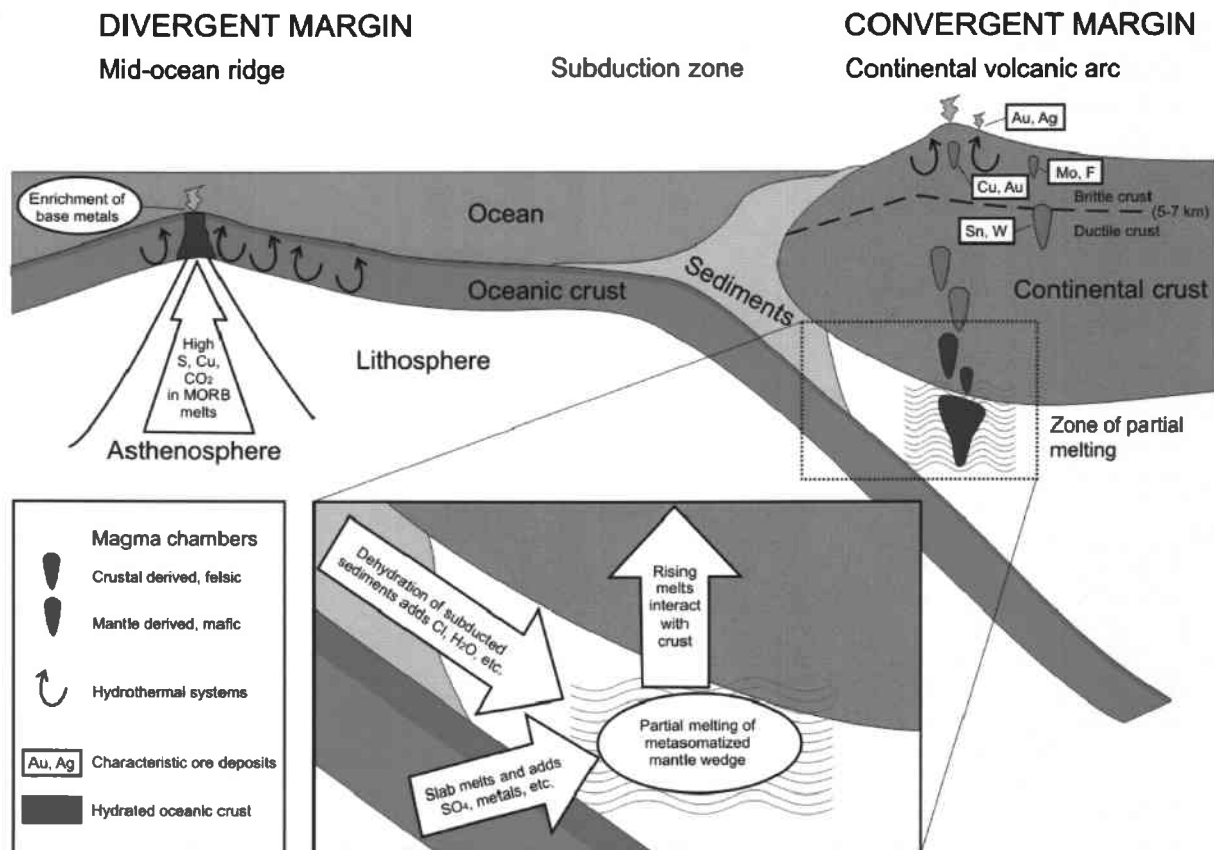
Figure 3.1: Schematic section illustrating the principal components of magma genesis, fluid flow, and metallogenesis in divergent and convergent margin settings (after Hedenquist and Lowenstern, 1994).

Porphyry ore deposits commonly form over the temperature range of 700 to 300°C, at depths of 2 to 5 km under initially lithostatic pressure (Figure 3.2; Hedenquist and Lowenstern, 1994). They are centered on porphyritic stocks, which are known to be cupolas above deeper intermediate to felsic plutons (Sillitoe, 1973). The intrusions themselves are altered, with a central potassic zone of biotite and minor K-feldspar that typically gives way outward to a phyllic zone of quartz and chlorite, commonly overprinted by a sericitic zone of sericite and pyrite (Lowell and Guilbert, 1970). The wall rocks farther from the intrusion may be altered to epidote, chlorite, and albite (propylitic zone). Where preserved, these zones are capped by hypogene advanced argillic alteration that usually extends to the paleosurface and includes alunite, kaolinite, dickite, and pyrophyllite (Titley, 1975). Within porphyry systems there are several pulses of intrusion, with the earliest commonly hosting the highest-grade ore (Hedenquist and Richards, 1998). In most cases, mineralization extends from the subvolcanic intrusion into the immediately adjacent country rocks, as disseminations and constituents of quartz stockwork veins (Sillitoe, 1973; Arribas et al., 1995).
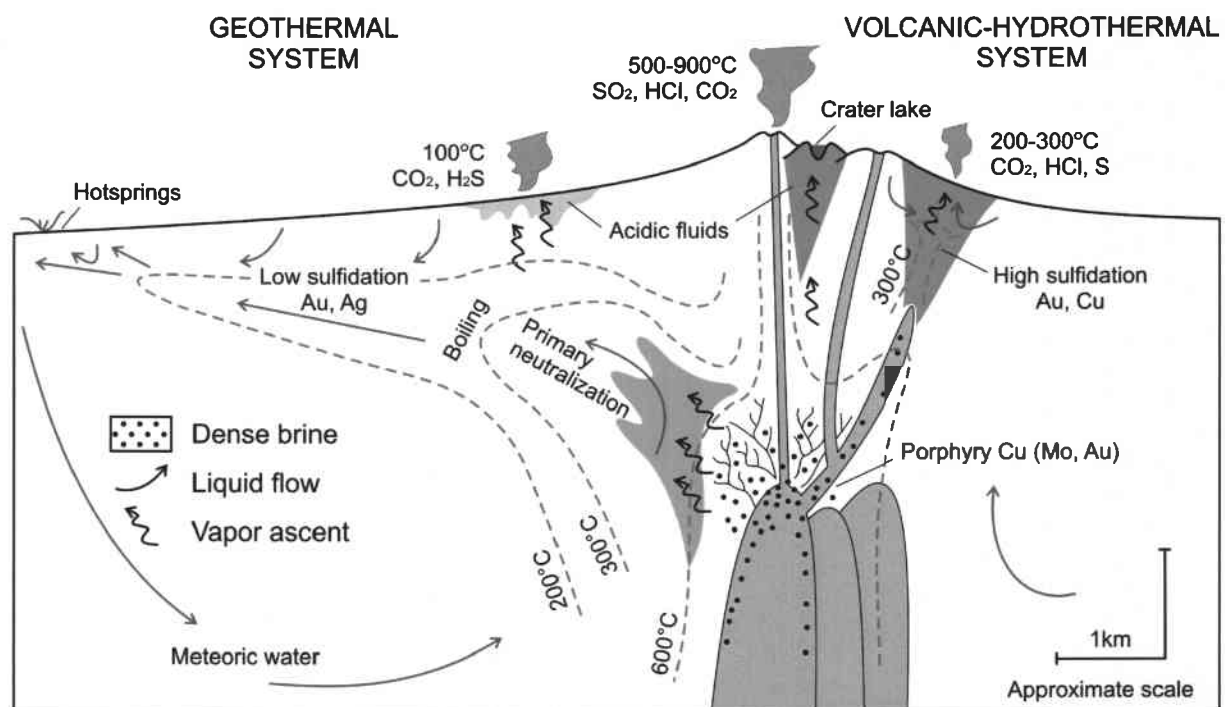
Figure 3.2: Schematic cross-section showing shallow, subvolcanic intrusions and related hydrothermal systems, including the environments deduced for the formation of porphyry and epithermal ore deposits (after Hedenquist and Lowenstern, 1994).

Epithermal ore deposits form at relatively low temperatures of 150 to 300°C, from just below the surface to more than 1 km depth under hydrostatic pressure (Hedenquist and Arribas, 1999). The hydrothermal activity is commonly associated with contemporaneous volcanism and related intrusions of calc-alkaline composition. However, some deposits do not show any spatial or temporal correlation with subvolcanic intrusions (Arribas, 1995). According to the chemical conditions of the hydrothermal fluid, two endmember types of epithermal ore deposits in contrasting volcanic settings can be distinguished (Heald et al., 1987; White and Hedenquist, 1995). They are called high sulfidation and low sulfidation, respectively, referring to the sulfidation state of their characteristic sulfide assemblages, an intrinsic feature of the deposit (Figure 3.2; Hedenquist and Arribas, 1999).

High-sulfidation systems are associated with acid alteration mineral assemblages, such as kaolinite, illite, and alunite, and formed from acid, oxidized fluids. They occur proximal to their magmatic source and are commonly hosted by andesite-rhyodacite volcanic rocks in an arc setting (Sillitoe, 1997). The early stage of these systems is characterized by extensive leaching of the host rocks, and an isotopic composition similar to that of magmatic vapor mixed with meteoric water (Hedenquist, 1995). The leaching creates a porous silica residue (i.e. vuggy silica) with a quartz-alunite halo, which is commonly underlain by roots of sericite or pyrophyllite (Hedenquist and Lowenstern, 1994). The early sulfide minerals are euhedral pyrite with enargite-luzonite, a high-sulfidation state assemblage. Where paragenetic studies have been conducted, gold is introduced after deposition of enargite, along with fine-grained pyrite, Fe-poor sphalerite, chalcopyrite, galena, and tennantite-tetrahedrite (Jannas et al., 1990; Hedenquist et al., 1998). High-sulfidation epithermal deposits share many mineralogical and stable-isotope characteristics with the adjacent advanced argillic alteration that commonly caps porphyry ore deposits (Sillitoe, 1973; Sillitoe and Bonham, 1990). Indeed, there is commonly a close spatial relationship between these deposits (Heald et al., 1987).

In contrast, low-sulfidation epithermal deposits are typically hosted by rhyolitic-dacitic rocks that have a bimodal character and formed in an extensional tectonic setting (Hedenquist and Arribas, 1999). Magmatic signatures in these deposits are more elusive, because they form distant from the inferred magmatic heat source (Heald et al., 1987). With increasing distance from the intrusion, meteoric water becomes dominant, and the fluid salinity and acidity decrease. Hence, low-sulfidation systems

form from near-neutral pH, reduced solutions and are commonly accompanied by the precipitation of quartz, adularia, and illite. The deposits show crustiform vein textures in which chalcedony dominates, indicating a relatively low temperature and shallow depths of formation (Saunders, 1994). Selenides are the dominant ore minerals, whereas sulfide minerals are subordinate and include pyrite, pyrrhotite, arsenopyrite, and Fe-rich sphalerite (John, 2001).

Although epithermal ore deposits are commonly associated with volcanic rocks of calc-alkaline series, shoshonitic or alkalic igneous host rocks may occur in mature intraoceanic arcs (e.g., Ladolam, Papua New Guinea; Muller and Groves, 1993) and in continental regions (e.g., Cripple Creek, Colorado; Kelley et al., 1998).

There has been much debate on whether or not these types of epithermal deposits are genetically related to each other, and to the underlying magmatic intrusion, which in some cases has formed a porphyry deposit. However, it is generally accepted that low-sulfidation epithermal deposits form in a distinctly different tectonic environment and magmatic affiliation from high-sulfidation deposits. In addition, low-sulfidation deposits are not known to occur in porphyry districts, probably because they are related to a more deeply seated magma chamber. For these reasons, the present study will focus only on high-sulfidation epithermal deposits and the evidence for a transition to the porphyry environment, using a case study of the Famatina mining district, NW Argentina.

Numerous studies have shown mineralogical and isotopic evidence that indicates a genetic link between porphyry Cu and high-sulfidation epithermal Cu-Au deposits (e.g., Sillitoe, 1973; Arribas et al., 1995; Hedenquist et al., 1998; Einaudi et al., 2003). However, the physical and chemical mechanisms of ore metal transport from the deep magmatic setting to the shallow epithermal environment is still debated. Undoubtedly, magmatogene hydrothermal fluids contributed to ore formation in both systems and the influence of magma chemistry on the metal content of the deposits must therefore be considered. On the other hand, there is also isotopic evidence for the involvement of meteoric water (e.g., Vennemann et al., 1993; Hedenquist et al., 1998), which circulates through brittle rock at hydrostatic pressure where temperatures are less than about 370°C (Fournier, 1999).

The behavior of the deep magmatic fluids has been modeled by Henley and McNabb (1978), who were the first to suggest that a low-density vapor commonly separates from the parental fluid upon decompression and discharges to the surface, leaving a

hypersaline liquid (i.e., brine) at depth. The gas-rich vapor phase includes H_2O, CO_2, SO_2, H_2S, HCl, and HF (Giggenbach et al., 1990) and is more mobile than the coexisting brine phase. Therefore, it can pass from the environment of lithostatic pressure in a magma chamber into overlying hydrostatically pressured hydrothermal systems. At moderately high temperatures and pressures, the vapor is capable of transporting relatively high concentrations of silica and metals (Krauskopf, 1957; Sawkins and Scherkenbach, 1981; Eastoe, 1982; Vennemann et al., 1993; Fournier, 1999). Consistently, Heinrich et al. (1992; 1999) and Ryan et al. (1993) noted appreciable Cu concentrations in vapor-rich inclusions in reduced, porphyry Sn-W deposits, possibly carried as volatile Cu sulfide complexes. Damman et al. (1996) and Ulrich et al. (2001) also found fluid inclusion evidence for Cu, Au, and As partitioning into the vapor phase in the Rosia Poieni and Bajo de la Alumbrera porphyry Cu-Au deposits, respectively. Recent thermodynamic studies support the hypothesis that Au and other metals are transported selectively in the vapor phase from the deep porphyry environment to the site of epithermal ore formation at shallower crustal levels; whereby at least Au can only be transported effectively due to sulfide complexation (Heinrich et al., 2004; Heinrich, 2005).

By contrast, the dense, Cl-rich brine phase will tend to remain at depth, adjacent to its parent intrusion (Fournier, 1999). Given the high metal content in brine inclusions associated with porphyry deposits, this fluid type has initially been considered as a major metal-transporting phase. This conclusion is based on experimental studies (e.g., Candela and Holland, 1984; Williams et al., 1995), which indicate that metals, such as Cu and Au, partition strongly from the melt into an aqueous chloride liquid. Hence, the dense, metal-rich brine was interpreted to ascend into shallow levels and to precipitate Cu and Au upon mixing with meteoric water (Hedenquist et al., 1994b). However, this model depends on the mobility of Au in magmatic fluids as Au-chloride complexes, which become unstable at temperatures below 400°C, thereby causing saturation and co-precipitation of Au with Cu near the core of the porphyry system (Gammons and Williams-Jones, 1997).

As an alternative explanation it can be considered that sericitic alteration and Cu-Au mineralization in both, the porphyry and the high-sulfidation epithermal system, are related to a common parental fluid of intermediate density (Hedenquist et al., 1998; Muntean and Einaudi, 2001). This fluid is thought to have exsolved directly from the magmatic source under supercritical conditions at depth and is then transferred, as a

whole, to the epithermal environment. However, a major factor in the ability of low- to intermediate-density fluids to carry dissolved Cu (and Au) into the low-temperature regions of epithermal ore deposition is the concentration of sulfur, which can act as a complexing agent (Fournier, 1999). Moreover, H_2S and SO_2 exsolved from the magma are interpreted to be the main agents for acid wall rock alteration related to high-sulfidation epithermal mineralization (Brimhall and Ghiorso, 1983; Giggenbach, 1992; Vennemann et al., 1993).

3.2   Objectives of research

As mentioned earlier, the spatial and temporal relationship between deep-seated porphyry Cu-Mo-Au systems and high-sulfidation epithermal Cu-Au deposits has been discussed by several authors (e.g., Sillitoe, 1973, , 1983; Arribas et al., 1995; Hedenquist et al., 1998). However, despite the demonstrable association in space and time, localities where the two types of mineralization occur together are rare. This may be due to erosion that has removed high-sulfidation epithermal veins originally present above currently exposed porphyry deposits. On the other hand, porphyry systems that underlie high-sulfidation epithermal deposits may exist far below the current limits of exploration.

In an effort to provide new insights into possible genetic links between porphyry and epithermal styles of mineralization, the present study investigated high-sulfidation epithermal Cu-Au veins in proximity to a porphyry Cu-Mo-Au system at Famatina, NW Argentina. Here, glacial erosion has uncovered the upper parts of a porphyry system in valleys, whereas numerous high-sulfidation epithermal veins are preserved along an adjacent ridge. Both styles of mineralization are essentially unmodified since their formation, largely due to the lack of supergene alteration under arid climatic conditions (Losada-Calderón et al., 1994). In addition, the epithermal veins grade downwards into quartz-sericite-pyrite (QSP) veins, which crosscut the more deeply exposed porphyry system. These observations indicate that the QSP veins may represent linking channelways for the ore-forming hydrothermal fluids generating the high-sulfidation epithermal deposit.

The distinct metallogeny and accessibility of the Famatina mining district provide a unique opportunity to test concepts relating to porphyry and epithermal ore formation.

Furthermore, it offers the possibility to explore the evolution of the ore-forming fluids from the deep magmatic source through the porphyry regime to the shallow high-sulfidation epithermal environment. Therefore, the aim of the present work is to use Famatina as a case study to try to discriminate between the three generic scenarios just explained by integrating petrographic, mineralogical, and fluid inclusion data. Key information comes from fluid inclusion salinities and homogenization temperatures obtained from microthermometry of fluid inclusions trapped in magmatic and hydrothermal quartz. Cathodoluminescence microscopy was combined with scanning electron microscopy (SEM-CL) in order to constrain the entrapment sequence of selected fluid inclusion assemblages. The application of laser-ablation inductively-coupled-plasma mass-spectrometry (LA-ICP-MS) on specific inclusion assemblages allowed determination of element concentrations in all fluid types.

The present level of exposure prevents sampling of the deeper parts of the porphyry system. Therefore, the approach of the present study is to compare the composition of early fluids from the currently exposed porphyry system (Chapter 6) with pre- to syn-ore fluids from the QSP stage (Chapter 7) and post-ore fluids from the high-sulfidation epithermal precious-metal veins (Chapter 8). Hence, critical observations obtained from the accessible material are used to reconstruct the fluid evolution from the porphyry to the epithermal environment (Chapter 9). This is followed by concluding remarks and a brief outlook into future investigations (Chapter 10).

3.3   Location and mining history

The Famatina mining district, latitude 29°00'S and longitude 67°45'W, is located in the Famatina Ranges, La Rioja province, NW Argentina. Within an area of less than 35 km^2, the property contains a porphyry Cu-Mo-Au system and a high-sulfidation epithermal Cu-Au-(Ag) deposit. Ore-grade epithermal mineralization in the La Mejicana deposit occurs at about 4800 m elevation, above and to the northwest of the Nevados de Famatina porphyry system. According to Losada-Calderón (1992), the porphyry system has estimated resources of more than 300 Mt, grading 0.37% Cu, 0.06% Mo, 0.6 g/t Ag, and 0.3 g/t Au . In addition, the estimated resources of the high-sulfidation epithermal veins are 1.67 Mt grading 1.3% Cu, 40 g/t Ag, and 32 g/t Au (H. Van Alphen, writ. commun.).

The Famatina mining district has been discovered in Spanish times and was the site of high-grade vein Cu-Ag-Au production by British settlers early in the last century. Large-scale mining activity commenced in 1904 and ceased in 1930. During the 1990's, the property was the subject of exploration by CRA-RTZ, which was focused on low-grade gold. In addition to several precious metal veins, the Nevados de Famatina porphyry system was discovered containing at least four porphyry Cu centers, known as La Estrechura, Portezuelo de Illanez, Caballo Muerto, and Los Bayitos. In early 2000, Corriente re-investigated the vein complex at La Mejicana and drill-tested the depth extent below some of the historic underground workings. Current exploration activity is jointly operated by Yamiri S.A. and Barrick Gold Corporation, and has now centered on a specific area of interest to the north and west of La Mejicana, known as Quebrada Ancha. Additional drilling programs will extent the current limits of mineralization to the north and the east.

3.4 Previous studies

Recognition of economic porphyry-epithermal Cu-Au mineralization in the 1990's has prompted detailed geological research into various aspects of the geology of the Famatina mining district, which will be discussed in the following sections. Prior to this, studies were limited to reconnaissance due to the remoteness, lack of roads, and high altitude of the area.

The earliest studies were done by Turner (1971) who mapped and described the basic geology. Later, Marcos and Zanettini (1982) initiated a series of studies that included sampling in the Nevados de Famatina porphyry system. McBride et al. (1976) investigated the geochronology and inferred orogenic history in this part of the Central Andes. Broad-scale geochemical and isotopic studies have been focused on the region overlying the flat subduction slab (Barazangi and Isacks, 1976), followed by compilations regarding the metallogeny of the Central Andes (e.g., Camus, 1990; Davidson and Mpodozis, 1991; Sillitoe, 1992; Sillitoe and Perello, 2005). More recently, Losada-Calderón et al. (1990; 1992; 1994; 1996) integrated stratigraphic work with mineralogical, geochronological, and fluid inclusion data in order to describe the relationship of igneous activity to Cu-Mo-Au mineralization in the Famatina mining district.

4   GEOLOGICAL BACKGROUND

4.1   Tectonic setting

The Andean region represents an active convergent plate margin between the oceanic Nazca plate and the South American continent. This subduction process created an 8000 km long orogenic belt, which extends along the western border of the South American plate (Figure 4.1). According to Jaillard et al. (2000), this belt can be divided into three segments of distinct orientations: the Colombian-Ecuadorian segment (12°N - 5°S), the Peruvian segment (5°S - 18°S), and the Chilean segment (18°S - 56°S). Characteristic features of the different segments are alternating dip angles, subduction vector changes, and variations in the absolute plate motion (Pomposiello et al., 1998).

At latitudes 26°S to 33°S of the Chilean segment, seismic activity indicates that the oceanic Nazca plate is being subducted nearly horizontally for over 300 km before descending steeply into the mantle (Figure 4.2, Jaillard et al., 2000). The resulting lack of asthenospheric material between the subducting slab and the overriding continent prevents arc magma generation (Cahill and Isacks, 1992) and causes an eastward migration of the volcanic front (Ramos et al., 2002). According to Reynolds et al. (1990), this Pampean flat slab attained its current low-angle inclination between 17 and 10 Ma. This shallowing of the subduction zone correlates with the collision of the Juan Fernandez Ridge in the Nazca Plate with the Chilean trench, propagating from north to south (Ramos et al., 2002). The propagation of the thrust front and migration of the arc magmatism into the foreland resulted in thermal weakening of the crust, accompanied by brittle-ductile failure that allowed basement block uplift and regional deformation. However, the present tectonic framework of the Pampean flat slab is characterized by its lack of an active volcanic arc and the occurrence of a deformed and faulted foreland (Ramos et al., 2002).

The Famatina Ranges are encompassed in the northern part of the Pampean flat slab and represent a 400 km long, N-S trending magmatic arc wedged between the Precordillera to the west and the Sierras Pampeanas to the east (Dávila et al., 2004). Both, the Precordillera thrust belt and the Sierras Pampeanas broken foreland are considered to be dominantly Tertiary features (Dávila and Astini, 2003). However,

both regions were involved into earlier deformational episodes, sharing Cenozoic history with the adjacent Andean foreland (Jordan and Alonso, 1987).

Each of the main tectonic events that affected Famatina is consistent with protracted subduction and recorded as a major angular unconformity (Dávila et al., 2003). General consensus holds that the Precordillera is an exotic block that was rifted from Laurentia and accreted to the western margin of Gondwana (Thomas and Astini, 2003). However, the timing of both events is still debated. Considering the strong record of Early Cambrian rifting, recent publications propose that the continental breakup of the Precordillera microcontinent took place by the end of the Cambrian. During the Middle to Late Ordovician, independent drift of the Precordillera terrane was followed by flexural subsidence and initiation of arc magmatism (Thomas and Astini, 2003). Apparently, subduction stopped when the Precordillera terrane entered the subduction zone, and the Famatina arc became an important source of extra-basinal clastic sediments (Famatinean orogeny). Thus, termination of arc magmatism was coincident with collision, deformation, and metamorphism of both, the leading edge of the Precordillera microcontinent and the Famatina arc complex. Silurian to Devonian compression was caused by the accretion of Chilenia to the outboard side of the Precordillera (Ramos et al., 1986). Continued plate convergence during the Carboniferous to Permian led to regional shortening, backarc extension, dextral transtensional fault reactivation, and fold amplification (Gondwanean orogeny, Dávila et al., 2003). However, the current tectonic configuration of the Famatina Ranges is largely a product of the shallowing of the Nazca plate (Andean orogeny), resulting in regional shortening in association with magma accumulation in the thickened continental crust (Ramos et al., 1986).

The latter features are typical for flat-slab subduction and appear to trigger porphyry and epithermal ore formation in the central Andes (Kay et al., 1994; Cooke et al., 2005). Other processes, such as metasomatism of the mantle wedge, hydration of the lithosphere above the flat slab, cessation of volcanism, and rapid erosion and exhumation are also vital for the development of economic ore deposits (Sillitoe, 1997; Cooke et al., 2006). The following sections will provide a short summary on the metallogenesis of the Central Andes with specific reference to the Famatina region.
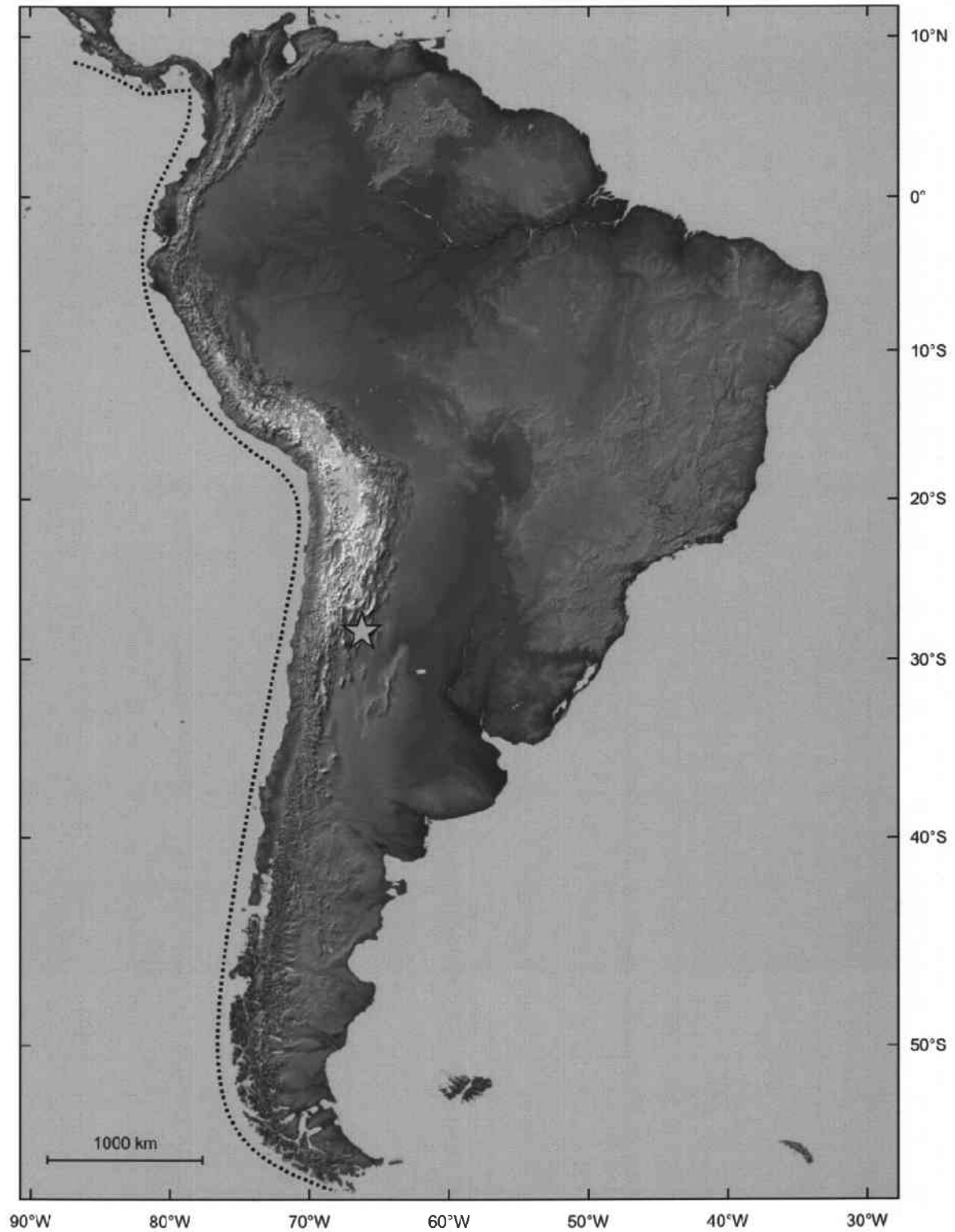
Figure 4.1: Satellite image of South America generated with data from the Shuttle Radar Topography Mission (SRTM; source: http://visibleearth.nasa.gov). The topographic relief is dominated by the Andes, which extend all along the Pacific Coast. Color coding is directly related to topographic height, with green at the lower elevations, rising through yellow and tan, to white at the highest elevations. The location of the Famatina Ranges is marked by the yellow star. The black dotted line along the western border of the South American plate indicates the subduction zone.
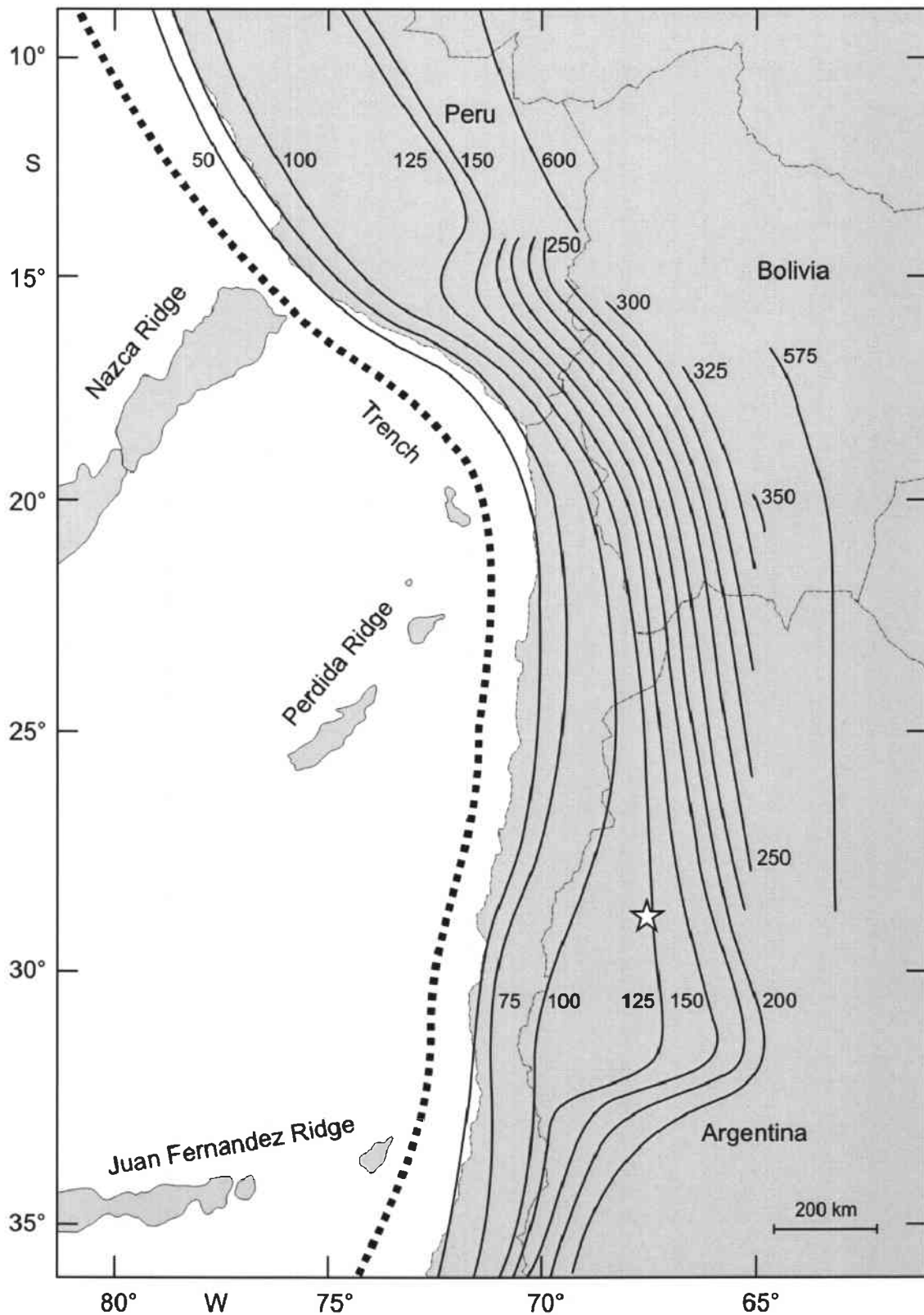
Figure 4.2: Geometry of the subduction zone along the Central Andes with indication of the Pampean flat slab at latitudes 26°S to 33°S (after Cahill and Isacks, 1992). Solid black lines display the contours of the Benioff Zone in 25 km intervals. The approximate location of the Famatina Ranges is marked by the white star.

4.2 Metallogeny of the Central Andes

The Central Andes host some of the world's richest and largest Cu and Au deposits, and have been subject to several cycles of mineral endowment during episodes of convergent plate tectonism (Sillitoe, 1992). These deposits are closely associated with volcano-plutonic arcs generated during eastward subduction of Pacific oceanic lithosphere beneath the archetypical Cordilleran continental margin (Sillitoe, 1991). According to Sillitoe (1988), three distinct Cenozoic epochs of Cu-(Au) mineralization are recognizable in the Central Andes: Paleocene to Early Eocene (66-52 Ma), Late Eocene to Early Oligocene (42-31 Ma), and Early Miocene to Pliocene (25-4 Ma). These metallogenic epochs are dominated by porphyry, skarn, and epithermal ore deposits, and account for more than 90% of the Andean Cu resources (Figure 4.3; Sillitoe, 1988). Most of these deposits were emplaced after the Cretaceous transition from extensional to compressional stress regimes at the plate margin caused by the shallowing of the subduction zone (Sillitoe, 1991). However, compressive tectonism and associated calc-alkaline magmatism were episodic and migrated eastward with time. Continued shallowing of the descending Nazca plate resulted in broadening of the volcanic front until extreme flattening of the underthrust slab extinguished the magmatic activity at the end of the Miocene between latitudes 28°S and 33°S (Kay and Mpodozis, 2002). Cessation of arc volcanism was synchronous with formation of giant porphyry Cu-Mo deposits on the southern flexure from flat to normal subduction (Hollings et al., 2005). In contrast, Cu-Mo-Au systems formed on the eastern flexure from flat to steep subduction, e.g., at Bajo de la Alumbrera (Harris et al., 2005) and at the smaller Agua Rica and Nevados de Famatina deposits (see Figure 4.2; Losada-Calderón et al., 1994; Landtwing et al., 2002).

Linking mineralization with a shallowing subduction zone implies that dehydration of the flat slab leads to the generation of hydrous magmas as fluids are progressively concentrated in the cooling mantle (Kay and Mpodozis, 2001). These fluids can be liberated as magmas are emplaced and cooled in shallow level magma chambers. Another key factor is that magmas intruding a thickened crust under compression have difficulty ascending and evolve at depth. Such conditions allow metals to be concentrated in the residual fluids of crystallizing magmas and may result in the formation of giant ore deposits above the shallowing subduction zone.
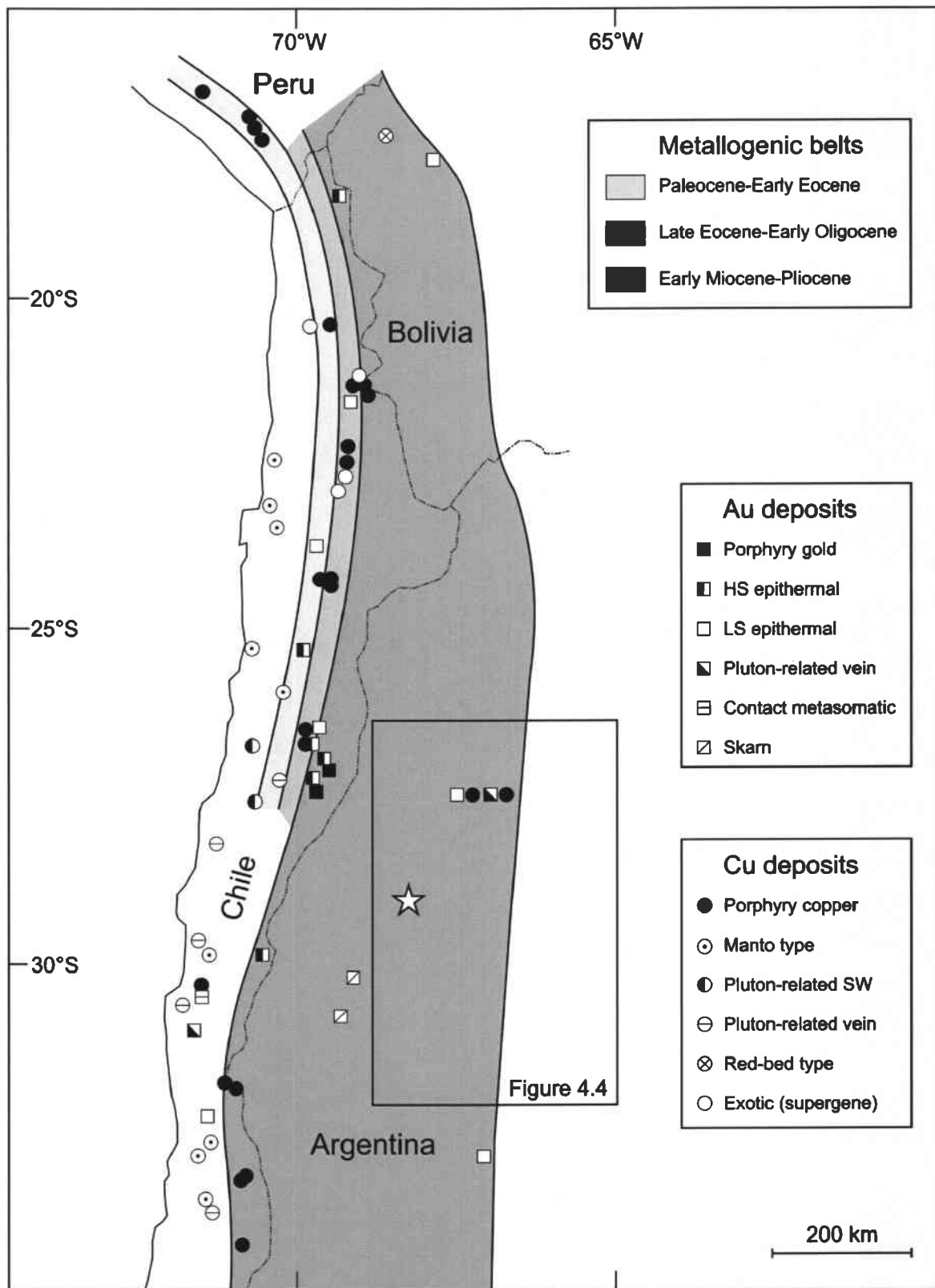
Figure 4.3: Types of principle Au and Cu deposits in the Central Andes (modified from Sillitoe, 1992). Metallogenic belts adapted from Sillitoe (1991) and Sillitoe and Perello (2005) are also shown. The approximate location of the Famatina mining district is indicated by the white star. Abbreviations: HS, high sulfidation; LS, low sulfidation; SW, stockwork.

4.3 Regional geology of the Famatina region

4.3.1 Introduction

The Famatina region, latitudes 27° to 31°S, is located in the southern Central Andes, La Rioja and Catamarca provinces, northwestern Argentina (Figure 4.4). Despite its position east of the main Andes, more than 400 km from the modern Chilean trench, peaks in the Famatina Ranges reach elevations of more than 6000 m above sea level. The main range in the region is the Sierra de Famatina. Most of the broken foreland consists of the Sierras Pampeanas, characterized by ranges of high-grade metamorphic and igneous basement rocks separated by broad basins filled with Cenozoic strata (Dávila et al., 2004). By contrast, the Famatina belt is composed of Lower Paleozoic volcano-sedimentary rocks that overlie a low-grade metamorphic basement (de Alba, 1979). The erosional history of this region is also different. Elsewhere in the Sierras Pampeanas, cooling history and landform studies indicate a simple protracted history of basement peneplain erosion of a late Paleozoic tectonic landscape that lasted until the Neogene (Jordan et al., 1989). The Famatina belt, however, underwent two episodes of rapid cooling due to tectonic uplift during the Early Eocene and the Miocene-Pliocene, with an episode of reheating in-between (Coughlin et al., 1998). Geochronological and petrographic evidence indicates that the reheating is related to hydrothermal alteration associated with small intrusions of dacitic porphyry (Losada-Calderón et al., 1994). Consistently, Dávila et al. (2004) provided evidence of magmatic activity in this region, which is synchronous with the initiation of shallow subduction at about 18 Ma.

The geology of the Famatina Ranges has been documented in detail by several authors (e.g., Harrington, 1956; Turner, 1971; McBride et al., 1976; de Alba, 1979; Losada-Calderón, 1992; Acenolaza et al., 1996). Therefore, the following sections will focus on the Famatina mining district, with particular emphasis on individual lithologies hosting the porphyry and the high-sulfidation epithermal mineralization. This study is based on own field observations combined with earlier stratigraphic work by Losada-Calderón (1992). The simplified stratigraphic column of the Famatina Ranges is provided in Table 4.1. Figure 4.5 details the geology of the mining district with two schematic cross sections illustrating the spatial and temporal relationships between the various porphyries and the epithermal system.
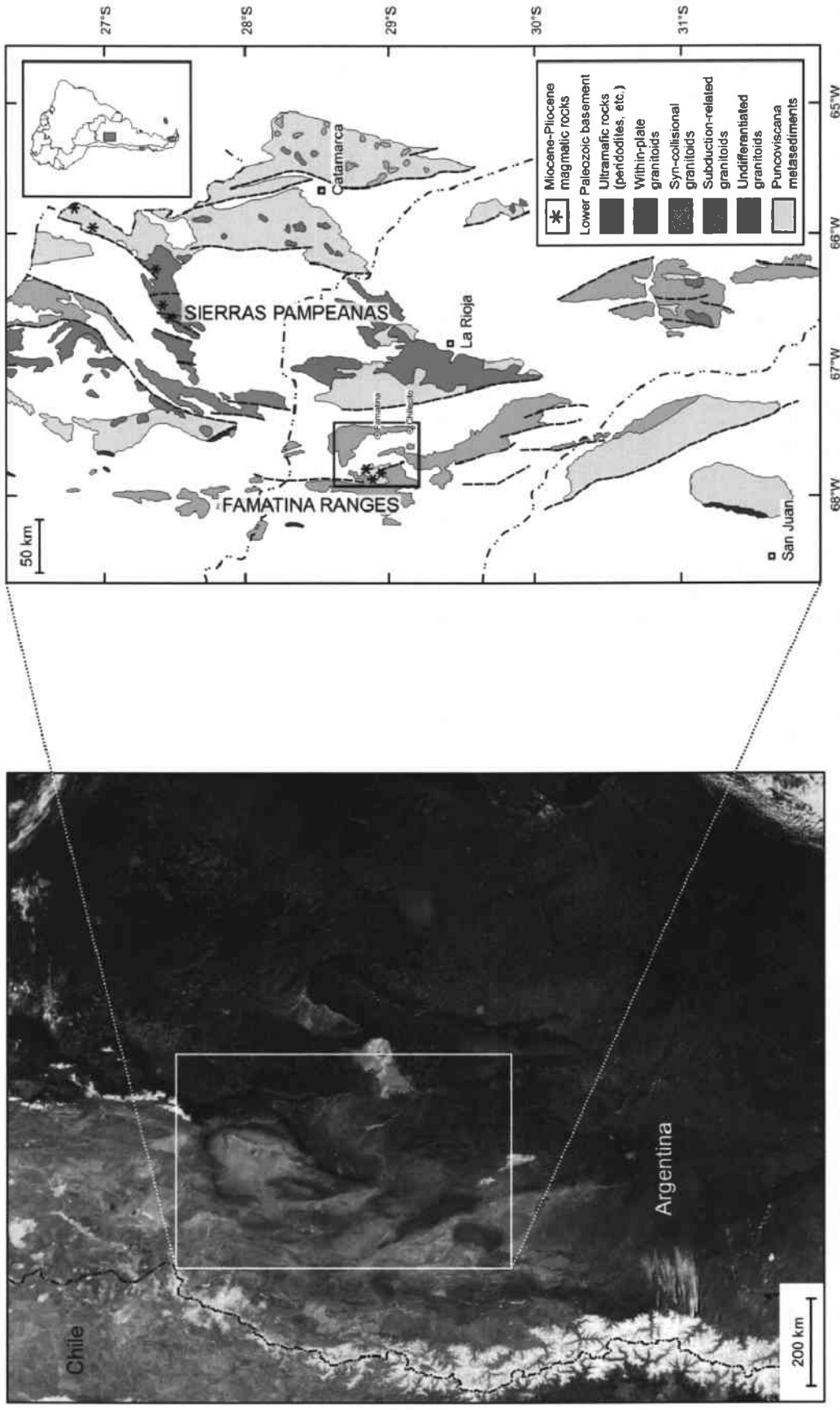
Figure 4.4: True-color satellite image (source: http://visibleearth.nasa.gov) and geology of the Lower Paleozoic basement of NW Argentina illustrating the different granitoid plutons of the Famatinean orogeny (after Lottner, 1986; Ramos, 2000). Late Cenozoic magmatic rocks are related to the Andean orogeny and developed as a consequence of the shallowing of the subduction zone (Ramos et al., 2002). The box within the geological map is enlarged in Figure 4.5.

Table 4.1: Simplified stratigraphic column of the Famatina Ranges modified from Harrington (1956), Turner (1970; 1971), Losada-Calderón (1992), and Davila et al. (2004) as illustrated in Figure 4.5. Major unconformities have been recognized at the end of the Cambrian, Ordovician, and Permian, and are marked by the black dotted lines. Units in **bold** correspond to lithologies present in the Famatina mining district and will be discussed in detail in chapter 4.3.3.

Geological period	Geological epoch	Stratigraphic unit	Lithology	Orogeny
Quaternary	Holocene	**Alluvial/colluvial cover**	bolders, gravels, sand, silt	Andean
	Pleistocene	Santa Florentina	fanglomerates, gravel beds	
		Cueva de Peréz	conglomerates, breccias	
Tertiary	Pliocene	**Mogote**	dacites, rhyodacites	
	Miocene	El Durazno (Angulos group)	conglomerates, volcaniclastics	
		Del Crestón	conglomerates, sandstones, volcaniclastics	
Permian	Rotliegendes	**Patquía**	conglomerates, sandstones	Gondwanean
Carboniferous	Pennsylvanian	**Agua Colorada**	conglomerates, sandstones	
Ordovician	Llanvirn	Molles	shales, sandstones, mudstones	Famatinean
	Arenig	Suri	rhyodacitic/dacitic volcanics, volcaniclastics	
		Ñuñorco	granites, granodiorites, aplites, pegmatites	
Cambrian	Early	**Negro Peinado**	shales, siltstones, phyllites, sandstones	

4.3.2 Stratigraphy

The stratigraphic sequence of the Famatina mining district commences with marine strata of the Cambrian Negro Peinado Formation (equivalent to the Puncoviscana Formation, see Figure 4.4), which were subject to low-grade metamorphism during the Lower Ordovician (Toselli, 1978). Phaneritic granites of the Ordovician Ñuñorco Formation (McBride et al., 1976) subsequently intruded the metasediments. Upper Paleozoic sedimentation corresponds to continental sediments of the Agua Colorada and Patquía Formations, which unconformably overlie these units (Losada-Calderón and McPhail, 1996). Numerous dacitic stocks and dykes of the Mogote Formation were emplaced during the Early Pliocene (Losada-Calderón et al., 1994). There is no evidence of volcanism related to the intrusive activity in this area. However, ash-flow tuff from the El Durazno Formation is probably synchronous with the Mogote dacites and occurs at the eastern flank of the Famatina Ranges (see Figure 4.5; Losada-Calderón et al., 1994). Pleistocene sediments of the Cueva de Peréz Formation and Quaternary alluvial and colluvial deposits cover all these units.

4.3.3 Host lithologies

The Cambrian **Negro Peinado Formation** is dominated by shales, siltstones, and phyllites representing a deep marine environment (Turner, 1971). Locally, basal conglomeratic beds occur, which are composed of quartz pebbles varying in size between 3 and 7 cm. The matrix consists of reddish-grey sandstone, which may be strongly silicified. This sequence is overlain by thin bedded shales and siltstones of characteristic greenish-grey color, which are largely composed of illite, chlorite, sericite, biotite, and magnetite. These fine-grained, unfossiliferous rocks represent the main host for the high-sulfidation epithermal Cu-Au veins. Related hydrothermal alteration is widespread and causes a distinctive bleaching of the sediments (Figure 4.6 A). No contemporaneous magmatic activity is known in this region. However, in proximity to the intrusive bodies of the younger Ñuñorco and Mogote Formations, the Cambrian beds exhibit typical features of contact metamorphism (Turner, 1971). According to Toselli (1978), the whole unit was subject to low-grade metamorphism and deformation during the Lower Ordovician. Isoclinal folding is also common in the metasediments, although locally more complex structures have been recognized. However, little or no metamorphic schistosity has been observed.

Legend:

- Alluvial/colluvial cover (Holocene)
- Santa Florentina fanglomerates (Pleistocene)
- Cueva de Peréz conglomerates (Pleistocene)
- Mogote dacitic porphyries (Pliocene)
- El Durazno volcaniclastics (Miocene)
- Del Crestón sediments (Miocene)
- Patquía sediments (Permian)
- Agua Colorada sediments (Carboniferous)
- Suri/Molles sediments (Ordovician)
- Ñuñorco granites (Ordovician)
- Negro Peinado metasediments (Cambrian)
- Faults and thrusts
- Projected epithermal veins
- Quartz-sericite-pyrite veins
- Porphyry stockwork veins

Figure 4.5 (previous page and this page): Regional geology of the Famatina mining district modified from Losada-Calderón (1992) and de Brodtkorb et al. (1996). The original map was provided by YAMIRI S.A. and updated based on own field observations in 2005. The location of the small, hypabyssal bodies of the Pozo dacitic porphyry (see Table 4.2) is known from drillcore material and indicated by the black stars. Schematic cross sections AA' and BB' reveal the temporal and spatial relationships between the numerous porphyries and the high-sulfidation epithermal system. Details at depth are largely inferred from superpositional and crosscutting relationships observed in the field and from filtered magnetic data of an airborne geophysical survey (CRA-RTZ, 1997).

The plutonic rocks of the **Ñuñorco Formation** were emplaced during the Ordovician (McBride et al., 1976) and occur in the southern part of the mining district. Granite is the predominant rock type, although granodiorites, aplites, and pegmatites have also been described (Turner, 1971). These subduction-related intrusives indicate the roots of the north-south trending magmatic arc and predate the volcano-sedimentary rocks comprising the Suri and Molles Formations (Mangano et al., 2003).

Paleozoic sedimentation corresponds to continental sediments of the Carboniferous **Agua Colorada** and Permian **Patquía Formations**, which strike northwest and have a shallow dip westwards (Losada-Calderón, 1992). Both units were deposited in a foreland basin and gently folded at the end of the Gondwanean orogeny. According to Turner (1971), contacts with the overlying Del Crestón and El Durazno Formations are unconformable, although these units do not occur in the mining district. However, ash-flow tuff from the El Durazno volcaniclastics is thought to be synchronous with the Mogote intrusive activity described below (Losada-Calderón et al., 1994).

The emplacement of the igneous **Mogote Formation** in the Famatina Ranges was the result of eastward migration of the volcanic front due to the shallowing of the subduction zone between 17 and 10 Ma (Reynolds et al., 1990). This series of dacitic stocks and dykes intruded at around 5.0 ± 0.3 Ma (Losada-Calderón et al., 1994) and is the main host for the porphyry Cu-Mo-Au mineralization. Furthermore, it seems to be associated with a later event characterized by the formation of quartz-sericite-pyrite (QSP) veins. These veins are accompanied by sericitic alteration envelopes and cut the potassic alteration of the porphyry system. Occasionally, they grade upwards into high-sulfidation epithermal assemblages, indicating that the QSP veins may represent linking channelways for the ore-forming fluids generating the epithermal deposit. Based on petrographic and geochronological evidence, seven porphyries can be distinguished, which form a granodioritic complex of calc-alkaline composition at depth (Losada-Calderón, 1992). However, selected sample material for this study originates from three distinct localities, which represent the igneous rocks subjacent to the high-sulfidation epithermal veins (see Figure 4.5).

i)   The dacitic rocks of *La Estrechura* exhibit a well-defined porphyritic texture, with phenocrysts of plagioclase, biotite, and quartz set in a fine-grained groundmass of sericite and quartz (Figure 4.6 B). Accessory minerals are monazite, apatite, magnetite, and zircon. Subhedral plagioclase phenocrysts often exhibit zoning and may form poikilitic textures with fine-grained biotite. Euhedral quartz is less

abundant, but usually occurs as porphyroblasts reflecting recrystallization. At higher elevations, the rocks are strongly silicified due to abundant quartz stockwork typical of the porphyry environment.

ii)   The intrusive stock at *Piedras Grandes* and the dacitic dyke of *La Mejicana* share many characteristics, despite the more intense hydrothermal alteration of the latter unit. Phenocrysts of quartz, plagioclase, and biotite are set in a very fine-grained groundmass composed of sericite and quartz (Figure 4.6 C+D). Accessory minerals include magnetite, zircon, and apatite. Euhedral plagioclase phenocrysts exhibit zoning, whereas quartz phenocrysts are partially resorbed and often embayed by the surrounding matrix. Sericitic alteration is widespread, causing mineral replacement by intergrowths of quartz, sericite, rutile, and illite. However, textural and mineralogical similarities indicate that the intrusive rocks at La Mejicana belong to a partly exposed dacitic dyke that may extend towards Piedras Grandes. Geophysical data from an airborne magnetic survey seem to support this hypothesis (CRA-RTZ, 1997).

The Pleistocene **Cueva de Peréz** Formation consists of consolidated conglomerates and clast-supported breccias, which contain fragments of the pre-glacial surface cemented with limonite (Sobral, 1921). These fragments vary in size from pebbles to boulders and include clasts from all metasedimentary and intrusive rocks exposed in the Famatina mining district (Losada-Calderón et al., 1994). However, the striking lack of epithermal assemblages implies that formation of the high-grade Cu-Au veins in this area postdates the extensive Pleistocene glaciation. By contrast, the Santa Florentina Formation records the Andean evolution east of the Sierra de Famatina (Dávila and Astini, 2003).

Quaternary alluvial and colluvial deposits cover more than 50 percent of the present-day surface of the mining district and consist of detrital country rocks dominated by clasts of the Negro Peinado Formation.
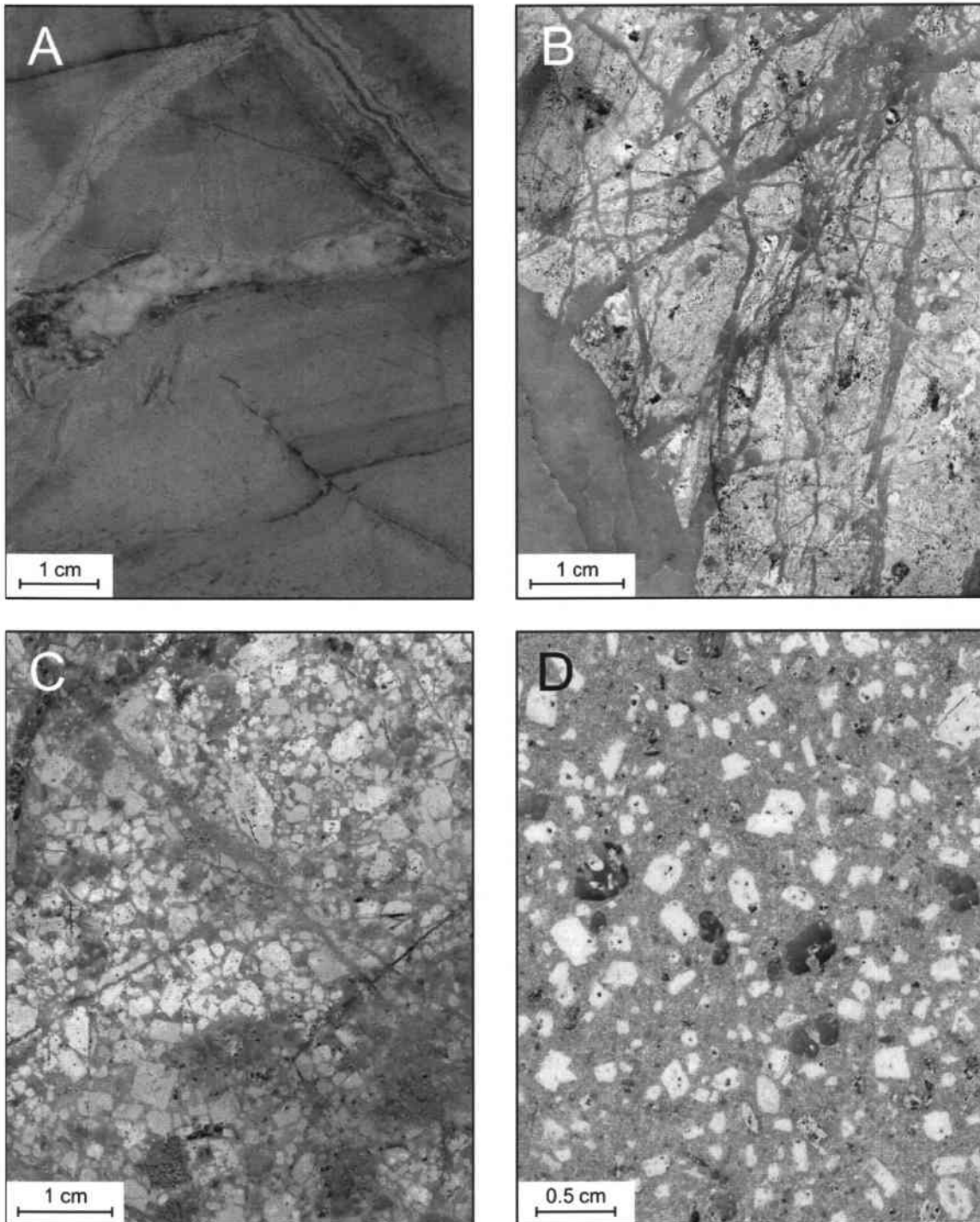
Figure 4.6: Photographs of the different host rocks illustrating the petrographic characteristics outlined in the text. (A) Hydrothermally altered metapelites of the Cambrian Negro Peinado Formation with relict sedimentary layering (sample FM-DH1-48.4). (B) Pervasively silicified dacitic porphyry of the La Estrechura area (sample FM-CP05-22). Supergene limonite replaces former Cu-Fe sulfides in this surface sample. (C) Strongly altered dacitic porphyry of the intrusive stock at Piedras Grandes (sample FM-DB99-03). Former phenocrysts of plagioclase, quartz, and biotite are set in a fine-grained groundmass. Cu-Fe sulfides are replaced by supergene limonite and jarosite. (D) Hydrothermally altered La Mejicana dyke illustrating the well-developed porphyritic texture (sample FM-DB99-37).

4.3.4 Geochronology

Radiometric age dating by Losada-Calderón et al. (1994) indicates that the igneous rocks of the Mogote Formation were emplaced at about 5.0±0.3 Ma (Table 4.2). However, the youngest intrusive activity in this area is represented by a quartz biotite monzonite, which intruded at greater depth and subsequently cooled below 350°C at about 4.0±0.1 Ma. During this time interval, the intrusion established a convective hydrothermal system, which resulted in porphyry Cu-Mo-Au mineralization adjacent to the intrusion and more distal high-sulfidation epithermal Cu-Au veins. Consistently, recent compilation of the lifespans of Central Andean Cu deposits by Sillitoe and Perelló (2005) suggests that most of them were active for about 1.2 to 2.1 My. Such long-lived hydrothermal activity has been interpreted by some investigators to result from superposition of two temporally discrete porphyry Cu systems (e.g., Reynolds et al., 1998; Ballard et al., 2001; Harris et al., 2004; Padilla-Garza et al., 2004). However, this concept has not been supported by petrographic evidence, such as the inversion of vein generations or the recurrence of the related alteration sequences (Sillitoe and Perello, 2005). Therefore, these time intervals are more likely to reflect multiple pulses of intrusion associated with hydrothermal circulation that are related to one magma chamber at greater depth (Cathles et al., 1997). This hypothesis is consistent with mineralogical similarities and the close temporal relationships between the quartz biotite monzonite and the pervasive sericitic alteration at about 4.2±0.4 and 3.7±0.2 Ma, respectively (see Table 4.2). However, previous studies using the less precise K-Ar technique yielded much younger ages for alunite from an epithermal vein, but are interpreted to reflect a supergene origin of the fine-grained sample (Losada-Calderón and Bloom, 1990).

4.3.5 Structures

The oldest regional fault systems in the Famatina Ranges strike northeast and northwest and were formed during the Famatinean orogeny (Losada-Calderón et al., 1994). However, the dominant structures are aligned fault blocks, which trend N-S and are bound by steeply dipping reverse faults (Losada-Calderón and McPhail, 1996). These blocks are the result of the Andean orogeny, as are the major N-S trending faults and fold axes. E-W trending faults, which formed as stress relief zones after the main tectonic event (Schalamuk and Logan, 1994), are unimportant on a

regional scale. Nevertheless, they appear to play a major role for the emplacement of the high-sulfidation epithermal Cu-Au veins. In contrast, almost all dacitic stocks and dykes of the Mogote Formation, which is the main host for the porphyry Cu-Mo-Au system, intruded along the pre-existing N-S trending structures (Losada-Calderón and Bloom, 1990). This regional aspect is characteristic for porphyry-related intrusions in the Central Andes of Chile and Argentina (Sillitoe, 1981).

Table 4.2: Radiometric age data of magmatic and hydrothermal (marked by the *) minerals from the Famatina mining district after Losada-Calderón et al. (1994; recalculated with Isoplot 3.00) and references therein. Numbers in **bold** represent plateau ages after the criterion of Ludwig (2003). All errors quoted for the Ar-Ar method are 2σ values, and 1σ for the K-Ar technique. The Pozo dacitic porphyry is not exposed in the mining district, but well known from drillcore material. The location of these small, hypabyssal bodies is indicated by the black stars shown in Figure 4.5.

Locality	Rock type	Analyte	Method	Age in Ma	Ar in %	Interpretation
El Durazno	tuff	biotite	Ar-Ar	6.6±0.8	99.9	cooling age
El Durazno	tuff	biotite	K-Ar	5.9±0.4	81.0	cooling age
El Durazno	tuff	biotite	K-Ar	5.7±0.4	81.0	cooling age
Los Bayos	dacite	biotite	K-Ar	5.9±0.2	27.0	cooling age
Caballo Muerto	rhyodacite	K-feldspar	Ar-Ar	5.9±0.5	100.0	cooling age
Caballo Muerto	rhyodacite	biotite	Ar-Ar	**5.3±0.1**	61.1	cooling age
Portezuelo de Illanez	dacite	biotite	Ar-Ar	5.2±0.1	100.0	cooling age
Portezuelo de Illanez	dacite	K-feldspar	Ar-Ar	**5.1±0.2**	84.1	cooling age
Pozo # 1	dacite	biotite	Ar-Ar	**5.3±0.1**	100.0	cooling age
Pozo # 2	dacite	K-feldspar	Ar-Ar	5.8±1.5	100.0	inherited core
Pozo # 3	dacite, altered	K-feldspar*	Ar-Ar	5.1±0.7	100.0	alteration age
Piedras Grandes	dacite	biotite	Ar-Ar	5.4±0.4	100.0	cooling age
La Estrechura	andesite	whole rock	Ar-Ar	6.2±1.2	100.0	mixed age
La Estrechura	andesite	whole rock	Ar-Ar	5.5±0.5	100.0	mixed age
La Estrechura	monzonite	biotite	Ar-Ar	**4.0±0.1**	89.6	cooling age
La Estrechura	dacite, altered	sericite*	Ar-Ar	4.2±0.4	100.0	alteration age
La Mejicana	dacite, altered	sericite*	Ar-Ar	**3.7±0.2**	83.5	alteration age
La Mejicana	epithermal vein	alunite*	K-Ar	1.7±0.5	94.8	alteration age
La Mejicana	epithermal vein	alunite*	K-Ar	1.7±0.8	95.0	alteration age

4.3.6 Geomorphology

The Late Cenozoic history of the Famatina mining district is mainly characterized by tectonic uplift and erosion, as indicated by accumulation of the Pleistocene Cueva de Peréz conglomerates (Figure 4.7 A+B). Apparently, glacial erosion has uncovered the upper parts of the porphyry system, whereas the high-sulfidation epithermal veins are preserved along an adjacent ridge (Figure 4.7 C+D). Both styles of mineralization are essentially unmodified since their formation, largely due to the lack of supergene alteration under arid climatic conditions that prevailed in this area for the last 15 My (Alpers and Brimhall, 1988). There is no evidence that the epithermal veins were overlain by substantial volcanic edifices. This observation implies that Pleistocene erosion and denudation caused major changes in the geomorphologic environment and may have had a direct effect on the superficial hydrodynamic regime, e.g., by fluid pressure changes leading to high-sulfidation epithermal ore deposition (Bissig et al., 2002). The rates of surface erosion, sediment transport, and landscape evolution are highly variable and largely depend on climate and/or tectonics (Kober et al., 2007). However, Cueva de Peréz conglomerates display abundant clasts of the Cambrian Negro Peinado Formation suggesting erosion of the deeper levels during Pleistocene glaciation and tectonic uplift. This hypothesis is consistent with investigations indicating that Cenozoic gravel accumulation along the Central Andes commonly exceeded 100 m/My and locally attained rates of up to 2-3 km/My (e.g., Reynolds et al., 1990; Kurtz et al., 1997; Horton, 2005).

In summary, the Nevados de Famatina porphyry system is associated with small hypabyssal bodies of dacitic porphyry of Early Pliocene age, the Mogote Formation (Losada-Calderón et al., 1994). Sericitic alteration assemblages and related QSP veins are associated with porphyry Cu-Mo-Au mineralization and may represent the roots of the epithermal Cu-Au deposit, hosted by metapelitic rocks of the Cambrian Negro Peinado Formation. The porphyry system formed prior to or synchronous with glacial erosion and denudation, probably as direct response to tectonic uplift and, hence, was incorporated into the valley pediments. By contrast, the high-sulfidation epithermal veins have been preserved along an adjacent ridge and developed clearly after incision of the Pleistocene Cueva de Peréz Formation.

Figure 4.7 A: Cueva de Peréz conglomerate just behind the mining camp at 3750 m elevation. The bottom of the valley is drained by the seasonal Río Amarillo River (photograph by J.W. Hedenquist).
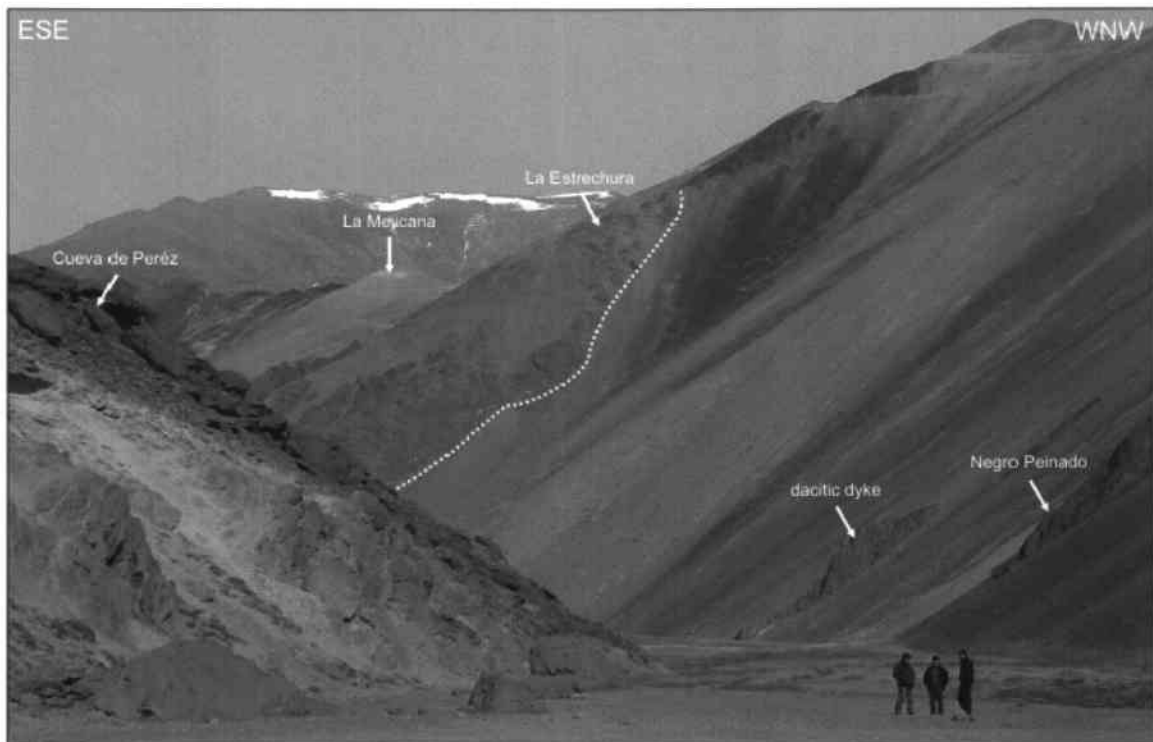
Figure 4.7 B: View from the mining camp up along the valley between Cueva de Peréz and the historic galleries of La Mejicana. Note the broadness of the valley's bottom (photograph by C.A. Heinrich).

Figure 4.7 C: Quebrada La Mejicana. The historic galleries of San Pedro, Restaurador, Estación, and Banco Nación are partly accessible and reflect the past high-grade Cu-Ag-Au vein production.

Figure 4.7 D: Quebrada Bello Plano looking south from La Estrechura. The small dacitic dyke at the northern flank of the ridge intruded into metasediments of the Cambrian Negro Peinado Formation.

5 APPROACH AND ANALYTICAL METHODS

5.1 Sample selection

The present study investigates the textural, mineralogical, and fluid inclusion characteristics in porphyry-type stockwork veins exposed at La Mejicana, Piedras Grandes, and La Estrechura, and in adjacent high-sulfidation epithermal ore veins preserved along the La Mejicana ridge. Samples were taken in their paragenetic and geologic context based on superpositional and cross-cutting relationships observed in the field and in cut hand specimens. Special emphasis was given to coarsely crystalline phases in order to increase the likelihood of finding workable fluid inclusions. The preexisting and well documented sample collection of D. Benkert formed the basis for this fluid inclusion study and was complemented by own field and drillcore sampling in 2005. Representative samples from the collection of A.J. Losada-Calderón served as reference material. The selection process involved searching hundreds of samples and included careful petrographic investigations in order to discriminate the various events of fluid entrapment. In detail, fluid inclusions were studied from quartz phenocrysts and in quartz crystals from different vein stages, corresponding to the spatial and temporal evolution of the magmatic-hydrothermal system at Famatina. However, appropriate fluid inclusions were only found in 14 samples and include drillcore sections, dumpsite material, and outcrop samples (Appendix figure 1, table 1).

5.2 Imaging approaches

5.2.1 Transmitted-light microscopy

Transmitted-light microscopy was used for fluid inclusion petrography in order to identify the types of fluid inclusions, their distribution, and the relative timing of fluid entrapment. All subsequent single inclusion measurements strictly concentrated on fluid inclusion assemblages, i.e., closely associated groups or trails of inclusions with visually identical phase ratios and similar shape (Goldstein and Reynolds, 1994). Petrographic analysis was conducted on doubly-polished, ca. 300 µm thick sections

using an Olympus BX-60 transmitted-light microscope equipped with a Nikon coolpix 5400 digital camera. Microscopic observation of the specific samples enabled us to discriminate inclusions that formed during initial mineral growth (i.e., primary and pseudosecondary fluid inclusions) from those that formed after mineral growth (i.e., secondary fluid inclusions). However, this classification of fluid inclusion origin after Roedder (1984) is a petrographic interpretation and provides no information about compositional variations in a crystal. Therefore, we used cathodoluminescence (CL) imaging in order to visualize the growth, fracturing, and recrystallization history of the crystals hosting fluid inclusions.

5.2.2 Cathodoluminescence

Cathodoluminescence (CL) microscopy has been used for the past 30 years in a number of different geological applications, such as sandstone petrography, ore mineral research, and microtectonics (e.g., Zinkernagel, 1978; Müller et al., 2000; Rusk and Reed, 2002; Redmond et al., 2004; Landtwing et al., 2005; Passchier and Trouw, 2005). In the present study, CL microscopy was combined with scanning electron microscopy (SEM) in order to visualize mineral textures at the scale of fluid inclusion entrapment. These textures result from variations in the luminescence of quartz caused by crystallographic imperfections, such as mineral nonstoichiometry, poor ordering of crystal structure, or trace element uptake (Götze et al., 2001). The defects that produce CL are a consequence of the specific physical and chemical conditions of quartz formation (Marshall, 1988). Based on this fact, we used the weak but highly variable CL characteristics of quartz in order to identify and correlate samples from different localities (Figure 5.1). However, the apparent luminescence observed in SEM-CL images depends on numerous operating conditions and cannot be easily quantified. Therefore, luminescence intensity is simply referred to as CL-black, CL-dark, CL-gray or -dull, and CL-bright. Measurements were carried out on carbon-coated, doubly-polished quartz wafers using a CamScan CS44LB instrument accomplished with special CL detectors. Samples were analyzed at 15 kV acceleration voltage, with 10 to 15 nA beam current, 0° sample tilt, and 35 mm working distance. These settings were kept constant throughout all measurements to allow comparison between the samples. Luminescence images were captured in about 30 s during CL operations by means of an EDAX Phoenix digital image

acquisition system. The obtainable image resolution was thereby largely dependent on the preparation of the sample and its sensitivity to beam damage.

5.3 Microthermometry

Fluid inclusion salinities and homogenization temperatures are essential pieces of information about the source or the pathways of fluids and about different processes during the fluid evolution. Accurate microthermometric fluid inclusion data are a prerequisite for such interpretations. In this study, fluid inclusions were measured on a Linkam THSMG-600 heating-freezing stage combined with a Leitz Wetzlar POL microscope and a Hamamatsu C5810 3CCD camera. Calibration of the system was performed on synthetic fluid inclusion standards manufactured by SYN FLINC®. Temperature readings are considered to be accurate to ±0.2°C for the melting point of CO_2 (-56.6°C) and H_2O (0.0°C), and to ±3°C for the critical point of pure H_2O (374.1°C). Apparent salinities of the natural fluid inclusions are reported in weight percent NaCl equivalent, based on the halite solubility equation for halite-saturated inclusions (Bodnar and Vityk, 1994) and on the final melting of ice (Bodnar, 1993) or clathrate (Diamond, 1992) for halite-undersaturated inclusions. Minor CO_2 may have been unnoticed in some fluid inclusions causing errors in the calculation of salinities. However, clathrates were generally absent or minor in abundance at the temperature of final ice melting.

Microthermometric results reported in Appendix tables 2, 3, and 4 strictly refer to fluid inclusion assemblages in the sense of Goldstein and Reynolds (1994). Freezing measurements and heating experiments up to the temperature of halite dissolution were carried out prior to LA-ICP-MS analysis to obtain the apparent salinities needed for internal standardization of elemental analyses (see below). Final homogenization provided minimum or absolute (in the case of boiling assemblages) fluid entrapment temperatures, but commonly led to stretching or decrepitation of some fluid inclusions. Therefore, limited high-temperature homogenization data were measured with fluid inclusions remaining in the same assemblage after LA-ICP-MS analysis. Average homogenization temperatures of these were then assumed for the analyzed fluid inclusions.
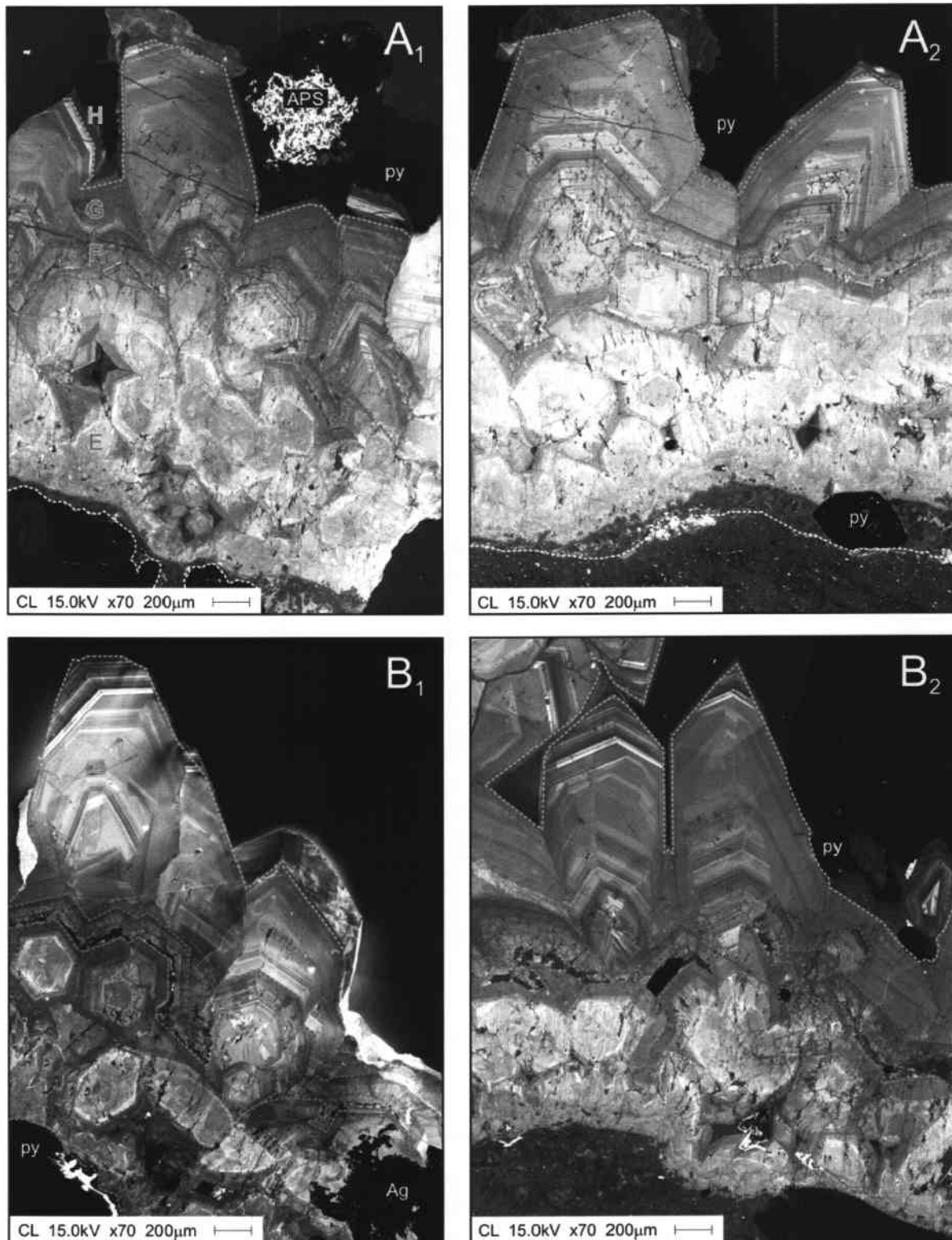
Figure 5.1: SEM-CL photomosaics of two separate QSP veins, which are about 5 cm apart from each other (sample FM-DH4-427.3, see Figure 7.1 D). Note the similarities in the CL characteristics of the successive quartz stages outlined in chapter 7. Dashed colored lines indicate the lower limit of each petrographic stage. (A$_1$) and (A$_2$) correspond to a vein exhibiting a small but well-defined sericitic alteration halo wedged between quartz E and the sedimentary host; whereas the alteration halo in (B$_1$) and (B$_2$) is less distinct. Locally, alumo-phosphate-sulfate (APS) minerals fill open spaces (A$_1$).

5.4 LA-ICP-MS

5.4.1 Introduction

Laser-ablation inductively-coupled-plasma mass-spectrometry (LA-ICP-MS) is widely used for determining the composition of fluid inclusions from major to trace element levels. In this study, we used quadrupole LA-ICP-MS for successive generations of fluid inclusion assemblages trapped in quartz in order to obtain *in situ* analysis at high spatial resolution. However, trace amounts of some geochemically relevant elements in the low mass region are difficult to detect due to polyatomic interferences produced by the carrier gas and the matrix (Pettke et al., 2000). Therefore, the non-interfered isotopes have been acquired instead. The quantitative analysis of fluid inclusions requires the use of an internal standard element whose concentration is known independently in the sample and the external standard (Longerich et al., 1996; Günther et al., 1998; Pettke et al., 2000; Heinrich et al., 2003). In this study, the concentration of Na was estimated from fluid inclusion salinities determined prior to laser ablation by microthermometry. Some elements are frequently below the limit of detection or were not measured for every fluid inclusion assemblage. Particularly, the analysis of Au concentrations in single fluid inclusions is a major achievement and was conducted under optimized conditions of the ICP-MS, for maximum response on ^{197}Au and a reduced element menu. Limits of detection are in the ppb to ppm region, depending on the volume and type of the individual fluid inclusion. Uncertainties on element concentrations from single analytical spots are about 3 to 5% at the two standard deviation level, mainly resulting from the flicker of the plasma ion source. This uncertainty increases to about 20 to 30% when concentrations approach their respective limits of detection. Similarly, accuracy is mainly limited by the analytical precision.

5.4.2 Experimental setup

A complete description of the instrumentation used in this study has been reported elsewhere (Günther et al., 1998; Heinrich et al., 2003; Pettke et al., 2004). Briefly, analyses were carried out with an Elan 6100 ICP-MS instrument (Perkin Elmer) combined with a prototype 193 nm ArF excimer laser system (Lambda Physik). For controlled ablation of the fluid inclusions, energy densities of 10 to 25 J/cm^2 and a

- 39 -

laser pulse frequency of 10 Hz were used. Efficient aerosol transport with a He-Ar carrier gas from the sample to the ICP was ensured by using a low internal volume ablation cell and a minimum length for the tubing (Heinrich et al., 2003). A limited element menu and short dwell times provided sufficient temporal resolution of the short transient signals typically produced by fluid inclusion analysis (Pettke et al., 2000). Combination of the excimer laser system with an imaging optical system permitted monitoring of the ablation process (Figure 5.2). Other parameters used for the fluid inclusion experiments are shown in Table 5.1.

5.4.3 Sample preparation

Prior to each LA-ICP-MS microanalysis, all fluid inclusion samples were thoroughly cleaned to remove surface contamination of the fluid inclusion signals, notably for shallow inclusions. The cleaning procedure included abrasive polishing with metal-poor diamond paste, followed by leaching with concentrated aqua regia (Klemm, 2005). This treatment was repeated in order to effectively minimize external contributions to the fluid inclusion signal, which may originate from the sample itself or from the polishing agent and equipment.

5.4.4 Laser ablation procedure

Experiments using the single-step ablation procedure with a pit size as big as the inclusion may lead to poor reproducibility due to partial loss of daughter minerals (Günther et al., 1998). This is especially problematic for complex polyphase fluid inclusions, e.g., brine inclusions. Therefore, we commonly used a stepwise opening procedure, with a small hole (4-8 μm pit) drilled first for the partial release of liquid and vapor. After detection of the first signal, the pit size was successively increased and finally expanded to the full size of the inclusion. This procedure was favorable for controlled ablation of the quartz samples and provided sufficient reproducibility for most major, minor, and trace elements measured in fluid inclusion assemblages. The resulting transient ICP-MS signals are fairly complex, but contain valuable qualitative information about the composition of individual crystals or micro-nuggets present in the inclusion (Figure 5.3).
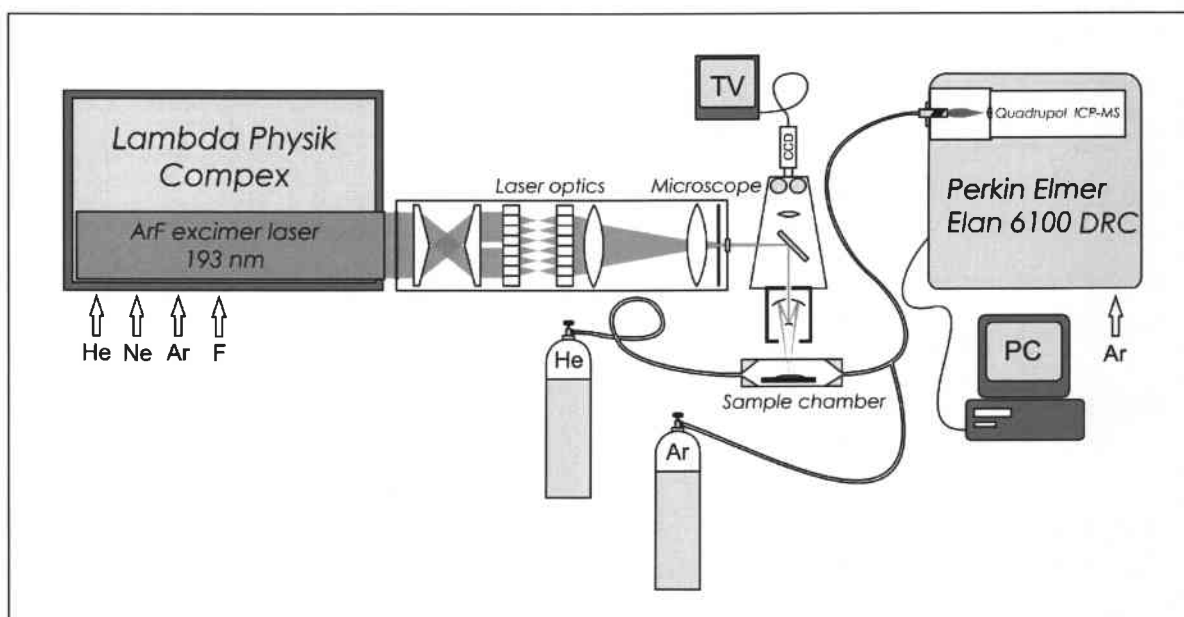
Figure 5.2: Experimental setup of LA-ICP-MS microanalysis used in this study. Measurements were carried out with an Elan 6100 ICP-MS instrument in combination with a 193 nm ArF excimer laser.

Table 5.1: Typical parameter set of LA-ICP-MS microanalysis used for the fluid inclusion experiments. For more detailed information the reader is referred to the text and references therein.

ICPMS instrument

Spectrometer	Elan 6100 DRC
rf-power	1350 W
Chamber gas flow	1.00 l min^{-1} (He)
Nebulizer gas flow	0.76 l min^{-1} (Ar)
Auxiliary gas flow	0.7 l min^{-1} (Ar)
Cool gas flow	14 l min^{-1} (Ar)
Analyzer vacuum	7.6 × 10^{-6} Torr
Cones	Al sampler cone, Pt or Ni skimmer cone
Resolution	0.7 amu
Dwell time	10 ms
Settling time	3 ms
Points per peak	1
Time per sweep	390 ms
Sweeps per reading	1
Isotopes	^{23}Na, ^{29}Si, ^{39}K, ^{55}Mn, ^{57}Fe, ^{65}Cu, ^{66}Zn, ^{75}As, ^{88}Sr, ^{95}Mo, ^{107}Ag, ^{121}Sb, ^{125}Te, ^{133}Cs, ^{197}Au (15x), ^{208}Pb

Laser ablation system

Laser	Compex 110 ArF excimer
Wavelength	193 nm
Energy density	10 - 25 J cm^{-2}
Repetition rate	10 Hz
Pit sizes	8 - 50 μm
Ablation chamber	In-house built plexiglas chamber

5.4.5 Data treatment

Absolute quantification of single inclusion LA-ICP-MS signals was carried out by integration of all elements including Na, correction for machine drift and host mineral contributions, comparison of intensity ratios with the external NIST glass standard SRM-610, and referencing the ratios to the absolute concentration of Na (Audétat et al., 1998; Günther et al., 1998; 1999; Heinrich et al., 2003). In this study, the concentration of Na was estimated from fluid inclusion salinities determined prior to laser ablation by microthermometry. These estimates are thought to be accurate to ±0.2% if the inclusions represent a simple model system whose phase relations are well known (Roedder, 1984). In chemically complex inclusions however, the apparent salinities were corrected for contributions of other major cations, such as K, Fe, and Pb, after the equation of Heinrich et al. (1992), which is based on the experimental observation that halide solubility and ice-melting isotherms depart at approximately right angles from the $NaCl-H_2O$ join in ternary phase diagrams with KCl, $CaCl_2$, and $FeCl_2$. This approach permits correct evaluation of absolute concentrations of all major and trace element concentrations in the fluid inclusions using the basic relationship of Longerich et al. (1996).

5.4.6 Limits of detection and uncertainties

The limit of detection (LOD) for each element strongly depends on the size and shape of individual inclusions and the laser ablation procedure. Since fluid inclusion assemblages usually comprise inclusions of variable size and shape, the LOD's of single inclusions may differ significantly. Therefore, LOD's have been calculated for each analysis individually, using 3 times the standard deviation of the background measurement ($3\sigma_{BG}$) divided by element sensitivity, after the corresponding equation of Longerich et al. (1996). For Au and other traces (e.g., As, Sb, Te) a slightly different approach was used, accounting for the poor instrument sensitivity and the very low abundance in natural fluid inclusions. Here, the inclusion intensities after background subtraction and host correction commonly fall below the significance limit. However, sometimes a Au signal can clearly be recognized as detected due to its intimate association with other elements, such as Cu (Figure 5.3). In these cases, the statistical significance limit was relaxed to $2\sigma_{BG}$ or $1\sigma_{BG}$ in order to obtain a semiquantitative concentration estimate. For fluid inclusion assemblages without a

signal, upper concentration limits (i.e., lowest measured LOD's based on $3\sigma_{BG}$) for these elements were selected and indicated as <VALUES. Typical uncertainties of ±20% are estimated from LA-ICP-MS analyses of several microthermometrically identical fluid inclusions in one assemblage, but they increase for small inclusions (<10 µm) and for element concentrations near the limit of detection (Ulrich et al., 1999; 2001).

5.4.7 The Au detection routine

Quadrupole ICP-MS instruments record transient signals sequentially, by cycling through all masses of interest and measuring each for a short period. Using typical parameters for data acquisition, this may lead to systematic errors due to non-representative sampling of the transient signal (Pettke et al., 2000). This is especially problematic for trace elements that tend to form clusters or nano-sized particles in the sample, such as Au in natural fluid inclusions. In order to enhance the reliability and reproducibility of Au analyses in fluid inclusions, Klemm (2005) developed a special routine measuring Au at every second position in one sweep. For a routine such as ^{23}Na, ^{197}Au, ^{29}Si, ^{197}Au, ^{39}K, ^{197}Au, ^{55}Mn, ^{197}Au, ^{57}Fe, ^{197}Au, ^{65}Cu, ^{197}Au, ^{66}Zn, ^{197}Au, ^{75}As, ^{197}Au, ^{88}Sr, ^{197}Au, ^{95}Mo, ^{197}Au, ^{107}Ag, ^{197}Au, ^{121}Sb, ^{197}Au, ^{125}Te, ^{197}Au, ^{133}Cs, ^{197}Au, ^{208}Pb, ^{197}Au, with a quadrupole settling time of 3 ms and 10 ms dwell time on each isotope, Au is analyzed for a total of 150 ms during one sweep of 390 ms. Due to software limitations, this procedure needs manual adjustment of the Au mass in very small steps (e.g., ±0.05 amu) around its real value of 196.9679 (Klemm, 2005). Averaging the count rates from the different Au "isotopes" for each sweep results in single Au values, which can be treated with conventional spreadsheet software (e.g., Lotus 1-2-3, Microsoft Office Excel).

5.4.8 Problems and observations

Au signals often originate from sources other than the fluid inclusion ablated for analysis, e.g., from Au-rich micronuggets naturally occurring in the host quartz, from surface contamination due to inadequate sample preparation, or from unstable accumulations of particles formed in corners and edges of the ablation cell and the tubing system. The latter two sources are easy to avoid by carefully cleaning the sample surface and by using streamlined aerosol transport systems with a minimum

of potential particle traps, respectively. However, the analysis of fluid inclusions hosted in Au-bearing quartz unavoidably leads to misleading results. Conventional host mineral corrections are most likely not applicable, because the distribution of solid inclusions is unknown and might be inhomogeneous. Recent SEM-CL studies on hydrothermal ore deposits in Bulgaria, Romania, and Utah revealed that Au-bearing quartz commonly exhibits a dark CL color (Kouzmanov, pers. commun.). This distinct characteristic may be used for identifying Au-rich zones in quartz in order to prevent fluid inclusion analysis and the resulting non-representative sampling.

LA-ICP-MS analysis of Au particles in fluid inclusions typically results in single, spike-like peaks, which may be misinterpreted as false signals. This problem can be solved to a certain extent by using the Au detection routine described above, which allows a better temporal resolution of the ICP-MS signal. However, Au contained in inclusions does not always form such particles (see Figure 5.3). This seems to be related to the time elapsed between microthermometry and LA-ICP-MS analysis. In detail, fluid inclusions that were heated for microthermometry several months before LA-ICP-MS analysis showed Au spikes, whereas samples of similar chemical composition homogenized directly prior to laser ablation did not. This observation indicates that homogenization of the inclusions causes re-dissolution of the Au nuggets and is reversible over time. Furthermore, it implies that Au spikes occurring in recently homogenized fluid inclusions most likely represent accidentally trapped particles. This assumption has been supported by anomalously high Au concentrations in single inclusions of selected fluid inclusion assemblages.

A further limitation in LA-ICP-MS analysis of fluid inclusions is the poor ablation behavior of the host quartz. The main problem encountered is thermal fracturing of the matrix ahead of the laser beam, enhancing premature release and loss of the inclusion fluid by leakage along microcracks (Shepherd and Chenery, 1995). According to own experience, the ablation process can be improved significantly by special homogenization optics allowing creation of a laterally homogeneous energy distribution across the laser pit, or by a stepwise increase in the diameter of the ablation crater using a laser ablation system with imaging optics.
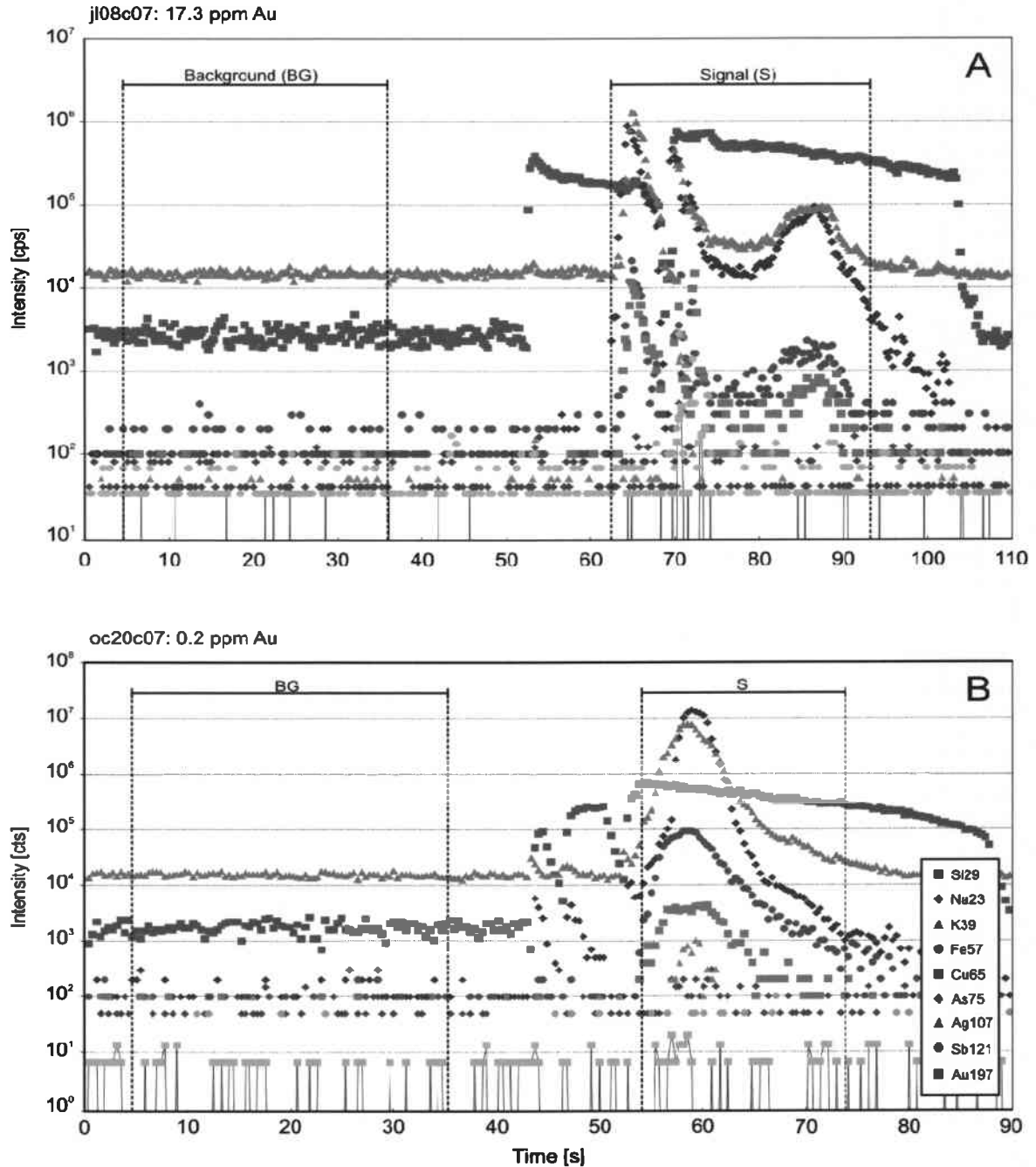
Figure 5.3: LA-ICP-MS signals from single inclusions of selected fluid inclusion assemblages achieved by stepwise increasing the diameter of the ablation crater. (A) Au nuggets in brine inclusions result in spike-like signals intimately associated with other siderophile elements, such as Cu, As, and Sb. The host sample was heated for microthermometry several months before LA-ICP-MS analysis. (B) The continuous Au signal from a sample homogenized directly prior to ablation yielded geologically more reasonable Au concentrations indicating accidental entrapment of Au in chart A.
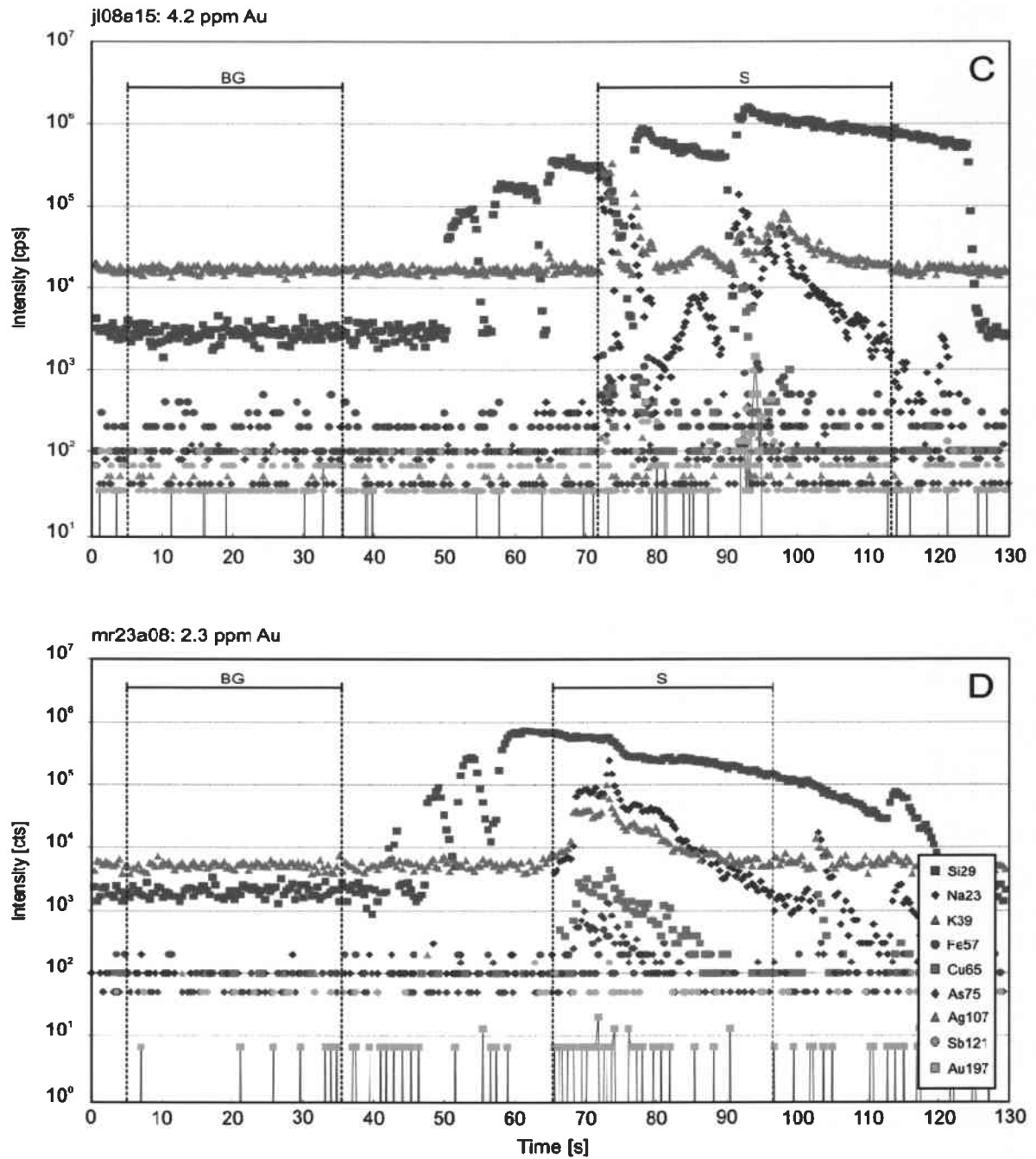
Figure 5.3 (cont.): LA-ICP-MS signals from single inclusions of selected fluid inclusion assemblages achieved by stepwise increasing the diameter of the ablation crater. (C) Au nuggets in aqueous inclusions may have formed after fluid entrapment at room temperature, but can be misinterpreted as accidentally trapped particles. (D) The continuous Au signal from a sample homogenized directly prior to ablation yielded similar Au concentrations indicating re-dissolution of the particle due to heating.

6   PORPHYRY-STAGE MINERALIZATION

6.1   Introduction

The Nevados de Famatina porphyry Cu-Mo-Au system comprises at least three stockwork-veined dacitic stocks of the igneous Mogote Formation, which intruded during the Early Pliocene (Losada-Calderón et al., 1994; see Chapter 4). Magma emplacement and subsequent hydrothermal activity caused intense fracturing and a superimposed network of various vein types in the porphyries and the adjacent sedimentary wall rocks. Based on mineralogical and textural observations, Losada-Calderón (1992) described five different mineralization stages: the pre-mineralization stage I and the late magmatic stage II, both associated with potassic alteration; the transitional stage III and the main hydrothermal stage IV, both accompanied with sericitic alteration assemblages; and the late hydrothermal stage V, which is more typical of a shallow high-sulfidation epithermal environment.

In this study, the classification scheme has been slightly modified paying particular attention to the early magmatic-hydrothermal processes. However, the current level of erosion prevents sampling of the deeper parts of the porphyry system. Therefore, selected samples originate from intrusions currently exposed at the surface, which occur subjacent to the high-sulfidation epithermal Cu-Au veins: i) the dacitic dyke at La Mejicana, ii) the intrusive stock at Piedras Grandes, and iii) the dacitic porphyry at La Estrechura (see Figure 4.5).

The following paragraphs are based on detailed petrographic investigations in combination with scanning electron microscopy cathodoluminescence (SEM-CL). This approach enabled us to identify and correlate the different quartz formation stages at all sampling sites and to reconstruct the overall paragenetic sequence of the porphyry system. Furthermore, it formed the basis for selection of representative fluid inclusion assemblages suitable to be analyzed by microthermometry and laser-ablation inductively-coupled-plasma mass-spectrometry (LA-ICP-MS). The results allowed an interpretation of the evolution of the ore-forming magmatic-hydrothermal fluids across the P-T-X space.

6.2 Mineralization and alteration

Hydrothermal processes in the Famatina Cu-Mo-Au district are deduced largely from the distribution of the different vein types. The vein types recognized in the porphyry system are A-veinlets and B-veins (Gustafson and Hunt, 1975; see Figure 6.1). The earliest vein type, the so-called A-veinlets, represent the pre-mineralization stage I and correspond to epigranular quartz veinlets with variable amounts of K-feldspar, biotite, magnetite, ilmenite, hematite, and anhydrite. A-veinlets range in thickness from 1 mm to about 2 cm and occur in all dacitic stocks investigated. They also extend into the metasediments of the Cambrian Negro Peinado Formation, in close proximity to the intrusive rocks. Vein quartz has a characteristic vitreous luster and anhedral granular texture. A-veinlets are associated with potassic alteration. The lack of internal symmetry or open vugs and the irregular but sharply defined walls suggest that they formed in still partly ductile rocks.

B-veins correspond to late-magmatic stage II and transitional stage III veins after Losada-Calderón (1992), which were not discriminated in this study. In general, they consist of quartz, molybdenite, and pyrite, with minor orthoclase, magnetite, biotite, rutile, ilmenite, hematite, chalcopyrite, bornite, and late chalcocite. Quartz is mostly granular, but grains oriented perpendicular to the vein walls occur as well. Vein centers are locally vuggy and vein walls are parallel and slightly wavy. B-veins range in thickness from 2 mm up to 6 cm and have been observed in all dacitic porphyries as well as in the adjacent sedimentary wall rocks. The sulfides either occur in vein centers or fill fractures that cut the coarser grained veins. B-veins are commonly associated with potassic alteration envelopes; grading upwards into texturally destructive sericitic alteration assemblages. This transition appears to be synchronous with the introduction of Cu-bearing minerals. Cross-cutting relationships clearly indicate that B-veins generally postdate A-veinlets.

The potassic alteration assemblage associated with A-veinlets and B-veins includes quartz, orthoclase, biotite, sericite, magnetite, hematite, ilmenite, rutile, and minor anhydrite. In intensely altered *igneous rocks* at Piedras Grandes, a fine-grained intergrowth of K-feldspar and quartz has completely obliterated the original texture. Magnetite commonly alters to hematite and ilmenite, whereas secondary biotite and chlorite partially replace amphiboles. In some cases, primary biotite has been

partially replaced by ilmenite and rutile. Anhydrite occurs as isolated grains in microfractures and may be altered to gypsum. B-veins that cut through *metapelitic rocks* are commonly associated with fine-grained alteration halos of secondary biotite, orthoclase, and minor ilmenite-rutile intergrowths.

Sericitic alteration assemblages occur in the upper part of the system and comprise quartz, sericite, pyrite, illite, and rutile. In the *porphyry* samples feldspar is altered to sericite and illite, and biotite has been totally replaced by intergrowths of sericite, pyrite, rutile, and minor chalcopyrite. Magnetite alters to rutile±pyrite aggregates. In *metapelitic rocks* quartz-sericite-pyrite halos around B-veins are common and may reach widths of several cm. Sericite is slightly phengitic in composition (Losada-Calderón, 1992), and occurs as selvages or as well-developed flakes and fans. Pervasive sericitic alteration predominates in vicinity of the dacitic dyke at La Mejicana and usually obliterates the original rock texture.

Propylitic alteration assemblages include chlorite, epidote, calcite, and minor albite, and occur mainly in the distal and cooler parts of the system, i.e., near the southern and northeastern limits of the district (Losada-Calderón, 1992). Here, veins are rare and therefore, this type of alteration will not be discussed any further.

Advanced argillic alteration tends to be localized on top of the intrusive bodies and generally obliterates previous alteration assemblages. This texturally destructive type of alteration consists of alunite, kaolinite, clay minerals, pyrophyllite, quartz, alumo-phosphate-sulfate (APS) minerals, sericite, pyrite, and rutile, with minor zunyite, fluorite, and anhydrite. Alunite is the dominant mineral and shows either a bladed, pseudocubic, or epigranular habit. Previous electron probe microanalyses (EPMA) revealed a minor natro-alunite component that appears to decrease with depth (Losada-Calderón, 1992). Zunyite has only been observed in the uppermost part of the La Estrechura porphyry. Locally, pervasively altered *igneous and metapelitic rocks* show a gradual transition into highly siliceous zones, where quartz replaces all previous mineral assemblages. These discontinuous and small zones occur as patches within the advanced argillic alteration and are particularly abundant in the dacitic porphyry at La Estrechura.

Supergene alteration minerals are rare but occur throughout the district and include jarosite, goethite, limonite, and hematite, with minor chalcocite, gypsum, alunite, and kaolinite. According to Losada-Calderón (1992), ferrimolybdite, turquoise, and cuprite are also present.
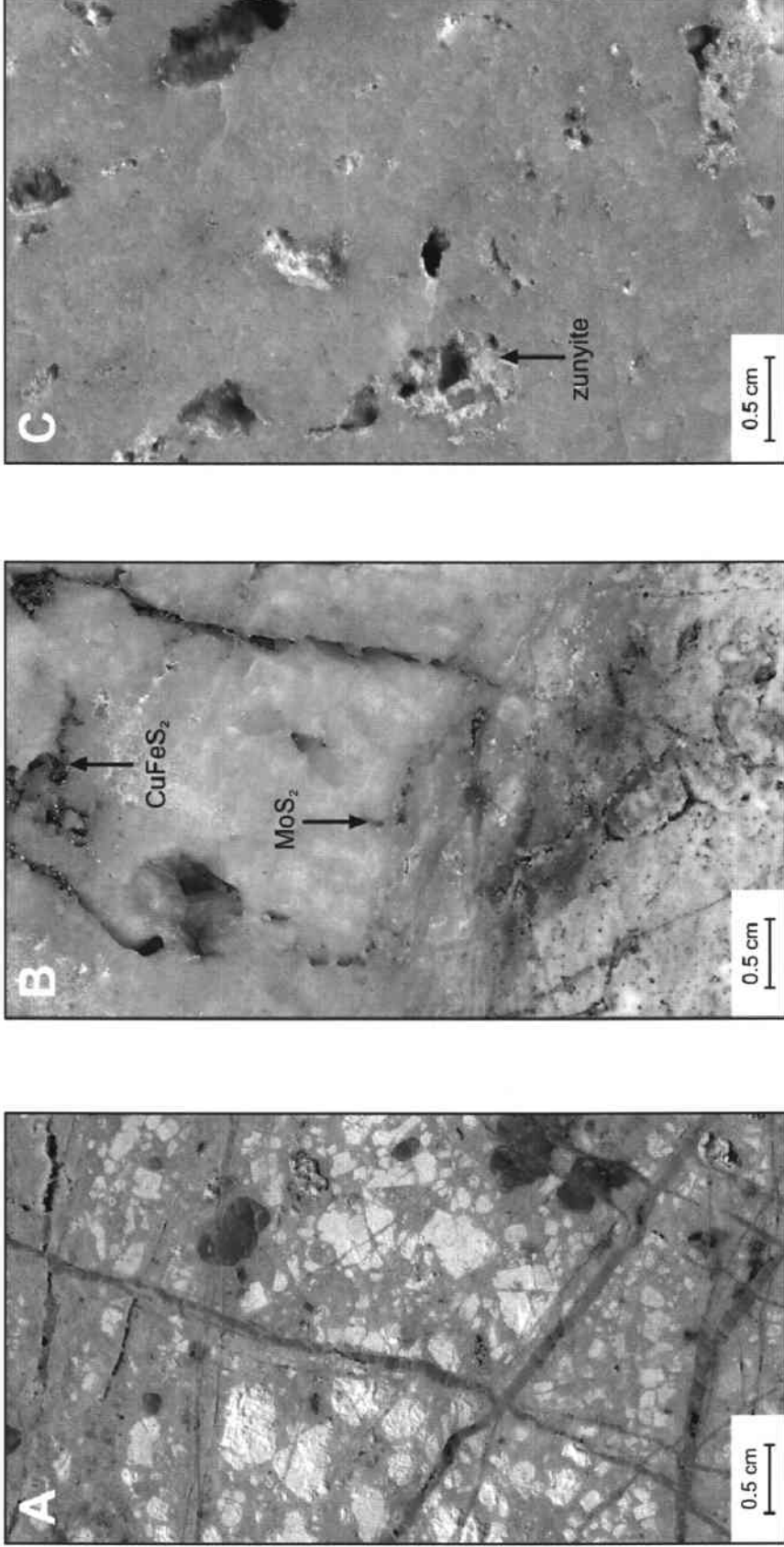
Figure 6.1: Photographs of selected porphyry veins illustrating the characteristics of the different vein types in the porphyry system of the Famatina mining district. (A) Crosscutting A-veinlets in a pervasively altered dacitic porphyry of the Los Bayos intrusion shown on map 4.5 (sample FM-DB99-66). The original potassic mineral assemblage has been overprinted by sericitic alteration. (B) Sulfide-bearing B-vein in sericitic altered metasediments of the Negro Peinado Formation (sample 28-05). Sulfides occur either along vein margins or in vein centers and include molybdenite, chalcopyrite, and minor covellite. (C) Quartz stockwork in the La Estrechura dacitic porphyry (sample FM-CP05-20). Advanced argillic alteration and extreme silicification completely obliterate the original rock texture. Open spaces are filled with alunite, kaolinite, and euhedral zunyite.

6.3 Paragenetic sequence

6.3.1 Macroscopic observations

The present study is based on surface samples, dumpsite material, and drillcore sections collected within the mining district with particular emphasis on the relative timing of the vein stages. Vein chronology was deduced from superpositional and cross-cutting relationships observed in the field and from hand specimen. In detail, selected sample material originates from three localities, which represent spatially separated intrusions of the igneous Mogote Formation. The next paragraphs will provide a short summary of the geologic, mineralogical, and textural characteristics at all three sample locations followed by a tentative correlation of the different vein stages (Table 6.1).

The paragenetic sequence observed in dumpsite material of the *La Mejicana* dacitic dyke (LMD) can be summarized as follows: crystallization of subhedral quartz phenocrysts; formation of irregular, crosscutting A-veinlets; precipitation of quartz and minor pyrite in straight B-veins; re-activation of these veins during formation of euhedral QSP mineralization clearly associated with pervasive sericitic alteration; brecciation of the previous mineral assemblage by quartz-bearing enargite-pyrite veins. In summary, five discrete events of quartz formation have been recognized. The latter two do not correspond to the porphyry-stage mineralization, but represent later mineralization stages that will be discussed separately.

The vein sequence recorded in the mineralized stock of the *La Estrechura* dacitic porphyry (LEP) is dominated by quartz stockwork veins, which are interpreted to reflect the flow lines of the ore-forming fluids. Here, irregular A-veinlets that lack any sulfides are cut and off-set by straight B-veins, which are commonly associated with potassic alteration halos. These clear to milky white quartz veins contain variable amounts of sulfides, including pyrite, molybdenite, and minor chalcopyrite. Pervasive silicification appears to be restricted to the upper parts of the intrusion and commonly results in recrystallization and complete obliteration of the original rock texture. Locally, late QSP veins cut through the porphyry and the adjacent metasediments of the Negro Peinado Formation.

The paragenetic sequence observed in the weakly mineralized *Piedras Grandes* dacitic porphyry (PGP) can be summarized as follows: crystallization of subhedral

quartz phenocrysts; formation of hairline magnetite veinlets; fracturing of the outer carapace and formation of irregular A-veinlets; precipitation of quartz and minor molybdenite and pyrite (± chalcopyrite) in straight B-veins commonly associated with potassic alteration halos; formation of euhedral QSP veins, which mainly occur in the upper parts of the intrusive body and are accompanied with pervasive sericitic alteration. The early magnetite veinlets are only known from drillcore material and contain little or no quartz. The alteration halo surrounding these veins is composed of magnetite, K-feldspar, biotite, anhydrite, and secondary hematite and ilmenite. Due to their rare occurrence they were not considered for further investigations.

Detailed mineralogical and textural studies on individual intrusions of the Mogote Formation formed the basis for establishing the overall paragenetic sequence of the porphyry system. However, correlation of single veins between the different localities remains speculative due to the fact that they were generated during spatially separated pulses of magmatic and related hydrothermal activity. Being aware of these limitations and assuming that the magmatic source is the same for all porphyries, it is possible to tentatively correlate the different vein stages. Hence, the selected samples are interpreted to represent one major event genetically related to formation of the Nevados de Famatina porphyry Cu-Mo-Au system.

Table 6.1: Summary and tentative correlation of the different vein stages observed in the porphyry system linked with the trapping chronology of discrete fluid inclusion types. **X** highlights representative vein stages and fluid inclusion types selected for further investigations. Abbreviations: PGP, Piedras Grandes porphyry; LEP, La Estrechura porphyry; LMD, La Mejicana dyke.

Host	Sample ID	Vein stages			Quartz stages					Fluid inclusion types									
		Phenos	A-vein	B-vein	P	A	B	C	D	ID_P	ID_A	V_A	B_A	V_B	B_B	V_C	B_C	V_D	L_D
PGP	FM-DB99-15		**X**	**X**		X	X	X	X				**X**	**X**	**X**	**X**	**X**	**X**	**X**
PGP	FM-CP05-27	X	X	X		X		X						**X**	**X**				**X**
LEP	FM-CP05-21	X	X			X		X			**X**	**X**	**X**						**X**
LEP	FM-CH04-02	X	X	X		X	X				**X**	**X**	**X**			X	X		
LMD	FM-CP05-37	**X**	X	X	X	X		X	X	**X**	**X**	**X**							**X**
LMD	FM-CP05-34	**X**	X	X	X	X			X	**X**	**X**	**X**							**X**

6.3.2 Microscopic observations

Following field sampling with special emphasis on the local time relations of the vein stages, more than 50 thick sections were prepared and studied by mineral and fluid inclusion petrography. Out of this material, six representative samples were selected for further investigations. For the exact sample location the reader is referred to the geologic map shown in Appendix figure 1. Constraints on the magmatic-hydrothermal evolution of the porphyry system were obtained from transmitted-light microscopy in combination with SEM-CL (Appendix figure 2). This approach enabled us to identify and correlate the different generations of quartz and to reconstruct the succession of quartz formation. Samples from the collection of A.J. Losada-Calderón served as reference material in order to link the trapping chronology of fluid inclusions to the established paragenetic sequence. This link was possible because changes in the characteristics of the host quartz are consistent with the entrapment of discrete fluid inclusion types (see Table 6.1). In summary, the evolution of the porphyry system is multiphase but systematic and can be generalized as follows (Figure 6.2):

The earliest fluids in the magmatic-hydrothermal system are preserved in large quartz phenocrysts (P) hosted in dacitic porphyries at all sample locations. Most of these phenocrysts have subhedral forms due to early growth within the crystallizing magma. Commonly, they are deeply embayed by the surrounding melt (i.e., matrix) and show no evidence for recrystallization. Therefore, they are thought to represent the *late magmatic stage* of the porphyry system. The CL petrography of these quartz phenocrysts clearly reveals zonation with a darker core surrounded by progressively lighter rims. This zonation is thought to reflect subtle changes in the melt composition due to p-T variations in a progressively crystallizing magma.

The *early hydrothermal stage* corresponds to a locally dense network of irregular quartz veinlets without a distinct alteration halo. Several generations of crosscutting quartz veins indicate repeated fracturing of the semi-plastic host rock. These typical A-veinlets consistently cut through the quartz phenocrysts and were formed prior to porphyry mineralization. The CL characteristics of this quartz generation (A) include a dull luminescence (CL-gray) and a very weak zonation.

The *main hydrothermal activity* is characterized by straight B-veins that are commonly associated with potassic alteration halos. B-veins typically show early deposition of molybdenite, followed by remobilization and co-precipitation with Cu-

bearing sulfides, such as chalcopyrite. Therefore, they are interpreted to represent the main mineralization stage of the porphyry system. The CL petrography reveals two distinct quartz generations. The first one (**B**) exhibits a bright luminescence and oscillatory growth zoning. The second generation of quartz (**C**) has a dark CL color and occurs as overgrowths or fills microfractures that cut the earlier quartz generations. These cobweb-like networks of CL-dark quartz result from corrosion of CL-bright quartz along microfractures, followed by precipitation of CL-dark quartz in the corrosion cavities (Rusk and Reed, 2002).

The *late hydrothermal activity* corresponds to sericitic alteration assemblages that occur mainly in the upper part of the system. This alteration type is associated with petrographically late quartz, which occurs as overgrowths or fills open spaces. This last phase of quartz formation (**D**) is characterized by a black CL color and commonly mantles the bulk of ore metals precipitated at the contact to quartz C. Here, quartz C is patchy, discontinuous, and has embayed boundaries against quartz D. These textures indicate that the CL-dark quartz C formed first and was subsequently dissolved by quartz-undersaturated fluids (Rusk and Reed, 2002). The resulting pore space was infilled by ore metals, followed by precipitation of CL-black quartz D and associated sericitic alteration assemblages from a chemically distinct fluid.

Figure 6.2 (next page): Sample FM-DB99-15: Paragenetic sequence of quartz formation in a typical porphyry vein of the Famatina mining district acquired by SEM-CL. (A) The SEM-CL photomosaic illustrates the petrographic characteristics of the four generations of hydrothermal quartz as outlined in the text. Note the absence of the late magmatic stage represented by subhedral quartz phenocrysts. (B) Schematic map of the CL image highlighting the succession of quartz formation by different colors.

Quartz D

Quartz C

Quartz B

Quartz A

CL 15.0kV x70 400µm

CL 15.0kV x70 400µm
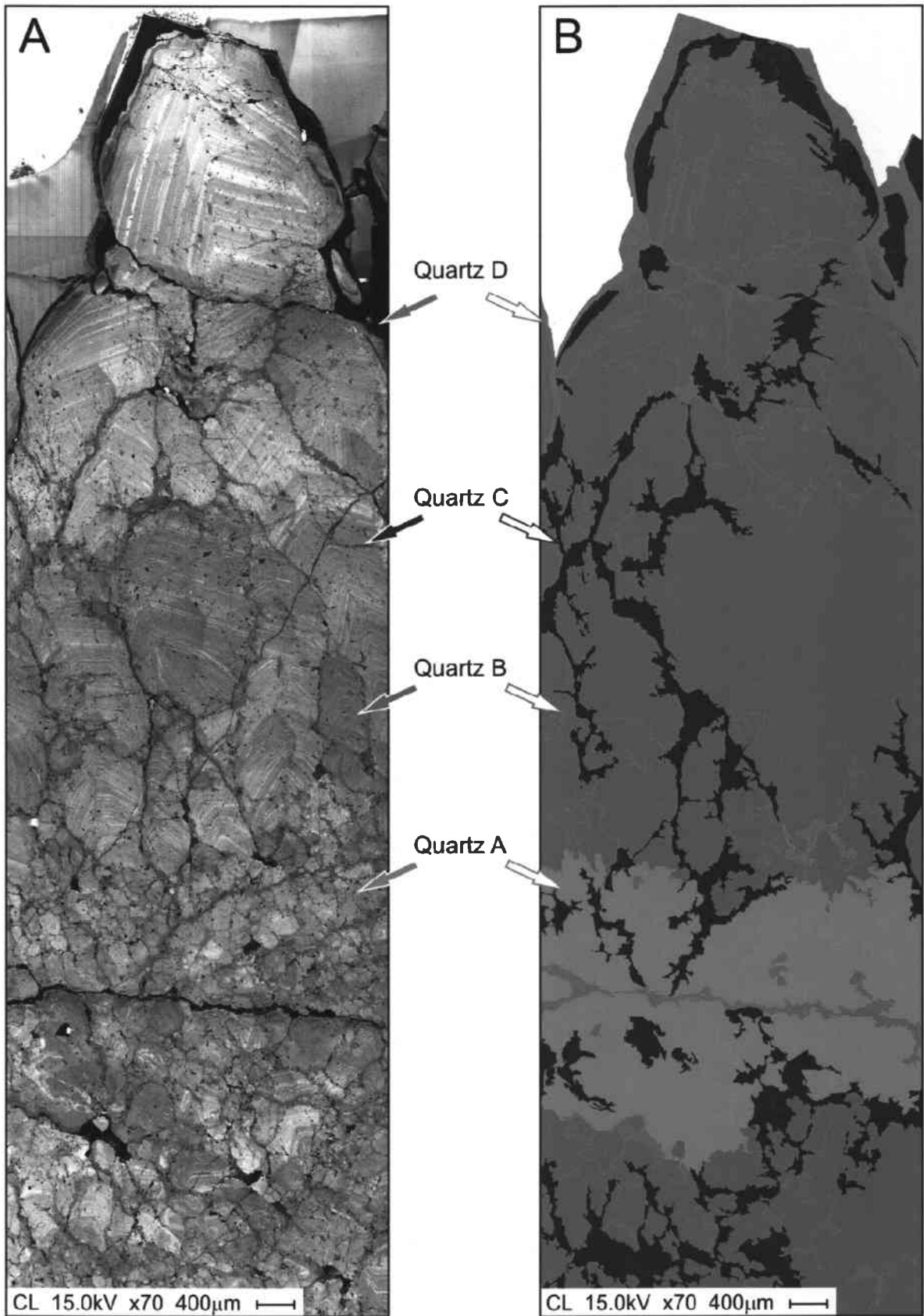
6.4 Fluid inclusion study

6.4.1 Types of fluid inclusions

The classification of fluid inclusion types employed in this study is based on phase relations observable at room temperature. All inclusion descriptions strictly refer to fluid inclusion assemblages in the sense of Goldstein and Reynolds (1994). Where possible, single inclusions were avoided in order to prevent non-representative sampling (Roedder, 1984). In general, the following fluid inclusion types have been recognized in the Nevados de Famatina porphyry system.

Intermediate density (ID): This type of inclusion contains two phases, a liquid and a vapor bubble amounting to 40 to 60 percent of the inclusion volume. One reddish or opaque daughter mineral, probably hematite, may occur. ID inclusions are commonly negative-crystal shaped, isometric, and range between 20 and 40 μm in size. They are ubiquitous in quartz phenocrysts and less frequent in A-veinlets.

Vapor-rich (V): These inclusions generally contain two phases, liquid plus more than 70 percent vapor. No daughter crystals and no liquid CO_2 could be observed. Vapor-rich inclusions commonly have a negative crystal shape and range between 20 and 40 μm in size. They are generally abundant in A-veinlets and B-veins and occur next to, or in coexistence with brine inclusions along individual boiling trails.

Hypersaline liquid (B): These so-called brine inclusions contain well-formed, cubic halite and generally several other daughter minerals. The second isotropic daughter mineral, sylvite, has rounded edges and a lower relief than halite. Reddish or opaque hematite commonly occurs as euhedral, hexagonal or trigonal plates. The vapor bubble occupies about 20 to 30 percent of the inclusion volume. Brine inclusions are ubiquitous in vein quartz and usually negative-crystal shaped, ranging in size between 10 and 40 μm.

Aqueous liquid (L): Aqueous inclusions are commonly irregularly shaped and up to 70 μm in size. They contain two phases, a liquid and a small vapor bubble, which occupies about 10 to 30 percent of the inclusion volume. One birefringent mineral, probably muscovite (i.e., sericite), may be present in variable proportions. This rare type of inclusion is restricted to the last phase of quartz formation (D), which is commonly associated with sericitic alteration assemblages.

6.4.2 Fluid inclusion petrography and microthermometry

The distribution of fluid inclusions in porphyry quartz was studied using standard techniques for petrography (optical microscopy, SEM-CL) and microthermometry. Samples examined for fluid inclusion study are representative of the paragenetic quartz stages described above and include quartz phenocrysts (P), A-veinlets (A), and B-veins (B, C, D). Host quartz is colorless and shows weak undulose extinction but commonly no recrystallization features. SEM-CL imaging of the individual quartz grains and vein sections revealed numerous reactivation textures. According to petrographic and microthermometric distinction criteria, such as daughter minerals, bubble size, salinities, homogenization behavior and temperature, host quartz, and relative age relationships, the following inclusion generations could be distinguished (Figure 6.3, see also Table 6.1):

O Late magmatic stage intermediate-density inclusions (ID_P)

● Early hydrothermal stage intermediate-density inclusions (ID_A)

▲ Early hydrothermal stage vapor-rich inclusions (V_A)

■ Early hydrothermal stage brine inclusions (B_A)

▲ Main hydrothermal stage vapor-rich inclusions, early sub-stage (V_B)

■ Main hydrothermal stage brine inclusions, early sub-stage (B_B)

▲ Main hydrothermal stage vapor-rich inclusions, late sub-stage (V_C)

■ Main hydrothermal stage brine inclusions, late sub-stage (B_C)

▲ Late hydrothermal stage vapor-rich inclusions (V_D)

◆ Late hydrothermal stage aqueous inclusions (L_D)

Microthermometric results are presented as averages of inclusion assemblages with one standard deviation uncertainty and are summarized in Table 6.2. Individual fluid inclusion data are reported in the Appendix table 2. Relative age relationships of the fluid inclusion generations present in the porphyry system and their assignment to the different quartz formation stages are shown in Appendix figures 2 A-F.

The salinity within a single assemblage is quite uniform (typically ±3 wt% $NaCl_{equiv}$) but varies greatly between different assemblages. However, measuring several fluid inclusion assemblages of identical petrographic appearance in different vein samples generally showed consistent salinities and homogenization temperatures, indicating that correlation of the vein stages between the separated intrusions is valid.
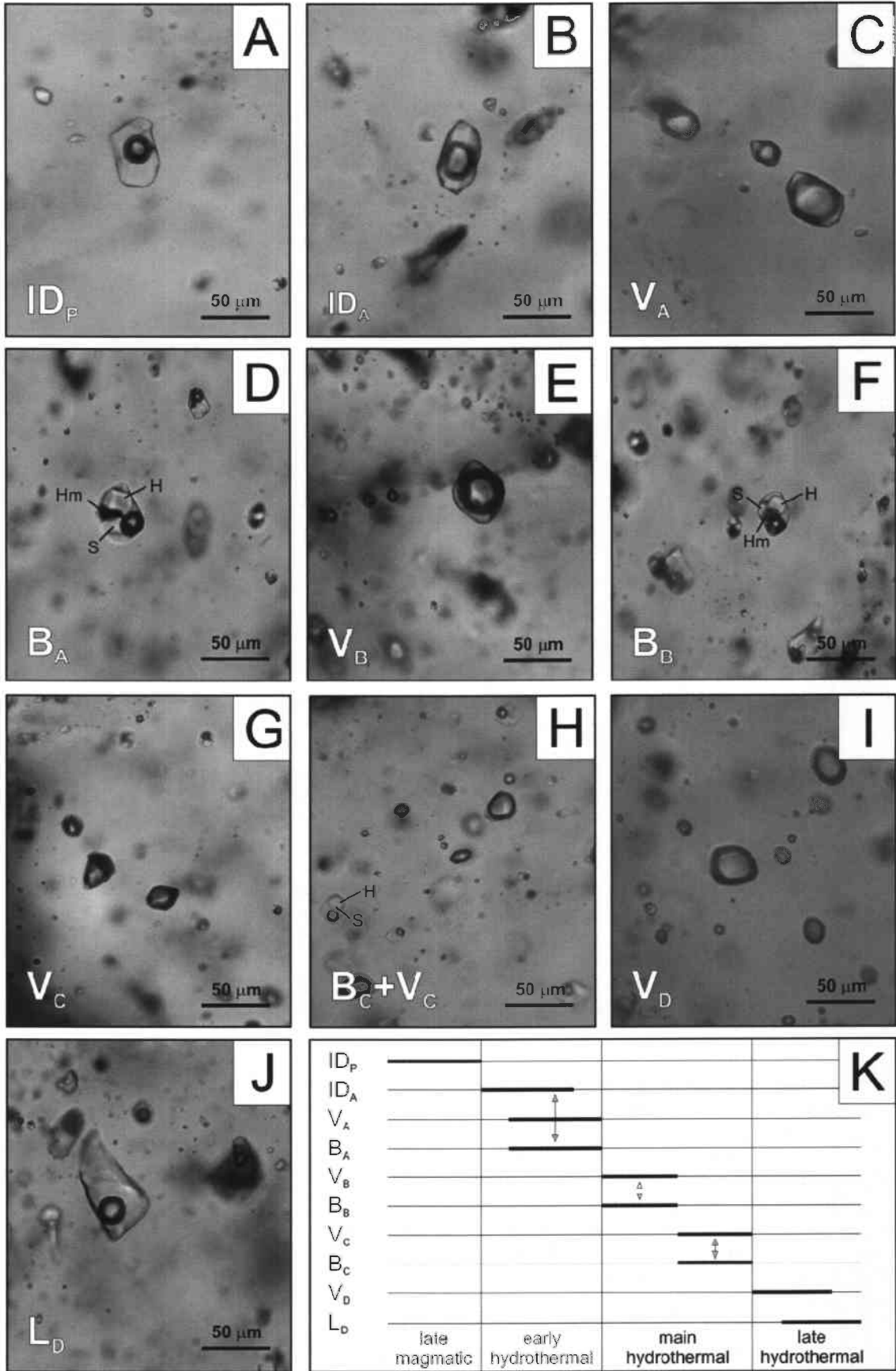
Figure 6.3 (previous page): Photomicrographs illustrating the fluid inclusion types of the porphyry system color-coded after their assignment to the different quartz formation stages. Intermediate-density fluid inclusions of type ID_P (A) are interpreted to represent a single phase fluid directly exsolved from the magma. The second type of intermediate-density fluid inclusions, ID_A (B), is petrographically later. The low-salinity vapor V_A (C) and the high-salinity liquid B_A (D) are the product of phase separation. Petrographically later high-salinity liquids B_B (F) resemble the B_A brines and occur next to or in coexistence with V_B vapors (E). Moderate-salinity B_C brines (H) occasionally coexist with low-salinity V_C vapors (G). Both are optically distinct from the previous inclusion assemblages, e.g., B_C brines have no hematite daughter, whereas V_C vapor bubbles occupy more than 80% of the inclusion volume. V_D inclusions (I) occur on late primary growth zones or on secondary trails. Aqueous fluids are represented by irregularly shaped L_D inclusions (J). Internal reflexion makes it difficult to detect accidentally trapped minerals, such as sericite. A schematic summary of the relative age relationships of the fluid inclusion generations determined by petrography is shown in (K). Vertical arrows indicate coexisting phases locally observed in individual boiling trails.

ID_P inclusions have a medium-sized vapor bubble (40-60 Vol%) and occasionally contain one tiny opaque daughter crystal. They are restricted to quartz phenocrysts and occur as primary inclusions along growth zones. Microthermometry revealed ice melting temperatures between -3.8±3.2°C (5.8±4.1 wt% $NaCl_{equiv}$) and -15.1±4.9°C (18.5±4.1 wt% $NaCl_{equiv}$) and total homogenization temperatures between 461±56 and more than 600°C. Where observed, total homogenization occurred near-critically (meniscus fading) or by vapor bubble disappearance into the liquid phase.

ID_A inclusions occur as primary inclusions in A-veinlets and on secondary trails in quartz phenocrysts crosscutting primary ID_P inclusions. They are optically identical to ID_P inclusions (40-60 Vol% vapor bubble) and can only be distinguished by relative age relationships and occasionally by their distinct homogenization behavior. Final melting of ice between -1.8±0.7°C and -12.4±1.5°C indicates slightly more consistent salinities within inclusion assemblages between 3.0±1.1 and 16.3±1.4 wt% $NaCl_{equiv}$. Total homogenization occurred mainly into the vapor phase between 408±16 and more than 600°C, but also near-critically or by vapor bubble disappearance into the liquid phase.

V_A inclusions have large vapor bubbles (80-90 Vol%) and are commonly negative-crystal shaped. No daughter crystal has been observed. V_A inclusions are generally abundant in A-veinlets and less frequent on secondary trails in quartz phenocrysts. Microthermometry was difficult to conduct due to the poor visibility of the liquid phase. Where final melting of ice was observable, apparent salinities range between

1.8±0.4 (-1.1±0.2°C) and 3.7±1.0 wt% NaCl$_{equiv}$ (-2.2±0.6°C). Total homogenization could not be observed.

The earliest brine generation, **B$_A$**, is characterized by a high density. The inclusions contain well-formed, cubic halite and generally several other daughter minerals, such as sylvite, hematite, and chalcopyrite. The vapor bubble fills about 20 to 30% of the inclusion volume. B$_A$ inclusions are subordinate in A-veinlets and commonly very small. Usually they occur next to or in coexistence with V$_A$ vapors. Apparent salinities of one assemblage were determined by final dissolution of halite at 534±5°C yielding values of 64.4±0.7 wt% NaCl$_{equiv}$. Total homogenization into the liquid phase did not occur up to 600°C.

A second group of vapor-rich inclusions, **V$_B$**, has smaller bubbles ranging between 70 and 80 Vol%. These high-density vapor inclusions occur as clusters or along growth zones in B-veins, indicating primary origin. Where final melting of ice was observable, the derived salinities range between 11.7±3.6 and 12.8±3.2 wt% NaCl$_{equiv}$. Due to the small amount of liquid, total homogenization could not be determined reliably.

B$_B$ brines occur as primary inclusions in B-veins and are commonly associated with V$_B$ inclusions. B$_B$ brines are optically identical to B$_A$ inclusions (20-30 Vol% vapor bubble, multiple daughter minerals) and can only be distinguished by relative age relationships and microthermometry. Salinities were determined by final dissolution of halite between 453±50 and 486±13°C, yielding values of 53.8±6.5 and 57.9±1.7 wt% NaCl$_{equiv}$. Total homogenization into the liquid phase mainly occurred by vapor bubble disappearance between 491±12 and 503±39°C. However, in some individual B$_B$ brines of two distinct inclusion assemblages, halite was the last phase to dissolve upon heating.

V$_C$ inclusions have large vapor bubbles (85-95 Vol%) and occur as primary inclusions along growth zones or on pseudo-secondary trails in B-veins. Daughter crystals were not observed. Microthermometry was difficult to conduct due to the poor visibility of the liquid. However, melting temperatures of ice between -1.9±0.1 and -3.0±0.1°C indicate rather consistent salinities between 3.1±0.1 and 5.0±0.2 wt% NaCl$_{equiv}$. Total homogenization could not be observed. However, for one boiling assemblage, the homogenization temperature has been inferred from coexisting B$_C$ brines.

B$_C$ brines represent the petrographically latest brine generation and occur on pseudo-secondary trails in B-veins. The inclusions generally contain cubic halite and a second isotropic daughter mineral with rounded edges, probably sylvite. The vapor

bubble fills about 20 to 30% of the inclusion volume. Final dissolution of halite occurred between 277±99 and 396±18°C, corresponding to salinities of 37.6±7.1 and 47.1±2.0 wt% $NaCl_{equiv.}$ Total homogenization into the liquid phase occurred by vapor bubble disappearance and took place between 455±21 and 552±38°C. Boiling assemblages of B_C brines coexist with V_C vapors on pseudo-secondary trails. They represent phase separation and yield temperatures of homogenization of 515±55°C, determined from brine inclusions by vapor bubble disappearance.

Low-density vapor inclusions of type V_D are restricted to the last phase of quartz formation in B-veins. These inclusions have a large vapor bubble (85-95 Vol%) and no daughter crystals. Final melting of ice occurred at -1.8±0.3°C, yielding salinities of 3.1±0.5 wt% $NaCl_{equiv.}$ Total homogenization into the vapor phase occurred between 335±6 and 357±11°C.

Aqueous inclusions of type L_D are also restricted to the last phase of quartz formation in the porphyry system. They either occur on late primary growth zones in free-grown quartz crystals in B-veins or on secondary trails that cut the older quartz generations. These fluid inclusions are commonly irregularly shaped and up to 70 μm in size. Large inclusions often contain accidentally trapped sericite, which was identified by LA-ICP-MS microanalysis. The vapor bubble occupies up to 30% of the fluid inclusion volume. Final melting of ice occurred between -1.0±0.3 and -9.9±8.3°C and indicates variable salinities between 1.8±0.5 and 12.6±8.1 wt% $NaCl_{equiv.}$ Total homogenization into the liquid phase by vapor bubble disappearance was observed between 219±8 and 294±86°C.

6.4.3 Pressure estimates

Even though it is not possible to document the entire fluid history in time at any point of the porphyry system, a generalized fluid evolution model can be deduced on the assumption that each intrusion and its fluid pulse followed a similar P-T path. This assumption is supported by the microthermometric results yielding consistent salinities and homogenization temperatures between several inclusion assemblages of identical petrographic appearance in different vein samples (Appendix table 2). Based on these data, pressure estimates can be calculated using the methods outlined in Roedder and Bodnar (1980), Roedder (1984), Bodnar et al. (1985), and more recently in Driesner and Heinrich (in press). Pressures determined for non-

boiling assemblages are derived from the homogenization temperature and represent minimum values. By contrast, boiling assemblages will give absolute fluid entrapment temperatures and, thus, provide the most accurate and unambiguous geobarometry data available (Roedder, 1984).

Evidence of boiling in the Nevados de Famatina porphyry system is widespread and occurs in quartz stages A, B, and C. However, due to the common trapping of a mixture of the two coeval phases (i.e., brine and vapor), particular attention was paid to individual trails of pure endmember inclusions, probably yielding more reliable salinities. In addition, compositional deviations of the fluids from the binary H_2O-NaCl model system introduce systematic uncertainties. Therefore, the following pressure estimates, which are summarized in Appendix table 2, should be considered as minimum values, if not stated otherwise.

Vapor pressure estimates calculated for low- to intermediate-salinity ID_P inclusions range between 450 and more than 910 bars. Petrographically later ID_A inclusions show a wider scatter from 280 to more than 900 bars, and cluster mainly between 300 and 650 bars. Therefore, they are interpreted to reflect a vapor-like fluid that has been trapped at lower pressures.

The uncertainty in the values derived from low-salinity vapor inclusions is obviously much greater, due to the very poor visibility of the liquid phase. However, pressure estimates for high-temperature V_A vapors commonly exceed 760 bars. Coexisting high-salinity B_A brines were observed in both samples from the La Estrechura porphyry. Unfortunately, only inclusions in sample FM-DB99-15 from the intrusive stock at Piedras Grandes were sufficiently large for microanalysis, indicating fluid entrapment at any pressure higher than 510 bars.

Experimental difficulties prevented calculation of pressure estimates for vapor-rich inclusions of type V_B. However, coeval B_B brine inclusions probably represent pure endmembers of the boiling liquid and yield values between 300 and 340 bars.

Similarly, pressure estimates for low-density V_C vapors were impossible to conduct due to the small amount of condensed liquid. Therefore, the pressure has been calculated from the homogenization temperature of the coexisting B_C brines, yielding values of 300 to 570 bars. Most strikingly, these estimates do not match the apparent salinities determined for the coeval vapor phase. This observation implies that single vapor inclusions may have trapped a mixture of the two phases due to the enhanced wetting force of the coexisting brine (Roedder and Bodnar, 1980).

Low-density V_D vapors are restricted to the last phase of quartz formation and may have been trapped prior to formation of aqueous liquids of type L_D. Both inclusion types provide minimum values based on vapor pressure. Estimates for the vapor-rich inclusions yield values of 176 bars, whereas minimum pressures for L_D inclusions range between 22 and 75 bars. However, due to the lack of boiling no independent evidence exists indicating how much the pressure of fluid entrapment might have exceeded the vapor pressure.

Table 6.2: Overview of fluid inclusion types and their assignment to the different quartz generations based on petrographic distinction criteria and microthermometric observations. For more information, the reader is referred to the text and Appendix table 2. Abbreviations: Qtz, quartz; FI, fluid inclusion; NaCl, apparent salinity in wt% NaCl equivalent; Th, total homogenization temperature in °C; Hm, hematite; H, halite; S, sylvite; n.d., not determined; occ., occasionally; acc., accidentally.

Qtz stage	FI type	Vapor Vol%	Daughter minerals	NaCl min.	NaCl max.	Th min.	Th max.	Th mode	Distinction criterion
P	ID_P	40-60	Hm	5.8±4.1	18.5±4.1	461±56	>600	V-->L	primary in phenocrysts
A	ID_A	40-60	Hm	3.0±1.1	16.3±1.4	408±16	>600	L-->V	cross-cutting ID_P
A	V_A	80-90	none	1.8±0.4	3.7±1.0		>600	L-->V	occ. coexisting with B_A
A	B_A	20-30	H, S, Hm	64.4±0.7			>600	S--H--V-->L	primary in A-veinlets
B	V_B	70-80	none	11.7±3.6	12.8±3.2	n.d.	n.d.	L-->V	occ. coexisting with B_B
B	B_B	20-30	H, S, Hm	53.8±6.5	57.9±1.7	491±12	503±39	S--H--V-->L	primary in B-veins
C	V_C	85-95	none	3.1±0.1	5.0±0.2	n.d.	n.d.	L-->V	occ. coexisting with B_C
C	B_C	20-30	H, S	37.6±7.1	47.1±2.0	455±21	552±38	S--H--V-->L	cross-cutting B_B
D	V_D	85-95	none	3.1±0.5		335±6	357±11	L-->V	Th below 400°C
D	L_D	20-30	none	1.8±0.5	12.6±8.1	219±8	294±86	V-->L	acc. trapped sericite

6.5 LA-ICP-MS microanalysis

LA-ICP-MS microanalysis was carried out on 164 individual fluid inclusions from 29 petrographic inclusion assemblages (see Appendix table 5). Generally, all inclusion types contain considerable amounts of Na, K, Fe, and Cu, with traces of As, Mo, Ag, Sb, Te, Cs, Au, and Pb. Most strikingly, element ratios, such as K/Na, Pb/Na, or Cs/(Na+K+Fe), remain almost uniform across the entire inclusion sequence and do not show a salinity-dependent variation (Figure 6.4 A, E, G). Some minor deviations in the K/Na ratio between coexisting brine and vapor inclusions seem to confirm that NaCl dissolves preferentially over KCl in the vapor phase (Anderko and Pitzer, 1993), or simply correspond to potassic alteration (Figure 6.4 I). By contrast, other elements show significant fluctuations (Fe, Cu, and Mo) or are frequently below the limit of detection (As, Ag, Sb, Te, and Au). LA-ICP-MS data discussed below are presented as average values of inclusion assemblages, in the context of their spatial and temporal evolution (Table 6.3), based on the established paragenetic sequence.

The intermediate-density inclusion types, ID_P and ID_A, are chemically very similar. They exhibit highly variable concentrations of Cu (150 ± 60 to 2800 ± 2100 µg/g) and Fe (5300 ± 4900 µg/g to 4.7 ± 1.5 wt%), but plot on an intermediate position compared to brines and vapors with regard to element ratios (Figure 6.4 H). Mo (20 to 430 µg/g) and other trace elements show a considerable scatter and are frequently below the limit of detection.

The high-salinity brine inclusions, B_A, B_B, and B_C, exhibit extremely variable Cu concentrations between 240 ± 110 and 1500 ± 800 µg/g. Fe values are remarkably uniform within inclusion assemblages and range between 5.9 ± 3.3 and 8.7 ± 3.8 wt%. Mo and Au are often below the limit of detection, but were detected between 8 and 2700 µg/g and 0.2 and 1.3 µg/g, respectively.

The low-salinity inclusion types V_A, V_B, V_C, and V_D share many characteristics, despite the elevated salinities of V_B inclusions and the higher homogenization temperatures of V_A vapors (Figure 6.4 K). Cu values are highly variable and range between 270 ± 160 and 5500 ± 2200 µg/g. Fe concentrations are remarkably high and exhibit roughly constant values between 0.3 ± 0.2 and 1.4 ± 0.7 wt%. Generally, their trace element composition is less precise due to the small mass of analyte. Mo and Au are frequently below the limit of detection, but were detected between 6 ± 2 and

70±20 μg/g and 0.3 to 3.7 μg/g, respectively. The observed fractionation of certain elements between this fluid type and coexisting brines indicates a relative enrichment in Cu, Mo, and Au, and possibly As, Ag, Sb, and Te in the vapor phase (Figure 6.4 D). The degree of element fractionation between brine and vapor can be calculated as a relative enrichment factor (E_x) for "coeval" inclusion assemblages (Figure 6.4 B). Here, the concentrations (C) of element X in vapor and brine are expressed as element ratios, normalized to Na.

$$E_X = \left[\frac{C_X^{vapor}/C_{Na}^{vapor}}{C_X^{brine}/C_{Na}^{brine}} \right]$$

As mentioned earlier, vapor inclusions of boiling assemblages generally have higher salinities than expected from the binary H_2O-NaCl phase diagram. This indicates co-entrapment of some high-salinity liquid in the vapor inclusions, probably due to preferential surface wetting by the coexisting brine phase. Nonboiling assemblages (i.e., pure vapor trails) show rather consistent salinities of about 2 to 4 wt% $NaCl_{equiv}$, which are still too high with respect to the theoretical values. This discrepancy implies that either the vapor inclusions also trapped some brine or that the physico-chemical properties of the complex natural fluids deviate significantly from the simple (binary) model system. Assuming a salinity of 2.0 wt% $NaCl_{equiv}$ for the pure vapor phase coexisting with B_C brines, endmember compositions can be extrapolated using the trendlines produced by phase separation, which can be calculated for each element (Figure 6.4 C). Here, calculations yield lower bulk concentrations for elements such as Na (0.5 wt%), K (0.5 wt%), Fe (0.3 wt%), Mo (10 μg/g), and Cs (2 μg/g), and similar values for Cu (380 μg/g) and Au (1.1 μg/g). The results show a close correspondence in all elements (except for Mo and Cu) with the nonboiling inclusion assemblages trapped in the same quartz (Figure 6.4 B).

Inclusions of type L_D are rare and resemble the composition of vapor-rich inclusions (Figure 6.4 J). However, major and trace elements show a considerable scatter and are frequently below the limit of detection, mostly because of the small size and irregular shape of the analyzed inclusions. Nevertheless, the scarce data show a considerable enrichment in Te (500 and 670 μg/g) compared to V_A inclusions (Figure 6.4 J). One analysis yielded significant concentrations of Au (3.2 μg/g), which is meaningful in the light of consistently higher LOD's for other analyses of the same inclusion type (see Appendix table 5).
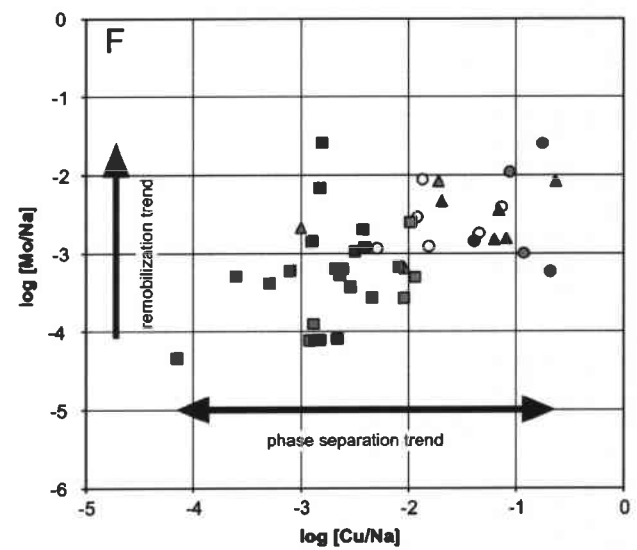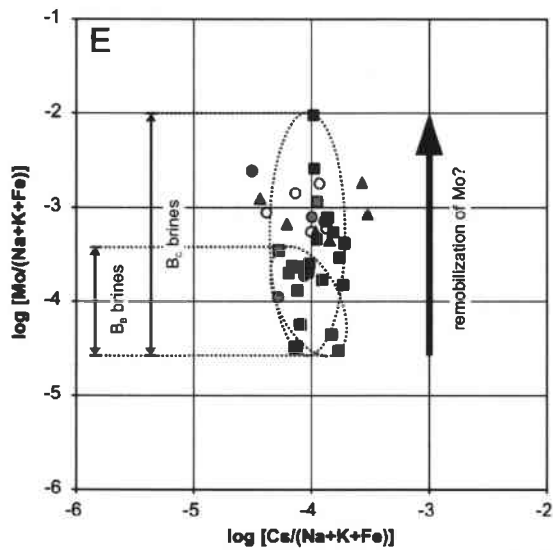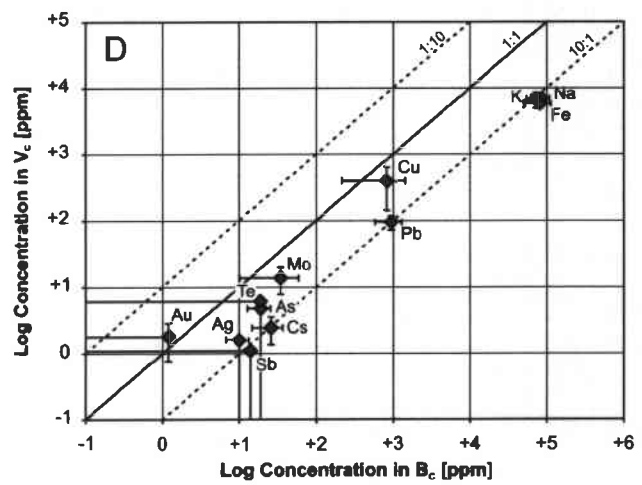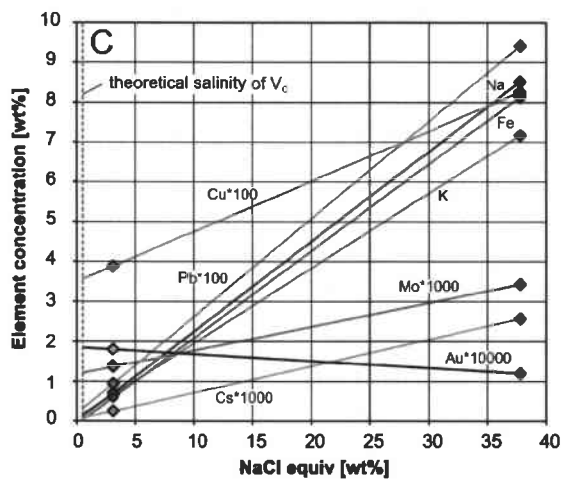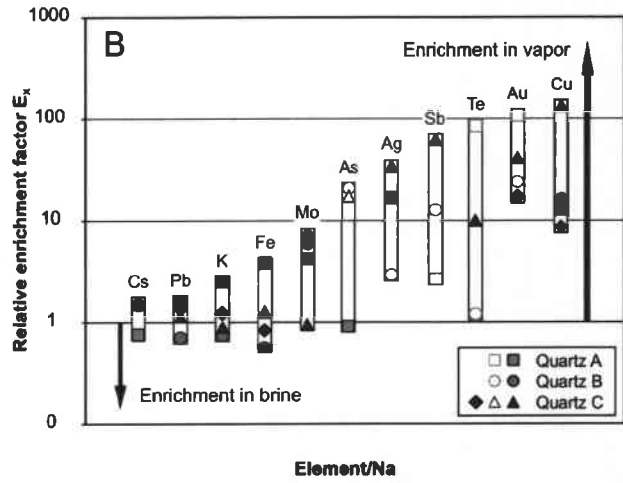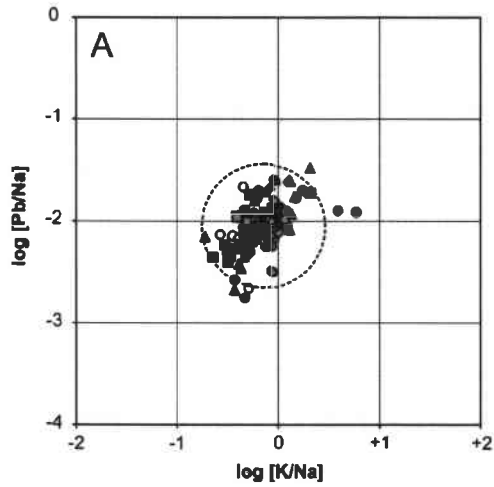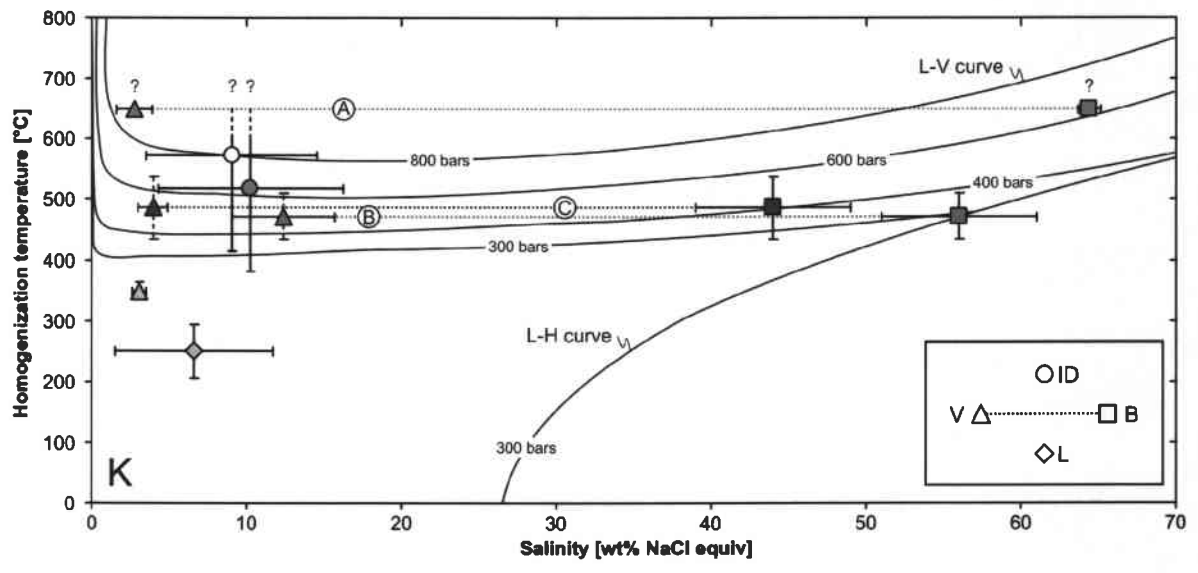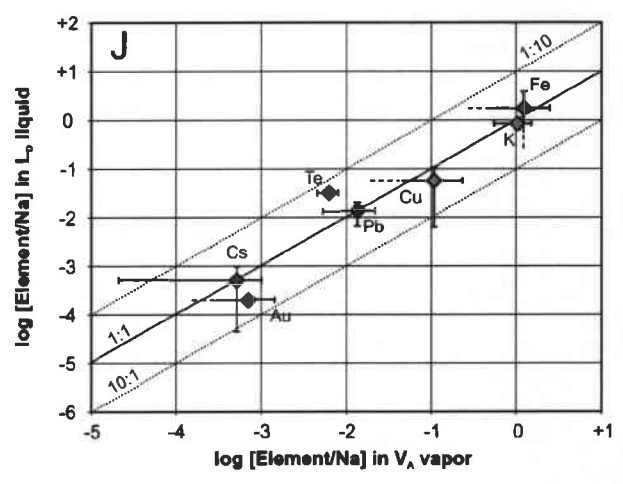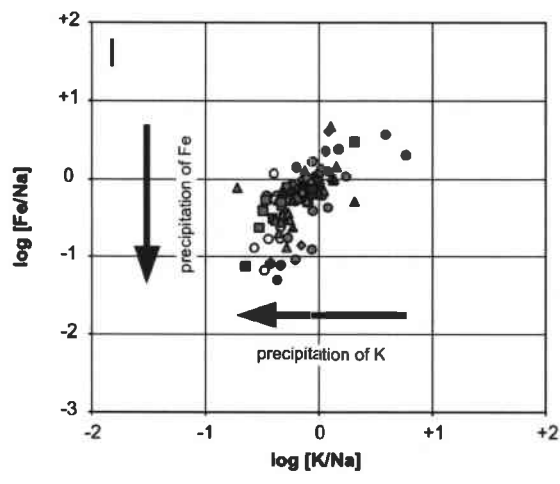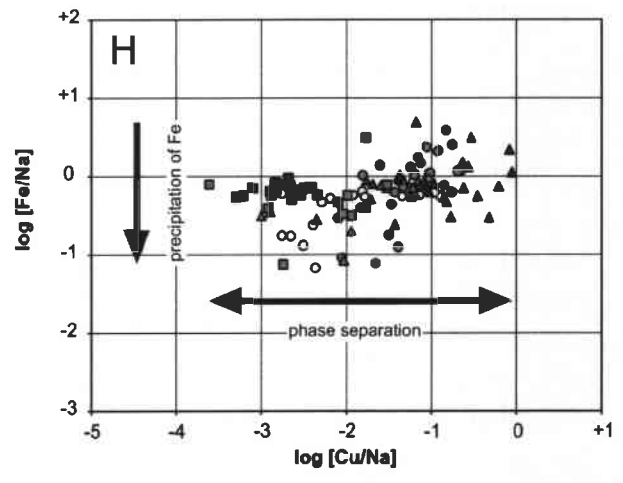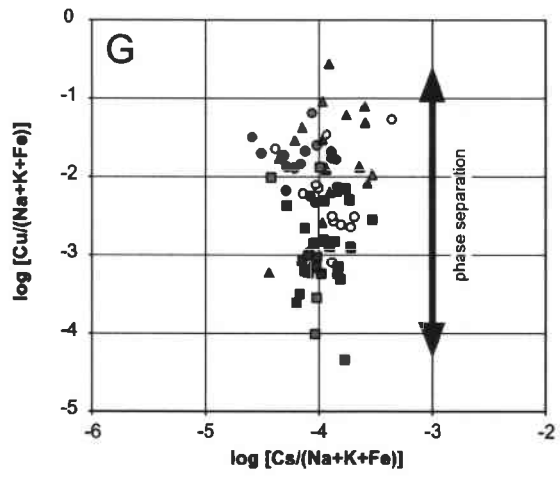
Figure 6.4 (previous pages): Selected element plots showing LA-ICP-MS data from individual fluid inclusions of selected inclusion assemblages color-coded after the petrographic quartz stages outlined in the text. Fluid types are indicated by the same symbol and corresponding intrusions are listed in brackets. To avoid uncertainties in the bulk salinity of the vapor inclusions, LA-ICP-MS data are mainly plotted as element ratios, which are independent of the true salinity, either normalized to Na or to the sum of major cations potentially present as chloride salts. (A) Element ratios, such as K/Na and Pb/Na, behave passively and define a comparatively narrow range. Larger deviations in the K/Na ratio of stage A and B probably reflect potassic alteration. (B) Mean element fractionation between vapors and "coexisting" brines of the same quartz stage illustrated by the relative enrichment factor E_X. The blue diamonds represent the boiling pair illustrated in Figure 6.4 D. Dashed colored symbols indicate limits of detection. (C) Average concentrations of V_C vapors coexisting with B_C brines from a boiling assemblage (sample FM-DB99-15). Trendlines for each element, except Cu, Mo, and Au, indicate co-entrapment of some brine in the vapor inclusions. Deviations from "zero" are due to the relative (for Cu and Mo) and absolute (for Au) enrichment of these elements in the vapor phase. Note that the measured salinities of the vapor inclusions are too high with respect to the theoretical value of 0.5 wt% $NaCl_{equiv}$ (after Driesner and Heinrich, in press). (D) Average concentrations in V_C inclusions coexisting with B_C brines from a boiling assemblage. Note the fractionation of Cu, Mo, and Au in favor of the vapor relative to the brine phase. The solid blue lines indicate limits of detection. (E) Largest variations in the Mo/(Na+K+Fe) ratio probably reflect remobilization of Mo in quartz stage C. Note the relatively narrow range defined by the Cs/(Na+K+Fe) ratio. (F) Selected element ratios illustrating the different behavior of Mo and Cu. Cu/Na ratios display the strong effect of phase separation between vapors and coeval brines, whereas the limited Mo data vary independent of the fluid type and exhibit the largest scatter in B_C brines. (G) Large variations in the Cu/(Na+K+Fe) ratio are interpreted to reflect phase separation. (H) Selected element ratios reflecting the effect of element fractionation upon fluid boiling. However, precipitation of Fe-(Cu)-sulfides may also play a role, but is interpreted to be of minor importance due to the similar scatter observed in the early fluids (V_A and B_A), which are unrelated to ore metal deposition. The overlap of vapors and brines with intermediate-density fluids demonstrates their close relation. (I) Variations in the Fe/Na and K/Na ratios are most pronounced in quartz stages A and B, which are associated with potassic alteration assemblages, and probably reflect precipitation of magnetite and orthoclase. (J) Inclusions of type L_D resemble the composition of V_A vapors within analytical uncertainty. (K) Summary plot of microthermometric measurements averaged over fluid inclusion generations outlined in the text. The liquid-vapor (L-V) coexistence curves were calculated for 800, 600, 400, and 300 bars using the equations of Driesner and Heinrich (in press). The homogenization temperatures of vapor inclusions were commonly approximated from "coexisting" brines. Note also that the salinities determined for vapor inclusions are too high with respect to the theoretical values, indicating co-entrapment of some high-salinity liquid.

Table 6.3: LA-ICP-MS concentration data of fluid inclusion types from the porphyry system. Data are presented as average values of inclusion assemblages, with 1 standard deviation (stdev) and the number of significant concentrations (N) in brackets. <VALUE reports lowest limits of detection using the 3 sigma criterion. * denotes boiling assemblages. Abbreviations: LMD, La Mejicana dyke; LEP; La Estrechura porphyry; PGP, Piedras Grandes porphyry.

	Host	Salinity wt%	Na wt%	stdev	(N)	K wt%	stdev	(N)	Fe wt%	stdev	(N)	Cu ppm	stdev	(N)	As ppm	stdev	(N)	Mo ppm	stdev	(N)
ID_P																				
FM-CP05-34	LMD	11.4	2.9	0.6	(5)	1.8	0.5	(5)	2.1	0.6	(4)	2800	2100	(5)	<150			120	-	(1)
FM-CP05-37	LMD	8.1	2.8	-	(1)	1.2	-	(1)	<0.2			<40			<50			<20		
FM-CP05-37	LMD	6.6	1.8	0.3	(9)	1.0	0.2	(8)	1.0	0.2	(7)	830	1200	(9)	<20	7	(2)	60	70	(4)
FM-CP05-37	LMD	13.8	4.4	2.1	(4)	1.6	0.6	(4)	0.9	0.2	(4)	150	60	(4)	30			50	-	(1)
FM-CP05-37	LMD	18.5	5.8	1.8	(3)	2.3	0.5	(3)	1.4	0.8	(3)	280	70	(2)	<20			<20		
ID_A																				
FM-CP05-21	LEP	16.6	3.4	0.7	(4)	3.7	1.2	(4)	3.7	1.5	(4)	2100	1200	(3)	<50			<40		
FM-CP05-21	LEP	12.0	3.1	0.8	(10)	2.4	0.6	(9)	1.5	1.2	(8)	1600	1100	(9)	<20			50	-	(1)
FM-CP05-21	LEP	11.6	4.0	0.6	(2)	1.2	1.0	(2)	0.6	-	(1)	700	600	(2)	30	-	(1)	<20		
FM-CP05-21	LEP	16.3	2.5	1.4	(2)	4.5	2.0	(2)	4.7	1.5	(2)	2200	10	(2)	<180			<150		
FM-CH04-02	LEP	16.6	3.4	1.3	(10)	4.0	3.1	(10)	3.7	2.0	(10)	2400	2200	(10)	30	-	(1)	70	90	(3)
FM-CP05-37	LMD	3.4	0.9	0.1	(4)	0.6	0.1	(4)	0.9	-	(1)	550	250	(3)	<40			<30		
FM-CP05-37	LMD	5.9	1.9	0.4	(6)	0.7	0.1	(6)	0.5	0.5	(4)	1200	1600	(3)	20	-	(1)	160	230	(3)
V_A																				
FM-CP05-21	LEP	3.4	0.8	0.1	(10)	0.8	0.2	(10)	0.7	0.3	(7)	670	460	(10)	<8			40	10	(3)
FM-CP05-34	LMD	1.9	0.5	0.1	(5)	0.4	0.1	(5)	0.3	0.2	(4)	270	160	(5)	2	-	(1)	6	2	(2)
FM-CP05-37	LMD	2.2	0.4	0.1	(2)	0.3	0.1	(2)	1.4	-	(1)	1100	1300	(2)	<80			<50		
FM-CP05-37	LMD	3.8	0.9	0.1	(2)	0.7	0.4	(2)	0.7	0.1	(2)	580	-	(1)	<10			<20		
B_A																				
FM-CP05-37	LMD	64.4	19.6	2.3	(4)	8.1	2.2	(4)	5.9	3.3	(4)	1500	800	(4)	60	60	(4)	190	200	(3)
V_B																				
FM-CP05-27	PGP	11.7	3.4	0.4	(14)	1.6	0.4	(14)	1.4	0.7	(13)	3300	5100	(8)	<20			70	20	(2)
B_B																				
FM-CP05-27	PGP	50.9	12.8	2.6	(11)	7.8	2.4	(11)	8.7	3.8	(11)	880	1100	(11)	<7			50	30	(6)
FM-CP05-27	PGP	58.2	16.9	1.1	(4)	6.9	1.6	(4)	7.6	2.2	(4)	50	50	(2)	6	2	(2)	40	40	(2)
V_C																				
FM-DB99-15	PGP	3.2	0.8	0.1	(10)	0.6	0.1	(8)	0.5	0.1	(9)	2100	4600	(10)	<9			20	20	(2)
FM-DB99-15	PGP	4.2	0.9	0.2	(6)	0.7	0.1	(4)	1.0	0.4	(3)	5500	2200	(5)	<60			<50		
FM-DB99-15*	PGP	3.1	0.7	0.1	(5)	0.7	0.2	(5)	0.6	0.1	(4)	390	250	(4)	<5			10	6	(3)
B_C																				
FM-DB99-15	PGP	45.7	11.0	0.5	(12)	9.6	0.5	(12)	7.7	0.9	(12)	240	110	(12)	8	5	(6)	360	770	(12)
FM-DB99-15*	PGP	37.8	8.5	2.3	(8)	7.1	1.8	(8)	8.1	3.1	(8)	820	610	(7)	20	6	(3)	30	20	(5)
V_D																				
FM-DB99-15	PGP	3.2	0.7	0.1	(3)	0.6	0.1	(3)	0.6	0.2	(3)	1500	350	(3)	<10			<7		
L_D																				
FM-CP05-27	PGP	6.2	0.7	-	(1)	0.9	-	(1)	3.0	-	(1)	<130			<170			<60		
FM-CP05-21	LEP	2.7	0.6	-	(1)	0.5	-	(1)	0.6	-	(1)	570	-	(1)	<60			<40		
FM-CP05-37	LMD	6.4	2.0	-	(1)	<0.4			<1.2			<500			<270			160	-	(1)
FM-CP05-37	LMD	7.3	2.1	0.7	(5)	1.7	0.8	(5)	0.2	-	(1)	380	-	(1)	<50			<50		

Table 6.3 (cont.): LA-ICP-MS concentration data of fluid inclusion types from the porphyry system. Gray numbers for Au correspond to the 1 sigma significance limit representing a semiquantitative concentration estimate.

	Host	Salinity wt%	Ag ppm	stdev	(N)	Sb ppm	stdev	(N)	Te ppm	stdev	(N)	Cs ppm	stdev	(N)	Au ppm	stdev	(N)	Pb ppm	stdev	(N)
ID_P																				
FM-CP05-34	LMD	11.4	<20	-		<30			<130			8			<10			260	50	(3)
FM-CP05-37	LMD	8.1	<10			<10			<80			<3		(1)	<3			200	-	(1)
FM-CP05-37	LMD	6.6	<5			<5			<30			6	5	(7)	<1			150	60	(9)
FM-CP05-37	LMD	13.8	2		(1)	<2			90			9	6	(4)	<1			460	250	(4)
FM-CP05-37	LMD	18.5	<5			<3			<30			10	4	(3)	<1			390	110	(3)
ID_A																				
FM-CP05-21	LEP	16.6	30		(1)	<20			<90			10	10	(3)	<6			340	110	(3)
FM-CP05-21	LEP	12.0	<5			20	-	(1)	<40			6	2	(4)	<1			400	150	(8)
FM-CP05-21	LEP	11.6	<8			<9			<50			3		(1)	<3			170	-	(1)
FM-CP05-21	LEP	16.3	70			<50			<190			<20			<20			200	6	(2)
FM-CH04-02	LEP	16.6	20	-	(1)	<7			<40	3	(7)	8	3	(7)	<1			240	110	(10)
FM-CP05-37	LMD	3.4	<8	9	(2)	<10			<30		(1)	3		(1)	<2			110	80	(4)
FM-CP05-37	LMD	5.9	4		(1)	4	-	(1)	<30	2	(5)	3	2	(5)	<1			80	40	(3)
V_A																				
FM-CP05-21	LEP	3.4	10		(1)	<3		(1)	60	-	(1)	5	3	(3)	<1			90	30	(7)
FM-CP05-34	LMD	1.9	<5			<1			<2			1	1	(4)	0.9	-	(1)	60	40	(4)
FM-CP05-37	LMD	2.2	<30			<20			<60			<3			3.7	-	(1)	60	20	(2)
FM-CP05-37	LMD	3.8	<3			<4			40		(1)	5			<1			70	20	(2)
B_A																				
FM-CP05-37	LMD	64.4	20		(1)	5		(1)	<10			50	20	(4)	<1			1700	500	(4)
V_B																				
FM-CP05-27	PGP	11.7	<5			<6			<20			9	6	(10)	<1			200	60	(13)
BB																				
FM-CP05-27	PGP	50.9	7	2	(5)	2	-	(1)	50	60	(2)	40	30	(11)	<1			1100	350	(11)
FM-CP05-27	PGP	58.2	7	2	(3)	<1			<2			30	10	(4)	<1			930	130	(4)
V_C																				
FM-DB99-15	PGP	3.2	20	-	(1)	3			20			3	2	(5)	0.3	-	(1)	110	40	(7)
FM-DB99-15	PGP	4.2	30	-	(1)	<20			<50			3		(1)	3.5	-	(1)	70	3	(3)
FM-DB99-15*	PGP	3.1	<2			<1		(3)	<6			3	1	(4)	1.1	-	(1)	90	20	(5)
B_C																				
FM-DB99-15	PGP	45.7	9	1	(8)	1	1	(2)	30			30	10	(12)	0.6	0.5	(4)	1200	160	(12)
FM-DB99-15*	PGP	37.8	10	3	(3)	10	-	(1)	<20			30	10	(8)	1.2	-	(1)	940	360	(8)
V_D																				
FM-DB99-15	PGP	3.2	<3			<3			<20			3		(1)	<1			90	30	(3)
L_D																				
FM-CP05-27	PGP	6.2	<40			<40			<200			<8			<10		(1)	180	-	(1)
FM-CP05-21	LEP	2.7	<10			<10			<110			<5			<4			60	-	(1)
FM-CP05-37	LMD	6.4	<110			<80			670		(1)	<20			<10			230	-	(1)
FM-CP05-37	LMD	7.3	<20			<10			500		(1)	10	20	(2)	3.2	-		310	250	(4)

6.6 Interpretation and discussion

Linking the trapping chronology of specific fluid inclusion types to the established paragenetic sequence of quartz formation, it is possible to gain useful information about the physico-chemical conditions at the time of fluid entrapment and to constrain a generalized model of the fluid evolution. The fluid composition was analyzed on the same assemblages that were used to define the P-T-X conditions in the system. Although experimental difficulties prevent documentation of the entire fluid history, the systematic differences between the inclusion generations described above indicate a similar fluid evolution for each intrusion investigated. The observed succession of quartz formation and ore mineral precipitation can be explained by an ultimately similar or even common source fluid, exsolving from one (or several) crystallizing magma chamber(s) at depth. During ascent through the crust towards the surface, individual batches of magmatic-hydrothermal fluid are thought to have experienced different P-T paths (Figure 6.5) related to local differences in rock permeability, interpreted as the dominant cause for their chemical differentiation.

6.6.1 P-T-X evolution and fluid succession

The inferred fluid evolution is quantitatively consistent with experimental data of fluid phase relations in the binary $NaCl-H_2O$ system (see Figure 6.5). Intermediate-density fluid inclusions of type ID_P most closely represent a single-phase fluid directly exsolved from (a) crystallizing magma(s) at depth. The second type of intermediate-density fluid inclusions, ID_A, is petrographically later but can only be distinguished from ID_A by relative age relationships and homogenization behavior. The bulk of ID_P inclusions homogenize critically or to the liquid; whereas homogenization of the ID_A inclusions occurred mainly into the vapor phase, reflecting a slightly lower density. Assuming that these inclusions represent essentially the same single-phase fluid, they are taken to reflect the initial composition of the source fluid prior to phase separation. Indeed, ID_P and ID_A inclusions have similar element ratios and cover the range of later V_A vapors and coexisting B_A brines (see Figure 6.4 H). However, ID inclusions exhibit a large scatter for certain elements (see Figure 6.4 E+F), which may reflect initiation of phase separation. Geologic and fluid inclusion data indicate that fluid pressures of the high-temperature and low- to moderate-salinity inclusions

approached lithostatic conditions during fluid entrapment. A minimum depth of 1.7 km is estimated for these early fluids if a lithostatic regime is favored. Under hydrostatic conditions an unrealistically high value of around 9 km overburden is calculated, which is not supported by the stratigraphy of the Famatina mining district. However, progressive crystallization of the magma(s) and resulting fluid overpressure probably caused hydraulic fracturing of the wall rocks (Burnham and Ohmoto, 1980), thereby opening the magmatic-hydrothermal system to hydrostatic conditions.

Decompression of the input fluid commonly results in phase separation, leading to a minor fraction of hypersaline brine and large volumes of vapor (see Figure 6.5). A rough estimate of the mass proportions of brine and vapor fluids can be calculated knowing the composition of the initial fluid (ID_A) and of the two products (V_A and B_A). Here, the bulk salinity of ID_A fluids equals the sum of the apparent salinities of V_A vapors and B_A brines times their corresponding mass proportions, as illustrated in Figure 6.5 B:

$$NaCl_{ID_A} = \frac{b}{a+b} \times NaCl_{V_A} + \frac{a}{a+b} \times NaCl_{B_A}$$

Calculations based on microthermometric measurements yield a vapor:brine mass ratio of 88:12 (Table 6.4). Similarly, calculations based on average concentrations derived from LA-ICP-MS analysis of non-reactive elements led to a vapor:brine mass ratio of 89:11 for Na and 89:11 for Pb. However, due to the very small amount of condensed liquid in vapor inclusions, determination of the apparent salinities and related element concentrations is less reliable than for brine inclusions. Therefore, LA-ICP-MS data are mainly plotted as element ratios, which are independent of the true values.

Successive boiling assemblages (B_A+V_A, B_B+V_B, B_C+V_C) indicate several episodes of phase separation, repeatedly forming minor quantities of brine (12-22%) and large amounts of expanding vapor (78-88%), and are probably related to local pressure and temperature fluctuations (Figure 6.5 A+B). Indeed, pressure estimates based on microthermometry reveal that quartz A was formed by high-temperature fluids under near lithostatic conditions, at any pressure higher than 510 bars (see page 63). By contrast, vein quartz from stages B and C precipitated from moderate-temperature fluids during transition from a lithostatic to a hydrostatic regime. The minimum depth estimated for A-veinlets ranges from 1.9 to 2.9 km, whereas B-veins were probably covered by 1.1 km (lithostatic) to 3.0 km (hydrostatic) overburden.

Late stage V_D inclusions occur in the last stage of quartz formation (D) and exhibit the lowest temperatures of homogenization. Pressure estimates for these low-density fluids yield values of 176 bars, indicating depths of cover between 660 m (lithostatic) and stratigraphically more realistic 1.8 km (hydrostatic).

The latest hydrothermal activity in the porphyry system is represented by a rare liquid-like fluid of low to intermediate salinity, L_D (see Table 6.2). These aqueous liquids were commonly interpreted to be meteoric in origin, with small contributions of magmatic brine (e.g., Hedenquist et al., 1994a). However, our data demonstrate a significant enrichment in Cu, Te, and Au in these fluids, which are not coupled with dilution of brine. Instead, we think that L_D fluids were formed by separation of vapor from brine at elevated temperatures and pressures, and subsequent cooling and contraction of the vapor to an aqueous liquid (Heinrich et al., 2004; Heinrich, 2005). This hypothesis is consistent with compositional similarities between L_D liquids and pre-ore vapor inclusions of type V_A (see Figure 6.4 J). Minimum pressures for L_D liquids range between 22 and 75 bars, indicating minimum depths of 280 to 760 m under hydrostatic conditions. Due to the lack of independent pressure constraints, the true value may exceed this estimate by far. The significance of such aqueous liquids, which predominate in the transitional QSP veins, will be discussed more extensively in the subsequent chapter.

Table 6.4: Bulk element ratios of ID_A fluids and and estimated mass proportions of the corresponding "boiling" pair composed of B_A brines and V_A vapors. Calculations based on microthermometry yield a vapor:brine mass ratio of 88:12. Using this mass ratio to determine the metal budget of the source fluid, the calculated element ratios agree resonably well with those measured for the ID_A fluids, except for Au, which was below the limit of detection in the ID_A and B_A inclusions.

	ID_A measured	B_A measured	B_A %	V_A measured	V_A %	ID_A 12% B_A + 88% V_A
$NaCl_{equiv}$	10.25	64.41	12	2.77	88	10.17
K/Na	0.77	0.43	43	1.03	57	0.96
Fe/Na	0.97	0.32	28	1.22	72	1.12
Cu/Na	0.07	0.01	41	0.11	59	0.10
Pb/Na *10	0.10	0.21	25	0.13	75	0.14
Mo/Na *100	0.60	0.11	24	0.45	76	0.41
As/Na *1000	0.99	0.31	51	0.28	49	0.28
Ag/Na *1000	1.33	0.13	41	2.17	59	1.93
Sb/Na *1000	0.44	0.02	48	0.06	52	0.06
Te/Na *1000	1.17	0.07	82	6.29	18	5.55
Cs/Na *1000	0.22	0.25	92	0.51	8	0.48
Au/Na *10000	0.36	0.03	95	7.07	5	6.23

6.6.2 Element fractionation and ore metal precipitation

Where textural evidence for phase separation is unambiguous, measurements of the metal concentrations in coexisting brines and vapors can provide insight into the fractionation of elements. The partitioning of certain ore metals (e.g., Cu, As, Au) into the low-density vapor phase is known from a variety of porphyry-type ore deposits (Heinrich et al., 1999; Ulrich et al., 2001; Landtwing, 2004; Rusk et al., 2004; Klemm, 2005). Similarly, the results of the present study indicate that separation of a low-salinity vapor from a hypersaline liquid leads to significant fractionation of ore-forming components. Figure 6.4 B illustrates the relative enrichment factors (E_X) of selected elements between coexisting brine and vapor inclusions. The data demonstrate that elements such as Cs, Pb, K, Fe, and Mo have no systematic preference, whereas Cu, Au, Te, Sb, Ag, and As partition in favor of the vapor phase, relative to Na. The magnitude of this fractionation into the vapor varies significantly from assemblage to assemblage and is particularly evident for Au and Cu. However, it should be noted that average concentrations of V_C vapor and B_C brine imply co-entrapment of some high-salinity liquid in the vapor phase (see Figure 6.4 C). This observation has implications on the absolute element concentrations calculated for vapor-rich inclusions coexisting with brines. Assuming that the apparent salinities of the vapor inclusions are too high with respect to the theoretical values, absolute element concentrations for the low-density vapor phase cannot be determined reliably. Nevertheless, true element concentrations can be extrapolated using the salinity of the inferred endmember (see page 65). The data indicate a significant enrichment of Cu, Au, Te, Sb, Ag, and As in the vapor phase relative to the main salt components Na, K, and Fe in the cogenetic brine phase (see Figure 6.4 B).

In general, data for all fluid inclusion generations show a wide range in absolute concentrations and element ratios. Cu concentrations in vapor-rich inclusions vary from 0.5±0.2 wt% for V_C vapors to very low concentrations of a few hundred ppm (see Table 6.3). A similar range has been observed for Cu/Na ratios in the brine inclusions; particularly for B_B and B_C brines (see Figure 6.4 G). Highest variations in the Cu/Na ratios of vapors and coeval brines occur in the main hydrothermal stage (see Figure 6.4 H), which is associated with a significant drop in temperature and pressure. These trends are interpreted to reflect minor sulfide mineral precipitation between 455 and 552°C (see Table 6.2), in response to decreasing temperature as

the dominant parameter. However, the overall variation is probably dominated by element fractionation caused by fluid boiling (see Figure 6.4 H). This observation is consistent with elevated Cu concentrations in low-temperature V_D vapors, which occur in the last generation of porphyry quartz and are probably synchronous with sericitic alteration. Differences in the Fe content are less apparent due to high initial Fe concentrations in the parental fluids. However, variations in the Fe/Na and K/Na ratios are most pronounced in quartz stages A and B, which are associated with potassic alteration assemblages, and therefore, are interpreted to reflect precipitation of magnetite and orthoclase (see Figure 6.4 I). The scarce data for Mo exhibit a similar range in absolute concentrations and Mo/(Na+K+Fe) ratios. However, a correlation with temperature is difficult to constrain due to the limited data set. The largest variation has been detected in B_C brine inclusions (see Figure 6.4 E) and is interpreted to reflect remobilization of Mo from previously deposited sulfide ore in quartz stage B. This assumption is consistent with petrographic evidence indicating early precipitation of molybdenite, followed by remobilization and re-deposition (see Appendix figure 2 F).

In summary, large variations in absolute concentrations and element ratios are interpreted to reflect element fractionation between vapors and coexisting brines upon fluid boiling. However, precipitation and re-dissolution of sulfide minerals may also play a role, but are interpreted to be of minor importance (at least for Cu) due to the similar scatter observed in the early fluids (V_A and B_A), which are unrelated to ore metal precipitation.

6.7 Conclusions

Detailed fluid inclusion petrography and microthermometry of more than 35 inclusion assemblages from 5 different quartz stages followed by LA-ICP-MS analyses allowed reconstruction of the fluid evolution of the Nevados de Famatina porphyry system. Even though it was not possible to document the entire fluid history in time at any point of the mining district, a generalized model can be deduced on the assumption that each intrusion (i.e., LMD, LEP, PGP) and its fluid pulse followed a similar range of P-T-X paths.

In summary, a single-phase intermediate-density fluid exsolving from a crystallizing magma at depth rises and unmixes at a shifting horizon caused by strong pressure and temperature fluctuations (see Figure 6.5). Several episodes of phase separation repeatedly form minor quantities of brine and large amounts of expanding vapor. Mass proportion and salinity of brine and vapor depend on the bulk composition of the precursor fluid (ID_A) and on ambient temperature and pressure conditions. The apparent salinity of the parental fluid in the porphyry system ranges between 3.0 ± 1.1 and 18.5 ± 4.1 wt% $NaCl_{equiv}$. Phase separation generally occurs on the vapor side of the critical curve resulting in condensation of some hypersaline brine (Figure 6.5 B). In all stages, the mass proportions of fluid types are in clear favor of the buoyant vapor phase (V_A, V_B, V_C), which represents the main transport agent of precious ore metals in this system. Consistently, Geiger et al. (2005; 2006) show in their numerical fluid flow model that vapor-like fluids ascend through the crust, whereas the coexisting high-density brines tend to pond and remain at greater depth. Subsequent cooling and contraction of the rising vapor leads to an aqueous liquid, which is significantly enriched in Au and Te. Petrographic evidence indicates that precipitation of Mo is temporally decoupled from that of Cu and is associated with potassic alteration assemblages. Remobilization of Mo and re-deposition along with main introduction of Cu occurs at the end of stage C and appears to be synchronous with a transition from potassic to sericitic alteration. Nevertheless, it should be noted that precipitation of ore minerals is subeconomic at present times.

In general, fluid compositions, densities, and evolution are not significantly different from those reported for Bingham (Landtwing et al., 2005). If it is valid to assume that each porphyry intrusion was mineralized by essentially the same input fluid and roughly at the same time, the poor ore grades may reflect incomplete focusing of the ore-forming fluids through three (or four) spatially separated exit points. More focused fluid flow into one porphyry could have led to a smaller but economic porphyry Cu-Mo-Au deposit.
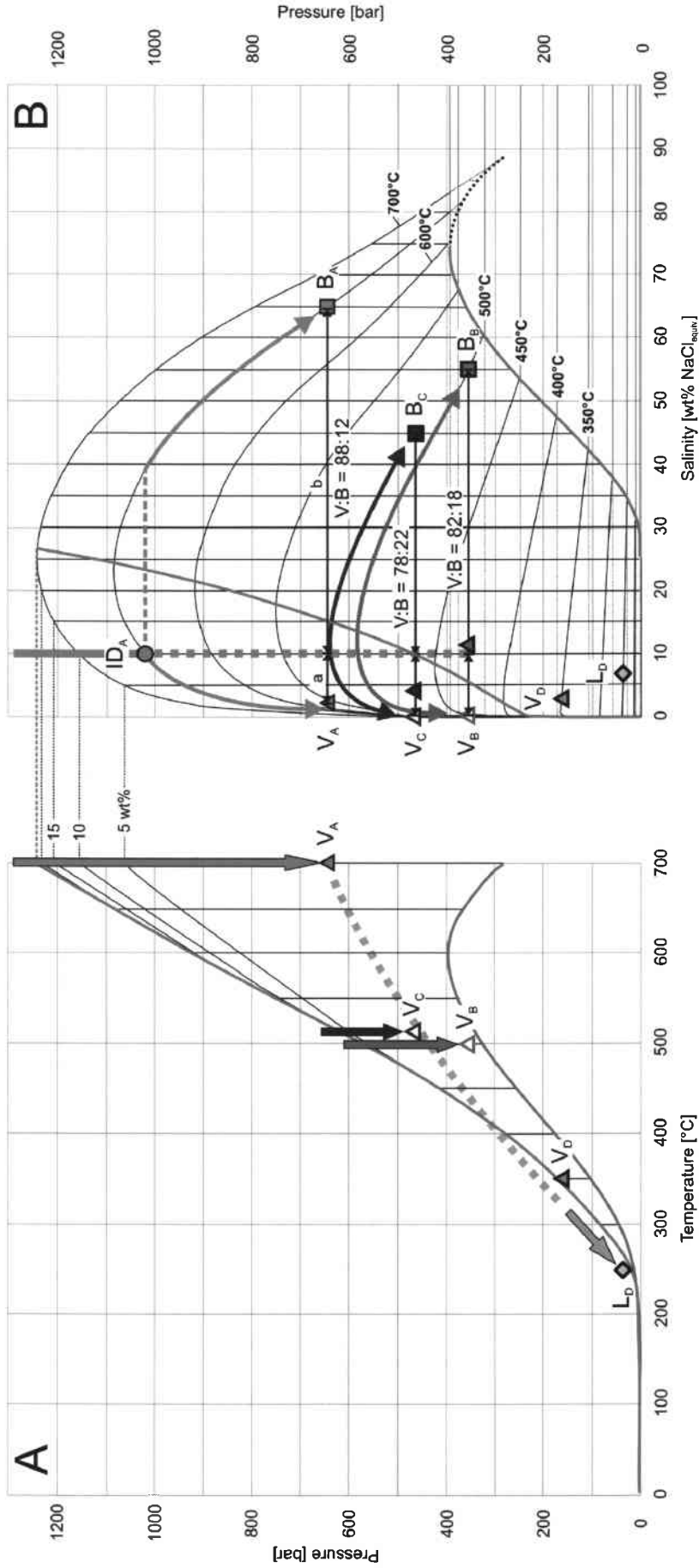
Figure 6.5: 3D phase diagram of the H$_2$O-NaCl system without halite saturation curve after Driesner and Heinrich (in press) illustrating the simplified fluid evolution of the porphyry system. Symbol colors correspond to the different fluid inclusion generations discussed in chapter 6.4.2. The phase boundary surface between the single-phase field (above) and the two-phase field (below) is contoured for temperature in black, with the critical curve on its crest (red line). The halite-liquid-vapor surface is contoured for temperature in blue. (A) Vapor limb of the solvus separated along the critical curve: The fluid pathway illustrates several episodes of phase separation related to local pressure and temperature fluctuations. Progressive cooling causes vapor contraction and results in the formation of late stage liquids. (B) Mass proportions between brines and coexisting vapors are in favor of the vapor phase. The bulk salinities (filled triangles) of the vapor inclusions are too high with respect to the theoretical values (open triangles), which have been used for the calculations.

7 TRANSITIONAL QSP-STAGE MINERALIZATION

7.1 Introduction

The transitional QSP stage largely corresponds to the main hydrothermal stage IV after Losada-Calderón (1992) and postdates the potassic alteration of the porphyry system. This stage is characterized by the formation of quartz-sericite-pyrite veins, which are accompanied by sericitic alteration envelopes. Locally, they grade upwards into high-sulfidation epithermal assemblages, indicating that the QSP veins probably represent linking channelways for the ore-forming fluids generating the epithermal deposit. Analyses were performed on samples from two distinct localities and include outcrop material and drillcore sections: i) the northwestern extension of the La Estrechura porphyry, and ii) the La Mejicana ridge. The following paragraphs are based on detailed petrographic studies in combination with scanning electron microscopy cathodoluminescence (SEM-CL). This approach enabled us to identify and correlate quartz grains from the different sample locations and to reconstruct the crystallization history of the QSP veins. Furthermore, it formed the basis for linking the established paragenetic sequence of the porphyry system with the early quartz generations of the QSP veins. Visualizing quartz textures at the scale of micrometers was essential for discriminating fluid inclusion assemblages and for selecting inclusion assemblages suitable to be analyzed by microthermometry and LA-ICP-MS. Fluid inclusion analysis revealed that fluids associated with QSP veins are dominated by aqueous liquids of low to intermediate salinity, which are chemically similar to the intermediate-density and vapor-like fluids prevailing in the early quartz generations of the porphyry system. By correlating the inclusion characteristics of the transitional QSP veins with specific stages of quartz formation, the results allowed interpretation on the fluid evolution across the P-T-X space.

7.2 Mineralization and alteration

QSP veins are quartz-sericite-pyrite veins with minor amounts of bornite, idaite, chalcocite, chalcopyrite, covellite, sulfosalts, and sphalerite. They tend to be thicker

and more continuous than A-veinlets and B-veins, have fairly straight walls and are locally vuggy (Figure 7.1). Quartz is euhedral, with a glassy to glassy-white color, and commonly precipitated on top of an older generation of epigranular quartz, which exhibits undulose extinction. Pyrite either occurs in vein centers or along vein margins, and contains abundant sulfide inclusions, such as chalcopyrite, bornite, and covellite. Anhedral grains are slightly fractured and tend to be more abundant in vicinity to the high-sulfidation epithermal veins. Sericite occurs as selvages or as well-developed flakes and fans of up to 15 μm length. Locally, it fills open spaces between pyrite grains. Vugs are often filled with typical high-sulfidation epithermal mineral assemblages, including alunite, kaolinite, pyrophyllite, and alumo-phosphate-sulfate (APS) minerals. QSP veins are not restricted to an individual host rock. Commonly, they cross lithological contacts, thereby causing subtle changes in vein mineralogy, morphology, and related hydrothermal alteration. However, QSP veins are associated with sericitic alteration, which includes quartz, sericite, pyrite, illite, and rutile. This dominant alteration assemblage generally obliterates original textures and is easy to recognize in the igneous rocks and the metasediments, respectively.

7.3   Vein petrography

7.3.1 Field relations

QSP veins appear to be most abundant in vicinity of the high-sulfidation epithermal veins, which are preserved along a ridge adjacent to the currently exposed porphyry system. The present study is based on macroscopic time relations observed in the field and from hand specimens. In any given sample, QSP veins postdate A-veinlets and B-veins of the porphyry system (Figure 7.2 A). Locally, they grade upwards into high-sulfidation epithermal veins (Figure 7.2 B). Selected samples originate from two distinct localities and represent the limited material that contained fluid inclusions appropriate for further investigations. Vein chronology corresponds to that described in the porphyry system (pages 51-52) and can be summarized as follows: formation of irregular A-veinlets; precipitation of quartz and pyrite (±molybdenite, ±chalcopyrite) in straight B-veins that cut the A-veinlets; formation of euhedral QSP assemblages; high-sulfidation epithermal minerals filling open spaces and late fractures.
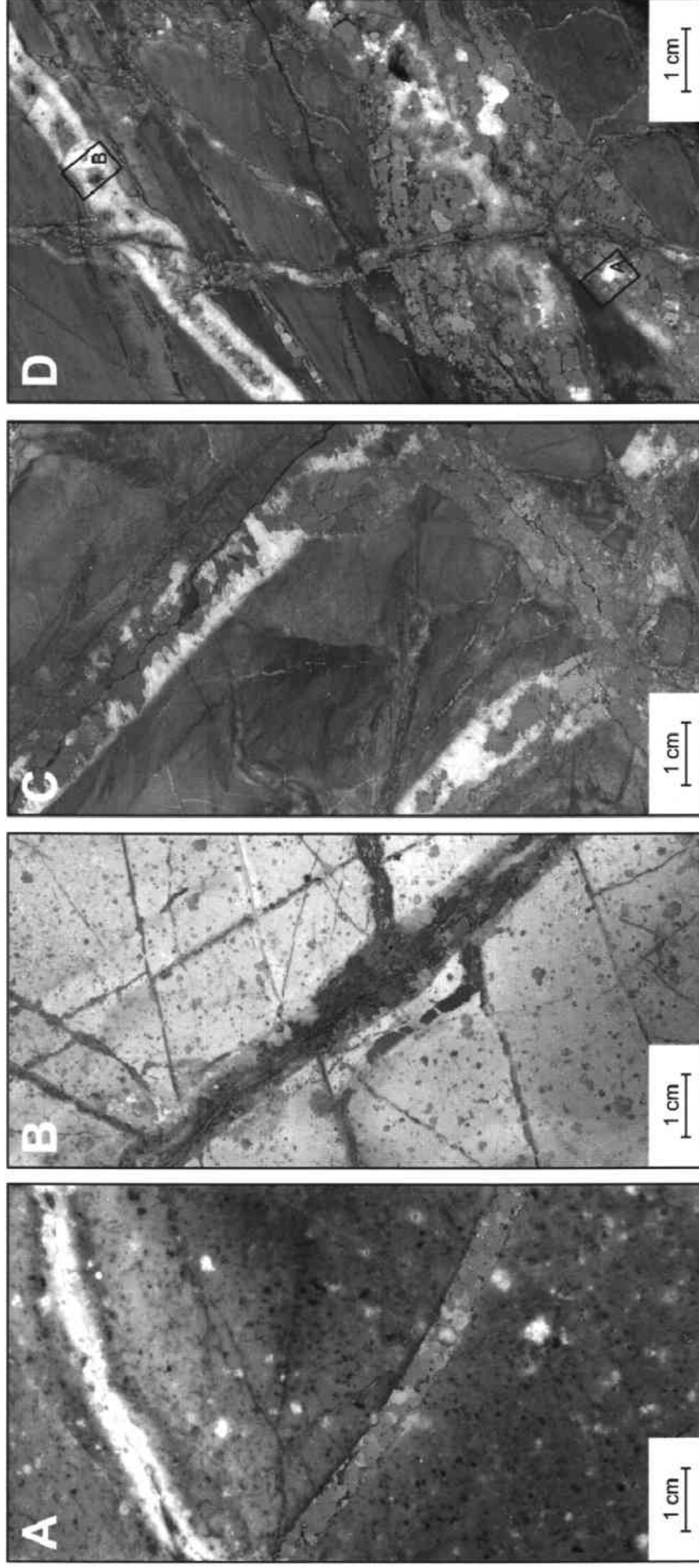
Figure 7.1: Photographs of selected QSP veins from drillholes below the La Mejicana ridge illustrating the relationship between vein mineralogy and host lithology. (A) Pyrite-rich QSP vein in porphyritic host rock of the Mogote Formation (sample FM-DH4-350.5). (B) Pervasively altered porphyritic dacite cut by numerous QSP veinlets, which in turn are cut and off-set by a thick QSP vein. Note the small sericitic halo associated with this stage (sample FM-DH4-352.1). (C) Crosscutting QSP veins with varying amounts of pyrite (sample FM-DH4-187.5). Host rocks are strongly altered metasediments of the Negro Peinado Formation. (D) Crosscutting QSP veins in fine-grained metapelites of the Negro Peinado Formation exhibiting abundant quartz (sample FM-DH4-427.3). Euhedral quartz crystals line open vugs, which are locally filled with high-sulfidation epithermal mineral assemblages. Note the relict sedimentary layering of the beige-colored host rock. The boxes indicate the location of the CL images shown in Figure 5.1.
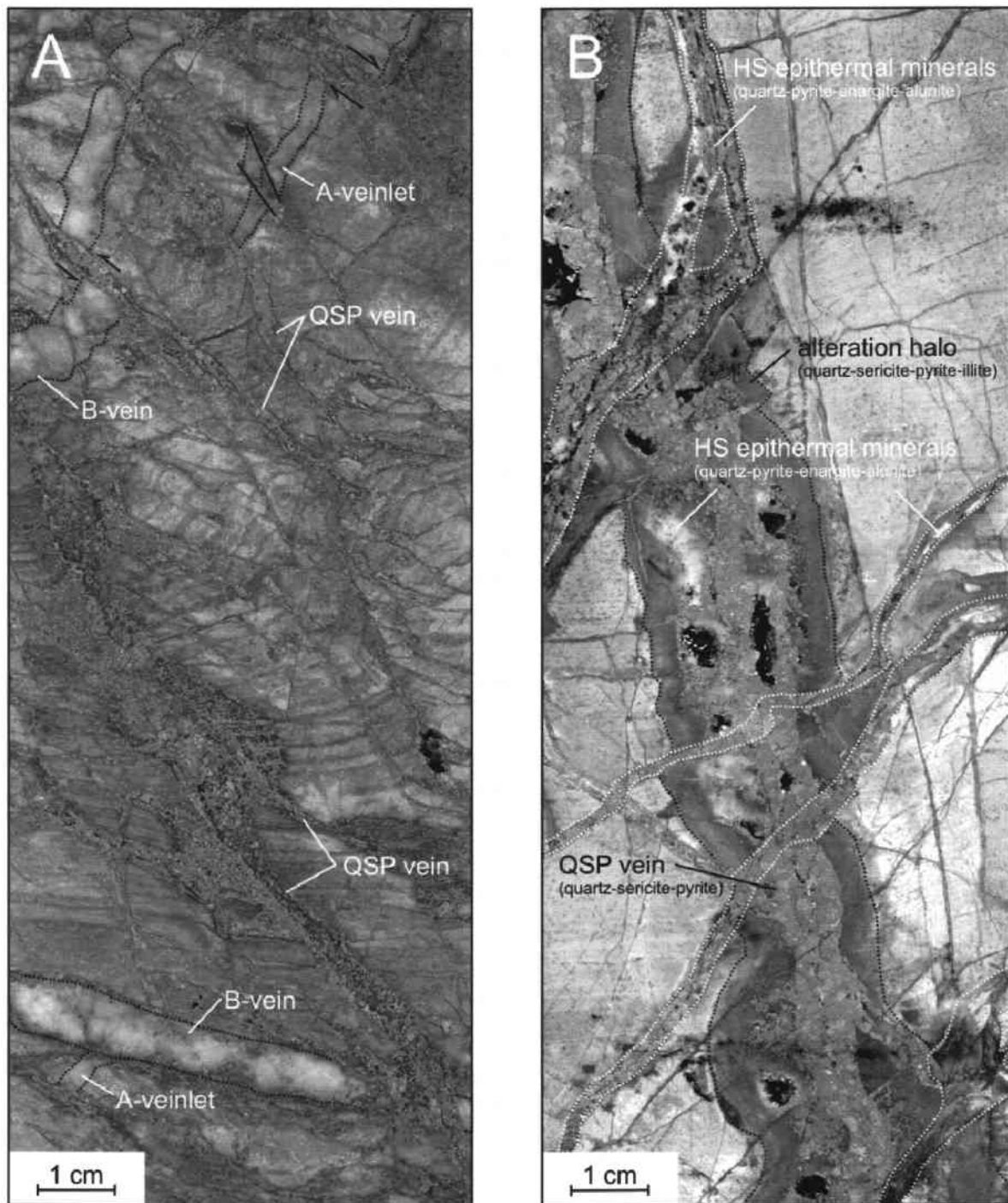
Figure 7.2: Drillcore sections of typical QSP veins illustrating the paragenetic sequences based on macroscopic time relations. (A) Numerous irregular QSP veins that cut and off-set the pre-existing vein stages of the porphyry system (sample FM-DH1-85.5). Host rocks are fine-grained metasediments of the Negro Peinado Formation exhibiting complex foliation. (B) Numerous irregular QSP veins in pervasively altered metasediments of the Negro Peinado Formation grading into or cut by high-sulfidation epithermal mineral assemblages (sample FM-DH4-276.6). Note the sericitic alteration envelope associated with this mineralization stage, indicated by the dotted black line.

7.3.2 Paragenetic sequence

Constraints on the spatial and temporal evolution of the transitional QSP stage were obtained from six representative samples, including surface material and drillcore sections originating from greater depth (Appendix figure 3 A-F). For the exact sample location the reader is referred to the geological map shown in Appendix figure 1. In detail, we used the weak but highly variable CL characteristics of quartz in the QSP veins in order to identify and correlate grains from different localities. Numerous investigations have shown that a general physico-chemical correlation of quartz based on the CL properties is not always possible. This is due to the fact that quartz grains with similar CL colors and emission spectra may have grown under different genetic conditions (e.g., metamorphic quartz; Götze et al., 2001). Despite these limitations, the differences in the CL characteristics of the selected samples indicate a surprisingly simple crystallization history, which has not been outlined by previous studies. In general, the internal paragenetic sequence of the QSP veins is multiphase but systematic, and can be summarized as follows (Figure 7.3 A):

E) Epigranular vein quartz is the earliest phase in QSP veins and forms euhedral to subhedral crystals exhibiting a strong oscillatory zonation and a bright CL color. This quartz shares many characteristics with B-veins of the porphyry stage (quartz B). Therefore, it is thought to represent an earlier vein generation, which was reopened and overgrown by the QSP assemblage. This interpretation is consistent with macroscopic observations at all sampling sites indicating local reactivation of the preceding vein stages.

F) The next quartz generation reveals multiple stages of growth zoning, including discontinuities and dissolution horizons. This quartz shows a weak CL response and occurs along grain boundaries or fills voids and fractures. Locally, it forms free grown crystals. Solid inclusions of primary hematite are common, and clearly restricted to this quartz type.

G) The almost undisturbed growth zoning of the following quartz generation indicates continuous growth from a steadily evolving fluid. This dull-luminescent quartz forms euhedral crystals settled on top of the older quartz generations and is frequently overgrown by euhedral pyrite crystals. The pyrite contains numerous solid inclusions, such as bornite and covellite.

H) The youngest quartz generation corresponds to dark CL colors. Commonly, it overgrows the older generations of quartz, fills open spaces, and surrounds or truncates anhedral pyrite grains. The pyrite is fractured and contains numerous mineral assemblages of high sulfidation state, such as enargite/famatinite and tennantite/tetrahedrite. Locally, pseudo-cubic alunite fills open spaces of the QSP assemblage. These textures indicate that deposition of the high-sulfidation epithermal minerals either occurred synchronous with or slightly after formation of this quartz type.

As shown above and in Appendix figure 3, the combination of detailed petrographic investigations with SEM-CL enabled us to identify four different generations of QSP vein quartz and to reconstruct the succession of quartz formation for all samples investigated. However, it should be noted that samples from the deeper parts of the system are easier to correlate due to the lack of epithermal overprint and the full details of all four quartz generations. Time relations to the earlier vein stages of the porphyry system were observed in the field, but samples were primarily selected based on the presence and quality of the usually very small fluid inclusions. Although the majority of inclusions were too small for analysis, they could be used to constrain a general time sequence, which seems to be common to all locations investigated.

7.4 Trace element composition of quartz

Several studies have explored the relationship between CL response and trace element composition of quartz crystals (e.g., Müller et al., 2000; e.g., Götze et al., 2001; Landtwing, 2004). Generally, the incorporation of foreign cations, such as H^+, Li^+, K^+, Na^+, Fe^{++}, Cu^+, and Ag^+, is considered a key factor in controlling the cathodoluminescence of quartz. In this study, twelve trace elements were measured by LA-ICP-MS in order to correlate the observed luminescence behavior with the composition of the host quartz. Data are reported for Na, K, Fe, Cu, As, Mo, Ag, Sb, Te, Cs, Ag, and Pb (Table 7.1). LA-ICP-MS analyses were done with a 30 μm beam diameter. This size reflects a compromise between high resolution and a sufficiently low limit of detection. Absolute quantification was carried out by integration of signal intensities for all elements, correction for background contributions, and external standardization using the NIST glass standard SRM 610 (Günther et al., 1998). The obtained element concentrations were transformed into "true" values by internal standardization to 99.99 wt% SiO_2 for the quartz, resulting in a total of 99.990 to 100.012 wt% element oxides.

Concentrations of Na, K, and Fe vary considerably in the different quartz generations and reveal a generally positive correlation between trace element abundance and CL response. Highest concentrations were obtained for the bright-luminescent vein quartz, representing the oldest quartz generation observed in QSP veins (Figure 7.3). Concentrations of the other traces are subordinate and uniform across the various CL zones. However, the most striking aspect is the significant decrease in K, which corresponds to the first appearance of aqueous inclusions and may be related to a decline in the K^+ activity of the fluid. In conclusion, the luminescence behavior of QSP quartz is variable and relates to the sum of trace elements incorporated into the crystal structure. Quartz with bright luminescence is usually enriched in Na, K, and Fe. We suggest that changes in the physico-chemical conditions of quartz formation, such as temperature, pH, fluid chemistry, and growth rate, are the primary control of trace element uptake and therefore responsible for changes in the CL emission (Landtwing, 2004). Therefore, the general trend from early bright to late dark CL colors with decreasing trace element concentrations is interpreted to reflect the compositional evolution of the magmatic-hydrothermal fluids with time.

Table 7.1: Selected LA-ICP-MS element concentrations in successive quartz generations of a QSP vein from the magmatic-hydrothermal system at Famatina, NW Argentina. <VALUE reports values below the limit of detection using the 3 sigma criterion.

Sample ID LA-ICP-MS	Quartz type	Na µg/g	SiO₂ wt%	K µg/g	Fe µg/g	Cu µg/g	As µg/g	Mo µg/g	Ag µg/g	Sb µg/g	Te µg/g	Cs µg/g	Au µg/g	Pb µg/g	Total wt%
Sample FM-DH4-427.3															
ja06a06	E	70.5	99.99	101.8	46.0	4.0	0.40	0.03	0.07	0.09	0.25	0.05	<0.01	0.57	100.012
ja06a12	E	18.0	99.99	77.3	28.6	0.78	0.49	0.03	0.01	0.07	0.45	0.05	0.01	0.30	100.003
ja06b12	E	25.8	99.99	57.9	21.8	1.8	0.21	0.11	0.36	0.12	0.71	0.05	0.03	0.22	100.001
ja06a11	F	10.3	99.99	75.4	6.9	0.52	1.9	0.11	<0.05	0.46	0.12	<0.02	0.01	0.11	100.000
ja06b10	F	44.9	99.99	59.2	36.5	0.54	0.37	0.21	0.08	0.28	0.12	0.01	<0.03	0.17	100.004
ja06b11	F	20.6	99.99	59.3	22.7	0.55	0.53	<0.14	<0.09	0.18	0.95	0.01	0.02	0.30	100.001
ja06a03	G	0.12	99.99	2.9	17.3	0.16	0.44	0.09	0.06	0.07	0.84	<0.01	0.02	0.07	99.992
ja06a15	G	0.21	99.99	<0.56	<2.9	0.51	0.20	0.09	0.08	0.06	0.58	<0.02	0.03	0.17	99.990
ja06b06	G	0.43	99.99	1.1	10.8	0.12	0.34	0.05	0.04	0.07	1.2	0.01	0.01	0.09	99.991
ja06b03	H	1.7	99.99	0.58	50.0	2.6	0.41	0.12	2.9	0.20	<0.08	0.01	0.03	0.16	99.996
ja06b04	H	4.3	99.99	<0.51	1.2	0.34	0.28	<0.06	0.27	<0.02	1.3	<0.01	0.01	<0.07	99.991
ja06b05	H	1.0	99.99	<0.84	7.8	0.70	<0.40	0.14	0.24	0.09	0.56	<0.02	<0.03	0.21	99.991
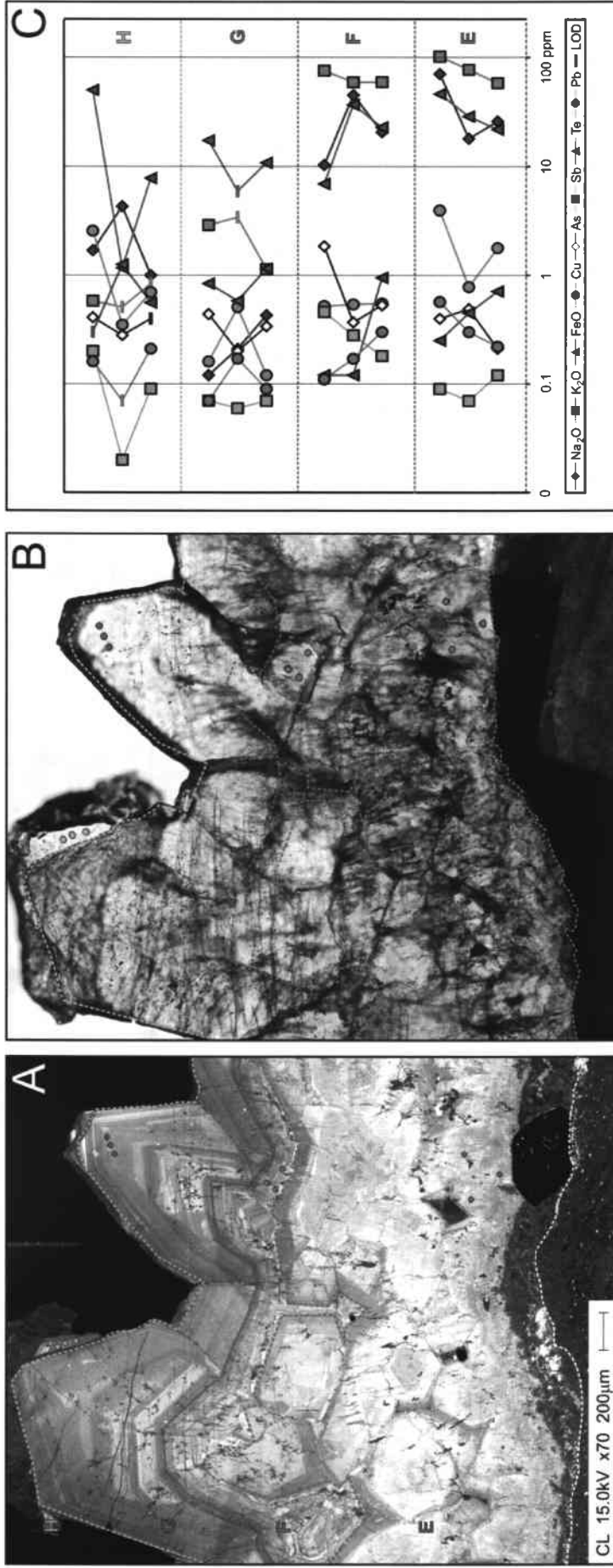
Figure 7.3: Selected trace element concentration data on successive quartz generations in a QSP vein based on SEM-CL and LA-ICP-MS. (A) Dashed colored lines indicate the lower limit of each petrographic stage revealed by CL (sample FM-DH4-427.3). Note the small band of dull-luminescent quartz wedged between the oldest quartz generation and the sedimentary host rock. This band represents the sericitic alteration assemblage, which is associated with the QSP veins. (B) Conventional photomicrograph of the same sample highlighting the importance of SEM-CL for petrographic interpretation. Location of the laser ablation pits is indicated by circular holes of 30 µm size. (C) LA-ICP-MS concentration data vary considerably in the different quartz generations, displaying a positive correlation between trace element abundance and CL response. Note the significantly higher concentrations in K and Na in the early, bright luminescing quartz generations E and F.

7.5 Fluid inclusion study

7.5.1 Types of fluid inclusions

The distribution of fluid inclusions in QSP vein quartz was studied using standard techniques for petrography (microscopy, SEM-CL) and microthermometry. Moreover, the CL colors were used to relate distinct fluid inclusion assemblages to specific quartz stages from different localities. This approach enabled us to distinguish six fluid inclusions generations in the QSP veins. Fluid inclusion analyses provide key information on the composition and physical state of ore-forming fluids in magmatic-hydrothermal systems. The main purpose of the present study was to investigate fluid inclusion assemblages trapped in transitional QSP veins, which predate epithermal ore deposition and may record the fluid composition prior to ore-mineral saturation. According to phase relations at room temperature, three different types of fluid inclusions can be recognized (Figure 7.4):

Vapor-rich (V) inclusions contain two phases, liquid plus more than 80 percent vapor (Figure 7.4 A). No daughter crystals could be observed. Vapor-rich inclusions commonly have negative crystal shape and range between 8 and 40 μm. They are generally abundant in euhedral quartz crystals and less frequent in subhedral vein quartz. Petrographically early vapor-rich inclusions coexist with brine inclusions and appear to be somewhat denser than late vapor-rich inclusions.

Hypersaline liquid or brine (B) inclusions contain a well-formed, cubic halite crystal and occasionally another daughter mineral (Figure 7.4 B). This second isotropic crystal, probably sylvite, has rounded edges, and a lower relief than halite. The vapor bubble occupies about 20 to 30 percent of the inclusion volume. Reddish or opaque hematite may occur as euhedral hexagonal or trigonal plates, but is restricted to inclusions hosted in the oldest quartz generation. Brine inclusions are usually negative-crystal shaped and range in size from 10 to 40 μm. They are not very common in QSP veins, but occur next to or in coexistence with vapor inclusions.

Liquid-rich (L) or aqueous inclusions cluster in two groups; L1 and L2 (Figure 7.4 C). *L1* inclusions have a regular shape and the vapor bubble occupies about 30 percent of the inclusion volume. One birefringent mineral, probably sericite, may have been trapped. The presence of CO_2 is likely, but generally insufficient to form discrete liquid CO_2 at room temperature. However, in some cases it could be revealed by

clathrate melting. *L2* inclusions are irregularly shaped and have a small vapor bubble of 10 to 20 percent inclusion volume. No daughter crystals are visible. They look similar to L1 inclusions but are petrographically later. Aqueous fluid inclusions are generally widespread in QSP veins and range in size from around 5 to 40 μm.
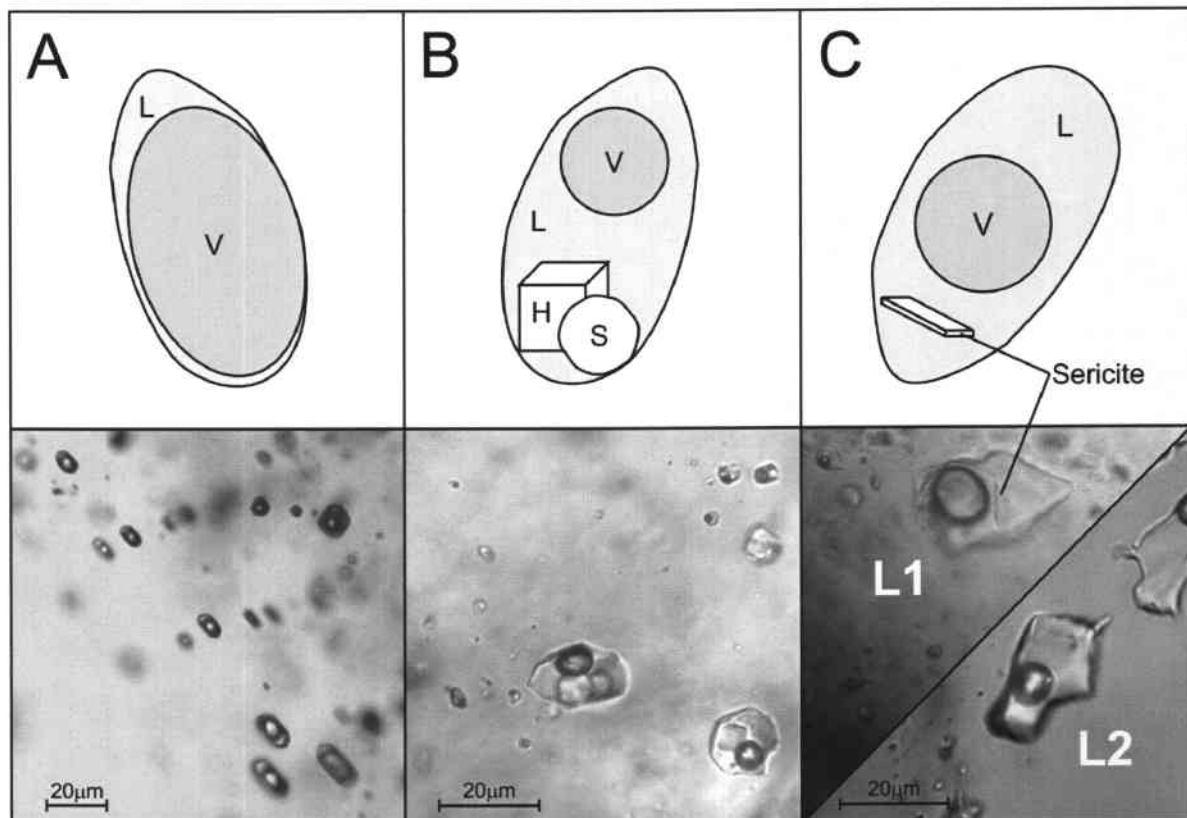
Figure 7.4: Sketches and photomicrographs of typical fluid inclusion types observed in transitional QSP veins at Famatina, NW Argentina. Fluid inclusion types correspond to those described in the text. (A) Pseudo-secondary trail of vapor-rich inclusions exhibiting negative crystal shape. (B) High-salinity brine inclusions with cubic halite and rounded sylvite daughter crystal. (C) Liquid-rich inclusions of both types, L1 and L2. Please note the slightly smaller vapor bubble and the absence of sericite in the L2 inclusions. Abbreviations: V, vapor; B, brine; L, liquid; H, halite; S, sylvite.

7.5.2 Fluid inclusion petrography and microthermometry

Petrographic observations and fluid inclusion data reported below are summarized for each of the four established quartz crystallization stages (Table 7.2, Figure 7.5). Microthermometric results of individual fluid inclusions from inclusion assemblages are documented in the Appendix table 3. As mentioned earlier, six specific types of fluid inclusion assemblages could be distinguished in the QSP veins. Figure 7.6 provides an example of the relative age succession of these fluid inclusion types and their assignment to the different quartz generations.

The oldest quartz generation (E) appears bright and strongly zoned, hosting clusters of brine inclusions (B_E) of possibly primary origin. Reddish or opaque hematite may occur. However, these inclusions are too small for microthermometric measurements and therefore not well constrained.

The next quartz generation (F) is host for primary assemblages of coexisting brine (B_F) and vapor-rich inclusions (V_F). Apparent salinities of the brine inclusions were determined by final dissolution of halite and yield values of 38.9 ± 1.6 wt% $NaCl_{equiv}$. Microthermometry on coeval vapor-rich inclusions was difficult to conduct due to the poor visibility of the liquid phase. Where final melting of ice was observed, the derived salinities of 3.9 ± 0.2 wt% $NaCl_{equiv}$ are higher than expected from the binary $NaCl-H_2O$ phase diagram, indicating co-entrapment of some brine (Roedder, 1971). One non-boiling vapor trail yielded salinities of 2.1 ± 0.3 wt% $NaCl_{equiv}$, which are still too high with respect to the theoretical value. Temperatures of homogenization were derived from coexisting brines by vapor bubble disappearance and yield values of $349 \pm 12°C$.

The third generation of quartz (G) forms euhedral crystals settled on top of the older quartz generations. This quartz type is host for a number of distinct fluid inclusion assemblages with clear crosscutting relationships. Primary brine inclusions (B_G) are subordinate and contain a halite daughter crystal; occasionally sylvite is present. The halite dissolves at $325 \pm 11°C$ (40.2 ± 0.9 wt% $NaCl_{equiv}$). Total homogenization through vapor bubble disappearance occurs at $350 \pm 9°C$. Aqueous inclusions of regular shape ($L1_G$) are somewhat later and occur along growth zones or in pseudo-secondary trails. Large inclusions often contain accidentally trapped sericite, which was identified by LA-ICP-MS microanalysis. The salinities were determined by final melting of ice and yield values of 5.0 ± 2.1 wt% $NaCl_{equiv}$. Total homogenization by

vapor bubble disappearance occurred at $362\pm10°C$. In one pseudo-secondary fluid inclusion assemblage, the presence of CO_2 was clearly revealed by clathrate melting at $+5.7\pm0.1°C$, yielding salinities of 8.0 ± 0.1 wt% $NaCl_{equiv}$. Here, total homogenization into the liquid phase occurred at significantly lower temperatures ($259\pm18°C$) either reflecting cooling or trapping of a different, CO_2-rich fluid.

The youngest quartz generation (H) hosts numerous vapor-rich inclusions and two groups of aqueous inclusions, L1 and L2. $L1_H$ inclusions are generally regularly shaped and occur along growth zones or in fractures that cut the older quartz generations. Microthermometric analyses reveal salinities of 5.7 ± 2.5 wt% $NaCl_{equiv}$ and total homogenization into the liquid phase at $327\pm53°C$. Clathrates have not been observed in any of the fluid inclusion assemblages. $L2_H$ inclusions are often irregular in shape and most frequent in secondary trails. In rare cases, they occur along late growth zones, indicating a primary origin. Salinities were determined by final melting of ice, yielding values of 1.5 ± 0.5 wt% $NaCl_{equiv}$. Total homogenization was determined by vapor bubble disappearance, which occurred at $229\pm28°C$. Vapor-rich inclusions (V_H) are widespread and have large bubbles that occupy more than 90 percent of the inclusion volume. Commonly, they occur along late fractures that clearly cut through all quartz generations present. Therefore, they are interpreted to reflect the last pulse of hydrothermal activity in QSP veins. Microthermometry was impossible to conduct due to the poor visibility of the liquid phase.

7.5.3 Pressure and depth estimates

Pressure estimates are documented for each fluid inclusion assemblage in Appendix table 3 and have been calculated after Driesner and Heinrich (in press). Due to the rare occurrence of boiling assemblages, the following data should be considered as minimum values. Petrographic evidence indicates that the shallow QSP veins were formed by moderate- to low-temperature fluids at the transition from lithostatic to hydrostatic conditions. This allowed incursion of ambient meteoric water and the development of a hydrothermal convection system.

Vapor pressure estimates calculated for B_F brine inclusions coexisting with V_F vapors yield values of 108 bars, indicating depths of cover between 400 m (lithostatic) and 1.1 km (hydrostatic). Similarly, minimum pressures for B_G brines range between 103 and 127 bars, yielding depth estimates of 385 and 480 m under lithostatic conditions

and more than 1.3 km overburden if a hydrostatic regime is favored. By contrast, vapor pressures calculated for aqueous fluid inclusions of type $L1_G$ yield values of 172 to 204 bars, indicating minimum depths of 650 to 770 m under lithostatic conditions. Under hydrostatic conditions, a value of around 2 km overburden is calculated, which is not supported by stratigraphic constraints. Aqueous $L1_H$ inclusions have a similar petrographic appearance but show a much wider scatter from 50 to 215 bars, yielding minimum depths of 185 to 800 m (lithostatic) and 500 m to 2.2 km (hydrostatic). This variation indicates that multiple cycles of sealing of the fracture system caused a repeated increase in pressure due to mineral precipitation. Minimum pressures for low-temperature $L2_H$ liquids yield values that cluster around 20 bars, indicating formation under hydrostatic conditions at more than 200 m depth. Experimental difficulties prevent calculation of pressure estimates for low-density, vapor inclusions of type V_H, which are interpreted to reflect the last pulse of hydrothermal activity in the transitional QSP stage.

Table 7.2: Overview of fluid inclusion types and their assignment to different quartz generations (see Appendix figure 3) based on petrographic distinction criteria and microthermometric measurements. Abbreviations: FI, fluid inclusion; p, primary; ps, pseudo-secondary; s, secondary; H, halite; S, sylvite; Hm, hematite; (Ser), accidentally trapped sericite; n.d., not determined; Th, total homogenization temperature. For more detailed information see Appendix table 3.

Quartz type	FI type	Vapor Vol%	Age relation	Daughter minerals	NaCl$_{equiv}$ wt%	Th °C	Distinction criteria
E	B$_E$	10-20	p	H, S, Hm	n.d.	n.d.	multiple daughter minerals
F	B$_F$	20-30	p	H, ±S	38.9±1.6	349±12	occasionally coexisting with V$_F$
F	V$_F$	>80	p	none	2.3±0.6	n.d.	occasionally coexisting with B$_F$
G	B$_G$	20-30	p	H, ±S	40.2±0.9	350±9	petrographically similar to B$_F$
G	L1$_G$	20-30	p, ps	(Ser)	5.0±2.1	362±10	cross-cutting B$_G$
G	L1$_G$	20-30	ps		8.0±0.1	259±18	clathrates
H	L1$_H$	20-30	p, ps, s	(Ser)	5.7±1.8	326±53	petrographically similar to L1$_G$
H	L2$_H$	10-20	p, s	none	1.5±0.5	229±28	smaller vapor bubble than L1$_H$
H	V$_H$	>90	s	none	n.d.	n.d.	latest fluid, small degree of fill
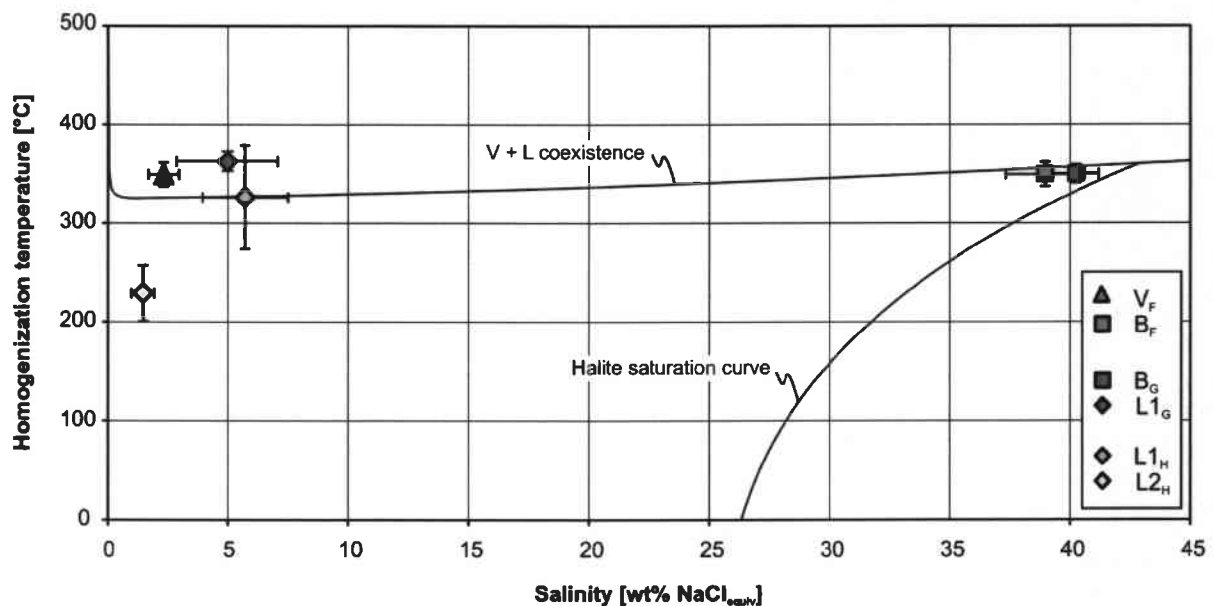
Figure 7.5: Summary plot of microthermometric measurements of the fluid inclusion generations outlined in the text. Symbol colors correspond to the different quartz formation stages illustrated in Figure 7.6. Vapor-liquid coexistence and halite saturation curves were calculated for 110 bars using the equations of Driesner and Heinrich (in press). The homogenization temperature of V$_F$ vapors was approximated from coexisting brine inclusions. Note that the apparent salinities determined for these vapor inclusions are too high with respect to the theoretical values, indicating co-entrapment of some high-salinity liquid. CO$_2$-rich aqueous inclusions of type L1$_G$ are not shown in this plot.
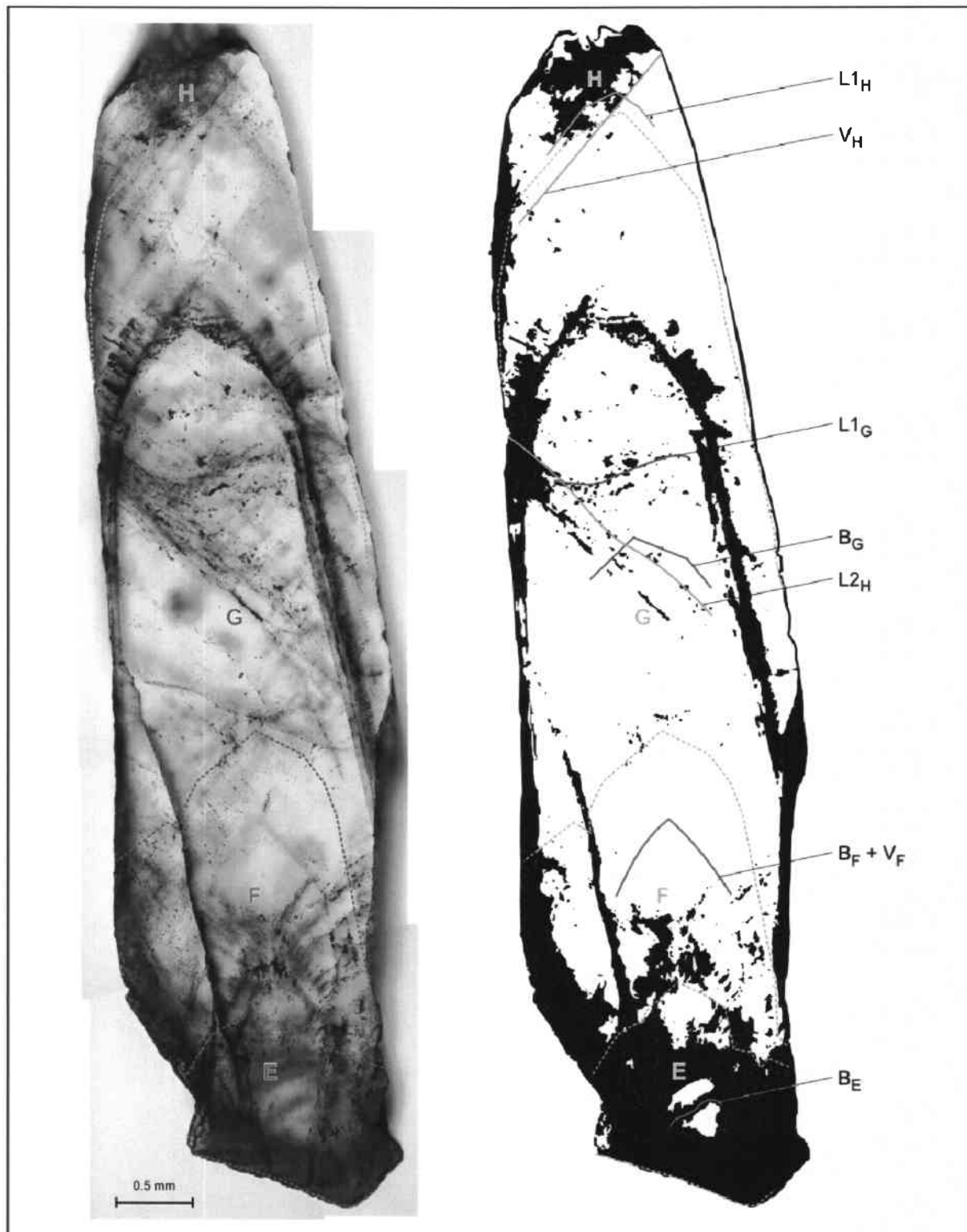
Figure 7.6: Detailed map of the time relations between quartz generations and fluid inclusion types in a euhedral quartz crystal of the transitional QSP stage (sample FM-DH4-277.6). The dashed colored lines in the photomicrograph represent the lower limit of each quartz generation outlined in the text. The solid line colors on the right hand side correspond to the petrographic stages to the left. For more detailed information the reader is referred to the text and to Appendix figure 3 C.

7.6   LA-ICP-MS microanalysis

LA-ICP-MS microanalysis was carried out on 120 individual fluid inclusions from 25 selected petrographic inclusion assemblages (see Appendix table 6). Generally, all inclusion types contain considerable amounts of Na, K, Fe, Cu, and Zn, and minor As, Sr, Ag, Sb, Te, Cs, Au, and Pb. Most strikingly, non-reactive element ratios, such as K/Na, Cs/Na, and Pb/Na, remain almost uniform across the entire inclusion sequence (Figure 7.7 A+B). By contrast, other elements show significant fluctuations (e.g., Fe, Cu) or are repeatedly below the limit of detection (e.g., Au). LA-ICP-MS data reported below are presented as average values of distinct fluid inclusion assemblages with 1 standard deviation uncertainty, in the context of their spatial and temporal evolution (Table 7.3).

Hypersaline B_F brines exhibit roughly constant values of Fe (5.2±1.8 wt%) and Cu (4600±1600 µg/g), but are highly variable in their trace element composition. Au is often below the limit of detection. Three analyses within one inclusion assemblage yielded significant but anomalously high values of 3.5, 3.6, and 17.3 µg/g Au, with the latter being thought to reflect an accidentally trapped Au-particle (i.e., micronuggets; see Chapter 5.4.8). This interpretation is supported by consistently lower LOD's of the other fluid inclusions in the same assemblage. Coexisting, low-salinity vapor-rich inclusions (V_F) show much lower Fe concentrations (0.8±0.2 wt%), but are relatively enriched in Cu (1300±300 µg/g). In general, their trace element composition is less precise due to the overall smaller mass of analyte at a given size. Au is below the limit of detection, and the scarce data of the other traces show a considerable scatter. However, the observed fractionation between V_F vapors and coeval B_F brines indicates absolute (for Te) or relative (for Cu, As, and Sb) enrichment of these elements in the vapor phase (Figure 7.7 J). Despite the limitations mentioned above, it has been noted that vapor inclusions of boiling pairs have higher salinities than expected from the binary H_2O-NaCl phase diagram (Figure 7.8). This observation indicates co-entrapment of some high-salinity liquid in the vapor inclusions (Figure 7.7 I), probably due to the enhanced wetting force of the coeval brine phase. True absolute element concentrations for the low-density vapor phase can be extrapolated using the trendlines produced by phase separation (see Figure 7.7 I). Knowing the theoretical salinity of the pure endmember vapor phase (0.0014 wt% $NaCl_{equiv}$;

Driesner and Heinrich, in press), calculations yield lower bulk concentrations for elements such as Cu (880 µg/g), Zn (380 µg/g), As (20 µg/g), and Sb (10 µg/g), and slightly higher values for Te (20 µg/g).

Primary **B$_G$** inclusions are remarkably consistent, with high concentrations of Fe (4.6±1.1 to 6.3±1.4 wt %) and Cu (3000±1900 to 3800±2400 µg/g). Au (0.9 µg/g) and other trace elements are commonly below the limit of detection. The low-salinity inclusion types **L1$_G$** and **L1$_H$** are chemically similar except for the higher Cu and Au concentrations in the L1$_G$ liquids (Figure 7.7 G). Large fluid inclusions often contain accidentally trapped sericite resulting in anomalously high K concentrations. These values were either discarded or corrected for small crystals using the mean K/Na ratio of the corresponding fluid inclusion assemblage. Cu contents are consistent within inclusion assemblages and vary between 130±70 µg/g and 5500±2400 µg/g. Au is often below the limit of detection but includes some values of several ppm, consistent with the calculated LOD's of the other inclusions in these assemblages (Figure 7.7 P). The limited data indicate a significant enrichment in L1$_G$ inclusions compared to L1$_H$ liquids (13.0±6.3 µg/g versus 1.8±0.8 µg/g) and correspond to high Cu concentrations (Figure 7.7 O). However, the unusually high Au concentrations in one particular L1$_G$ inclusion assemblage may result from an over-estimation of the Au content due to non-representative sampling of the short transient signal, as described by Pettke et al. (2000). Therefore, the lower but consistent Au values detected in several assemblages of L1$_H$ inclusions are considered to be more reliable.

The low-temperature **L2$_H$** inclusions are chemically comparable to L1$_H$ inclusions, despite their lower salinities and homogenization temperatures. Cu values are highly variable and range between 30±2 and 2900±680 µg/g. Fe concentrations are low and frequently below the limit of detection. Where detected, As and other traces show a considerable scatter within petrographically assigned fluid inclusion assemblages. One analysis yielded significant Au concentrations (4.2 µg/g), as indicated by the consistently higher LOD's of the other fluid inclusions in the same assemblage. The absolute element concentrations in **V$_H$** vapors cannot be accurately constrained due to the lack of salinity estimates. Therefore, an arbitrary value of 0.3 wt% NaCl$_{equiv}$ was used in order to determine "dummy" absolute values and to obtain independent element ratios. One analysis yielded tentative Au concentrations of 3.5 µg/g.
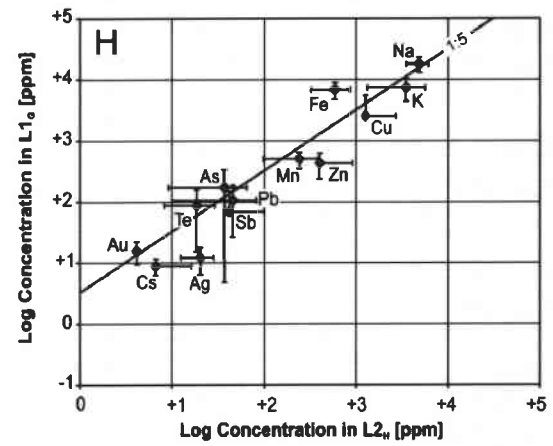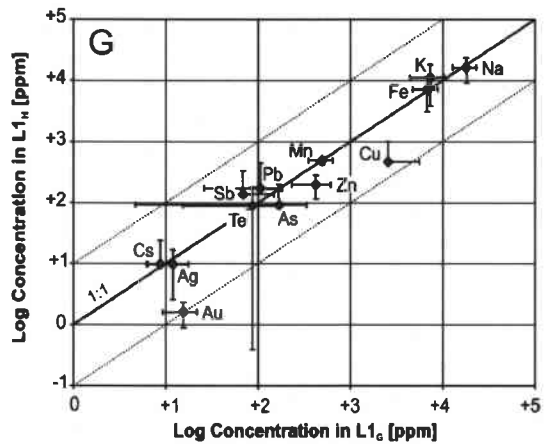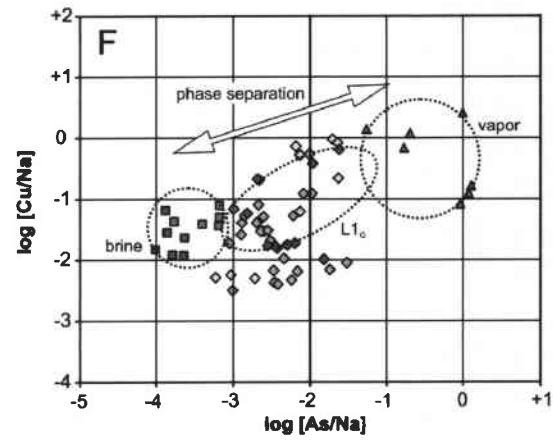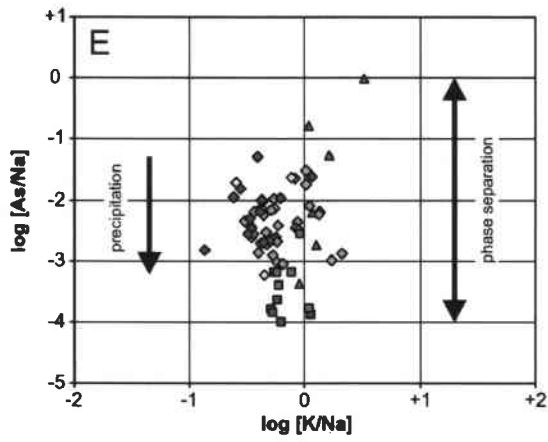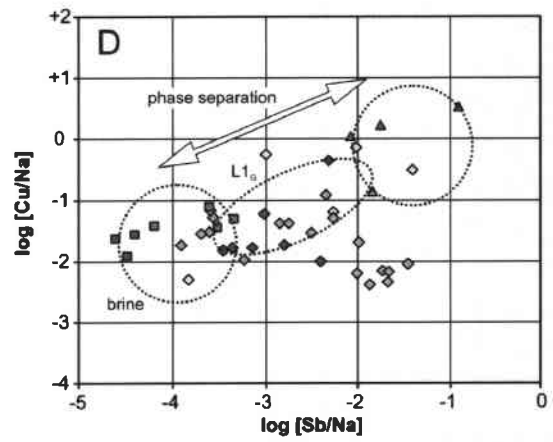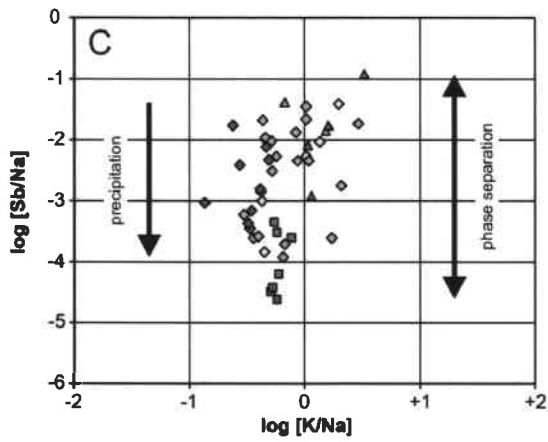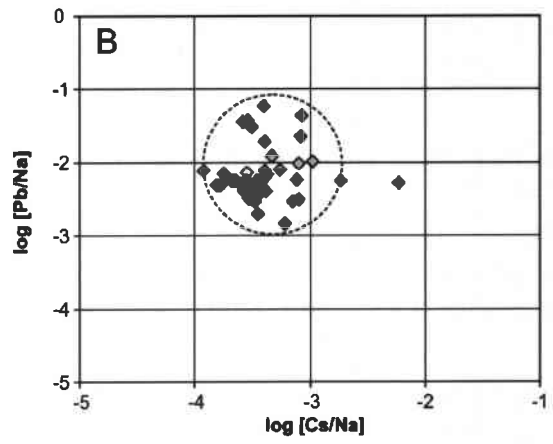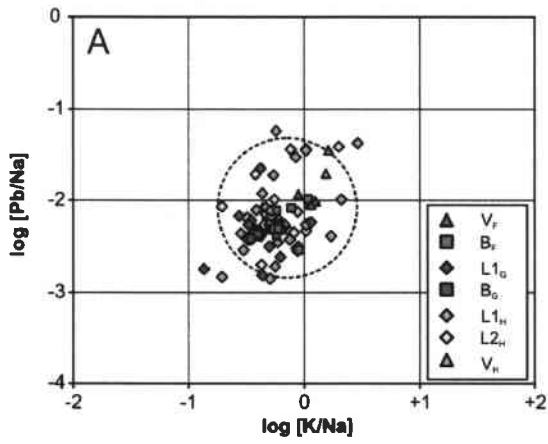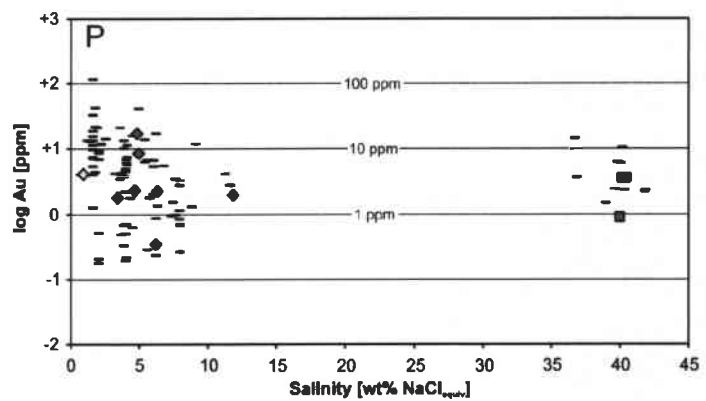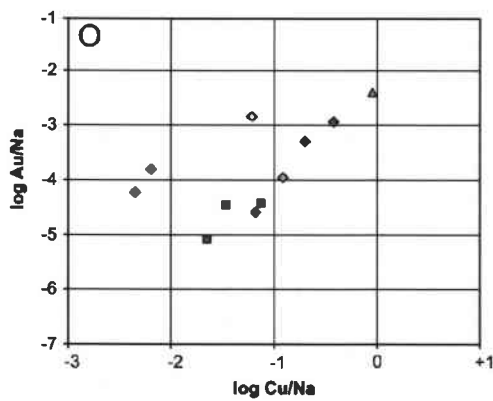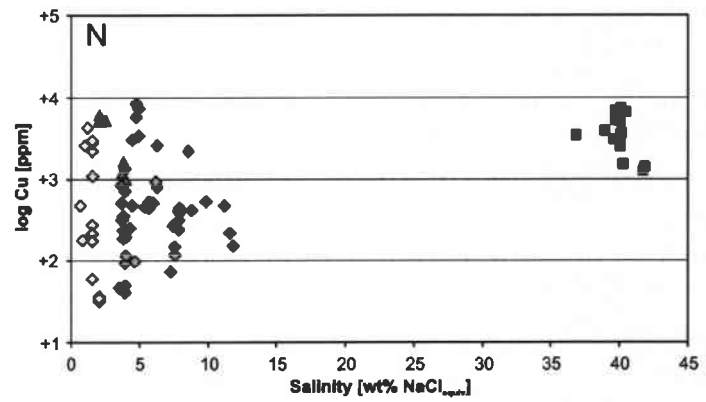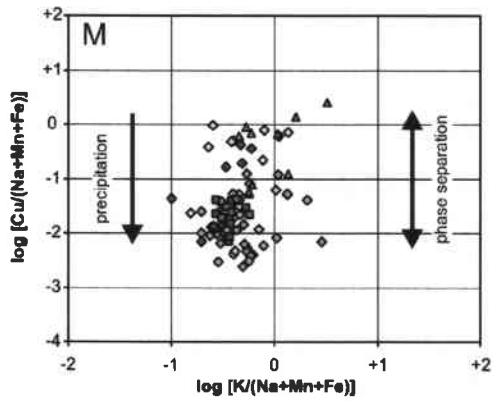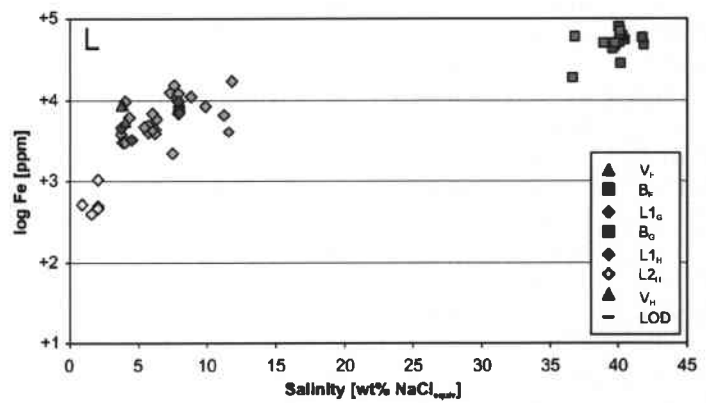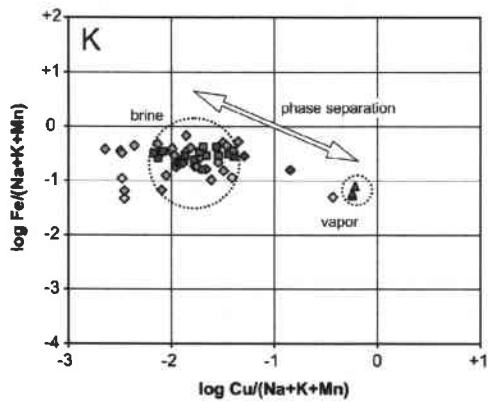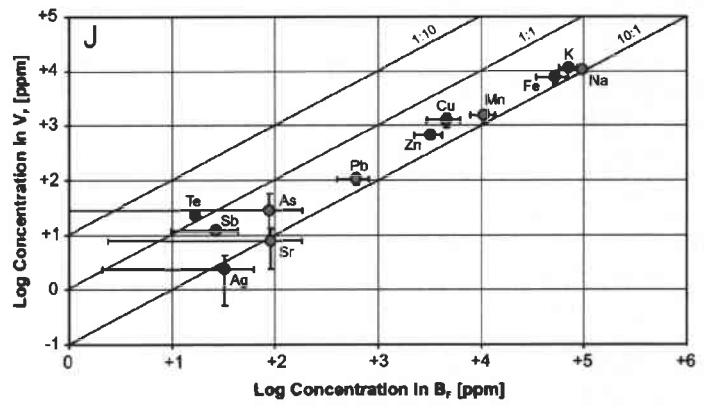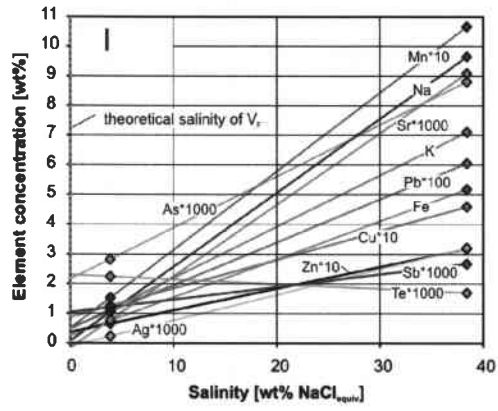
Figure 7.7 (previous pages): Selected element plots of the transitional QSP stage at Famatina illustrating LA-ICP-MS data of individual fluid inclusions color-coded after the petrographic quartz stages outlined in the text. Fluid types are indicated by the same symbol. To avoid uncertainties in the bulk salinity of vapor inclusions, most LA-ICP-MS data are plotted as element ratios, normalized to Na or to the sum of major cations present as chloride salts. (A+B) Non-reactive element ratios, such as K/Na, Cs/Na, and Pb/Na, behave passively and define a narrow range. (C-F) Large variations in the Sb/Na and As/Na ratios have been observed for all fluid generations and are interpreted to reflect two interacting processes: element fractionation upon phase separation and minor precipitation of high-sulfidation epithermal ore minerals, such as tennantite and tetrahedrite. In general, brines are depleted in Cu, As, and Sb, whereas coexisting vapors are enriched in those elements. Note that $L1_G$ liquids plot on an intermediate position between B_F brines and V_F vapors. (G) Element concentrations in $L1_G$ and $L1_H$ liquids demonstrate the compositional similarities between these fluids. Cu and Au are significantly enriched in the $L1_G$ liquid phase. (H) Element concentrations in aqueous liquids of type $L1_G$ and $L2_H$ illustrate the compositional differences between these fluids, probably related to 4-fold dilution of $L1_G$ by pure H_2O. (I) Average concentrations of V_F inclusions coexisting with B_F brines from a boiling assemblage (sample FM-DH4-276.6). Trendlines for each element indicate co-entrapment of some high-salinity liquid in the vapor phase. This hypothesis corresponds to the observed salinities of the V_F inclusions, which are too high with respect to the theoretical value. (J) Sample FM-DH4-276.6: Element concentrations in vapor inclusions of type V_F coexisting with B_F brines from a boiling assemblage. Note the fractionation of Cu, Zn, As, Sb, and Te in favor of the vapor relative to the brine phase. Au concentrations in the vapor are below the limit of detection and, therefore, have not been plotted. (K+M) Large variations in the $Cu/(Na+K+Mn)$ ratio of all fluid types probably reflect two interacting processes: element fractionation upon fluid boiling and minor precipitation of Cu-sulfides. (L) Absolute Fe concentrations are highest in the hypersaline brine inclusions and lowest in the low-salinity $L2_H$ inclusions. (N) Cu values do not show a salinity-dependent variation, but exhibit a large scatter in the vapor-rich and aqueous fluid inclusions. (O+P) Au is most frequently below the limit of detection, as indicated by the black bars. However, the scarce data indicate enrichment in the aqueous fluid inclusions and a positive correlation with Cu. Au concentrations in V_H vapors are not reliable due to the lack of bulk salinity estimates, and therefore have not been plotted.

Table 7.3: LA-ICP-MS concentration data of fluid inclusion types from the transitional QSP stage. Data are presented as average values of inclusion assemblages, with 1 standard deviation (stdev) and the number of significant concentrations (N) in brackets. <VALUE reports lowest limits of detection using the 3 sigma criterion. * denotes boiling assemblages. N.a. indicates elements that were not analyzed. Note that the bulk salinity for V_H vapors is estimated, yielding tentative absolute element concentrations.

	chip	Salinity wt%	Na wt%	stdev	(N)	K wt%	stdev	(N)	Fe wt%	stdev	(N)	Cu ppm	stdev	(N)	Zn ppm	stdev	(N)	As ppm	stdev	(N)
B_F																				
FM-DH4-276.6*	1	38.9	9.6	0.9	(6)	7.1	1.5	(6)	5.2	1.8	(6)	4600	1600	(6)	3200	930	(6)	90	100	(6)
V_F																				
FM-DH4-276.6*	1	3.9	1.0	0.1	(3)	1.1	0.1	(3)	0.8	0.2	(3)	1300	330	(3)	660	70	(3)	30	30	(3)
FM-DH4-277.6	1	2.1	0.5	0.2	(5)	0.7	0.1	(3)	<0.4			5400	430	(5)	n.a.			1200	870	(4)
B_G																				
FM-DH4-427.3	2-14	40.3	9.7	1.4	(3)	7.3	1.6	(3)	6.3	1.4	(3)	3000	1900	(3)	2300	950	(3)	20	9	(3)
FM-DH4-427.3	2-5	40.2	11.4	0.7	(5)	5.6	0.9	(6)	4.6	1.1	(6)	3800	2400	(6)	2200	370	(6)	20	5	(3)
$L1_G$																				
FM-DH4-277.6	2	7.9	2.5	0.1	(6)	0.8	0.1	(6)	0.8	0.1	(6)	390	70	(6)	n.a.			150	110	(6)
FM-DH4-427.3	2-2	4.1	1.4	0.1	(5)	0.4	0.2	(5)	0.5	-	(1)	810	-	(1)	290	-	(1)	240	270	(4)
FM-DH4-427.3	2-14	4.9	1.5	0.1	(5)	0.9	0.3	(5)	0.3	-	(1)	5500	2400	(5)	560	-	(1)	140	140	(4)
$L1_H$																				
FM-DH4-277.6	4	7.0	2.3	1.0	(4)	1.1	0.6	(4)	1.0	0.2	(4)	350	120	(4)	n.a.			<20		
FM-DH4-277.6	4	7.4	2.0	0.8	(5)	1.8	1.6	(5)	0.4	0.0	(2)	210	-	(1)	n.a.			110	10	(3)
FM-DH4-350.5	2	3.7	0.4	0.0	(4)	0.2	0.1	(4)	0.3	0.1	(4)	210	80	(4)	200	80	(4)	<2		
FM-DH4-427.3	2b	6.6	1.9	0.6	(4)	1.5	0.7	(4)	0.5	0.2	(4)	580	230	(4)	n.a.			20	6	(3)
FM-DH4-427.3	2-18	4.6	1.2	0.2	(10)	1.0	0.4	(10)	n.a.			440	430	(8)	n.a.			40	30	(7)
FM-DH4-427.3	3-2	5.9	1.6	0.1	(2)	0.8	0.1	(2)	1.0	0.2	(2)	200	30	(2)	n.a.			<5		
FM-DH4-427.3	3-2	6.9	2.3	0.4	(3)	1.0	0.6	(3)	<0.1			2400	230	(2)	n.a.			140	110	(2)
FM-DH4-277.6	2	5.7	1.8	0.3	(4)	1.4	0.6	(4)	<0.5			<160			n.a.			<110		
FM-DH4-352.1	1	6.3	2.0	0.3	(5)	0.8	0.2	(5)	0.5	0.2	(5)	600	260	(5)	n.a.			60	30	(5)
FM-CP05-06	1	6.0	1.6	0.8	(8)	1.3	0.5	(8)	1.2	0.4	(5)	130	70	(5)	n.a.			180	180	(7)
$L2_H$																				
FM-DH4-277.6	4	2.2	0.7	0.0	(3)	0.3	0.1	(3)	0.1	0.1	(3)	30	2	(3)	n.a.			8	5	(3)
FM-DH4-427.3	2-18	1.1	0.3	0.1	(4)	0.5	0.4	(4)	0.1	-	(1)	330	210	(2)	<7			40	20	(2)
FM-DH4-427.3	2-3	1.8	0.6	0.1	(3)	0.3	0.3	(3)	<0.2			<70			260	170	(2)	<50		
FM-DH4-427.3	2-2	1.6	0.5	0.1	(3)	0.3	0.1	(3)	<0.2			190	30	(2)	120	-	(1)	<80		
FM-DH4-427.3	2-2	1.4	0.4	0.1	(4)	0.3	0.1	(4)	<0.3			<210			210	-	(1)	<210		
FM-DH4-427.3	2-7	1.4	0.5	0.1	(6)	0.3	0.2	(6)	0.1	-	(1)	2900	680	(6)	150	50	(2)	50	20	(5)
FM-DH4-427.3	2-11	1.5	0.4	0.1	(3)	0.5	0.2	(3)	<0.1			470	540	(3)	810	760	(3)	<50		
V_H																				
FM-DH4-427.3	2-3	[0.3]	0.1	0.0	(6)	0.1	0.0	(6)	<0.1			440	340	(5)	80	-	(1)	<40		

Table 7.3 (cont.): LA-ICP-MS concentration data of fluid inclusion types from the transitional QSP stage. Data are presented as average values of inclusion assemblages, with 1 standard deviation (stdev) and the number of significant concentrations (N) in brackets. <VALUE reports lowest limits of detection using the 3 sigma criterion. * denotes boiling assemblages. N.a. indicates elements that were not analyzed. Note that the bulk salinity for V_H vapors is estimated, yielding tentative absolute element concentrations.

	chip	Salinity wt%	Ag ppm	stdev	(N)	Sb ppm	stdev	(N)	Te ppm	stdev	(N)	Cs ppm	stdev	(N)	Au ppm	stdev	(N)	Pb ppm	stdev	(N)
B_F																				
FM-DH4-276.6*	1	38.9	30	30	(3)	30	20	(4)	20	-	(1)	n.a.			8.1	7.9	(3)	600	210	(6)
V_F																				
FM-DH4-276.6*	1	3.9	1	-	(1)	10	-	(1)	20	-	(1)	n.a.			<1			110	30	(3)
FM-DH4-277.6	1	2.1	<40			110	110	(5)	<200			<4			<7			150	50	(3)
B_G																				
FM-DH4-427.3	2-14	40.3	6	-	(1)	3	-	(1)	<2			n.a.			0.9		(1)	550	150	(3)
FM-DH4-427.3	2-5	40.2	10	3	(4)	4	0	(2)	<30			n.a.			<2			540	50	(6)
$L1_G$																				
FM-DH4-277.6	2	7.9	8	-	(1)	30	40	(5)	<9			8	2	(6)	<1			130	30	(6)
FM-DH4-427.3	2-2	4.1	20	-	(1)	120	120	(3)	8	-	(1)	10	0	(2)	<6			170	200	(2)
FM-DH4-427.3	2-14	4.9	<20			80	-	(1)	130	30	(2)	n.a.			12.9	6.3	(2)	50	20	(4)
$L1_H$																				
FM-DH4-277.6	4	7.0	<3			<5			<30			6	2	(4)	<1			150	80	(4)
FM-DH4-277.6	4	7.4	<10			<20			<90			7	3	(4)	1.8	0.0	(2)	100	8	(3)
FM-DH4-350.5	2	3.7	<1			1			<2			n.a.			<1			20	5	(3)
FM-DH4-427.3	2b	6.6	<4			3	0		30	-	(1)	5	2	(3)	0.6	0.3	(2)	90	40	(4)
FM-DH4-427.3	2-18	4.6	n.a.			50	60		160	160	(2)	20	30	(9)	<1			60	20	(7)
FM-DH4-427.3	3-2	5.9	2		(1)	<1			10	5	(2)	7	0	(2)	<1			110	7	(2)
FM-DH4-427.3	3-2	6.9	<7			<5			90	-	(1)	10	2	(2)	1.8	0.7	(2)	670	820	(3)
FM-DH4-277.6	2	5.7	<30			<30			<150			10	4	(3)	<6			100	50	(3)
FM-DH4-352.1	1	6.3	<10			50	40		20	-	(1)	6	2	(4)	<1			80	10	(5)
FM-CP05-06	1	6.0	10			290	240		100	50	(4)	8	4	(7)	2.2	0.2	(2)	350	280	(6)
$L2_H$																				
FM-DH4-277.6	4	2.2	<1			<1			<5			2	0	(3)	<1			40	6	(3)
FM-DH4-427.3	2-18	1.1	<1			<1			9	-		n.a.			4.2	-	(1)	50	30	(2)
FM-DH4-427.3	2-3	1.8	<9			<20			<80			n.a.			<9			90	40	(2)
FM-DH4-427.3	2-2	1.6	<20			<9			<120			n.a.			<7			40	1	(3)
FM-DH4-427.3	2-2	1.4	<20			<20			n.a.			20		(1)	<10			<20		
FM-DH4-427.3	2-7	1.4	30	-	(1)	20	20	(4)	20	9	(2)	n.a.			<1			20	6	(3)
FM-DH4-427.3	2-11	1.5	10	-	(1)	80	80	(8)	<30			n.a.			<4			60	70	(3)
V_H																				
FM-DH4-427.3	2-3	[0.3]	20	-	(1)	20	20	(2)	n.a.			2	-	(1)	3.5	-	(1)	8	5	(4)

7.7   Interpretation and discussion

7.7.1   P-T-X fluid evolution paths

Linking the trapping chronology of specific fluid inclusion types with the established sequence of quartz and sulfide precipitation allowed reconstruction of the fluid evolution in the transitional QSP stage. This is followed by a discussion of the effects of phase separation and mineral precipitation on the composition of the ore-forming fluids. However, attempts to relate fluid inclusion characteristics to the QSP stage mineralization were difficult to constrain due to the scarcity and small size of the inclusions. Post-entrapment modification is another process that has to be evaluated before interpreting the data obtained from the fluid inclusion study. In many cases, modification of the fluid properties after entrapment remains undiscovered unless obvious features, such as decrepitation or sweat halos, are visible (Audétat and Günther, 1999). However, fluid inclusions analyzed for this study mainly originate from free-standing quartz crystals; hence modification related to deformation is unlikely. Moreover, the salinities, homogenization temperatures, and element ratios are remarkably uniform within the selected fluid inclusion assemblages. Therefore, it is suggested that the data represent reliable records of the original fluid properties. The systematic differences between the inclusion generations indicate a consistent fluid evolution of the QSP stage. The observed succession of quartz formation and fluid trapping can be explained by one source fluid ascending through the crust, thereby cooling and evolving towards the surface.

Petrographically early fluid inclusion assemblages in dense vein quartz (E) contain a hypersaline liquid (B$_E$) of unknown temperature and salinity. The host quartz is rich in trace elements and shares many characteristics with the B-veins (quartz B) of the porphyry stage. Therefore, it is interpreted to represent an earlier vein generation, which was reopened and overgrown by the QSP assemblage.

The next quartz generation (F) hosts abundant inclusions of low-density vapor (V$_F$), which separated from a Fe-rich brine (B$_F$) upon fluid boiling at 350°C and 108 bars (Figure 7.8 A). This pressure estimate is significantly lower than those calculated for boiling assemblages in the porphyry system and is consistent with petrographic evidence indicating vein formation at the transition from lithostatic to hydrostatic conditions. Apparent salinities of the vapor inclusions are too high with respect to the

theoretical value of 0.0014 wt% $NaCl_{equiv}$ (calculated after Driesner and Heinrich, in press) and probably reflect co-entrapment of some hypersaline liquid. However, V_F vapors show a considerable enrichment of Cu, Zn, As, Sb, and Te relative to the coexisting B_F brines. The host quartz exhibits a bright CL color, which corresponds to high concentrations in Na, K, and Fe.

The third generation of quartz (G) is characterized by a significant decrease in K, Na, and Fe, which coincides with a significant drop in salinity from primary B_G brines (40.2±0.9 wt% $NaCl_{equiv}$) to pseudosecondary $L1_G$ liquids (5.0±2.1 wt% $NaCl_{equiv}$). Hypersaline B_G brines were trapped at around 350°C and more than 103 bars, and are chemically similar to B_F brines. However, no coexisting vapor phase has been observed. By contrast, vapor pressures calculated for the low-salinity $L1_G$ inclusions commonly exceed 170 bars. These aqueous liquids homogenize at 360°C and are extremely rich in Cu, As, Ag, Sb, Te, and Au, with some gold analyses in the order of 10 ppm (Figure 7.7 P). This element suite corresponds closely to that of the subsequently deposited high-sulfidation epithermal veins at La Mejicana. Moreover, even the relative proportions of these elements are of comparable magnitude as the respective ore grades, which are not precisely known but include 1.3% Cu, 40 ppm Ag, and 32 ppm Au (Corriente press release September 29, 1999). Importantly, the $L1_G$ liquids are far too Cu-Sb-As-Ag-Te-Au rich to be generated by simple meteoric dilution of any brines recorded in the porphyry complex, including the most closely associated and immediately preceding B_F inclusions. Compositionally, the $L1_G$ liquids plot on an intermediate position between B_F brines and V_F vapors (Figure 7.7 D+F). Due to pressure and temperature constraints they cannot easily be explained as products of local remixing. It is possible that vein sealing between stage F and G resulted in a pressure increase from 108 to more than 170 bars, and thus permitted re-mixing of the otherwise immiscible phases (i.e., B_F and V_F), resulting in formation of the $L1_G$ liquids. However, $L1_G$ inclusions are more likely to record the initial composition of the source fluid originating from greater depth, either as a single-phase magmatic fluid of intermediate density, or as a vapor that condensed out some brine and then cooled at elevated pressure. These two alternatives will be discussed in more detail in Chapter 9. Large $L1_G$ inclusions often contain accidentally trapped sericite indicating that muscovite was stable at the given P-T-X conditions. This attribute corresponds to the observed feldspar-destructive sericitic alteration halo along QSP veins, leading to the typical overprint of earlier potassic alteration

assemblages. However, euhedral pyrite frequently overgrows the host quartz and contains abundant sulfide inclusions.

The youngest quartz generation (H) exhibits a dark luminescence color and is commonly associated with fractured pyrite, which contains numerous high-sulfidation epithermal minerals, such as tennantite and enargite. Locally, pseudo-cubic alunite fills open spaces of the QSP assemblage. This trace-element poor quartz occurs in vein centers and is host for low-salinity $L1_H$ inclusions (5.7±1.8 wt% $NaCl_{equiv}$), which were trapped at ~325°C. Estimated vapor pressures vary between 50 and 215 bars, indicating multiple cycles of vein sealing. These aqueous liquids are similar to $L1_G$ inclusions (Figure 7.7 G), but show a much wider range in their physico-chemical properties (Figure 7.7 C+E). However, $L1_H$ inclusions still contain much of the ore-forming components, including enhanced concentrations of Cu, As, Sb, Te, and Au relative to Na. Late primary inclusions trapped at the end of quartz H contain an aqueous liquid ($L2_H$) of low temperature (230°C) and salinity (1.5±0.5 wt% $NaCl_{equiv}$). The compositional differences observed between $L2_H$ fluids and earlier aqueous inclusions are consistent with dilution of $L1_G$ liquids by approximately 400% pure H_2O (Figure 7.7 H). This hypothesis is supported by pressure estimates of 20 bars, indicating formation under hydrostatic conditions, which permitted incursion of ambient meteoric water. The limited data presented in Chapter 8 indicate that $L2_H$ fluids reflect the transition to the main high-sulfidation epithermal stage, which is dominated by sulfides, sulfosalts, and alunite, but contains very little quartz. The last pulse of hydrothermal activity is recorded by secondary trails of low-density V_H vapor inclusions of unknown temperature and salinity.

7.7.3 Phase separation and ore metal precipitation

Despite significant variations in the salinity and density of fluids trapped in QSP veins (including vapors, brines, and aqueous liquids), the concentration ratios of elements that are not visibly associated with alteration and precipitation minerals (e.g., Cs/Na and Pb/Na) remain essentially constant within the analytical uncertainty of single inclusion assemblages. This contrasts with large variations in those elements that are either precipitating as sulfides, or fractionate significantly between coexisting brines and vapors relative to Na.

Boiling assemblages have been observed in quartz stage F, indicating phase separation at 108 bars. This process generated large volumes of vapor (87%, Figure 7.8 A), which is relatively enriched in certain ore metals, such as Cu, As, Sb, and Te. This typical element suite corresponds closely to that of the high-sulfidation epithermal ore veins at La Mejicana. However, pressure and temperature constraints indicate that the source fluid of this boiling assemblage is likely to be identical with aqueous fluids of type L1, which were trapped in the subsequent quartz stages G and H.

Cu solubility and Cu-sulfide ore deposition has been demonstrated to be strongly temperature dependent (Hezarkhani et al., 1999), suggesting that decreasing temperature is a major driving force for ore metal precipitation. The precipitation of ore metals upon cooling is a quantitative process leading to a decrease in metal concentration in the ore-forming fluid over several orders of magnitude. Large variations in element concentrations and ratios have been observed for all fluid types analyzed in this study. However, Cu concentrations are highest and most consistent in $L1_G$ inclusion assemblages, which are interpreted to record the initial composition of the ore-forming fluids prior to ore-mineral saturation. All succeeding fluid inclusion assemblages trapped in quartz H exhibit lower and more variable Cu concentrations (Figure 7.7 N). A similar trend has been observed for other elements (e.g., Sb and As) and their respective element ratios (Figure 7.7 C+E). This trend coincides with a significant decrease in temperature (325 to 230°C) and pressure (215 to 20 bars) and petrographic evidence indicating initiation of high-sulfidation epithermal ore-metal precipitation at the end of stage H. Cooling of the hydrothermal fluids was probably enhanced by a 4-fold dilution with ambient meteoric water (see Figure 7.7 H), in transition to the overlying high-sulfidation epithermal Cu-Au veins. However, some low-temperature, low-salinity $L2_H$ fluid inclusions show very high Cu concentrations (2900±680 µg/g), possibly indicating local re-dissolution of previously deposited sulfide ore (see Figure 7.8 B). Here, fluids probably became increasingly acid due to physical isolation from acid-consuming wall-rock minerals, e.g., in vein centers or at the transition from sericitic to advanced argillic alteration, similar to El Teniente (Klemm, 2005) and Bingham (Landtwing et al., 2005). Another possible explanation is that these inclusions represent a new and probably more acid fluid pulse of lower temperature, introducing the main stage of high-sulfidation epithermal ore deposition at La Mejicana.

7.8 Conclusions

Detailed fluid inclusion petrography and microthermometry followed by LA-ICP-MS analyses of more than 100 individual fluid inclusions allowed reconstruction of the fluid evolution of the QSP veins, which are transitional in time and space between the preceding porphyry and the subsequent epithermal mineralization.

Paragenetic vein relationships and fluid inclusion data indicate that precious ore metals are mainly transported by a high-temperature aqueous liquid of about 5 wt% $NaCl_{equiv}$ salinity that enters the system through QSP veins. These veins grade upwards into high-sulfidation epithermal assemblages, but cut through the upper parts of the porphyry system and postdate potassic alteration. Therefore, they are interpreted to represent linking channelways of the ore-bearing fluids generating the high-sulfidation epithermal deposit. Cooling of these fluids was probably enhanced by contribution of surface-derived fluids (ambient meteoric water) and eventually resulted in formation of the high-sulfidation epithermal Cu-Au veins at La Mejicana.

Figure 7.8 (next page): Summary plots of the transitional QSP stage illustrating the evolution of the magmatic-hydrothermal fluids. Note that fluid types are indicated by the same symbol. Symbol colors correspond to the petrographic quartz stages outlined in the text. (A) 3D phase diagram of the binary H_2O-NaCl system after Driesner and Heinrich (in press) illustrating the simplified fluid pathway. Phase separation occurred at 103 bars and 350°C. Composition of the source fluid is estimated from $L1_G$ inclusions. The apparent salinities (filled triangles) of V_F vapor inclusions are too high with respect to the theoretical values (open triangles) indicating co-entrapment of some B_F brine. (B) Large variations in the Cu/Na ratio can be explained by one source fluid ascending through the crust, thereby cooling and evolving towards the surface. Mixing with meteoric water probably enhanced cooling of the hydrothermal fluids and eventually resulted in precipitation of high-sulfidation epithermal minerals. Local re-dissolution of previously deposited sulfide ore was caused by more acid fluids, which were physically isolated from acid-consuming wall-rock minerals. Fluid temperatures reflect estimates based on homogenization temperatures and relative age relationships of the fluid inclusion assemblages.
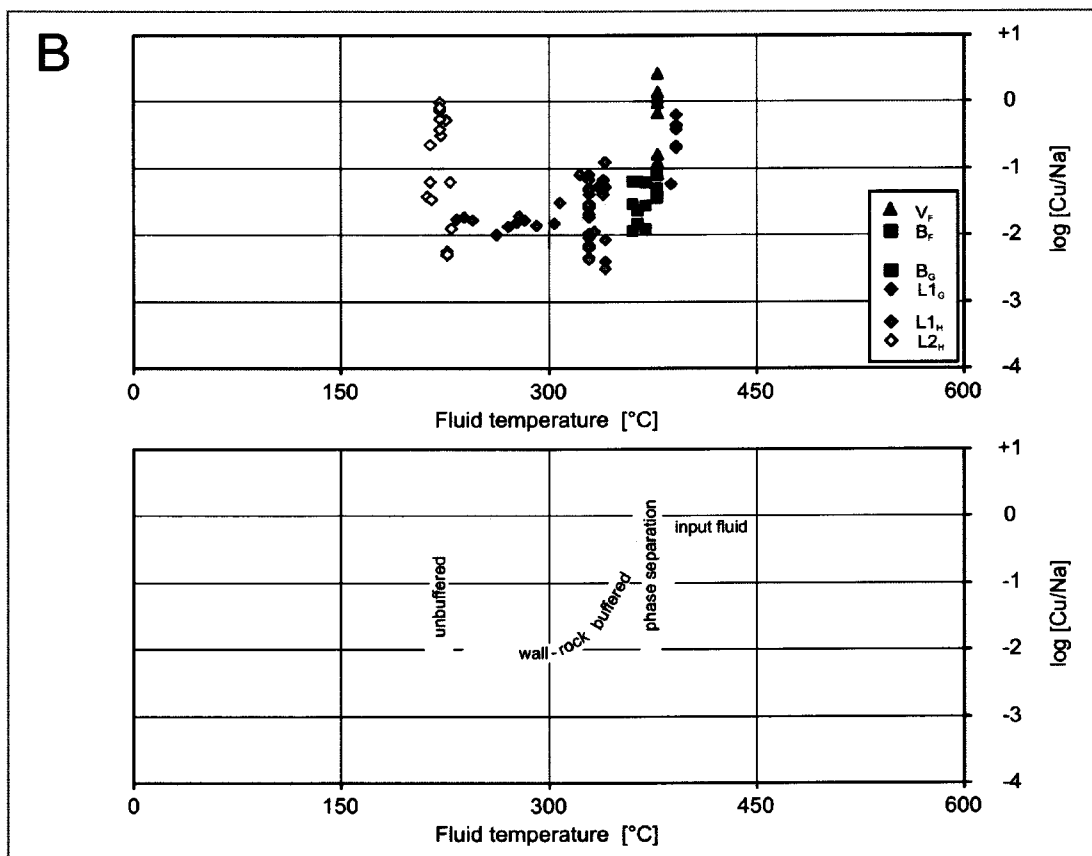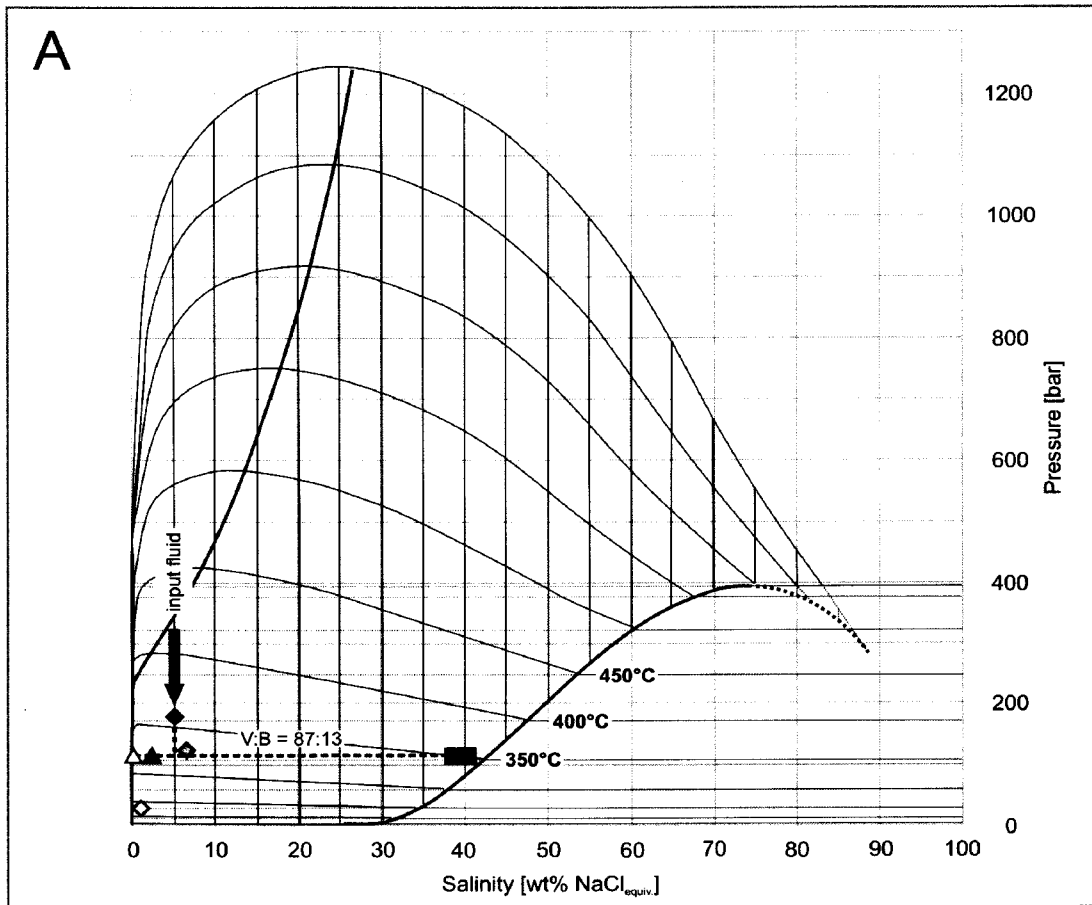
8   HIGH-SULFIDATION EPITHERMAL-STAGE MINERALIZATION

8.1   Introduction

High-sulfidation epithermal-stage mineralization at La Mejicana occurs between 4335 and 4750 m elevation (see Figure 4.5). Textural and structural evidence indicates that the high-sulfidation epithermal Cu-Au veins postdate A-veinlets, B-veins, and QSP veins. This final stage of mineralization is associated with E-W trending faults and fractures that formed after the main tectonic event during tensional relief (Schalamuk and Logan, 1994). Therefore, epithermal mineralization is defined as the period of hydrothermal activity that occurred after cessation of intrusive activity at present levels of exposure. However, epithermal alteration occurs in proximity to the porphyries and includes alunitic, alsic, kaolinitic, and sericitic assemblages. Spatial and temporal transitions between porphyry Cu and shallow epithermal Au deposits have been suggested by many workers (e.g., Sillitoe, 1973; Heald et al., 1987; Rye, 1993; Muntean and Einaudi, 2001; Einaudi et al., 2003). However, the current knowledge about the composition of porphyry-derived fluids and their role in the formation of epithermal ore deposits is still not well constrained. To address the above issue, this study focuses on fluid inclusions trapped in epithermal quartz, which corresponds to the alunitic alteration. However, attempts to relate physico-chemical properties to inclusion assemblages were difficult to conduct due to the scarcity and small size of the fluid inclusions. Therefore, the following sections are mainly based on field observations, mineralogical studies of drillcore material and dump-site samples, and previous investigations by Losada-Calderón (1992).

8.2   Mineralization and alteration

High-sulfidation epithermal Cu-Au veins at La Mejicana are steeply dipping (60-90°), E-W trending veins, with widths of centimeters to meters. The vein material consists of famatinite, enargite, pyrite, and alunite in variable proportions, with minor quartz, kaolinite, dickite, diaspore, pyrophyllite, tennantite, tetrahedrite, sphalerite, gold, tellurides, covellite, and chalcopyrite (Losada-Calderón and Bloom, 1990). Quartz

has a microcrystalline texture and commonly lines open spaces. Alunite is mainly of hypogene origin, indicated by its coarse grain size, bladed crystal habit, and its close association with hypogene Cu minerals. Gold occurs as free gold and in tellurides, such as calaverite and sylvanite (Losada-Calderón and McPhail, 1996). Enargite and famatinite are the dominant sulfosalts and Cu-bearing minerals, and form massive granular intergrowths. Covellite occurs either as rims on tennantite-tetrahedrite or as isolated grains within alunite. Pyrite is also common and usually constitutes the cores of grains with marcasite overgrowths. Chalcopyrite occurs as a minor constituent, often as inclusions in sphalerite and pyrite. Argentite, freibergite, and native silver have also been reported, but only occur in the upper levels of the deposit (Losada-Calderón, 1992).

Epithermal alteration minerals are particularly abundant in the northwestern part of the district and include alunite, kaolinite, illite, dickite, pyrophyllite, diaspore, zunyite, and sericite. These minerals are characteristic of the advanced argillic alteration (Hedenquist and Arribas, 1999) and overprint all previous (porphyry-style) alteration assemblages. Based on the dominant mineral constituents, four types of epithermal alteration could be distinguished (Figure 8.1):

Texturally destructive *alunitic* alteration, usually less than 1 m wide, includes quartz and alunite, and occurs discontinuously along nearly vertical faults or fractures. Fine-grained quartz is dominant and may contain small inclusions of hematite, whereas alunite occurs as well-developed crystals that exhibit growth zones.

With increasing distance from the vein center, alunite becomes progressively more abundant, grading into an assemblage of quartz, pyrophyllite, alunite, and pyrite. This so-called *alsic* alteration (Hudson, 2003) is zoned laterally outward and vertically upward from the alunitic alteration. Quartz lines vugs and may contain hematite inclusions. Alunite and pyrophyllite form intergrowths that cluster around sulfides and sulfosalts.

The *kaolinitic* assemblage forms zones of up to 200 m width and occurs laterally outward and vertically upward from the alsic alteration. Both, dickite and kaolinite are present, but their distribution has not been studied. With increasing elevation, the kaolinitic alteration grades into an assemblage of anhydrite and barite closely associated with kaolinite. In subsurface samples, the anhydrite has been altered to gypsum.

The *sericitic* assemblage is found at depth and consists of sericite, quartz, rutile, illite, and pyrite. It is considered to represent shallow transitional QSP veins associated with sericitic alteration, which have been described in detail in Chapter 7.

A general textural variation with regard to elevation is also evident. Massive sulfide veins dominate the deeper parts of the system, whereas crustiform textures are more common in the upper levels. Mineralized breccias are rare, but have been reported at different stratigraphic levels, and may be the result of post-mineralization faulting (Losada-Calderón, 1992). These clast-supported breccias contain fragments of the Negro Peinado Formation cemented by sulfosalts, tellurides, and pyrite.
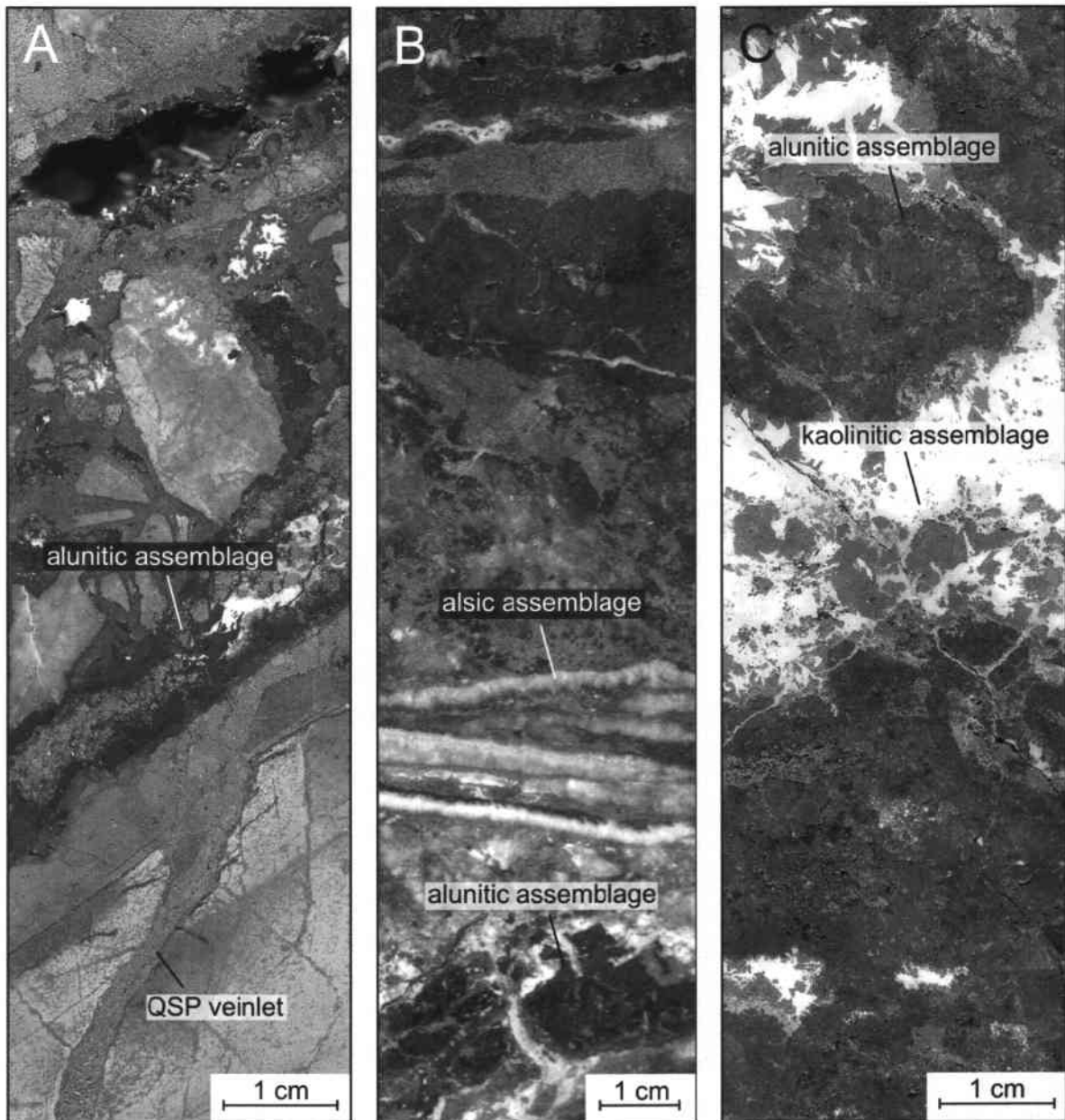
Figure 8.1: Photographs of selected high-sulfidation epithermal veins illustrating the paragenetic sequences based on vein intersections. (A) Small QSP veinlet grading upwards into a high-sulfidation alunitic assemblage consisting of quartz, alunite, pyrite, and enargite (sample FM-DH7-116.7). Host rocks are partly brecciated metapelites of the Negro Peinado Formation. (B) Massive high-sulfidation epithermal vein exhibiting alunitic assemblages, which are cut by an alunite-rich alsic assemblage (sample FM-SP-24). (C) Massive granular intergrowth of enargite and famatinite illustrating the alunitic assemblage, locally replaced by kaolinitic assemblages of kaolinite, dickite, pyrite, and marcasite (sample FM-DH7-116.4).

8.3　Fluid inclusion study

8.3.1　Types of fluid inclusions

Fluid inclusions in minerals from the high-sulfidation epithermal veins are extremely sparse due to the poor preservation in alunite and the rare occurrence of crystalline quartz in this mineralization stage. However, according to phase relations at room temperature, two types of fluid inclusions can be recognized (Figure 8.2).

Over 80% of the fluid inclusions are *vapor-rich* inclusions with no recognizable liquid (Figure 8.2 A). They are generally abundant in barite and alunite and less frequent in quartz. Vapor-rich inclusions commonly range between 5 and 20 μm in size and have mostly smooth equant shapes.

Less than 20% of the fluid inclusions are *aqueous* inclusions and contain a liquid phase and a small vapor bubble (10-20 Vol%, Figure 8.2 B). Locally, they occur together with vapor-rich inclusions but never in clear boiling assemblages. Aqueous inclusions are irregularly shaped and usually very small (<5 μm). They look similar to $L2_H$ inclusions described in the transitional QSP stage and are generally abundant in quartz. Here, they may reach sizes of up to 10 μm in diameter, which were suitable for microthermometric measurements.
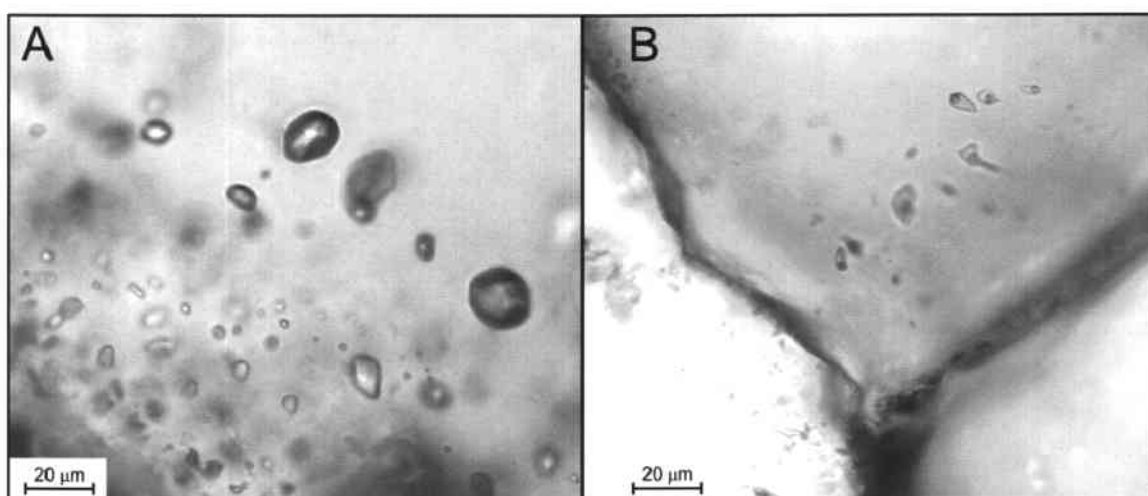
Figure 8.2: Photomicrographs of typical but rarely measurable inclusion types observed in epithermal minerals at La Mejicana. (A) Sample FM-CP05-47: Low-density vapor inclusions with no recognizable liquid hosted in barite. Note the co-existence of aqueous inclusions indicating phase separation (i.e. boiling). (B) Sample FM-CP05-28: Irregular aqueous inclusions in crystalline quartz look similar to $L2_H$ fluids described in the transitional QSP veins. The liquid occupies more than 80 Vol% of the inclusion.

8.3.2 Fluid inclusion petrography and microthermometry

One quartz-rich sample (FM-CP05-28) of the alunitic mineral assemblage contained aqueous fluid inclusions sufficiently large to allow microthermometric investigations (Appendix figure 4 A). Fluid inclusion data reported below are presented as average values with 1 standard deviation uncertainty. Individual fluid inclusion data are listed in the Appendix table 4.

Aqueous fluid inclusions of type $L2_J$ occur on late growth zones in euhedral quartz crystals indicating primary origin. In general, these inclusions are rare and only a few were suitable for heating and freezing experiments. Salinities were determined by final melting of ice at -1.5±0.2°C, yielding values of 2.6±0.3 wt% $NaCl_{equiv}$. Total homogenization occurred by vapor bubble disappearance into the liquid phase at 175±13°C. Minimum pressures calculated for this inclusion assemblage yield values of 9 bars using the method described in Driesner and Heinrich (in press). These data are in good agreement with the microthermometric properties of petrographically similar $L2_H$ inclusions trapped in QSP veins, indicating that these fluids record the transition to the main high-sulfidation epithermal stage.

Consistently, Losada-Calderón (1992) described primary aqueous inclusions in epithermal quartz of the intermediate assemblage, which corresponds to the alunitic mineral paragenesis. His heating and freezing experiments yielded rather consistent salinities of 2 to 4 wt% $NaCl_{equiv}$ and temperatures of homogenization that range between 200 and 290°C. In addition, he observed low-salinity (1-2.5 wt% $NaCl_{equiv}$) vapor inclusions coexisting with hypersaline brines (31-36 wt% $NaCl_{equiv}$) exhibiting temperatures of homogenization that range between 250 and 370°C. However, these data correspond to the sericitic assemblage and are consistent with fluid inclusion results obtained from quartz stage F in the transitional QSP veins, which underlie and slightly predate the high-sulfidation epithermal veins at La Mejicana.

8.4   Interpretation and discussion

Fluid inclusions in the epithermal system at La Mejicana are so sparse and small that the few data provided by microthermometry may not be representative. However, studies of active geothermal systems indicate that crystalline quartz will form as a direct precipitate at temperatures above 220°C (Fournier and Potter, 1982). At lower

temperatures, the precipitate may form an amorphous gel and few, if any, primary inclusions will be trapped. This hypothesis is consistent with the abundance of microcrystalline quartz present in the epithermal system at La Mejicana and agrees well with the fluid inclusion data obtained from this study and from previous work by Losada-Calderón (1992). Thus, the temperature of 220°C is set as an approximate base for homogenization temperatures of primary fluid inclusions in high-sulfidation epithermal quartz.

In conclusion, fluid inclusions were identified and classified mainly according to their petrographic characteristics. These observations reveal that two different fluid types, a vapor and an aqueous liquid, were involved in the formation of the high-sulfidation epithermal Cu-Au veins at La Mejicana. These fluids look similar to $L2_H$ and V_H inclusions trapped in transitional QSP veins, which underlie and slightly predate the epithermal veins. The apparent coexistence of vapor-rich and aqueous inclusions may be the result of phase separation under hydrostatic/vaporstatic pressure. This is consistent with the shallow depths at which deposition of the epithermal ore metals occurs. However, no clear boiling assemblages have been observed. Epithermal ore deposition is therefore more likely to be the result of cooling and dilution of the ore-bearing fluids due to mixing with meteoric water. This hypothesis is supported by stable isotope data indicating contribution of meteoric water in both, the transitional QSP stage and the epithermal veins (Losada-Calderón, 1992; Appendix table 7).

9   FLUID EVOLUTION FROM THE PORPHYRY TO THE EPITHERMAL ENVIRONMENT

9.1   Introduction

Linking the trapping chronology of specific fluid inclusion types to the established paragenetic sequence of vein formation, it is possible to constrain a generalized model of the fluid evolution at Famatina. The observed succession of quartz and sulfide precipitation can be explained, as a first approximation, by one common source fluid, which exsolved from a hydrous magma reservoir at greater depth. This hypothesis is supported by stable isotope data indicating involvement of magmatic fluids for all mineralization stages, with increasing contribution of meteoric water towards the paleosurface (Losada-Calderón, 1992; Appendix table 7). During ascent through the crust, individual batches of this magmatic-hydrothermal fluid experienced different P-T-X paths due to local differences in rock permeability. The genetic model presented below will define possible fluid evolution paths from the deep magmatic setting through the porphyry to the shallow epithermal environment based on textural and petrographic observations in combination with fluid inclusion data.

However, the present level of erosion prevents sampling of the deeper parts of the porphyry system. Therefore, the approach of the present study is to draw conclusions from fluid inclusions trapped within a vertical exposure of roughly 500 m and to discuss the likelihood of a genetic link between the porphyry Cu-Mo-Au system and the adjacent high-sulfidation epithermal Cu-Au deposit (see Figure 4.5). Figure 9.1 summarizes the observed paragenetic sequence of the magmatic-hydrothermal system at Famatina, based on the assumption that the initial composition of the porphyry-derived fluids exposed at the present-day surface is essentially similar to later intrusions emplaced at greater depth.

In the following sections, fluid inclusion data will be summarized and discussed in the light of their respective time relations, based on their bulk fluid composition derived from microthermometry and LA-ICP-MS analysis. Figure 9.2 schematically illustrates these time relations along a vertical fluid path, based on textural and petrographic characteristics observed in the field and in hand specimens. The figure also shows a summary of best-estimate inclusion characteristics of each quartz formation stage,

which form the basis for interpreting the overall magmatic to hydrothermal evolution in the present chapter.

9.2 Magma emplacement and porphyry mineralization

The Nevados de Famatina porphyry Cu-Mo-Au system is hosted by dacitic stocks and dikes of the Mogote Formation, which were emplaced during the Early Pliocene (Losada-Calderón et al., 1994). Magma emplacement and subsequent hydrothermal activity caused intense fracturing and a superimposed network of various vein types in the porphyries and the adjacent sedimentary wall rocks. Radiometric age dating by Losada-Calderón et al. (1994) indicates that the magmatic activity in this area may have prevailed for around 2 My. This time interval is interpreted to reflect multiple pulses of intrusion, each associated with hydrothermal circulation, that are related to one magma chamber at greater depth. This hypothesis is consistent with textural and mineralogical similarities between three spatially separated centers of porphyry-style mineralization (i.e., LMD, LEP, PGP). However, the available Ar-Ar data are not sufficiently systematic to allow a detailed temporal resolution (see Table 4.2).

Petrographic observations and fluid inclusion data indicate that a single-phase fluid of intermediate density directly exsolved from a crystallizing magma at pressures and temperatures well above 800 bars and 600°C, respectively (Figure 9.3). This early high-temperature fluid is recorded in quartz phenocrysts (ID_P) and A-veinlets (ID_A), which formed within the consolidating portions of the porphyries under lithostatic conditions, at depths greater than 1.7 km. However, intermediate-density inclusions of both types show a large variation in salinity and element concentrations within petrographically assigned inclusion assemblages, possibly indicating initiation of phase separation.

Cooling and decompression of this input fluid is recorded in the subsequent stages of stockwork mineralization and led to phase separation by condensation of a small fraction of hypersaline brine (B_A) from large volumes of low-salinity vapor (V_A). Calculations based on microthermometric measurements yield a vapor:brine mass ratio of 9:1, as detailed in Chapter 6.6.1 (see also Table 6.4). The dominant and buoyant low-density vapor phase will contain most of the volatile components of its parental fluid (ID_A), particularly CO_2, SO_2, and H_2S (White and Hedenquist, 1995).
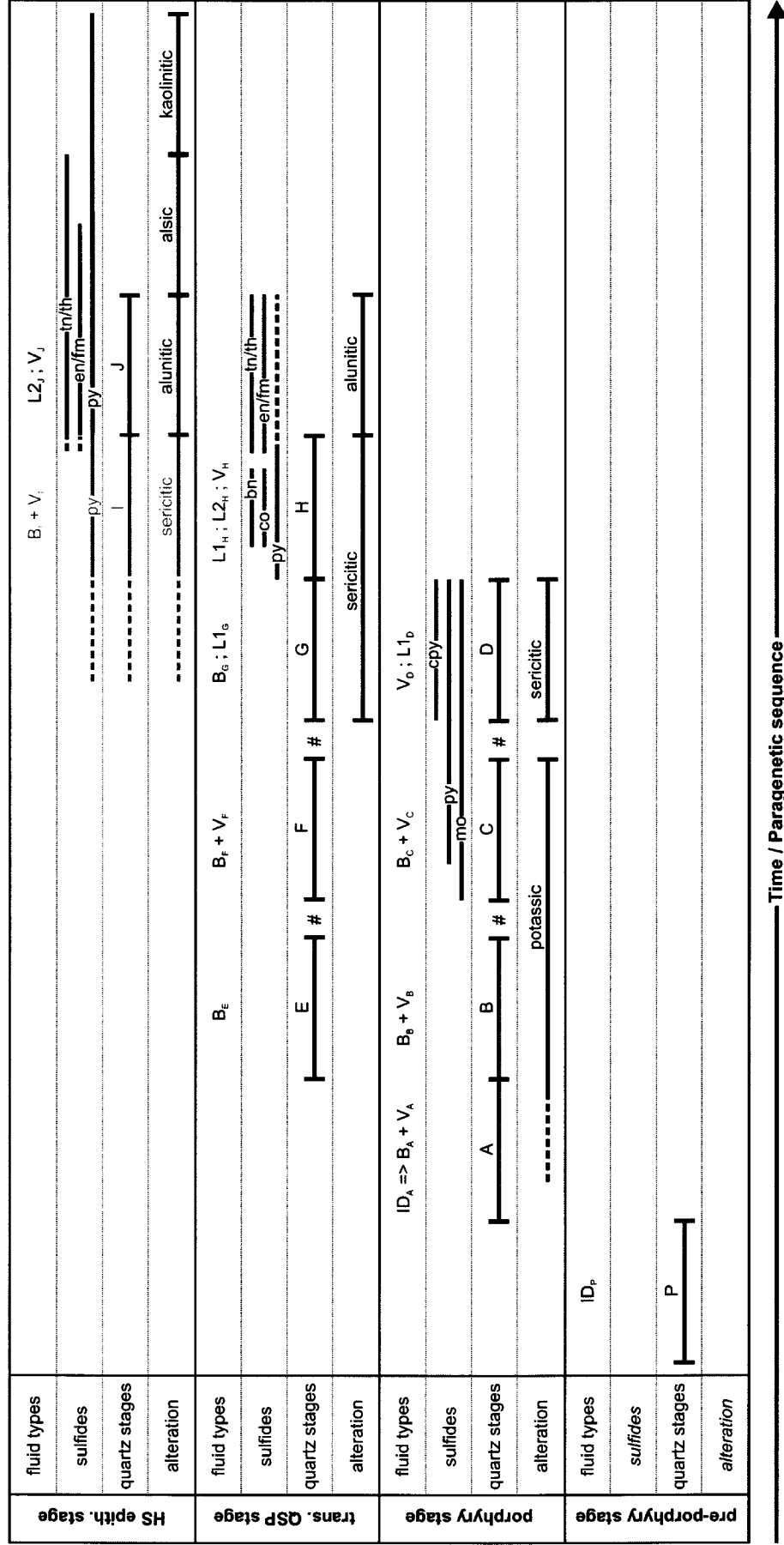
Figure 9.1: Schematic summary of the paragenetic sequence of the telescoped magmatic-hydrothermal system based on petrographic observations in combination with fluid inclusion studies. Gray letters correspond to observations by Losada-Calderón (1992) that could not be confirmed in the present study. The high-sulfidation epithermal record is limited to its early stages in terms of fluid inclusions due to the lack of measurable inclusions in the late stages. Abbreviations: mo, molybdenite; cpy, chalcopyrite; py, pyrite; co, covellite; bn, bornite; en/fm, enargite/famatinite; tn/th, tennantite/tetrahedrite. # denotes dissolution of quartz discovered by SEM-CL.
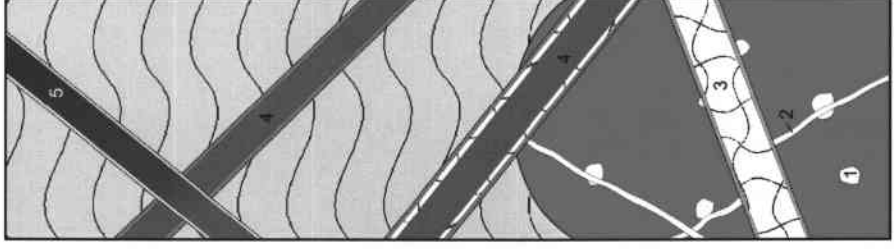
Cartoon	Veins	Alteration	Quartz	FI	Salinity	Th [°C]	Na [wt%]	K [wt%]	Fe [wt%]	Cu [wt%]	Ag [ppm]	Cs [ppm]	Au [ppm]	Pb [ppm]
5 Epithermal	alunitic		J	L2$_J$	2.6±0.3	175±13	n.d.	n.d.	n.d.	n.d.	n.d.	n.d.	n.d.	n.d.
4 QSP vein	sericitic		H	V$_H$	n.d.	n.d.	n.d.	n.d.	n.d.	n.d.	n.d.	n.d.	n.d.	n.d.
				◇ L2$_H$	1.5±0.5	229±28	0.5±0.1	0.3±0.2	0.05±0.02	0.10±0.13	20.3±7.8	6.7±9.6	4.2	45±35
				◆ L1$_H$	5.7±1.8	326±53	1.6±0.7	1.1±0.7	0.68±0.46	0.04±0.05	9.7±7.1	9.7±14.3	1.6±0.7	173±271
			G	◆ L1$_G$	5.0±2.1	362±10	1.8±0.5	0.7±0.2	0.68±0.20	0.25±0.29	11.9±5.6	8.7±2.5	15±6	105±79
				■ B$_G$	40.2±0.9	350±9	10.8±0.1	6.1±1.3	5.19±1.39	0.35±0.21	9.8±3.2	n.d.	0.9	540±85
			F	▲ V$_F$	2.3±0.6	n.d.	1.0±0.1	1.1±0.1	0.75±0.18	0.38±0.21	2.4±1.9	n.d.	<1	128±41
				■ B$_F$	38.9±1.6	349±12	9.6±0.9	7.1±1.4	5.17±1.82	0.45±0.16	32.1±30.7	n.d.	8.1±7.9	605±207
			E	■ B$_E$	n.d.	n.d.	n.d.	n.d.	n.d.	n.d.	n.d.	n.d.	n.d.	n.d.
3 B-vein	sericitic		D	◇ L$_D$	6.6±5.1	250±44	1.7±0.8	1.3±0.7	1.27±1.53	0.04±0.01	<11	13.8±15.5	3.2	244±203
				▲ V$_D$	3.1±0.5	349±15	0.7±0.1	0.5±0.1	0.58±0.20	0.15±0.03	<3	3.3	<1	92±26
	potassic		C	▲ V$_C$	4.0±1.0	n.d.	0.8±0.2	0.6±0.1	0.63±0.25	0.26±0.38	21.7±7.3	2.6±1.2	1.9±1.5	95±32
				■ B$_C$	44.0±5.0	486±51	9.9±1.9	8.6±1.6	7.86±2.03	0.04±0.04	9.4±1.9	28.6±10.9	0.7±0.5	1096±280
			B	▲ V$_B$	12.4±3.3	n.d.	3.4±0.4	1.6±0.3	1.37±0.69	0.33±0.51	<5	8.6±5.9	<1	199±59
				■ B$_B$	56.0±5.0	472±38	13.8±2.9	7.6±2.1	8.42±3.37	0.07±0.10	7.4±1.8	34.0±24.9	<1	1057±311
2 A-veinlet	potassic		A	▲ V$_A$	2.8±1.1	>600	0.6±0.2	0.6±0.3	0.63±0.37	0.06±0.05	12.7	2.9±2.5	2.3±2.0	74±28
				■ B$_A$	64.4±0.7	>600	19.5±2.2	8.0±2.2	5.94±3.28	0.15±0.07	24.8	48.0±17.1	<1	1670±501
				● ID$_A$	10.2±6.0	>600	2.8±1.2	2.5±2.1	2.56±1.96	0.17±0.15	27.9±27.5	6.6±5.0	<1	252±151
1 Phenocryst	none		P	○ ID$_P$	9.0±5.5	>600	3.1±1.7	1.4±0.5	1.28±0.62	0.11±0.16	2.0	8.3±5.0	<1	264±173

Figure 9.2: Schematic vertical section through the Famatina Cu-Mo-Au system illustrating the simplified fluid evolution from the deep magmatic setting through the porphyry to the shallow epithermal environment. Data were derived from microthermometry and LA-ICP-MS analysis and are presented as average values of fluid types, with 1 standard deviation. <VALUE reports the lowest limit of detection using the 3 sigma criterion. Abbreviations: n.d., not determined; FI, fluid inclusion type. Salinity denotes the apparent salinity of the fluid inclusions in wt% NaCl$_{equiv}$.

Successive boiling assemblages (V_A+B_A, V_B+B_B, V_C+B_C) indicate several episodes of phase separation related to local pressure and temperature fluctuations, between 300 and 800 bars and 450 and more than 600°C, respectively. Microanalytical results show that separation of a low-salinity vapor phase from a hypersaline brine leads to significant fractionation of ore metals and the selective enrichment of certain elements. Salt components, such as Na, K, Fe, Cs, Pb, and Mo preferentially partition into the hypersaline brine, whereas Cu, Au, Te, Sb, Ag, and As partition in favor of the vapor, at least in relative terms compared to Na and the other salts (see Figure 6.4 B). Cu concentrations in vapor inclusions vary from 0.5±0.2 wt% to very low concentrations of a few hundred ppm. A similar range has been observed for Cu/Na ratios in the coexisting brine inclusions (see Figure 6.4 G). This large variation probably reflects a combination of brine-vapor fractionation and minor precipitation of Cu-Fe-sulfides from both phases at lower temperatures, because the early fluids of quartz A petrographically predate any Cu-Fe sulfide precipitation (see Figure 6.4 H). Selective fractionation of Cu into the vapor is probably also responsible for elevated Cu concentrations in low-temperature V_D vapor inclusions (0.15±0.03 wt%), which occur in the last generation of porphyry vein quartz and may be synchronous with a transition from potassic to sericitic alteration assemblages. Thus, the voluminous vapor phase is interpreted to be the predominant fluid contributing to porphyry-stage Cu mineralization. Au was difficult to detect due to its very low abundance in all fluid inclusions. The limited data indicate a relative enrichment in vapor inclusions. Here, concentrations range between 0.3 and 3.7 ppm, and correlate with high Cu values (see Table 6.3). By contrast, B_C brines exhibit lower absolute Au concentrations that range between 0.2 and 1.3 ppm (see Appendix table 5).

Variations in the Fe/Na and K/Na ratios are most pronounced in quartz stages A and B and are interpreted to reflect precipitation of magnetite and orthoclase related to early potassic alteration. Differences in Fe also correlate with Cu, probably reflecting deposition of Cu-Fe sulfides during quartz stage C, but are less apparent due to the high Fe concentrations in the parental fluids ID_P and ID_A (see Figure 6.4 I). The scarce data for Mo also exhibit a large range in absolute concentrations and element ratios (see Figure 6.4 E). Exceptionally high Mo concentrations have been detected in B_C brine inclusions and are interpreted to reflect redissolution of Mo from previously deposited sulfide ore in quartz stage B. This hypothesis is consistent with petrographic observations indicating early precipitation of molybdenite, followed by

remobilization and re-deposition. However, ore grades in the porphyry intrusions are currently subeconomic, probably due to incomplete focusing of the ore-forming fluids through three (or more) spatially separated exit points.

The late hydrothermal stage of the porphyry system is characterized by low-salinity V_D vapors and relatively rare but important liquid-like inclusions (L_D) of low salinity, trapped at around 250°C. Such aqueous liquids were previously interpreted to be meteoric in origin, with small contributions of magmatic brine (e.g., Hedenquist et al., 1994a). However, our data demonstrate very high concentrations of Cu, Te, and Au in these Fe-poor fluids, which is not consistent with dilution of any of the brines analyzed at Famatina. Instead, we propose that the L_D inclusions represent a magmatic vapor that contracted to an aqueous liquid at greater depth. Chemical analyses indicate that this parental vapor was compositionally similar to vapor-rich inclusions of type V_A (see Figure 6.4 K).
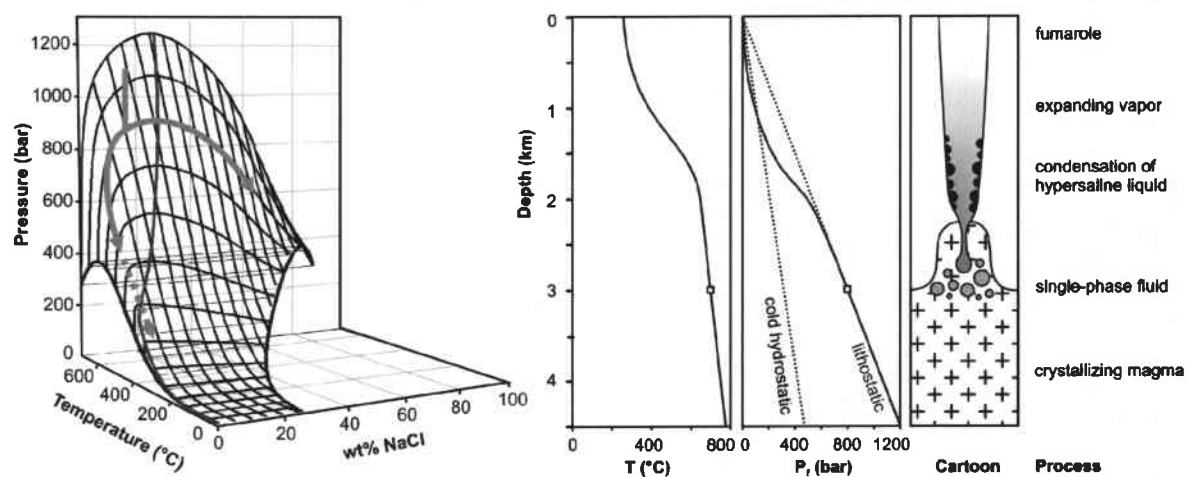
Figure 9.3: Semiquantitative interpretation of the fluid evolution of the Nevados de Famatina porphyry Cu-Mo-Au system illustrated by the grey arrows, modified from Heinrich (2007) and adapted to the specific conditions estimated from fluid inclusion data presented in this study. The P-T-X diagram (left) of the H_2O-NaCl system from Driesner and Heinrich (in press) schematically illustrates the fluid evolution paths occurring above a single intrusion, as indicated by the cartoon (right). Gray-scale shading qualitatively indicates fluid density from black (= liquid-like, ~1 g cm^{-1}) to white (= vapor at ~1 bar). The physical fluid properties are demonstrated by the temperature- and pressure-depth diagrams (center). The square indicates the approximate P-T conditions at which the source fluid exsolved from the crystallizing magma chamber at greater depth.

9.3 Transitional quartz-sericite-pyrite mineralization

The transitional QSP stage is characterized by the formation of euhedral quartz-sericite-pyrite veins, which are associated with the dacitic porphyries of the igneous Mogote Formation. Bleached halos of sericitic alteration accompany these euhedral quartz veins, which crosscut or reopen earlier veins of the porphyry stockwork and postdate potassic alteration. The close association of the QSP stage with sericitic alteration implies that the respective magmatic-hydrothermal fluids are weakly acid, with a pH consistent with the muscovite stability field. QSP veins appear to be most abundant in the vicinity of the epithermal vein system at La Mejicana. According to field observations by Losada-Calderón (1992) and limited own investigations in the historic galleries at La Mejicana, some large QSP veins continually grade upwards into alunitic assemblages of the epithermal mineralization stage. These textural and mineralogical characteristics indicate that the QSP veins probably represent linking channelways for the metal-bearing fluids generating the high-sulfidation epithermal Cu-Au-(As-Sb-Te) deposit.

Based on petrographic and microthermometric investigations, two types of aqueous liquid inclusions can be distinguished in the transitional QSP veins, described as L1 (5±2 wt% $NaCl_{equiv}$) and L2 (2±1 wt% $NaCl_{equiv}$). The slightly more saline L1 liquids predominate and occur at temperatures between 360 and 325°C (see Figure 7.8). These liquids are extraordinary rich in Cu, As, Sb, Te, and Au, far higher than ever reported for low-salinity fluids in other high-sulfidation epithermal ore deposits or active geothermal systems, such as Ladolam (Simmons and Brown, 2006), White Island (Hedenquist et al., 1993), or Broadlands (Simmons and Browne, 2000). This element suite corresponds closely to that of the subsequently deposited high-sulfidation epithermal veins at La Mejicana, which overlie and slightly postdate the transitional QSP veins. Moreover, the relative proportions of these elements are of comparable magnitude as the respective ore grades. Importantly, these aqueous L1 liquids are far too Cu-Sb-As-Ag-Te-Au rich to be generated by simple meteoric dilution of porphyry-derived brines, as has been suggested for similar systems, such as Lepanto-Far Southeast (Hedenquist et al., 1994b). Therefore, L1 liquids are interpreted to originate from greater depth and record the initial composition of a magmatic fluid prior to ore-mineral saturation. The fluid evolution and precious metal

transport from the deep magmatic setting through the porphyry to the shallow epithermal environment can be explained by two alternative processes.

One possibility is that L1 inclusions were formed by contraction of a vapor phase that condensed out some brine and then cooled at elevated pressure (Heinrich et al., 2004; Heinrich, 2005). As an alternative explanation it can be considered that sericitic alteration and porphyry Cu-Au mineralization are related to a common single-phase fluid of intermediate density (Hedenquist et al., 1998; Muntean and Einaudi, 2001). Such a fluid similar to the intermediate-density inclusions ($ID_{P/A}$) could have exsolved directly from the magmatic source at greater depth and was then transferred to the epithermal environment by a similar process of vapor contraction, but without an intermediate stage of brine separation.

The compositional similarity between the ID's and the high-temperature vapor inclusions implies that both are good candidates to be equivalent to precursor fluids for the $L1_G$ inlusions, assuming that only a small fraction of brine was separated. The two alternative mechanisms thus will not lead to major differences in the derived aqueous liquid, with the possible exception of undetected, highly volatile gas species. A comparison of the bulk composition of intermediate-density fluids and early vapor inclusions with the $L1_G$ liquids demonstrate a close correspondence in all analyzed elements in either case, and no clearly diagnostic difference in favor of one or the other hypothesis, neither in terms of element ratios (Figure 9. 4) nor in absolute element concentrations (Figure 9.5). Compared with the V_A vapors, the $L1_G$ liquids show almost perfect overlap, except for As and Sb, which are known to fractionate to the vapor relative to brine, but are even higher in $L1_G$ than expected (Figure 9.4 A). The ID_P inclusions also overlap with $L1_G$ within their rather limited and poor analytical data (Figure 9.4 B), but tend to be deficient in those elements known to prefer the vapor relative to coexisting brine (see Figure 6.4 B). Notably Au, Ag, Sb, and As, and to a lesser degree also Te and Cu, are elevated in $L1_G$ liquids compared with ID_P fluids. By contrast, Fe is lower in the $L1_G$ inclusions than in the V_A and ID_P fluids, which is again consistent with some brine substraction at greater depth.

The origin of these Cu-Au-Ag-As-Sb-Te-rich low-salinity fluids remains speculative at this stage, because hydrothermal transport of Au and other species at the relevant conditions has not been fully explored by experimental studies. The variably high but unquestionably significant Au concentrations in aqueous liquid inclusions may reflect the presence of colloidal Au particles, which can exist at temperatures as high as

350°C in silica-bearing solutions (Frondel, 1938). These fluids are trapped in well-crystallized quartz, and clearly transported Au through the QSP veins without significant precipitation. By contrast, the subsequent stage of high-grade epithermal Au-sulfide-telluride deposition is characterised by only minor quartz, which is mostly present as microcrystalline material that may well have been originally precipitated as amorphous silica. This possibility matches similar interpretations for other high-grade epithermal Au deposits, such as Sleeper, Nevada (Saunders, 1994). Alternatively, limited experimental thermodynamic data indicate that Cu and Au can be transported as stable sulfur complexes in dense vapor-like and low-salinity aqueous fluids (Gammons and Williams-Jones, 1997; Stefánsson and Seward, 2004; Nagaseki and Hayashi, 2006; Pokrovski et al., 2006). To maintain Au concentrations in relatively low-temperature aqueous liquids at comparable levels to those detected in L-type inclusions at Famatina, the fluids require an initial excess of dissolved sulfide over Fe (Heinrich, 2005). This can be achieved by condensing out some Fe-rich brine from a low-salinity vapor enriched in volatile sulfur, prior to contraction of this vapor to aqueous liquid (Heinrich et al., 2004). Although we cannot analyze the sulfur content of the L1 liquids, the relatively low Fe concentrations of the Famatina fluids match the thermodynamic model predictions for optimal Au transport. Hence, the ore-bearing aqueous L1 liquids are interpreted to reflect a contracted, probably S-rich vapor that formed at deeper levels, in response to the retracting crystallization front of the fluid-exsolving magma.
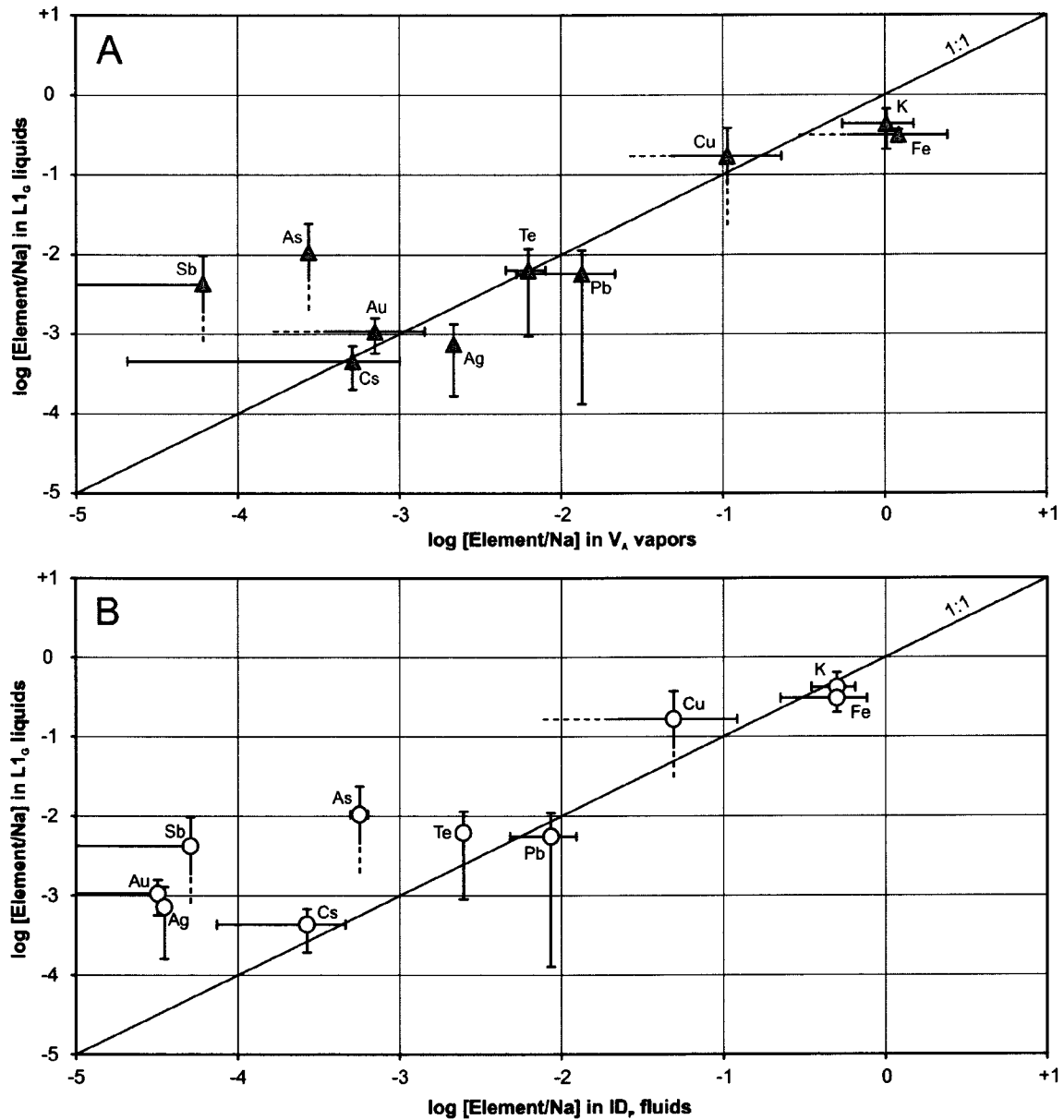
Figure 9.4: Mean element ratio plots illustrating LA-ICP-MS data of the different fluid generations outlined in the text. The solid lines indicate limits of detection for Sb and Au. (A) Element ratios in fluid inclusions of type V_A and $L1_G$ demonstrate the striking compositional similarities between these fluids. Note that Fe/Na ratios in the V_A vapors are biased due to the fact that absolute Fe concentrations in individual inclusions were frequently below the limit of detection. (B) Element ratios in ID_P inclusions record the initial fluid composition prior to phase separation and correlate with $L1_G$ liquids, except for minor deviations in elements, which commonly partition into the vapor phase and correspond closely to the element suite of the high-sulfidation epithermal ore veins.
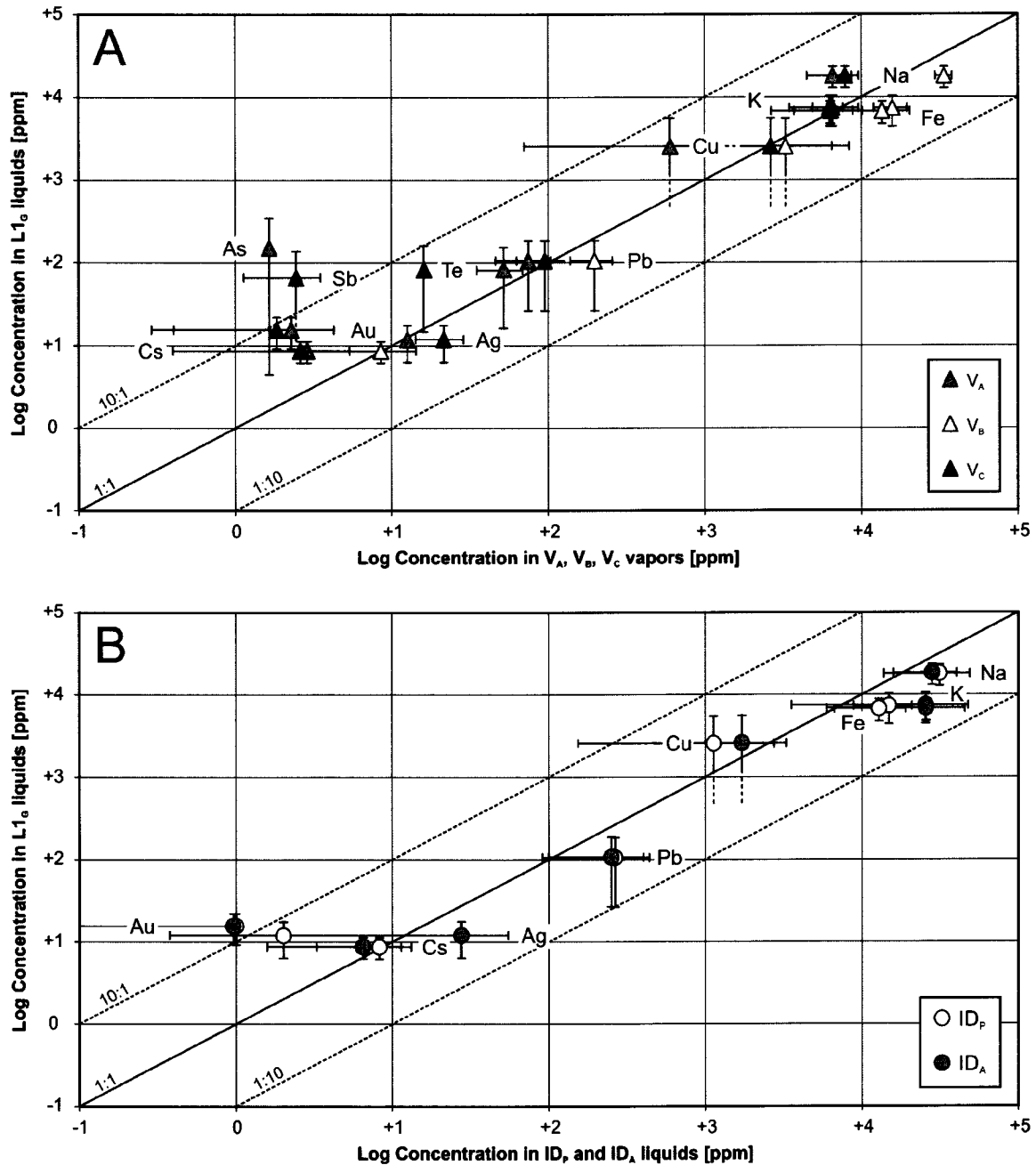
Figure 9.5: Selected element plots illustrating the bulk composition of the different fluid types outlined in the text. Data were derived from LA-ICP-MS analysis and are presented as average values of fluid types with 1 standard deviation, as shown in Figure 9.2. The solid lines indicate limits of detection for Au using the 3 sigma criterion. (A) Element concentrations in vapor-rich and aqueous inclusions demonstrate the compositional similarities between the vapor phase of the porphyry system and the ore-bearing liquids of the QSP stage. (B) Single-phase fluids of intermediate density record the initial composition of the ore-bearing fluids prior to phase separation. These precursor fluids are also very similar to L1G liquids, but have inadequately low Au and relatively higher Fe. The very high Au concentrations in the L1G liquids may be due to an overestimation of the short transient signal.

9.4 High-sulfidation epithermal mineralization

High-sulfidation epithermal mineralization at La Mejicana occurs between 4335 and 4750 m elevation, about 500 m above the currently exposed porphyry system. This final stage of mineralization is associated with E-W trending faults and fractures, which formed as stress relief zones after the main tectonic event. Sericitic alteration and related quartz-sericite-pyrite (QSP) veins appear to represent the roots of the main Cu-Au mineralization in the epithermal deposit, which has a lower limit near the top of porphyry Cu-Mo-Au ore. Fluid inclusions trapped in these transitional QSP veins confirm this hypothesis.

However, the actual stratigraphic difference between the porphyry system and the shallow epithermal veins contradicts depth estimates derived from fluid inclusions of the early porphyry vein stages. Moreover, stratigraphic evidence indicates that a sedimentary cover of 800 m has been eroded prior to high-sulfidation epithermal ore formation, and was accumulated as piedmont deposits of the Pleistocene Cueva de Peréz Formation (Losada-Calderón, 1992). This observation implies that Pleistocene glaciation caused major changes in the geomorphologic environment and had a direct effect on the superficial hydrodynamic regime, perhaps actively promoting high-sulfidation epithermal ore deposition (Bissig et al., 2002). Therefore, any effort to link the physico-chemical processes between the two structurally superimposed deposit types must consider porphyry-derived fluids from greater depth (Figure 9.6). This fact has implications on the fluid evolution model presented above. If the ore-bearing aqueous liquids are related to a later pulse of intrusive activity, then the source fluid may correspond to Au-rich and Fe-poor intermediate-density fluid inclusions trapped at greater depth, which do not occur at the present level of exposure.

Attempts to characterize the fluids directly forming the high-sulfidation epithermal stage of mineralization have not been fully successful due to the scarcity and small size of the fluid inclusions. However, limited microthermometric data suggest that late aqueous liquids of low temperature trapped at the end of QSP quartz formation (L2$_H$) reflect the transition to the main high-sulfidation epithermal stage. Compositional differences observed between these L2$_H$ fluids and earlier aqueous inclusions are consistent with a 4-fold dilution of L1$_G$ liquids with pure water (see Figure 7.7 H). This

hypothesis is supported by pressure estimates of 9 to 20 bars, indicating formation under hydrostatic conditions, which permitted incursion of ambient meteoric water. Some L2$_H$ liquid inclusions still exhibit very high Cu concentrations (0.3±0.1 wt%), possibly indicating local re-dissolution of previously deposited sulfide ore. Here, fluids probably became increasingly acid due to physical separation from acid-consuming wall-rock minerals. Another possible explanation is that these inclusions represent a new and probably more acid fluid pulse of lower temperature (230°C), introducing the main stage of high-sulfidation epithermal ore deposition at La Mejicana.

The apparent coexistence of vapor-rich and aqueous fluid inclusions observed in the high-sulfidation epithermal veins may be the result of phase separation even at this low-temperature stage (175°C). If this is the case, it implies a very low fluid pressure and epithermal ore deposition close to the present erosion level. This would also aid the incursion of and mixing with surface-derived water, which is consistent with published stable isotope data indicating a contribution of meteoric water in the transitional QSP stage as well as the epithermal veins (Losada-Calderón, 1992; see Appendix table 7).
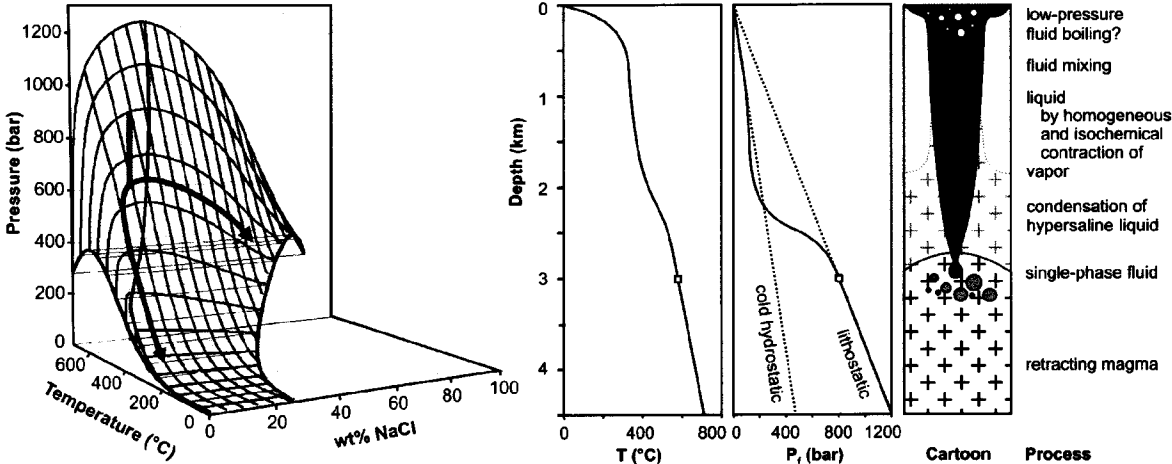
Figure 9.6: Fluid evolution of the high-sulfidation epithermal system modified from Heinrich (2007) and adapted to the specific fluid inclusion characteristics. The P-T-X diagram (left) of the H$_2$O-NaCl system from Driesner and Heinrich (in press) illustrates the fluid paths occurring above a single intrusion, as indicated by the cartoon (right). Gray-scale shading qualitatively indicates the fluid density from black (= liquid-like, ~1 g cm^{-1}) to white (= vapor at ~1 bar). The physical fluid properties are demonstrated by the temperature- and pressure-depth diagrams (center). The squares show the P-T conditions at which the source fluid exsolved from the crystallizing magma chamber at greater depth.

9.5 Summary

Geologic, petrographic, and fluid-chemical evidence indicates an intimate genetic link between subeconomic porphyry Cu-Mo-Au mineralization, transitional QSP veins, and high-grade epithermal Cu-Au-Ag-As-Sb-Te veins in the Famatina district. The magmatic-hydrothermal evolution was controlled by intrusion of small hypabyssal bodies of dacitic porphyry, probably apophyses of a single magma body at depth, followed by concurrent hydrothermal activity and successive erosion (Figure 9.7). As a result, fluid processes that occurred at progressively greater paleodepth as the magmatic system cooled are approximated by the fluid inclusion record in successive vein stages. Therefore, higher-temperature inclusions in earlier veins cannot directly represent the precursor fluid to a lower-temperature inclusion assemblage trapped at a later stage. Despite the restrictions given by limited vertical exposure and preservation, we observed a striking compositional similarity between vapor inclusions trapped in the porphyry stockwork and aqueous liquids trapped in barren QSP veins immediately predating and underlying the epithermal ore veins. These liquids have an exceptionally high Cu, As, Sb and Te content and partly very high Au concentrations (irregular possibly due to incipient oversaturation as colloidal particles), and the element concentrations in the transitional fluids approximately match the ore-metal budget of the high-grade epithermal ore veins.

All observations are consistent with a process in which magmatic fluid exsolves as a single-phase fluid from a cooling subjacent pluton. As a result of partial pressure release resulting from hydraulic fracturing recorded by the stockwork veins, the parental fluid separates a small amount of hypersaline brine by high-temperature condensation. The remaining vapor ascends and cools at sufficiently high pressure within the single-phase fluid stability field, allowing it to contract to an aqueous liquid. This is recorded by inclusions in the QSP veins, which are superimposed on the stockwork veinlets due to concurrent erosion of the uplifting mountain range. Continued erosion and decompression then draws similar metal-rich, low-salinity magmatic liquids from greater depth to the site of ore formation. Close to the present-day surface, this essentially magmatic and low-salinity aqueous liquid starts to boil and mix with surface-derived groundwater, thereby depositing high-grade epithermal ore metals.

Some key questions remain open in this story, but they can in principle be tested. The physical process implies a single evolving source of hydrous magma, generating magmatic-hydrothermal fluid while cooling and being uplifted at the same time. This scenario should be tested by more rigorous geochronology, because the published Ar-Ar data are inconclusive for the earliest and latest stages of mineralization. The chemical interpretation depends on very high sulfur concentrations in the vapor-derived fluids to maintain the unprecedented high Au concentration in relatively cool, low-salinity fluids under equilibrium conditions, but there is currrently no analytical technique of adequate sensitivity for quantitative sulfur analysis in these typically rather small inclusions. The possibility of colloidal transport, in an Au-oversaturated epithermal liquid derived from a Au-rich magmatic vapor, remains an alternative in light of the highly variable concentrations in individual inclusions.
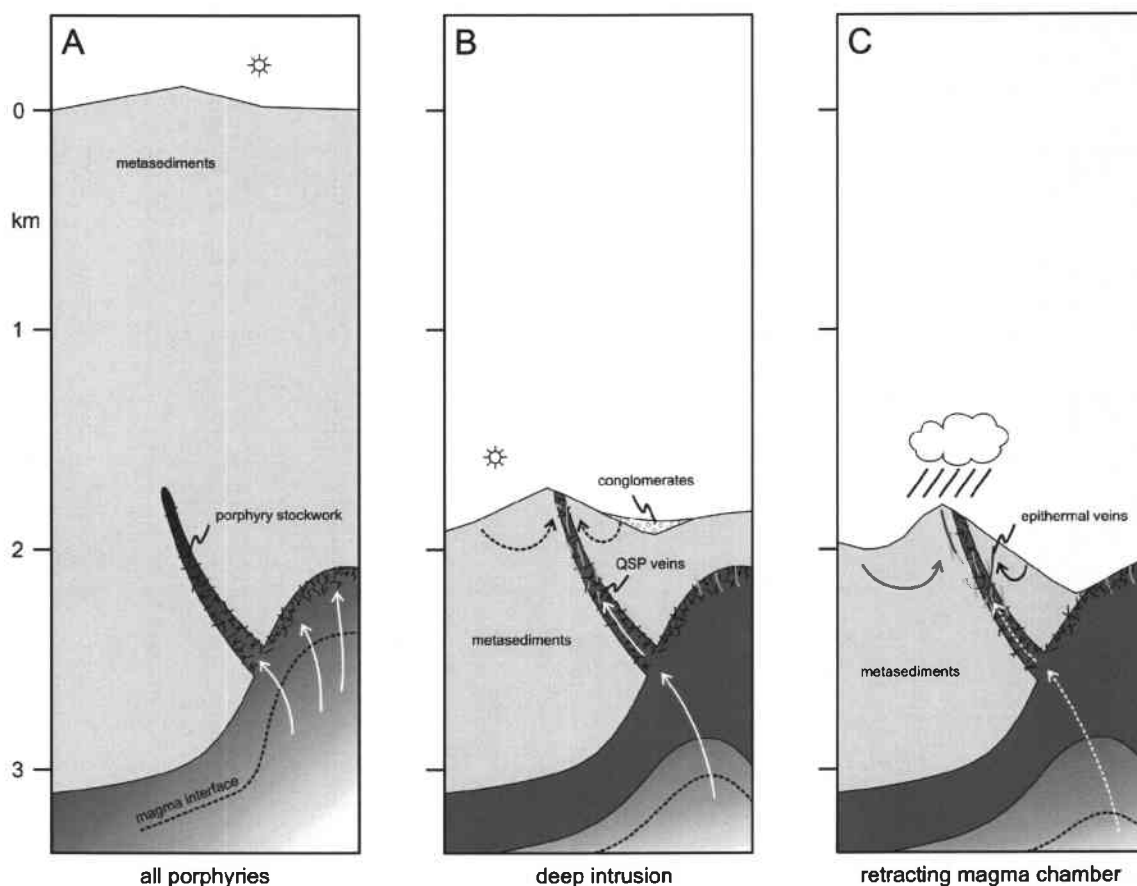
Figure 9.7: Schematic cross sections through the Famatina system illustrating the simplified fluid evolution paths from the deep porphyry setting (A) through the QSP stage (B) to the shallow high-sulfidation epithermal environment (C). The white arrows indicate the source fluid that exsolved from a crystallizing magma at depth. The black arrows highlight the progressive input of meteoric water.

10   GENERAL CONCLUSIONS AND OUTLOOK

Fluid inclusion studies from the Nevados de Famatina porphyry Cu-Mo-Au system and spatially related high-sulfidation epithermal Cu-Au veins at La Mejicana illustrate the role of fluid phase separation in selective metal transport and ore formation. Microanalysis of hypersaline brine coexisting with low-density vapor inclusions show that both fluids carry appreciable metal concentrations, and that some elements, including Cu, As, Sb, Te, and Au, are systematically enriched in the vapor phase. Subsequent cooling of this low-density vapor to an aqueous liquid is interpreted to be essential for effectively transporting Au and other ore-forming metals from the porphyry domain to the epithermal environment (Heinrich et al., 2004). Downward-tapering fracture zones with quartz, sericite, and pyrite (QSP veins) overprinting the potassic alteration of the porphyry system are the linking channelways for ore-bearing, vapor-derived fluids to the epithermal deposit. Epithermal ore deposition occurs upon cooling and mixing with meteoric water near the paleosurface. However, the total endowment of the entire magmatic-hydrothermal system is ultimately limited by the size of the fluid-producing magma chamber and the efficiency of the precipitation mechanism. Therefore, we think that the economic high-sulfidation epithermal deposit at La Mejicana is associated with a subeconomic porphyry system at depth, even though the successive fluid processes are intimately linked.

This thesis demonstrated the importance of a careful and detailed fluid inclusion study for investigating magmatic-hydrothermal ore systems. The significance of the resulting model of fluid evolution paths is essentially dependent on the sample material, which should include the whole system. In the present study, this attempt was not always realizable due to the poor exposure of the deeper parts of the system. Another key aspect was the relative timing of the inclusion assemblages in order to constrain the succession of fluid entrapment. Here, the use of SEM-CL has proven to be an excellent tool to complement the transmitted-light petrography.

Testing the processes discussed in this thesis will require more experimentation to determine the speciation of metals in the vapor phase and their partitioning between liquid and vapor. In particular, the intimate association between Au and Te in the

epithermal ore veins indicates that Au may be transported as telluride complexes in the aqueous solutions. However, little is known about the solubility of these metals in hydrothermal fluids and only well constrained experiments at variable temperatures and pressures will permit definitive conclusions regarding the mechanisms of Au transport. In addition, the discrepancy in the salinity of pure vapor inclusions between measured and theoretical values implies that the physico-chemical properties of the complex natural fluids deviate significantly from the simple binary H_2O-NaCl system. Therefore, future investigations should consider more appropriate fluid systems (e.g., the ternary H_2O-NaCl-KCl phase diagram), which are not available at present. These data will help to understand the dynamic processes of intrusion-related ore formation and to better predict the location and composition of economic ore deposits.

Infrared fluid inclusion microthermometry is another promising tool and has been used in recent years to collect directly data from fluid inclusions trapped in opaque ore minerals, such as enargite and pyrite (e.g., Mancano and Campbell, 1995; Kouzmanov et al., 2002; Kouzmanov et al., 2004). This method has proven essential in deposits with no appropriate visible-light-transparent minerals, and when it is doubted whether fluid inclusions trapped in transparent minerals adequately reflect conditions during ore mineral precipitation. However, current infrared microthermometric studies by Moritz (2006) have revealed that temperatures of phase changes vary with the infrared light source intensity, resulting in an overestimate of fluid salinities and an underestimate of homogenization temperatures. Thus, it is questioned whether the fluid inclusion data reported so far for opaque minerals are truly representative of the fluids involved during ore formation or if they are mainly analytical artifacts. Despite these limitations, infrared microscopy is a powerful technique for revealing growth textures in opaque minerals, and for comparing petrographic characteristics of fluid inclusion populations in coexisting transparent and opaque minerals.

REFERENCES

Acenolaza, F.G., Miller, H., and Toselli, A., 1996, Geologia del sistema de Famatina: München, Institut für Allgemeine und Angewandte Geologie der Ludwig-Maximilians-Universität, 410 p.

Alpers, C.N., and Brimhall, G.H., 1988, Middle Miocene Climatic-Change in the Atacama Desert, Northern Chile - Evidence from Supergene Mineralization at La-Escondida: Geological Society of America Bulletin, v. 100, p. 1640-1656.

Anderko, A., and Pitzer, K.S., 1993, Phase equilibria and volumetric properties of the systems KCl-H2O and NaCl-KCl-H2O above 573 K: Equation of state representation: Geochimica et Cosmochimica Acta, v. 57, p. 4885-4897.

Arribas, A., Hedenquist, J.W., Itaya, T., Okada, T., Concepcion, R.A., and Garcia, J.S., 1995, Contemporaneous formation of adjacent porphyry and epithermal Cu-Au deposits over 300 ka in northern Luzon, Philippines: Geology, v. 23, p. 337-340.

Arribas, A.J., 1995, Characteristics of high-sulfidation epithermal deposits, and their relation to magmatic fluid, in Thompson, J.F.H., ed., Magmas, Fluids, and Ore Deposits, Volume Short Course Series 23, Mineralogical Association of Canada, p. 419-454.

Audétat, A., and Günther, D., 1999, Mobility and H2O loss from fluid inclusions in natural quartz crystals: Contributions to Mineralogy and Petrology, v. 137, p. 1-14.

Audétat, A., Günther, D., and Heinrich, C.A., 1998, Formation of a magmatic-hydrothermal ore deposit: insights with LA-ICP-MS analysis of fluid inclusions: Science, v. 279, p. 2091-2094.

Ballard, J.R., Palin, J.M., Williams, I.S., Campbell, I.H., and Faunes, A., 2001, Two ages of porphyry intrusion resolved for the super-giant Chuquicamata copper deposit of northern Chile by ELA-ICP-MS and SHRIMP: Geology (Boulder), v. 29, p. 383-386.

Barazangi, M., and Isacks, B.L., 1976, Spatial distribution of earthquakes and subduction of the Nazca plate beneath South America: Geology, v. 4, p. 686-692.

Bissig, T., Clark, A.H., Lee, J.K.W., and Hodgson, C.J., 2002, Miocene landscape evolution and geomorphologic controls on epithermal processes in the El Indio-Pascua Au-Ag-Cu belt, Chile and Argentina: Economic Geology and the Bulletin of the Society of Economic Geologists, v. 97, p. 971-996.

Bodnar, R.J., 1993, Revised equation and table for determining the freezing point depression of H2O-Nacl solutions: Geochimica et Cosmochimica Acta, v. 57, p. 683-684.

Bodnar, R.J., Burnham, C.W., and Sterner, S.M., 1985, Synthetic fluid inclusions in natural quartz. III. Determination of phase equilibrium properties in the system H2O-NaCl to 1000[deg]C and 1500 bars: Geochimica et Cosmochimica Acta, v. 49, p. 1861-1873.

Bodnar, R.J., and Vityk, M.O., 1994, Interpretation of microthermometric data for H2O-NaCl fluid inclusions, in De Vivo, B., and Frezzotti, M.L., eds., Fluid Inclusions in Minerals: Methods and Applications, Virginia Tech, Blacksburg, VA, p. 117-130.

Brimhall, G.H., Jr., and Ghiorso, M.S., 1983, Origin and ore-forming consequences of the advanced argillic alteration process in hypogene environments by magmatic gas contamination of meteoric fluids: Economic Geology and the Bulletin of the Society of Economic Geologists, v. 78, p. 73-90.

Burnham, C.W., and Ohmoto, H., 1980, Late-stage processes of felsic magmatism: Mining Geology Special Issue, p. 1-11.

Cahill, T., and Isacks, B.L., 1992, Seismicity and shape of the subducted Nazca Plate: Journal of Geophysical Research-Solid Earth, v. 97, p. 17503-17529.

Camus, F., 1990, The geology of hydrothermal gold deposits in Chile: Journal of Geochemical Exploration, v. 36, p. 197-232.

Candela, P.A., and Holland, H.D., 1984, The partitioning of copper and molybdenum between silicate melts and aqueous fluids: Geochimica et Cosmochimica Acta, v. 48, p. 373-380.

Cathles, L.M., Erendi, A.H.J., and Barrie, T., 1997, How long can a hydrothermal system be sustained by a single intrusive event?: Economic Geology, v. 92, p. 766-771.

Cooke, D.R., Hollings, P., and Walsh, J.L., 2005, Giant porphyry deposits: Characteristics, distribution, and tectonic controls: Economic Geology, v. 100, p. 801-818.

Cooke, D.R., Hollings, P., and Walshe, J.L., 2006, Tectonic triggers for giant porphyry and epithermal deposits of the circum-Pacific region: Geochimica Et Cosmochimica Acta, v. 70, p. A110-A110.

Coughlin, T.J., O'Sullivan, P.B., Kohn, B.P., and Holcombe, R.J., 1998, Apatite fission-track thermochronology of the Sierras Pampeanas, central western Argentina: Implications for the mechanism of plateau uplift in the Andes: Geology, v. 26, p. 999-1002.

CRA-RTZ, 1997, Famatina project, La Rioja province, Argentina: Final report for the period October 1993 to December 1996, Corriente Resources Inc., Rio Tinto Mining and Exploration Ltd., p. 51.

Damman, A.H., Kars, S.M., Touret, J.L.R., Rieffe, E.C., Kramer, J.A.L.M., Vis, R.D., and Pintea, I., 1996, PIXE and SEM analyses of fluid inclusions in quartz crystals from the K-alteration zone of the Rosia Poieni porphyry-Cu deposit, Apuseni Mountains, Rumania: European Journal of Mineralogy, v. 8, p. 1081-1096.

Davidson, J., and Mpodozis, C., 1991, Regional Geologic Setting of Epithermal Gold Deposits, Chile: Economic Geology and the Bulletin of the Society of Economic Geologists, v. 86, p. 1174-1186.

Dávila, F.M., and Astini, R.A., 2003, Early Middle Miocene broken foreland development in the southern Central Andes: evidence for extension prior to regional shortening: Basin Research, v. 15, p. 379-396.

Dávila, F.M., Astini, R.A., Jordan, T.E., and Kay, S.M., 2004, Early Miocene andesite conglomerates in the Sierra de Famatina, broken foreland region of western Argentina, and documentation of magmatic broadening in the south Central Andes: Journal of South American Earth Sciences, v. 17, p. 89-101.

Dávila, F.M., Astini, R.A., and Schmidt, C.J., 2003, Unraveling 470 m.y. of shortening in the Central Andes and documentation of Type 0 superposed folding: Geology, v. 31, p. 275-278.

de Alba, E., 1979, El Sistema de Famatina, in Turner, J.C.M., ed., Segundo Simposio de Geología Regional Argentina, Volume 1: Córdoba, Argentina, Academía Nacional de Ciencias, p. 349-395.

de Brodtkorb, M.K., Schalamuk, I.A., Marcos, O., and Sardi, F., 1996, Mineralizaciones del Sistema de Famatina, in Acenolaza, F.G., Miller, H., and Toselli, A., eds., Geologia del sistema de Famatina, Volume 19: Muenchner Geologische Hefte. Reihe A, Allgemeine Geologie: Munich, Federal Republic of Germany, Institut fuer Allgemeine und Angewandte Geologie der Ludwig-Maximilians-Unviersitaet Muenchen, p. 359-388.

Diamond, L.W., 1992, Stability of CO2 clathrate hydrate + CO2 liquid + CO2 vapour + aqueous KCl-NaCl solutions: Experimental determination and application to salinity estimates of fluid inclusions: Geochimica et Cosmochimica Acta, v. 56, p. 273-280.

Driesner, T., and Heinrich, C.A., in press, The system H2O-NaCl. I. Correlation formulae for phase relations in temperature-pressure-composition space from 0 to 1000°C, 0 to 5000 bar, and 0 to 1 XNaCl: Geochimica et Cosmochimica Acta.

Eastoe, C.J., 1982, Physics and Chemistry of the Hydrothermal System at the Panguna Porphyry Copper-Deposit, Bougainville, Papua New-Guinea: Economic Geology, v. 77, p. 127-153.

Einaudi, M.T., Hedenquist, J.W., and Inan, E.E., 2003, Sulfidation state of fluids in active and extinct hydrothermal systems: transitions from porphyry to epithermal environments, *in* Simmons, S.T., ed., Volcanic, Geothermal and Ore-Forming Fluids. Economic Geology Special Publication, Volume 10, p. 304-321.

Fournier, R.O., 1999, Hydrothermal processes related to movement of fluid from plastic into brittle rock in the magmatic-epithermal environment: Economic Geology and the Bulletin of the Society of Economic Geologists, v. 94, p. 1193-1211.

Fournier, R.O., and Potter, I., Robert W., 1982, An equation correlating the solubility of quartz in water from 25[deg] to 900[deg]C at pressures up to 10,000 bars: Geochimica et Cosmochimica Acta, v. 46, p. 1969-1973.

Frondel, C., 1938, Stability of colloidal gold under hydrothermal conditions: Economic Geology, v. 33, p. 1-20.

Gammons, C.H., and Williams-Jones, A.E., 1997, Chemical mobility of gold in the porphyry-epithermal environment: Economic Geology and the Bulletin of the Society of Economic Geologists, v. 92, p. 45-59.

Geiger, S., Driesner, T., Heinrich, C.A., and Matthai, S.L., 2006, Multiphase thermohaline convection in the earth's crust: II. Benchmarking and application of a finite element - Finite volume solution technique with a NaCl-H2O equation of state: Transport in Porous Media, v. 63, p. 435-461.

Geiger, S., Driesner, T., Heinrich, C.A., and Mattthai, S.K., 2005, Coupled heat and salt transport around cooling magmatic intrusions: Geochimica Et Cosmochimica Acta, v. 69, p. A739-A739.

Giggenbach, W.F., 1992, Seg Distinguished Lecture - Magma Degassing and Mineral Deposition in Hydrothermal Systems Along Convergent Plate Boundaries: Economic Geology and the Bulletin of the Society of Economic Geologists, v. 87, p. 1927-1944.

Giggenbach, W.F., Garcia P, N., Londono C, A., Rodriguez V, L., Rojas G, N., and Calvache V, M.L., 1990, The chemistry of fumarolic vapor and thermal-spring discharges from the Nevado del Ruiz volcanic-magmatic-hydrothermal system, Colombia: Journal of Volcanology and Geothermal Research, v. 42, p. 13-39.

Goldstein, R.H., and Reynolds, T.J., 1994, Systematics of fluid inclusions in diagenetic minerals, Society for Sedimentary Geology, 199 p.

Götze, J., Plötze, M., and Habermann, D., 2001, Origin, spectral characteristics and practical applications of the cathodoluminescence (CL) of quartz - a review: Mineralogy and Petrology, v. 71, p. 225-250.

Günther, D., Audétat, A., Frischknecht, R., and Heinrich, C.A., 1998, Quantitative analysis of major, minor and trace elements in fluid inclusions using laser ablation inductively coupled plasma mass spectrometry: Journal of Analytical Atomic Spectrometry, v. 13, p. 263-270.

Günther, D., Jackson, S.E., and Longerich, H.P., 1999, Laser ablation and arc/spark solid sample introduction into inductively coupled plasma mass spectrometers: Spectrochimica Acta Part B: Atomic Spectroscopy, v. 54, p. 381-409.

Gustafson, L.B., and Hunt, J.P., 1975, Porphyry Copper-Deposit at El-Salvador, Chile: Economic Geology, v. 70, p. 857-912.

Harrington, H.J., 1956, Argentina, *in* Jenks, W.F., ed., Handbook of South American geology. An explanation of the geologic map of South America: Baltimore, MD, Geological Society of America, p. 378.

Harris, A., Allen, C., Bryan, S., Campbell, I., Holcombe, R., and Palin, J., 2004, ELA-ICP-MS U-Pb zircon geochronology of regional volcanism hosting the Bajo de la Alumbrera Cu-Au deposit: Implications for porphyry-related mineralization: Mineralium Deposita, v. 39, p. 46-67.

Harris, A.C., Golding, S.D., and White, N.C., 2005, Bajo de la Alumbrera copper-gold deposit: Stable isotope evidence for a porphyry-related hydrothermal system dominated by magmatic aqueous fluids: Economic Geology, v. 100, p. 863-886.

Heald, P., Foley, N.K., and Hayba, D.O., 1987, Comparative Anatomy of Volcanic-Hosted Epithermal Deposits - Acid-Sulfate and Adularia-Sericite Types: Economic Geology, v. 82, p. 1-26.

Hedenquist, J.W., 1995, The ascent of magmatic fluid: discharge versus mineralization, in Thompson, J.F.H., ed., Magmas, Fluids, and Ore Deposits, Volume Short Course Series 23, Mineralogical Association of Canada, p. 263-289.

Hedenquist, J.W., Aoki, M., and Shinohara, H., 1994a, Flux of volatiles and ore-forming metals from the magmatic-hydrothermal system of Satsuma Iwojima Volcano: Geology, v. 22, p. 585-588.

Hedenquist, J.W., and Arribas, A.J., 1999, Epithermal gold deposits: I. Hydrothermal processes in intrusion-related systems, and II. Characteristics, examples and origin of epithermal gold deposits, in Molnár, F., Lexa, J., and Hedenquist, J.W., eds., Epithermal mineralization of the western Carpathians, Volume Guidebook Series 31, Society of Economic Geologists, p. 13-63.

Hedenquist, J.W., Arribas, A.J., and Reynolds, T.J., 1998, Evolution of an intrusion-centered hydrothermal system: Far Southeast-Lepanto porphyry and epithermal Cu-Au deposits, Philippines: Economic Geology, v. 93, p. 373-404.

Hedenquist, J.W., and Lowenstern, J.B., 1994, The role of magmas in the formation of hydrothermal ore-deposits: Nature, v. 370, p. 519-527.

Hedenquist, J.W., Matsuhisa, Y., Izawa, E., White, N.C., Giggenbach, W.F., and Aoki, M., 1994b, Geology, Geochemistry, and Origin of High Sulfidation Cu-Au Mineralization in the Nansatsu District, Japan: Economic Geology and the Bulletin of the Society of Economic Geologists, v. 89, p. 1-30.

Hedenquist, J.W., and Richards, J.P., 1998, The influence of geochemical techniques on the development of genetic models for porphyry copper deposits, in Richards, J.P., and Larson, P.B., eds., Techniques in Hydrothermal Ore Deposits Geology, Volume 10: Reviews in Economic Geology, p. 235-256.

Hedenquist, J.W., Simmons, S.F., Giggenbach, W.F., and Eldridge, C.S., 1993, White-Island, New-Zealand, volcanic-hydrothermal system represents the geochemical environment of high-sulfidation Cu and Au ore deposition: Geology, v. 21, p. 731-734.

Heinrich, C.A., 2005, The physical and chemical evolution of low-salinity magmatic fluids at the porphyry to epithermal transition: a thermodynamic study: Mineralium Deposita, v. 39, p. 864-889.

Heinrich, C.A., 2007, Fluid-fluid interactions in magmatic-hydrothermal ore formation, in Liebscher, A., and Heinrich, C.A., eds., Fluid-fluid interactions, Volume 65: Reviews in Mineralogy and Geochemistry: Chantilly, Virginia, USA, Mineralogical Society of America, p. 363-387.

Heinrich, C.A., Driesner, T., Stefansson, A., and Seward, T.M., 2004, Magmatic vapor contraction and the transport of gold from the porphyry environment to epithermal ore deposits: Geology, v. 32, p. 761-764.

Heinrich, C.A., Günther, D., Audétat, A., Ulrich, T., and Frischknecht, R., 1999, Metal fractionation between magmatic brine and vapor, determined by microanalysis of fluid inclusions: Geology, v. 27, p. 755-758.

Heinrich, C.A., Pettke, T., Halter, W.E., Aigner-Torres, M., Audetat, A., Gunther, D., Hattendorf, B., Bleiner, D., Guillong, M., and Horn, I., 2003, Quantitative multi-element analysis of minerals, fluid and

melt inclusions by laser-ablation inductively-coupled-plasma mass-spectrometry: Geochimica et Cosmochimica Acta, v. 67, p. 3473-3497.

Heinrich, C.A., Ryan, C.G., Mernagh, T.P., and Eadington, P.J., 1992, Segregation of ore metals between magmatic brine and vapor - a fluid inclusion study using PIXE microanalysis: Economic Geology, v. 87, p. 1566-1583.

Henley, R.W., and McNabb, A., 1978, Magmatic vapor plumes and ground-water interactions in porphyry copper emplacement: Economic Geology, v. 73, p. 1-20.

Hezarkhani, A., Williams-Jones, A.E., and Gammons, C.H., 1999, Factors controlling copper solubility and chalcopyrite deposition in the Sungun porphyry copper deposit, Iran: Mineralium Deposita, v. 34, p. 770-783.

Hollings, P., Cooke, D., and Clark, A., 2005, Regional geochemistry of tertiary igneous rocks in central Chile: Implications for the geodynamic environment of giant porphyry copper and epithermal gold mineralization: Economic Geology, v. 100, p. 887-904.

Horton, B.K., 2005, Revised deformation history of the central Andes: Inferences from Cenozoic foredeep and intermontane basins of the Eastern Cordillera, Bolivia: Tectonics, v. 24.

Hudson, D.M., 2003, Epithermal Alteration and Mineralization in the Comstock District, Nevada: Economic Geology, v. 98, p. 367-385.

Jaillard, E., Hérail, G., Montfret, T., Díaz-Martínez, E., Baby, P., Lavenu, A., and Dumont, J.F., 2000, Tectonic evolution of the Andes of Ecuador, Peru, Bolivia and northernmost Chile, in Cordani, U.G., Milani, E.J., Thomas Filho, A., and Campos, D.A., eds., Tectonic evolution of South America / 31th International Geological Congress: Rio de Janeiro, Brazil, Academia Brasileira de Ciencias, p. 481-559.

Jannas, R.R., Beane, R.E., Ahler, B.A., and Brosnahan, D.R., 1990, Gold and copper mineralization at the El-Indio Deposit, Chile: Journal of Geochemical Exploration, v. 36, p. 233-266.

John, D.A., 2001, Miocene and early Pliocene epithermal gold-silver deposits in the Northern Great Basin, Western United States: Characteristics, distribution, and relationship to magmatism: Economic Geology and the Bulletin of the Society of Economic Geologists, v. 96, p. 1827-1853.

Jordan, T.E., and Alonso, R.N., 1987, Cenozoic stratigraphy and basin tectonics of the Andes Mountains, 20°-28° South Latitude: The American Association of Petroleum Geologists Bulletin, v. 71, p. 49-64.

Jordan, T.E., Zeitler, P., Ramos, V., and Gleadow, A.J.W., 1989, Thermochronometric data on the development of the basement peneplain in the Sierras Pampeanas, Argentina: Journal of South American Earth Sciences, v. 2, p. 207-222.

Kay, S.M., and Mpodozis, C., 2001, Central Andean ore deposits linked to evolving shallow subduction systems and thickening crust: GSA Today, v. 11, p. 4-9.

Kay, S.M., and Mpodozis, C., 2002, Magmatism as a probe to the Neogene shallowing of the Nazca plate beneath the modern Chilean flat-slab: Journal of South American Earth Sciences, v. 15, p. 39-57.

Kay, S.M., Mpodozis, C., Tittler, A., and Cornejo, P., 1994, Tertiary magmatic evolution of the Maricunga Belt in Chile: International Geology Review, v. 36, p. 1079-1112.

Kelley, K.D., Romberger, S.B., Beaty, D.W., Pontius, J.A., Snee, L.W., Stein, H.J., and Thompson, T.B., 1998, Geochemical and geochronological constraints on the genesis of Au-Te deposits at Cripple Creek, Colorado: Economic Geology and the Bulletin of the Society of Economic Geologists, v. 93, p. 981-1012.

Klemm, L.M., 2005, Cu-Mo-Au ratios in porphyry-type ore deposits: Constraints from fluid inclusion microanalysis [Ph.D. thesis]: Zurich, ETH Zurich.

Kober, F., Ivy-Ochs, S., Schlunegger, F., Baur, H., Kubik, P.W., and Wieler, R., 2007, Denudation rates and a topography-driven rainfall threshold in northern Chile: Multiple cosmogenic nuclide data and sediment yield budgets: Geomorphology, v. 83, p. 97-120.

Kouzmanov, K., Bailly, L., Ramboz, C., Rouer, O., and Beny, J.M., 2002, Morphology, origin and infrared microthermometry of fluid inclusions in pyrite from the Radka epithermal copper deposit, Srednogorie zone, Bulgaria: Mineralium Deposita, v. 37, p. 599-613.

Kouzmanov, K., Ramboz, C., Bailly, L., and Bogdanov, K., 2004, Genesis of high-sulfidation vinciennite-bearing Cu-As-Sn (+/- Au) assemblage from the Radka epithermal copper deposit, Bulgaria: Evidence from mineralogy and infrared microthermometry of enargite: Canadian Mineralogist, v. 42, p. 1501-1521.

Krauskopf, K.B., 1957, The heavy metal content of magmatic vapor at 600°C: Economic Geology, v. 52, p. 786-807.

Kurtz, A.C., Kay, S.M., Charrier, R., and Farrar, E., 1997, Geochronology of Miocene plutons and exhumation history of the El Teniente region, Central Chile (34-35 degrees S): Revista Geologica De Chile, v. 24, p. 75-90.

Landtwing, M.R., 2004, Fluid evolution and ore mineral precipitation at the Bingham porphyry Cu-Au-Mo deposit, Utah, deduced from cathodoluminescence imaging and LA-ICPMS microanalysis of fluid inclusions [PhD thesis]: Zürich, ETH Zürich.

Landtwing, M.R., Dillenbeck, E.D., Leake, M.H., and Heinrich, C.A., 2002, Evolution of the breccia-hosted porphyry Cu-Mo-Au deposit at Agua Rica, Argentina: Progressive unroofing of a magmatic hydrothermal system: Economic Geology and the Bulletin of the Society of Economic Geologists, v. 97, p. 1273-1292.

Landtwing, M.R., Pettke, T., Halter, W.E., Heinrich, C.A., Redmond, P.B., Einaudi, M.T., and Kunze, K., 2005, Copper deposition during quartz dissolution by cooling magmatic-hydrothermal fluids: The Bingham porphyry: Earth and Planetary Science Letters, v. 235, p. 229-243.

Longerich, H.P., Jackson, S.E., and Gunther, D., 1996, Laser ablation inductively coupled plasma mass spectrometric transient signal data acquisition and analyte concentration calculation: Journal of Analytical Atomic Spectrometry, v. 11, p. 899-904.

Losada-Calderón, A.J., 1992, Geology and geochemistry of Nevados del Famatina and La Mejicana deposits. La Rioja Province, Argentina [Ph.D. thesis]: Clayton, Monash University, Australia.

Losada-Calderón, A.J., and Bloom, M.S., 1990, Geology, paragenesis and fluid inclusion studies of a high-sulphidation epithermal/porphyry system, Nevados del Famatina district, La Rioja province, Argentina, in Metallurgy, T.A.I.o.M.a., ed., Pacific Rim Congress: Queensland, Australia, p. 457-464.

Losada-Calderón, A.J., McBride, S.L., and Bloom, M.S., 1994, The geology and 40Ar-39Ar geochronology of magmatic activity and related mineralization in the Nevados Del Famatina Mining District, La-Rioja Province, Argentina: Journal of South American Earth Sciences, v. 7, p. 9-24.

Losada-Calderón, A.J., and McPhail, D.C., 1996, Porphyry and high-sulfidation epithermal mineralization in the Nevados del Famatina mining district, Argentina, in Camus, F., Sillitoe, R.M., and Peterson, R., eds., Andean copper deposits: New discoveries, mineralization, styles and metallogeny, Volume 5: SEG Special Publication, Society of Economic Geologists, p. 91-118.

Lottner, U.S., 1986, Strukturgebundene Magmenentwicklung im altpaläozoischen Grundgebirge NW-Argentiniens am Beispiel der Sierra de Ancasti (Provinz Catamarca): Münsterische Forschungen zur Geologie und Paläontologie, v. 65, p. 180.

Lowell, J.D., and Guilbert, J.M., 1970, Lateral and vertical alteration-mineralization zoning in porphyry ore deposits: Economic Geology, v. 65, p. 373-408.

Ludwig, K.R., 2003, User's manual for Isoplot 3.00 - A geochronological toolkit for Microsoft Excel, Special Publication No. 4: Berkeley, Berkeley Geochronological Center.

Mancano, D.P., and Campbell, A.R., 1995, Microthermometry of enargite-hosted fluid inclusions from the Lepanto, Philippines, high-sulfidation Cu-Au deposit: Geochimica Et Cosmochimica Acta, v. 59, p. 3909-3916.

Mangano, M.G., Astini, R.A., Buatois, L.A., and Davila, F.M., 2003, The Ordovician System in the Famatina belt: Depositional and tectonic evolution, in Aceñolaza, F.G., ed., Aspects of the Ordovician System in Argentina, Volume Serie de Correlación Geológica 16: Tucumán, Instituto Superior de Correlación Geológica (INSUGEO), p. 295-312.

Marcos, O., and Zanettini, J.C., 1982, Geología y exploración del proyecto Nevados del Famatina: Buenos Aires, Ministerio de Economía, Subsecretaría de Minería, p. 126.

Marshall, D.J., 1988, Cathodoluminescence of geological materials: Boston (etc.), Unwin Hyman, 146 p.

McBride, S.L., Caelles, J.C., Clark, A.H., and Farrar, E., 1976, Palaeozoic radiometric age provinces in the Andean basement, latitudes 25[deg]-30[deg]S: Earth and Planetary Science Letters, v. 29, p. 373-383.

Moritz, R., 2006, Fluid salinities obtained by infrared microthermometry of opaque minerals: Implications for ore deposit modeling -- A note of caution: Journal of Geochemical Exploration, v. 89, p. 284-287.

Müller, A., Seltmann, R., and Behr, H.-J., 2000, Application of cathodoluminescence to magmatic quartz in a tin granite - case study from the Schellerhau Granite Complex, Eastern Erzgebirge, Germany: Mineralium Deposita, v. 35, p. 169-189.

Muller, D., and Groves, D.I., 1993, Direct and Indirect Associations between Potassic Igneous Rocks, Shoshonites and Gold-Copper Deposits: Ore Geology Reviews, v. 8, p. 383-406.

Muntean, J.L., and Einaudi, M.T., 2001, Porphyry-epithermal transition: Maricunga belt, northern Chile: Economic Geology and the Bulletin of the Society of Economic Geologists, v. 96, p. 743-772.

Nagaseki, H., and Hayashi, K., 2006, The effect of sulfur on the vapor-liquid distribution of Cu and Zn in boiling hydrothermal fluid at 500-650°C and 35-100 MPa, ISHR & ICSTR 2006: Sendai, Japan, International Mineralogical Association Meeting.

Padilla-Garza, R.A., Titley, S.R., and Eastoe, C.J., 2004, Hypogene evolution of the Escondida porphyry copper deposit, Chile, in Sillitoe, R.H., Perello, J., and Vidal, C.E., eds., Andean metallogeny; new discoveries, concepts, and updates., Society of Economic Geologists. Littleton, CO, United States. 2004.

Passchier, C.W., and Trouw, R.A.J., 2005, Microtectonics: Berlin, Heidelberg, Springer, 366 p.

Pettke, T., Halter, W.E., Webster, J.D., Aigner-Torres, M., and Heinrich, C.A., 2004, Accurate quantification of melt inclusion chemistry by LA-ICPMS: a comparison with EMP and SIMS and advantages and possible limitations of these methods: Lithos, v. 78, p. 333-361.

Pettke, T., Heinrich, C.A., Ciocan, A.C., and Gunther, D., 2000, Quadrupole mass spectrometry and optical emission spectroscopy: detection capabilities and representative sampling of short transient signals from laser-ablation: Journal of Analytical Atomic Spectrometry, v. 15, p. 1149-1155.

Pokrovski, G.S., Borisova, A.Y., and Harrichoury, J.-C., 2006, The effect of sulfur on vapor-liquid partitioning of metals in hydrothermal systems: An experimental batch-reactor study: Geochemica et cosmochemica acta, v. in press.

Pomposiello, C., Osella, A., Favetto, A., Sainato, C., Martinelli, P., and Aprea, C., 1998, Current channelling and three-dimensional effects detected from magnetotelluric data from a sedimentary basin in Sierras Pampeanas, Argentina: Geophysical Journal International, v. 135, p. 339-350.

Ramos, V.A., 2000, The Southern Central Andes, in Cordani, U.G., Milani, E.J., Thomas Filho, A., and Campos, D.A., eds., Tectonic evolution of South America: Rio de Janeiro, 31° International Geological Congress, p. 561-604.

Ramos, V.A., Cristallini, E.O., and Perez, D.J., 2002, The Pampean flat-slab of the Central Andes: Journal of South American Earth Sciences, v. 15, p. 59-78.

Ramos, V.A., Jordan, T.E., Allmendinger, R.W., Mpodozis, C., Kay, S.M., Cortes, J.M., and Palma, M., 1986, Paleozoic Terranes of the Central Argentine-Chilean Andes: Tectonics, v. 5, p. 855-880.

Redmond, P.B., Einaudi, M.T., Inan, E.E., Landtwing, M.R., and Heinrich, C.A., 2004, Copper deposition by fluid cooling in intrusion-centered systems: New insights from the Bingham porphyry ore deposit, Utah: Geology, v. 32, p. 217-220.

Reynolds, J.H., Jordan, T.E., Johnson, N.M., Damanti, J.F., and Tabbutt, K.D., 1990, Neogene deformation of the flat-subduction segment of the Argentine-Chilean Andes: Magnetostratigraphic constraints from Las Juntas, La Rioja province, Argentina: Geological Society of America Bulletin, v. 102, p. 1607-1622.

Reynolds, P., Ravenhurst, C., Zentilli, M., and Lindsay, D., 1998, High-precision 40Ar-39Ar dating of two consecutive hydrothermal events in the Chuquicamata porphyry copper system, Chile: Chemical Geology, v. 148, p. 45-60.

Roedder, E., 1971, Fluid Inclusion Studies on Porphyry-Type Ore Deposits at Bingham, Utah, Butte, Montana, and Climax, Colorado: Economic Geology, v. 66, p. 98-120.

Roedder, E., 1984, Fluid Inclusions: Washington, DC, United States, Mineralogical Society of America, 644 p.

Roedder, E., and Bodnar, R.J., 1980, Geologic pressure determinations from fluid inclusion studies: Annual Review of Earth and Planetary Sciences, v. 8, p. 263-301.

Rusk, B., and Reed, M., 2002, Scanning electron microscope-cathodoluminescence analysis of quartz reveals complex growth histories in veins from the Butte porphyry copper deposit, Montana: Geology, v. 30, p. 727-730.

Rusk, B.G., Reed, M.H., Dilles, J.H., Klemm, L.M., and Heinrich, C.A., 2004, Compositions of magmatic hydrothermal fluids determined by LA-ICP-MS of fluid inclusions from the porphyry copper-molybdenum deposit at Butte, MT: Chemical Geology, v. 210, p. 173-199.

Ryan, G.G., Heinrich, C.A., and Mernagh, T.P., 1993, PIXE microanalysis of fluid inclusions and its application to study ore metal segregation between magmatic brine and vapor: Nuclear Instruments and Methods in Physics Research Section B: Beam Interactions with Materials and Atoms, v. 77, p. 463-471.

Rye, R.O., 1993, The Evolution of Magmatic Fluids in the Epithermal Environment - the Stable Isotope Perspective: Economic Geology and the Bulletin of the Society of Economic Geologists, v. 88, p. 733-753.

Saunders, J.A., 1994, Silica and gold textures in bonanza ores of the Sleeper Deposit, Humboldt County, Nevada; evidence for colloids and implications for epithermal ore-forming processes: Economic Geology, v. 89, p. 628-638.

Sawkins, F.J., and Scherkenbach, D.A., 1981, High copper content of fluid inclusions in quartz from northern Sonora: implications for ore genesis theory: Geology, v. 9, p. 37-40.

Schalamuk, I.B., and Logan, M.A.V., 1994, Polymetallic Ag-Te-Bearing Paragenesis of the Cerro-Negro District, Famatina Range, La Rioja, Argentina: Canadian Mineralogist, v. 32, p. 667-679.

Shepherd, T.J., and Chenery, S.R., 1995, Laser ablation ICP-MS elemental analysis of individual fluid inclusions: An evaluation study: Geochimica et Cosmochimica Acta, v. 59, p. 3997-4007.

Sillitoe, R.H., 1973, The tops and bottoms of porphyry copper deposits: Economic Geology, v. 68, p. 799-815.

Sillitoe, R.H., 1981, Regional Aspects of the Andean Porphyry Copper Belt in Chile and Argentina: Transactions of the Institution of Mining and Metallurgy Section B-Applied Earth Science, v. 90, p. B15-B36.

Sillitoe, R.H., 1983, Enargite-bearing massive sulfide deposits high in porphyry copper systems: Economic Geology, v. 78, p. 348-352.

Sillitoe, R.H., 1988, Epochs of intrusion-related copper mineralization in the Andes: Journal of South American Earth Sciences, v. 1, p. 89-108.

Sillitoe, R.H., 1991, Gold Metallogeny of Chile - an Introduction: Economic Geology and the Bulletin of the Society of Economic Geologists, v. 86, p. 1187-1205.

Sillitoe, R.H., 1992, Gold and Copper Metallogeny of the Central Andes - Past, Present, and Future Exploration Objectives: Economic Geology and the Bulletin of the Society of Economic Geologists, v. 87, p. 2205-2216.

Sillitoe, R.H., 1997, Characteristics and controls of the largest porphyry copper-gold and epithermal gold deposits in the circum-Pacific region: Australian Journal of Earth Sciences, v. 44, p. 373-388.

Sillitoe, R.H., and Bonham, H.F., 1990, Sediment-Hosted Gold Deposits - Distal Products of Magmatic- Hydrothermal Systems: Geology, v. 18, p. 157-161.

Sillitoe, R.H., and Perello, J., 2005, Andean copper province: tectonomagmatic settings, deposit types, metallogeny, exploration, and discovery, in Hedenquist Jeffrey, W., Thompson John, F.H., Goldfarb Richard, J., and Richards Jeremy, P., eds., Economic Geology; one hundredth anniversary volume, 1905-2005.: Littleton, CO, United States, Society of Economic Geologists.

Simmons, S.F., and Brown, K.L., 2006, Gold in magmatic hydrothermal solutions and the rapid formation of a giant ore deposit: Science, v. 314, p. 288-291.

Simmons, S.F., and Browne, P.R.L., 2000, Hydrothermal minerals and precious metals in the Broadlands-Ohaaki geothermal system: Implications for understanding low-sulfidation epithermal environments: Economic Geology and the Bulletin of the Society of Economic Geologists, v. 95, p. 971-999.

Sobral, J.M., 1921, Some Physiographic Notes on the Sierra de Famatina: Geografiska Annaler, v. 3, p. 311-326.

Stefánsson, A., and Seward, T.M., 2004, Gold(I) complexing in aqueous sulphide solutions to 500°C at 500 bar: Geochimica et Cosmochimica Acta, in press.

Thomas, W.A., and Astini, R.A., 2003, Ordovician accretion of the Argentine Precordillera terrane to Gondwana: a review: Journal of South American Earth Sciences, v. 16, p. 67-79.

Titley, S.R., 1975, Geological Characteristics and Environment of Some Porphyry Copper Occurrences in Southwestern Pacific: Economic Geology, v. 70, p. 499-514.

Toselli, G.A., 1978, Edad de la Formación Negro Peinado, Sierra de Famatina, La Rioja: Revista de la Asociación Geológica Argentina, p. 86-89.

Turner, J.C.M., 1970, The Andes of Northwestern Argentina: Geologische Rundschau, v. 59, p. 1028-1063.

Turner, J.C.M., 1971, Descripcion geologica de la hoja 15d, Famatina: Buenos Aires, Ministerio de Industria y Mineria, 96 p.

Ulrich, T., Günther, D., and Heinrich, C.A., 1999, Gold concentrations of magmatic brines and the metal budget of porphyry copper deposits: Nature, v. 399, p. 676-679.

Ulrich, T., Günther, D., and Heinrich, C.A., 2001, The evolution of a porphyry Cu-Au deposit, based on LA-ICP-MS analysis of fluid inclusions: Bajo de la Alumbrera, Argentina: Economic Geology, v. 96, p. 1743-1774.

Vennemann, T.W., Muntean, J.L., Kesler, S.E., Oneil, J.R., Valley, J.W., and Russell, N., 1993, Stable Isotope Evidence for Magmatic Fluids in the Pueblo-Viejo Epithermal Acid Sulfate Au-Ag Deposit, Dominican-Republic: Economic Geology and the Bulletin of the Society of Economic Geologists, v. 88, p. 55-71.

White, N.C., and Hedenquist, J.W., 1995, Epithermal gold deposits: Styles, characteristics and exploration: SEG Newletter, p. 1-13.

Williams, T.J., Candela, P.A., and Piccoli, P.M., 1995, The partitioning of copper between silicate melts and two-phase aqueous fluids: An experimental investigation at 1 kbar, 800° C and 0.5 kbar, 850° C: Contributions to Mineralogy and Petrology, v. 121, p. 388-399.

Zinkernagel, U., 1978, Cathodoluminescence of quartz and its applications to sandstone petrology: Stuttgart, Schweizerbart, 69 p.

APPENDICES

Appendix figure 1: Regional geology and sample location
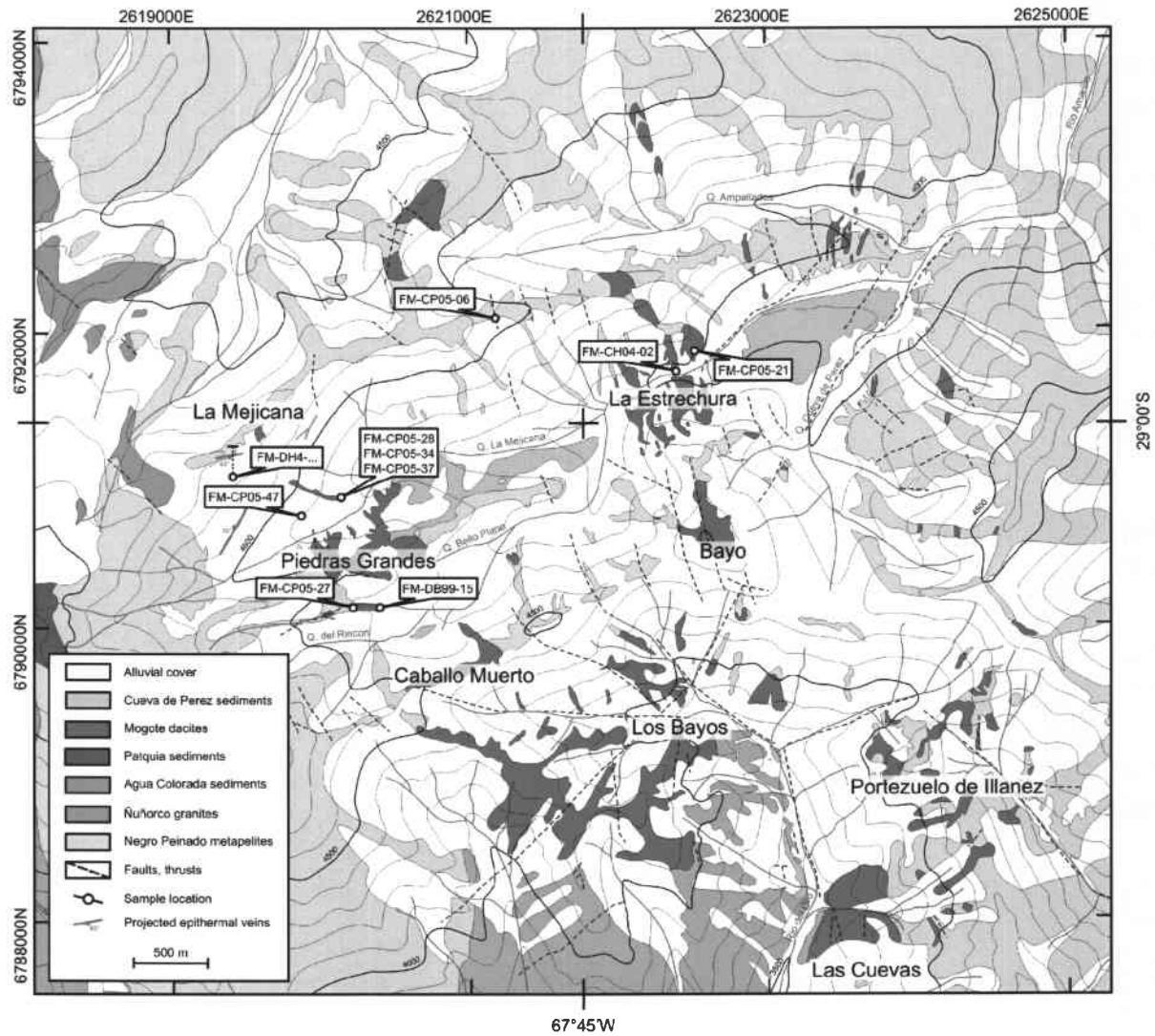
Regional geology of the Famatina mining district, La Rioja Province, NW Argentina (modified from Losada-Calderón, 1992). The original map was provided by YAMIRI S.A. and updated based on own field observations in 2005. White circles indicate the location of the sample material selected for the fluid inclusion study. FM-DH4-... refers to drillcore sections collected from an exploratory drillhole.

Appendix table 1: Sample description

sample ID	description	type	vugs	GPS / mine coordinates	altitude	host rock	alteration	ore minerals	TS	MT	LA	Losada-Calderón
04-02	B-vein	drillcore		6789.3 N, 2624.2 E	4116	Los Bayos dacitic porphyry	potassic	mo				stage II
06-09	QSP-veinlet	drillcore		6789.2 N, 2621.1 E	4346	Caballo Muerto dacitic porphyry	sericitic	py, ±bo, ±cv				stage IV
10-01	QSP-vein	drillcore	X	6790.1 N, 2620.4 E	4365	Piedras Grandes dacitic porphyry	sericitic	py	X			stage IV
16-03	A-veinlet	drillcore		6790.0 N, 2620.7 E	4315	Piedras Grandes dacitic porphyry	-	mt	X			stage I
19-05	B-vein	drillcore	X	6792.6 N, 2622.1 E	4138	La Estrechura dacitic porphyry	potassic	mo	X			stage II
21-05	epithermal vein	drillcore	X	6789.3 N, 2620.6 E	4547	Negro Peinado metasediments	alsic	cpy, cv, tn/th, sl	X			stage V
25-10	QSP-vein	drillcore		6792.2 N, 2622.9 E	3888	Negro Peinado metasediments	sericitic	py, ±bo, ±cv	X			stage IV
25-12	B-vein	drillcore	X	6792.2 N, 2622.9 E	3888	Negro Peinado metasediments	sericitic	mo, cpy	X			stage III
28-03	QSP vein	drillcore	X	6792.6 N, 2622.1 E	4138	La Estrechura dacitic porphyry	sericitic	py	X			stage IV
28-04	B-vein	drillcore		6792.6 N, 2622.1 E	4138	La Estrechura dacitic porphyry	potassic	mo	X			stage II
28-05	B-vein	drillcore	X	6792.6 N, 2622.1 E	4138	La Estrechura dacitic porphyry	sericitic	mo, cpy, cv	X			stage III
28-13	B-vein	drillcore		6792.6 N, 2622.1 E	4138	La Estrechura dacitic porphyry	potassic	mo	X			stage II
28-19	QSP vein	drillcore		6792.6 N, 2622.1 E	4138	La Estrechura dacitic porphyry	sericitic	py	X			stage IV
29-12	QSP vein	drillcore		6791.2 N, 2621.8 E	4067	Negro Peinado metasediments	sericitic	py				stage IV
34-04	B-vein	drillcore		6791.9 N, 2621.8 E	4276	Negro Peinado metasediments	sericitic	mo, cpy				stage III
37-13	B-vein	drillcore	X	6791.8 N, 2622.7 E	3905	La Estrechura dacitic porphyry	potassic	mo				stage II
37-14	B-vein	drillcore		6791.8 N, 2622.7 E	3905	La Estrechura dacitic porphyry	sericitic	mo, cpy				stage III
37-17	B-vein	drillcore	X	6791.8 N, 2622.7 E	3905	La Estrechura dacitic porphyry	potassic	mo	X			stage II
37-18	QSP vein	drillcore		6791.8 N, 2622.7 E	3905	La Estrechura dacitic porphyry	sericitic	py	X			stage IV
0106	epithermal vein	underground		Upulungus vein, Level 7	4336	Negro Peinado metasediments	alunitic	py, en, cv				intermediate
0208	epithermal vein	underground		San Pedro vein, Level 3	4637	Negro Peinado metasediments	alsic	py, tn/th				shallow
0209	epithermal vein	underground	X	Upulungus vein, Level 6	4335	Negro Peinado metasediments	alunitic	py, en, cv				intermediate
0507	QSP vein	underground	X	Upulungus vein, Level 5	4411	Negro Peinado metasediments	sericitic	py, ±bo, ±cv	X			deep
0806	QSP vein	underground		Upulungus vein, Level 6	4335	Negro Peinado metasediments	sericitic	py				deep
0906	QSP vein	underground		Upulungus vein, Level 6	4335	Negro Peinado metasediments	sericitic	py, ±tn/th				deep
0907	epithermal vein	underground	X	Upulungus vein, Level 5	4411	Negro Peinado metasediments	alunitic	py, en, cv				intermediate
1007	epithermal vein	underground	X	Upulungus vein, Level 5	4411	Negro Peinado metasediments	alunitic	py, en, cv				intermediate
FM-DB99-04	B-vein	outcrop		6790.7 N, 2620.2 E	4585	Piedras Grandes dacitic porphyry	potassic	mo	X			stage II
FM-DB99-05	B-vein	outcrop		6790.7 N, 2620.2 E	4542	Piedras Grandes dacitic porphyry	potassic	mo	X			stage II
FM-DB99-06	A-veinlet	outcrop		6790.7 N, 2620.2 E	4542	Piedras Grandes dacitic porphyry	-	mt	X			stage I

sample ID	description	type	vugs	GPS / mine coordinates	altitude	host rock	alteration	ore minerals	TS	MT	LA	Losada-Calderón
FM-DB99-15	B-vein	outcrop	X	6790.2 N, 2620.6 E	4370	Piedras Grandes porphyritic dacite	sericitic	mo, cpy	X	X	X	stage III
FM-DB99-16	B-vein	outcrop		6790.2 N, 2620.6 E	4370	Piedras Grandes porphyritic dacite	potassic	mo	X			stage II
FM-DB99-18	porphyritic dacite	outcrop		6790.2 N, 2620.6 E	4370	Piedras Grandes porphyritic dacite	-	mt	X			-
FM-DB99-19	vuggy silica	outcrop		6790.4 N, 2620.4 E	4400	Piedras Grandes porphyritic dacite	argillic	ja, hm	X			stage V
FM-DB99-20	B-vein	outcrop		6790.2 N, 2620.2 E	4450	Piedras Grandes porphyritic dacite	potassic	mo	X			stage II
FM-DB99-22	epithermal vein	outcrop		6791.0 N, 2620.0 E	4380	Negro Peinado metasediments	alsic	ja, hm	X			shallow
FM-DB99-23	B-vein	outcrop		6791.0 N, 2620.0 E	4380	La Mejicana porphyritic dacite	potassic	mo	X			stage II
FM-DB99-24	A-veinlet	outcrop		6791.0 N, 2620.0 E	4380	La Mejicana porphyritic dacite	silicic	-	X			stage I
FM-DB99-26	B-vein	dumpsite		6790.9 N, 2620.0 E	4500	La Mejicana porphyritic dacite	silicic	mo, ja, hm	X			stage II
FM-DB99-30	B-vein	outcrop		6790.9 N, 2620.0 E	4520	La Mejicana porphyritic dacite	sericitic	mo, cpy	X			stage III
FM-DB99-39	QSP vein	outcrop		6791.7 N, 2620.0 E	4570	Negro Peinado metasediments	sericitic	py	X			stage IV
FM-DB99-43	B-vein	outcrop		6789.8 N, 2620.5 E	4400	Caballo Muerto porphyritic dacite	potassic	mo	X			stage II
FM-DB99-45	vuggy silica	outcrop		6789.8 N, 2620.5 E	4400	Caballo Muerto porphyritic dacite	argillic	ja, hm	X			stage V
FM-DB99-46	B-vein	outcrop		6789.8 N, 2620.5 E	4400	Caballo Muerto porphyritic dacite	sericitic	-	X			stage II
FM-DB99-47	porphyritic dacite	outcrop		6789.7 N, 2620.9 E	4450	Caballo Muerto porphyritic dacite	sericitic	-	X			-
FM-DB99-48	B-vein	outcrop	X	6789.6 N, 2620.7 E	4470	Caballo Muerto porphyritic dacite	sericitic	mo, cpy	X			stage III
FM-DB99-51	epithermal vein	outcrop		6789.3 N, 2622.4 E	4460	Los Bayos porphyritic dacite	alsic	-	X			stage V
FM-DB99-53	B-vein	outcrop		6789.4 N, 2623.0 E	4350	Los Bayos porphyritic dacite	potassic	mo	X			stage II
FM-DB99-54	B-vein	outcrop		6789.4 N, 2622.9 E	4350	Los Bayos porphyritic dacite	potassic	mo	X			stage II
FM-DB99-56	B-vein	outcrop		6789.4 N, 2622.9 E	4350	Los Bayos porphyritic dacite	potassic	mo	X			stage II
FM-DB99-57	B-vein	outcrop		6789.5 N, 2622.3 E	4500	Los Bayos porphyritic dacite	sericitic	mo, ±cpy	X			stage III
FM-DB99-62	A-veinlet	outcrop		6789.8 N, 2622.2 E	4420	Los Bayos porphyritic dacite	silicic	-	X			stage I
FM-DB99-63	B-vein	outcrop		6789.8 N, 2622.4 E	4480	Los Bayos porphyritic dacite	potassic	mo	X			stage II
FM-DB99-66	A-veinlet	outcrop		6789.2 N, 2620.9 E	4450	Los Bayos porphyritic dacite	sericitic	-	X			stage I
FM-DB99-69	B-vein	outcrop		6789.2 N, 2621.0 E	4430	Negro Peinado metasediments	sericitic	mo, cpy	X			stage III
FM-U-05	QSP vein	underground		Upulungus vein, Level 5	4411	Negro Peinado metasediments	sericitic	py	X			deep
FM-SP-04	epithermal vein	underground		San Pedro vein, Level 3	4637	Negro Peinado metasediments	alunitic	py, en, cv	X			intermediate
FM-SP-05	epithermal vein	underground		San Pedro vein, Level 3	4637	Negro Peinado metasediments	alunitic	py, en, cv	X			intermediate
FM-SP-24	epithermal vein	underground		San Pedro vein, Level 3	4637	Negro Peinado metasediments	alsic	py, tn/th	X			shallow
FM-CH04-01	B-vein	dumpsite	X	6791.0 N, 2620.4 E	4270	Piedras Grandes porphyritic dacite	sericitic	mo, cpy	X			stage III
FM-CH04-02	A-veinlet	outcrop		6791.7 N, 2622.4 E	4480	La Estrechura porphyritic dacite	silicic	ja, hm	X	X	X	stage I
FM-CH04-03	QSP vein	dumpsite		Upulungus vein, Level 5	4411	Negro Peinado metasediments	sericitic	py	X			deep
FM-CP05-06	QSP vein	outcrop	X	S29.000678°, W67.765367°	4693	Negro Peinado metasediments	sericitic	py	X	X	X	stage IV

sample ID	description	type	vugs	GPS / mine coordinates	altitude	host rock	alteration	ore minerals	TS	MT	LA	Losada-Calderón
FM-CP05-11	QSP vein	outcrop	X	S29.000678°, W67.765367°	4693	Negro Peinado metasediments	sericitic	py, ±bo, ±cv	X			stage IV
FM-CP05-15	B-vein	outcrop		S29.000678°, W67.765367°	4693	La Estrechura porphyritic dacite	potassic	mo	X			stage II
FM-CP05-20	B-vein	outcrop	X	S29.003842°, W67.751950°	4036	La Estrechura porphyritic dacite	silicic	mo, ja, hm	X			stage II
FM-CP05-21	A-veinlet	outcrop		S29.003842°, W67.751950°	4036	La Estrechura porphyritic dacite	argillic	ja	X	X	X	stage I
FM-CP05-26	A-veinlet	outcrop	X	6790.1 N, 2620.0 E	4450	Piedras Grandes porphyritic dacite	argillic	ja	X			stage I
FM-CP05-27	B-vein	outcrop		S29.017367°, W67.771756°	4419	Piedras Grandes porphyritic dacite	potassic	mo, cpy	X	X	X	stage III
FM-CP05-28	epithermal vein	dumpsite	X	S29.010172°, W67.771644°	4348	Negro Peinado metasediments	alunitic	py, en, cv	X	X		intermediate
FM-CP05-34	quartz phenocryst	dumpsite		S29.010172°, W67.771644°	4348	La Mejicana porphyritic dacite	sericitic	py	X	X	X	-
FM-CP05-37	quartz phenocryst	dumpsite		S29.010172°, W67.771644°	4348	La Mejicana porphyritic dacite	sericitic	py	X	X	X	-
FM-CP05-38	QSP vein	dumpsite	X	S29.010172°, W67.771644°	4348	La Mejicana porphyritic dacite	sericitic	py	X			stage IV
FM-CP05-39	epithermal vein	dumpsite	X	S29.010172°, W67.771644°	4348	Negro Peinado metasediments	alunitic	py, en, cv	X			intermediate
FM-CP05-40	QSP vein	dumpsite	X	S29.010172°, W67.771644°	4348	Negro Peinado metasediments	sericitic	py	X			deep
FM-CP05-42	B-vein	dumpsite	X	S29.012806°, W67.774694°	4417	Negro Peinado metasediments	sericitic	mo, cpy	X			stage III
FM-CP05-47	epithermal vein	dumpsite	X	S29.012806°, W67.774694°	4417	Negro Peinado metasediments	alunitic	py, en, cv	X			intermediate
FM-DH1-89.7	QSP vein	drillcore	X	6791.2 N, 2619.3 E	4810	Negro Peinado metasediments	sericitic	py	X			stage IV
FM-DH3-133.7	QSP vein	drillcore	X	6791.5 N, 2619.5 E	4720	La Mejicana porphyritic dacite	sericitic	py, ±tn/th, ±en	X			stage IV
FM-DH4-187.5	QSP vein	drillcore		6791.0 N, 2619.4 E	4730	Negro Peinado metasediments	sericitic	py	X			stage IV
FM-DH4-276.6	QSP vein	drillcore	X	6791.0 N, 2619.4 E	4730	Negro Peinado metasediments	sericitic	py	X	X	X	stage IV
FM-DH4-277.6	QSP vein	drillcore	X	6791.0 N, 2619.4 E	4730	Negro Peinado metasediments	sericitic	py, ±tn/th	X	X	X	stage IV
FM-DH4-350.5	QSP vein	drillcore		6791.0 N, 2619.4 E	4730	La Mejicana porphyritic dacite	sericitic	py, ±tn/th, ±en	X	X	X	stage IV
FM-DH4-352.1	QSP vein	drillcore		6791.0 N, 2619.4 E	4730	La Mejicana porphyritic dacite	sericitic	py, ±bo, ±cv	X	X	X	stage IV
FM-DH4-427.3	QSP vein	drillcore	X	6791.0 N, 2619.4 E	4730	Negro Peinado metasediments	sericitic	py	X	X	X	stage IV
FM-DH4-434.4	QSP vein	drillcore		6791.0 N, 2619.4 E	4730	Negro Peinado metasediments	sericitic	py	X			stage IV
FM-DH7-110.7	epithermal vein	drillcore	X	6791.2 N, 2619.5 E	4750	Negro Peinado metasediments	alunitic	py, en, cv	X			intermediate
FM-DH7-112.2	QSP vein	drillcore		6791.2 N, 2619.5 E	4750	Negro Peinado metasediments	sericitic	py	X			stage IV
FM-DH16-182.5	B-vein	drillcore	X	S29.012222°, W67.760833°	4315	Piedras Grandes porphyritic dacite	potassic	mo	X			stage II
FM-DH37-281.5	B-vein	drillcore	X	S28.996111°, W67.739722°	3905	La Estrechura porphyritic dacite	sericitic	mo, cpy	X			stage III
FM-DH37-524.0	B-vein	drillcore	X	S28.996111°, W67.739722°	3905	La Estrechura porphyritic dacite	potassic	mo	X			stage II
FM-DH37-541.0	B-vein	drillcore	X	S28.996111°, W67.739722°	3905	La Estrechura porphyritic dacite	potassic	mo	X			stage II

List of samples of the Famatina mining district collected in 1999, 2004, and 2005. For reference, samples from the collection of Losada-Calderón (1992) are listed atop. Highlighted samples represent those selected for the fluid inclusion study and are described in detail in Appendix figures 2 to 4. Headings and abbreviations: altitude, elevation in meter above sealevel; TS, thick section; MT, microthermometry; LA, LA-ICP-MS microanalysis; py, pyrite; ja, jarosite; hm, hematite; mo, molybdenite; cpy, chalcopyrite; tn/th, tennantite/tetrahedrite; bo, bornite; en, enargite; cv, covellite.

Appendix figure 2: Petrography and SEM-CL textures in phenocrysts and vein quartz of the porphyry stage
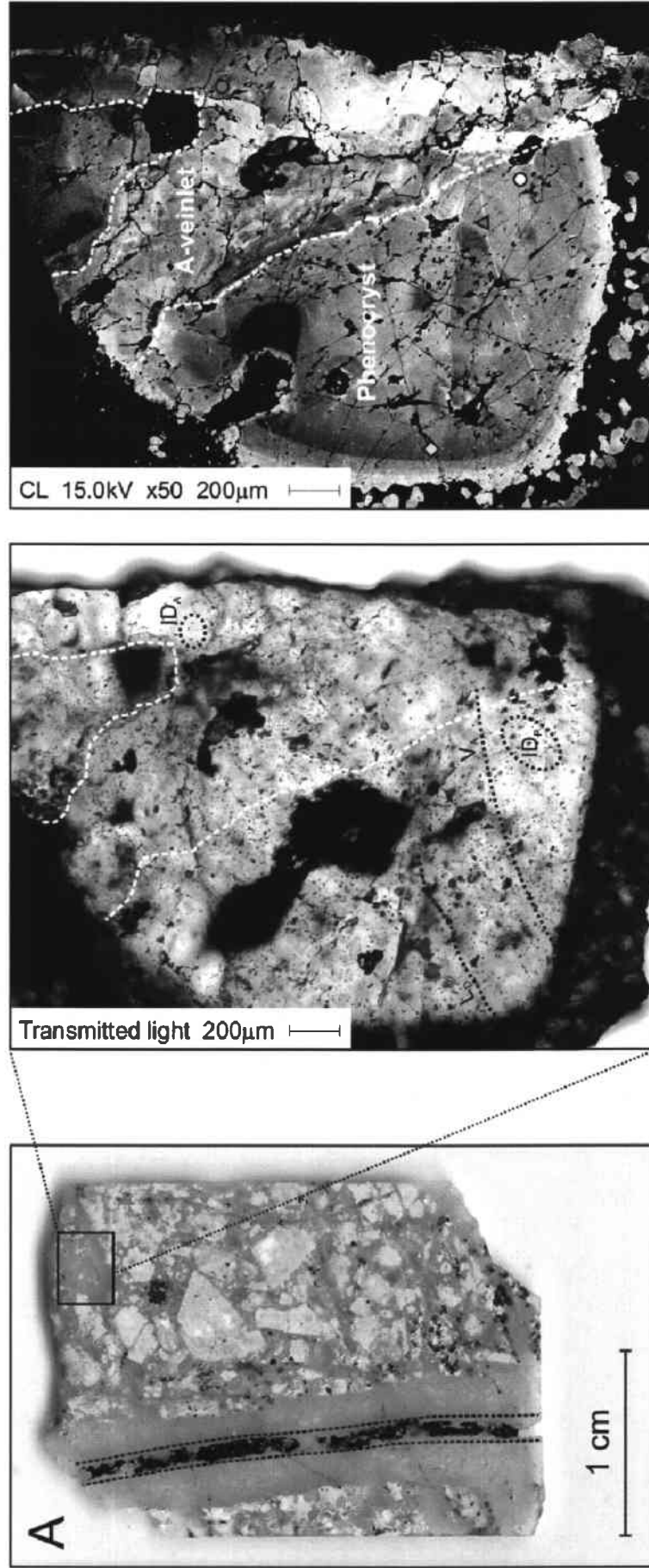
Figure 2: Images of selected porphyry samples acquired by transmitted-light microscopy and SEM-CL. Colored symbols in the SEM-CL images indicate the location of the inclusion assemblages discussed in Chapter 6.4.2. (A) Sample FM-CP05-34: Photomicrographs of the dacitic dyke at La Mejicana. Multiple generations of irregular A-veinlets are cut by a straight B-vein, which was reactivated by a euhedral QSP vein. Pervasive sericitic alteration is probably synchronous with formation of the last vein stage. The igneous host rock exhibits a porphyritic texture with phenocrysts of plagioclase, biotite, and quartz set in a fine-grained groundmass. The highlighted area in the upper right corner of the thick section displays a deeply embayed quartz phenocryst of about 3 mm size, which is cut by an irregular A-veinlet. As shown by transmitted-light microscopy, the quartz is transparent and has a mottled texture related to impurities and fluid inclusions. The CL image of the same area reveals growth zoning with a darker core surrounded by progressively lighter rims. By contrast, CL textures of the irregular A-veinlet consist of poorly zoned quartz grains of varying CL color indicating different conditions at the time of precipitation.
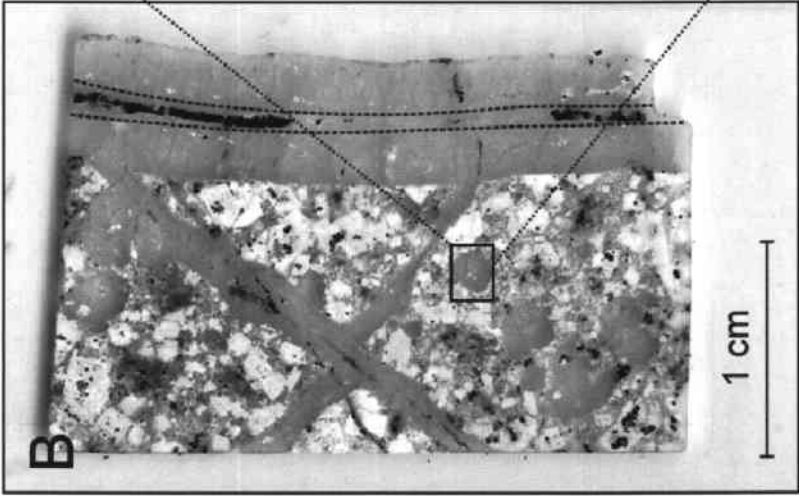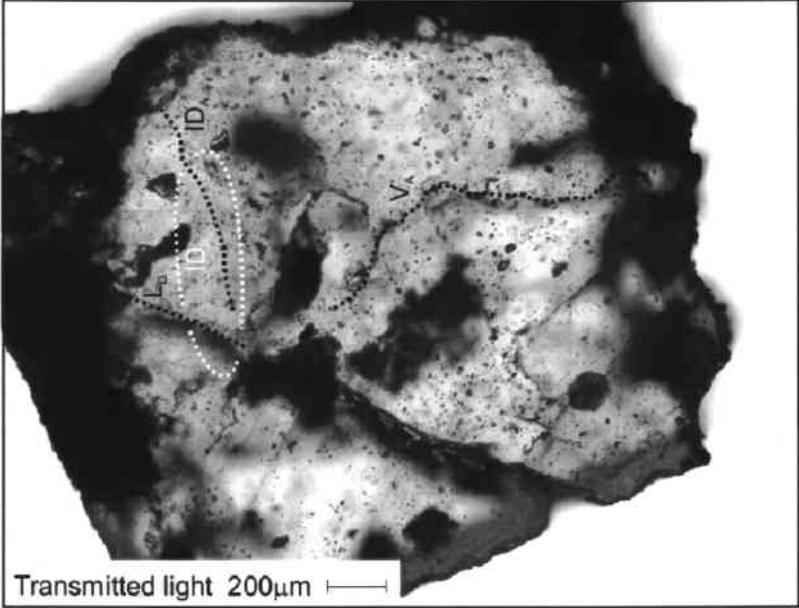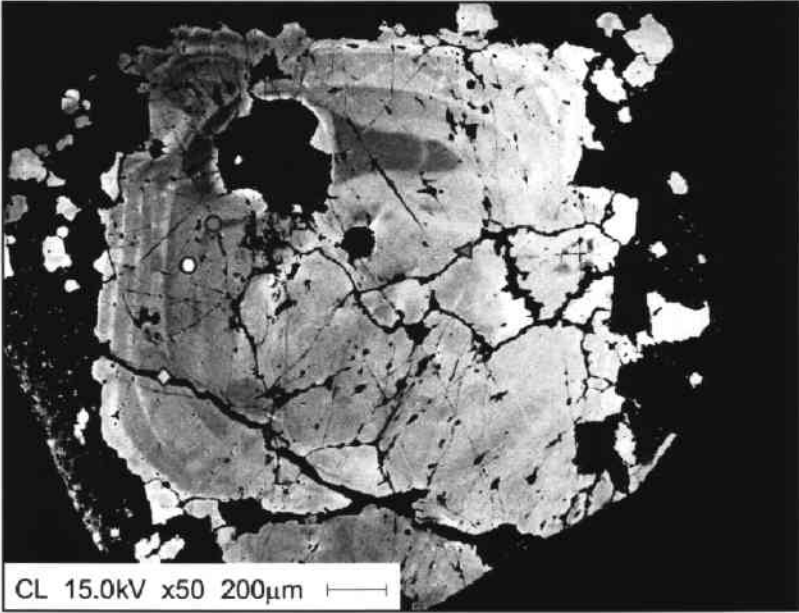
Figure 2 B: Sample FM-CP05-37: Photomicrographs of the dacitic dyke at La Mejicana. Pervasively altered dacitic porphyry crosscut by two irregular A-veinlets, which in turn are cut by a straight B-vein. The latter has been reactivated by a euhedral QSP vein. Related sericitic alteration obliterates the porphyritic texture of the igneous host rock. Plagioclase phenocrysts are altered to a fine intergrowth of quartz, sericite, illite, and pyrite. Primary biotite has been completely replaced by sericite, quartz, pyrite, and minor chlorite and rutile. Anhedral to subhedral quartz phenocrysts are widespread and unaltered, i.e., they show no evidence for recrystallization. Transmitted-light microscopy of a subhedral quartz phenocryst of 2 mm size reveals its mottled texture related to abundant fluid and mineral inclusions. The CL textures exhibit a weak zonation of the phenocryst, with a dark core surrounded by progressively lighter rims, and a large number of otherwise hardly visible cracks. Note the jigsaw-fitting pieces of CL-bright quartz indicating mechanical breaking of the outer rim of the crystal.
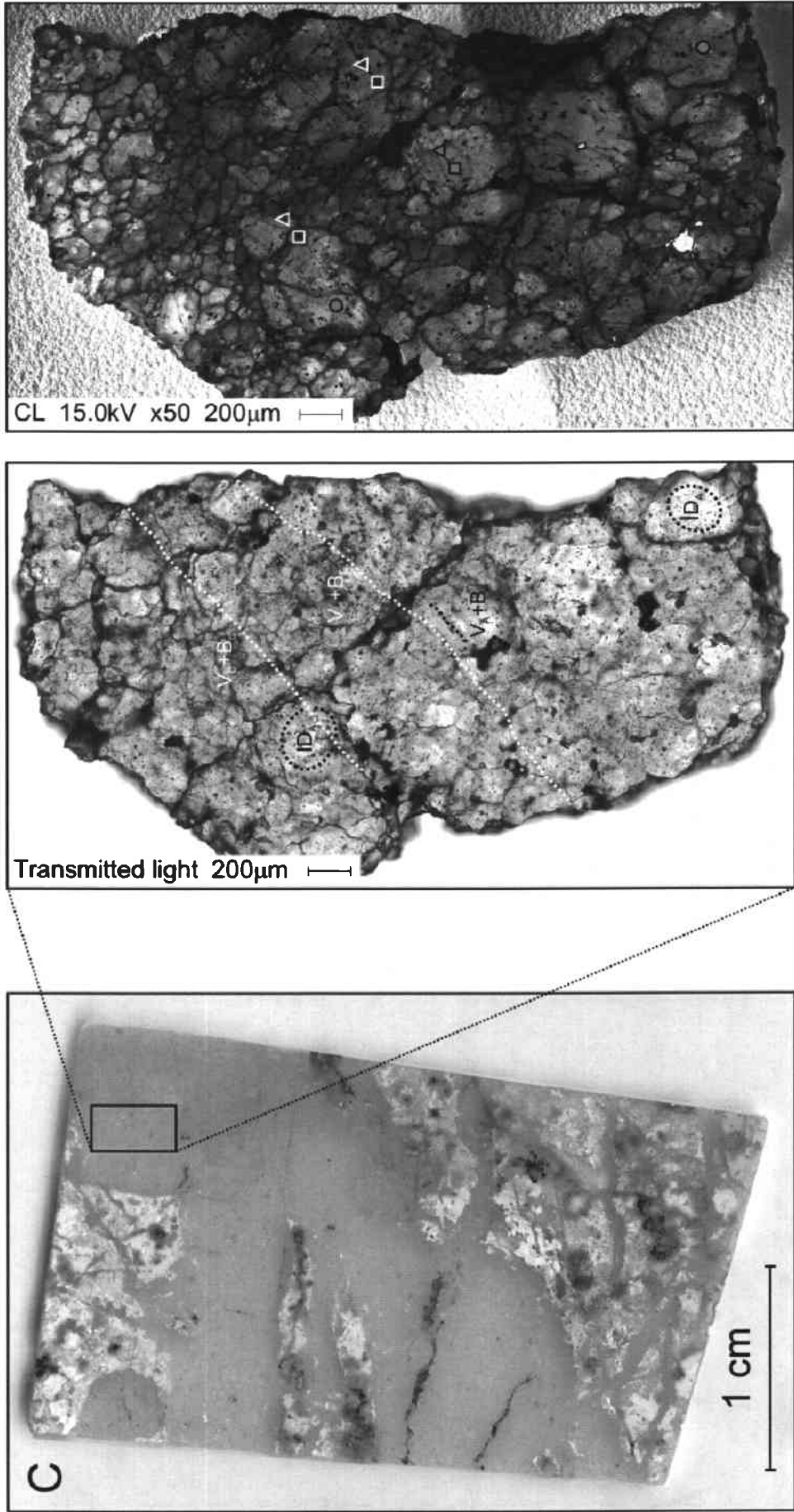
Figure 2 C: Sample FM-CH04-02: Photomicrographs of a dacitic porphyry from the La Estrechura area, which is pervasively silicified due to abundant quartz stockwork typical of the porphyry environment. However, the porphyritic texture of the igneous host rock is still recognizable, with quartz porphyroblasts reflecting recrystallization. Plagioclase phenocrysts are altered to a fine intergrowth of quartz, sericite, illite, and pyrite. Vein quartz is colorless and has an anhedral granular habit, as illustrated by transmitted-light microscopy. The CL petrography reveals two distinct quartz generations. The first one forms the bulk (about 80%) of the stockwork vein and exhibits a dull luminescence (CL-gray). By contrast, the second quartz generation has a dark CL color and occurs along grain boundaries or fills fractures that cut the older quartz generation.
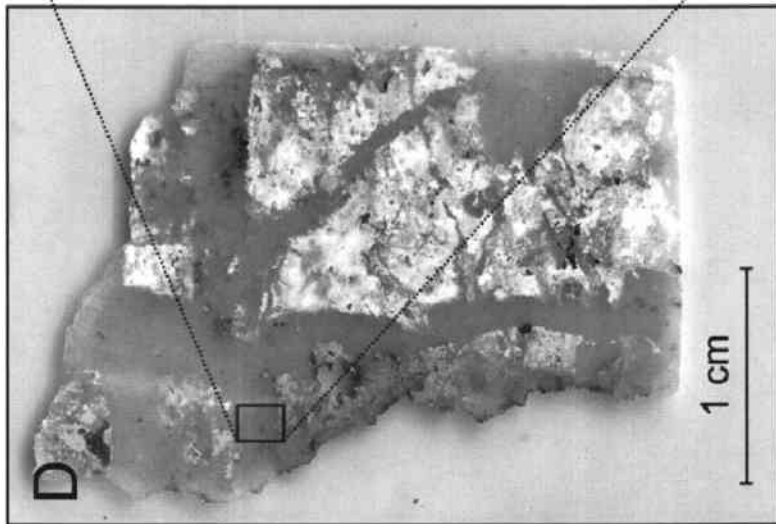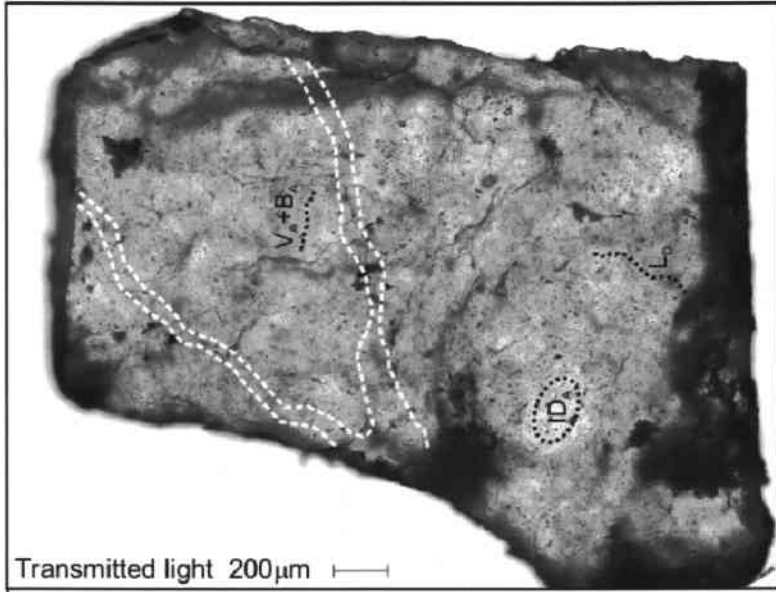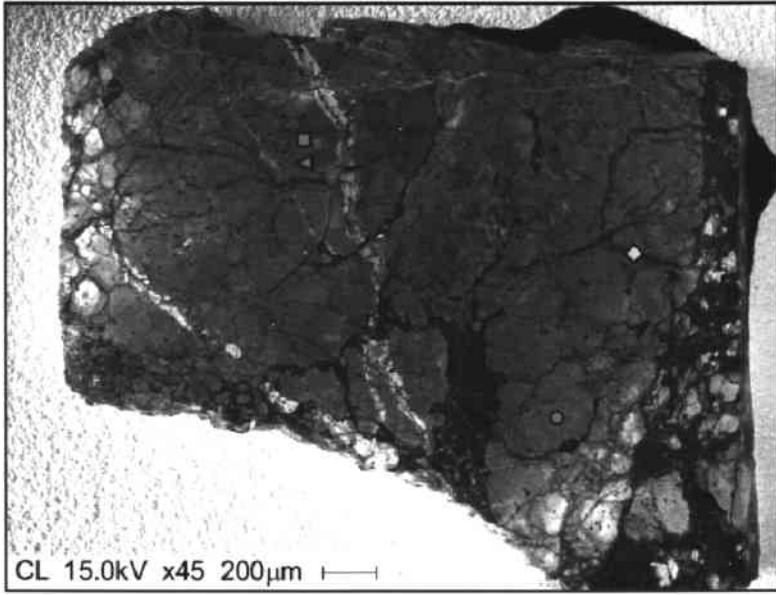
Figure 2 D: Sample FM-CP05-21: Photomicrographs of a pervasively altered dacitic porphyry from the La Estrechura area hosting multiple generations of irregular A-veinlets, which crosscut and off-set each other. Locally, supergene alteration minerals, such as jarosite and kaolinite, completely obliterate the original rock texture. Coarse-grained vein quartz has a characteristic vitreous luster and exhibits hematite staining. The CL image reveals three different stages of quartz formation. The one that forms the bulk of the vein (about 80%) is weakly zoned and has a gray CL color. The second quartz generation exhibits a bright luminescence and fills irregular fractures that cut the early quartz grains. The third generation of quartz has a very weak CL response and occurs as overgrowths or fills open vugs and microfractures.
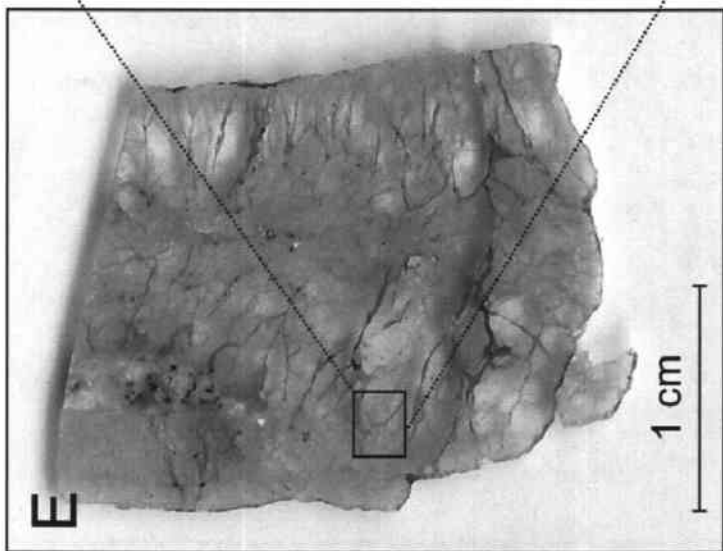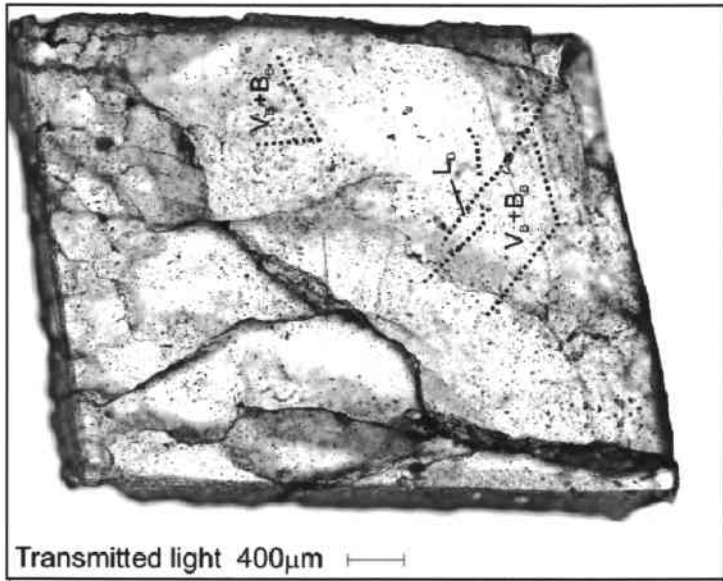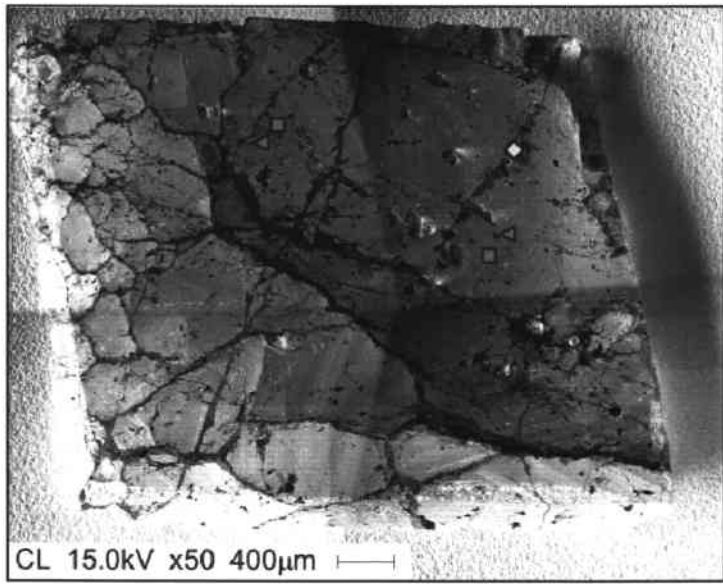
Figure 2 E: Sample FM-CP05-27: Photomicrographs of the porphyritic stock at Piedras Grandes representing a straight B-vein of 2 cm thickness composed of quartz, molybdenite, and minor chalcopyrite. Vein quartz is mostly granular, but grains oriented perpendicular to the vein walls occur as well. Vein centers are locally vuggy and filled with supergene alteration minerals, such as jarosite and limonite. Molybdenite and chalcopyrite are the dominant sulfides and occur mainly along fractures that cut the coarse-grained quartz vein. However, molybdenite inclusions in quartz are also common. Vein quartz is colorless and has a mottled texture related to numerous fluid inclusions. The CL image reveals two different generations of quartz. The first one shows a bright luminescence and oscillatory growth zoning. The second quartz has a dark CL color and fills open vugs or microfractures, which are associated with ore mineral precipitation.
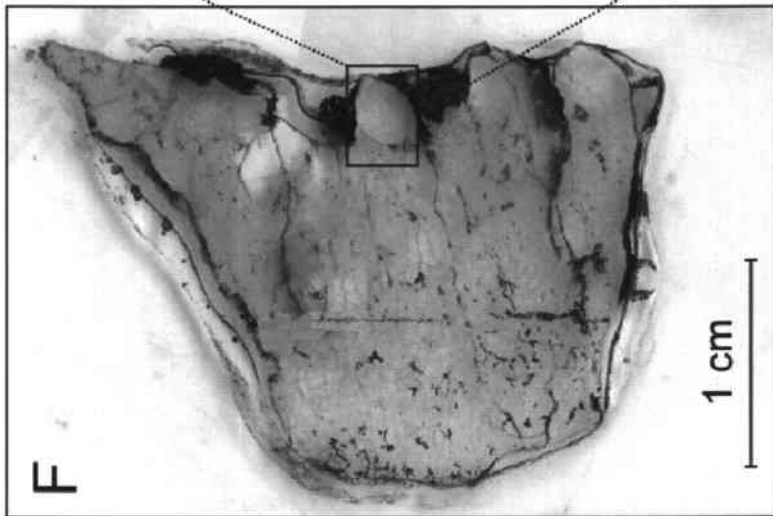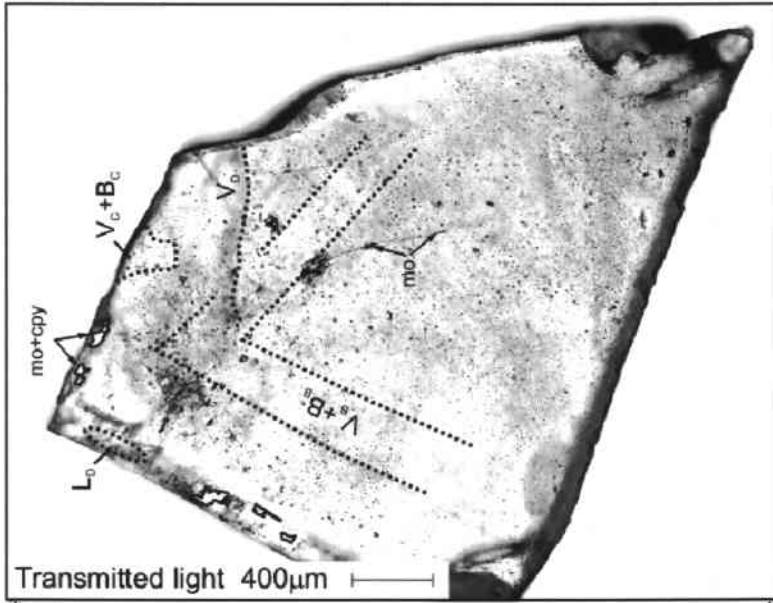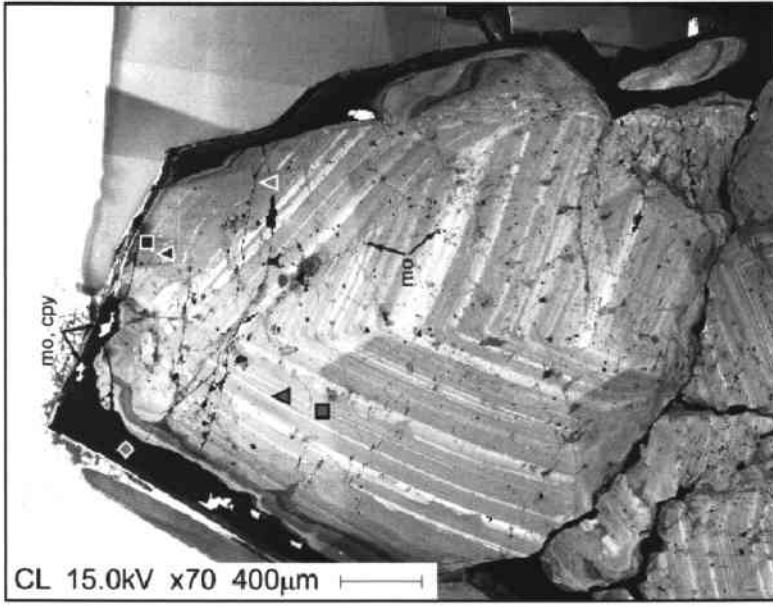
Figure 2 F: Sample FM-DB99-15: Euhedral quartz crystals in a straight B-vein hosted by a dacitic porphyry from the Piedras Grandes area representing the transition from potassic to sericitic alteration. Vein quartz is mostly granular and has a glassy to glassy-white color. Open spaces are commonly filled with supergene alteration minerals, such as hematite. Molybdenite (mo) and chalcopyrite (cpy) are the dominant sulfides and occur as solid inclusions in quartz (molybdenite) or along late fractures (molybdenite and chalcopyrite). Generally, sulfides are scarce but tend to be more abundant in the outermost part of the crystals. The CL image reveals three different generations of quartz. The first one shows a bright luminescence and is strongly zoned. The second generation of quartz has a weak CL response and occurs as overgrowths or fills microfractures that cut the first quartz generation. The third phase of quartz formation is characterized by a black CL color and commonly mantles the bulk of ore metals precipitated at the contact to the second quartz generation. This last stage of quartz formation has no internal structure and either forms the margin of euhedral crystals or fills late fractures that cut the coarse-grained vein.

Appendix figure 3: Petrography and SEM-CL textures in vein quartz of the transitional QSP stage
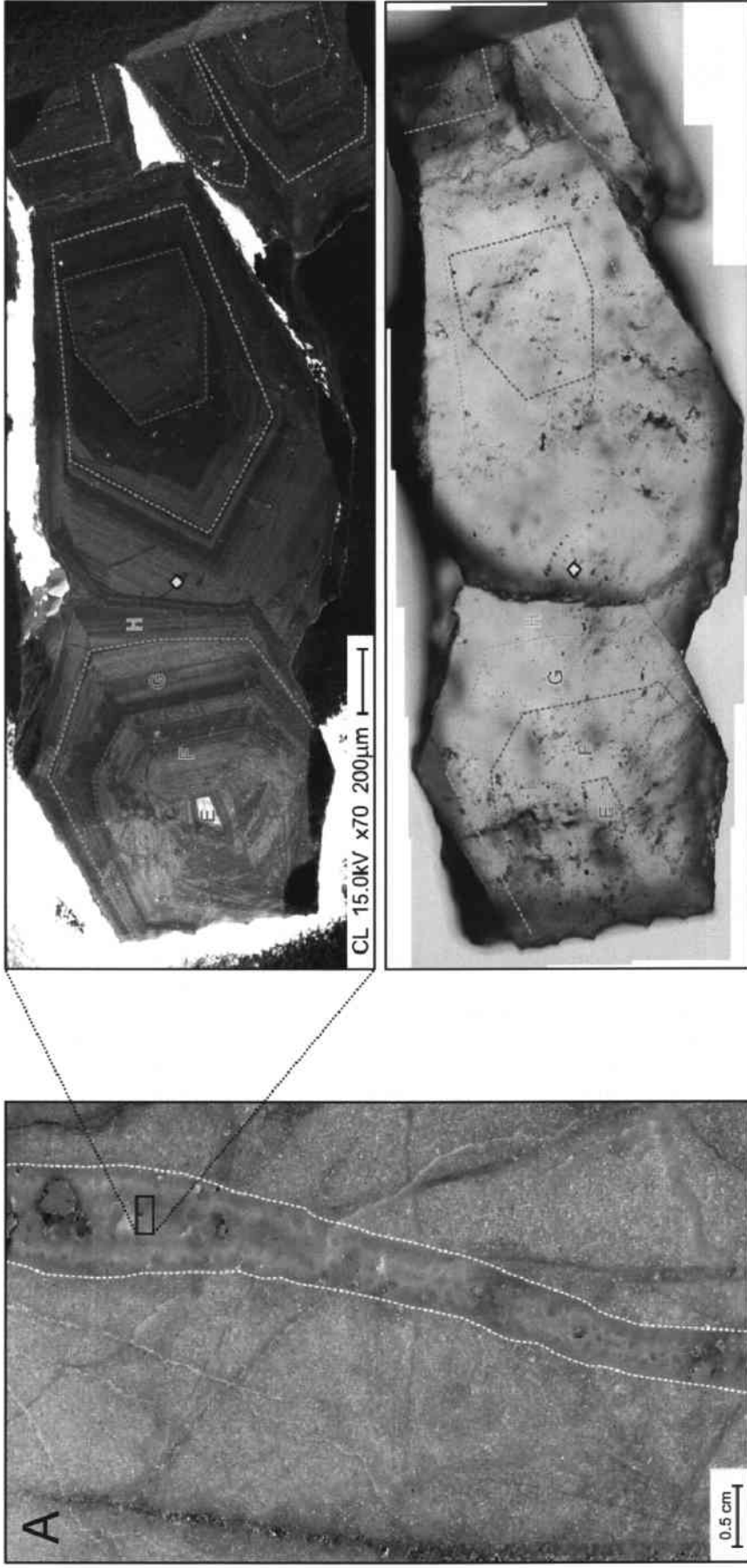
Figure 3: Images of selected QSP veins acquired by SEM-CL and optical microscopy. The dashed colored lines indicate the lower limit of each petrographic quartz stage outlined in chapter 7.3. Colored symbols indicate the approximate location of the fluid inclusion generations discussed in chapter 7.5. (A) Sample FM-CP05-06: Paragenetic sequence of a quartz-rich QSP vein hosted by Negro Peinado metasediments. Note the small rim of granular vein quartz in the photograph on the left hand side. This rim probably represents the oldest quartz generation, E, which is virtually absent in the images on the right hand side.
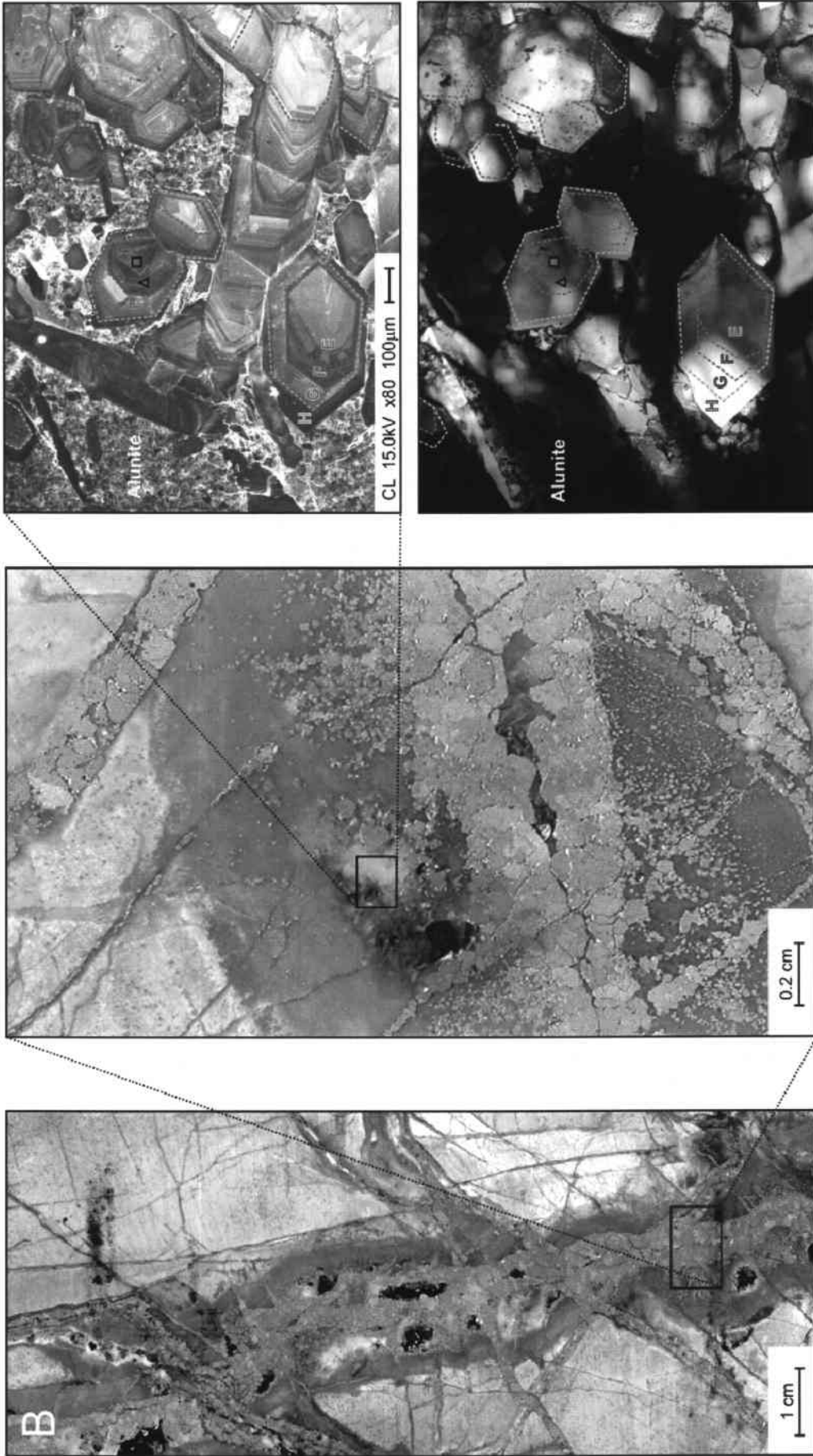
Figure 3 B: Sample FM-DH4-276.6: Paragenetic sequence of an irregular QSP vein hosted by fine-grained metasediments of the Negro Peinado Formation. Note the presence of high-sulfidation epithermal alunite, filling open spaces of the QSP assemblage. This alunite occurs as well-developed pseudo-cubic crystals, typical for the sedimentary host rock. Quartz is clear, with distinct growth zoning towards the vein centre. Fluid inclusions occur as dark spots within the quartz crystals and are clearly more abundant in the older quartz generations. Anhedral pyrite contains enargite/famatinite along microfractures.
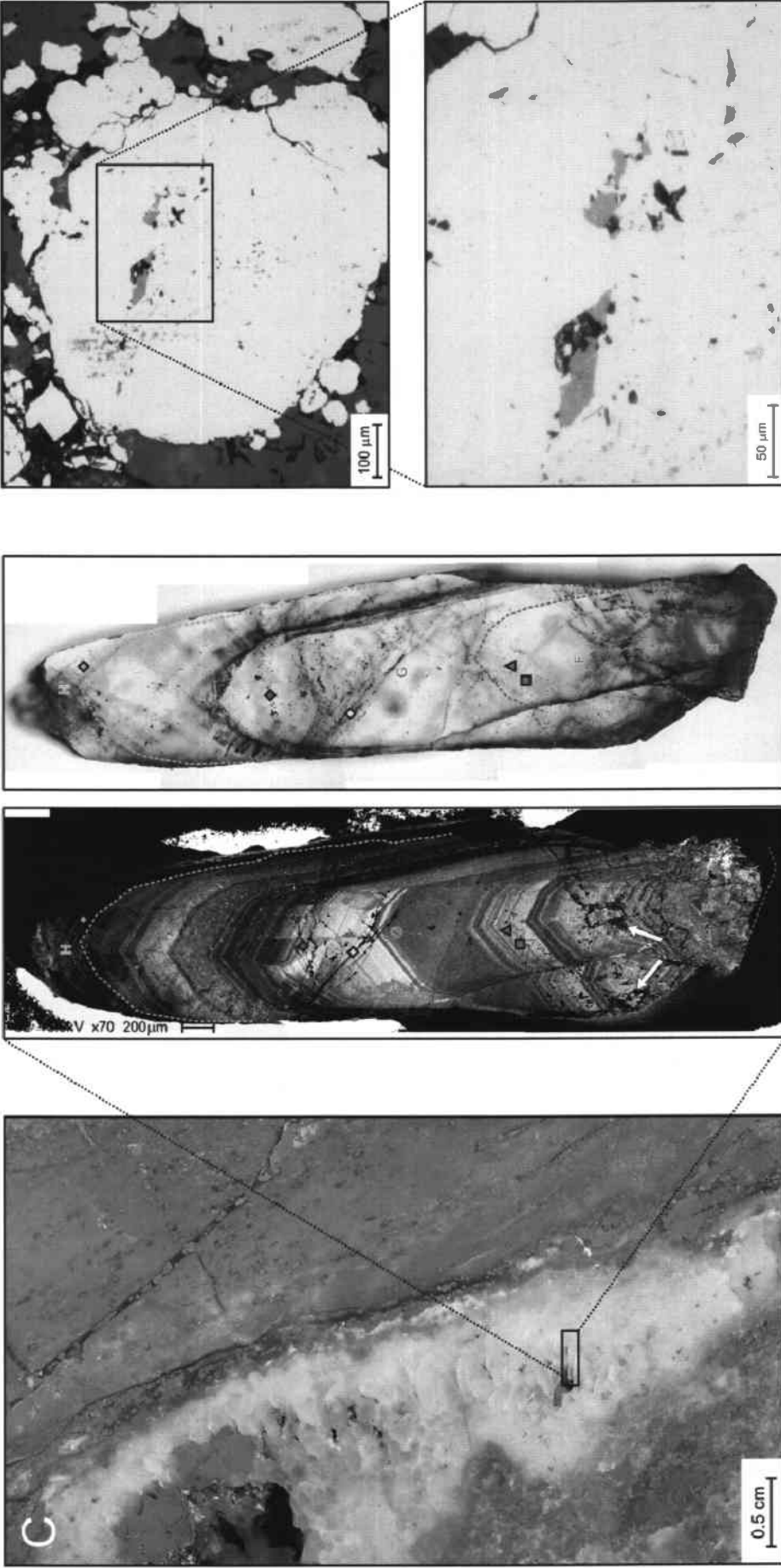
Figure 3 C: Sample FM-DH4-277.6: Euhedral quartz crystal from a QSP vein representing the internal paragenetic sequence revealed by SEM-CL. The fine-grained host rock consists of strongly altered metapelites of the Negro Peinado Formation. Note the abundance of dissolution textures in quartz F indicated by the white arrows. The transmitted-light photomicrograph highlights the importance of SEM-CL for petrographic interpretation. Reflected-light photomicrographs to the right show an anhedral pyrite grain illustrating the abundance of high-sulfidation ore minerals, in this case tennantite, which occur along microfractures.
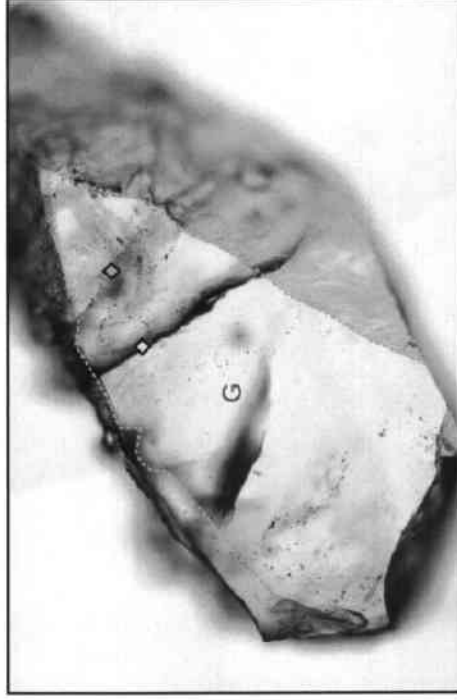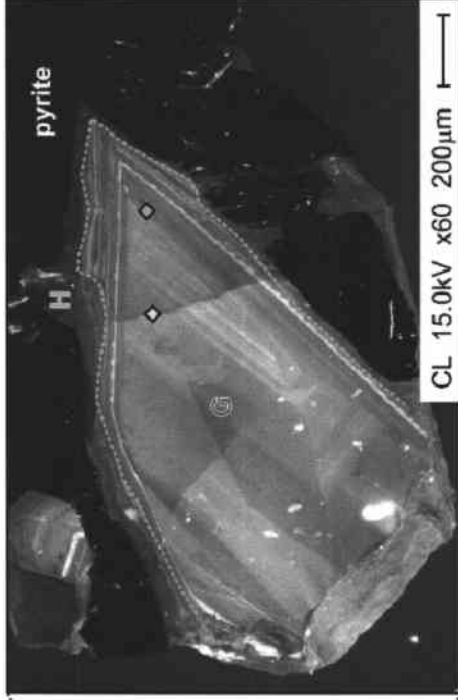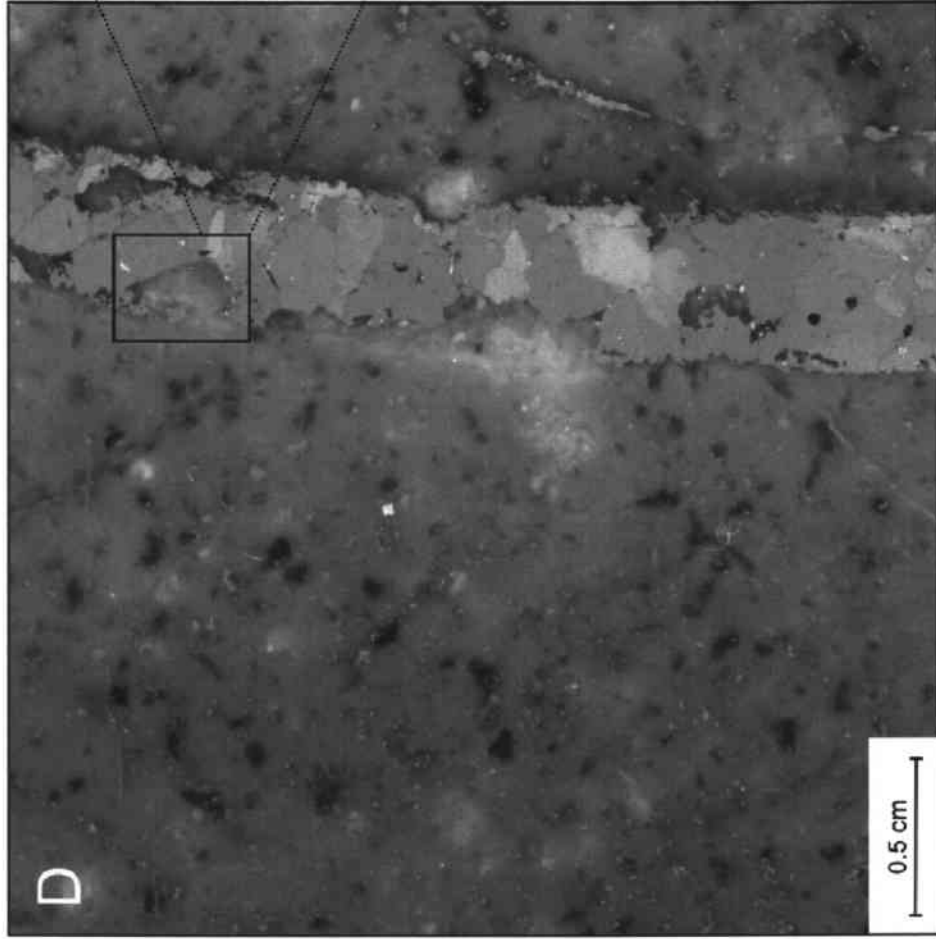
Figure 3 D: Sample FM-DH4-350.5: Pyrite-rich QSP vein that cuts through igneous rocks of the Mogote Formation, i.e. the dacitic dyke of La Mejicana. The paragenetic sequence of this sample is less complex due to the absence of the older quartz generations, E and F. The youngest quartz generation, H, clearly surrounds and truncates anhedral pyrite grains, which contain numerous high-sulfidation epithermal mineral assemblages, such as tennantite/tetrahedrite and enargite/famatinite. This textural evidence implies that precipitation of high-sulfidation epithermal mineral assemblages either occurred synchronous with or slightly after formation of this quartz type.
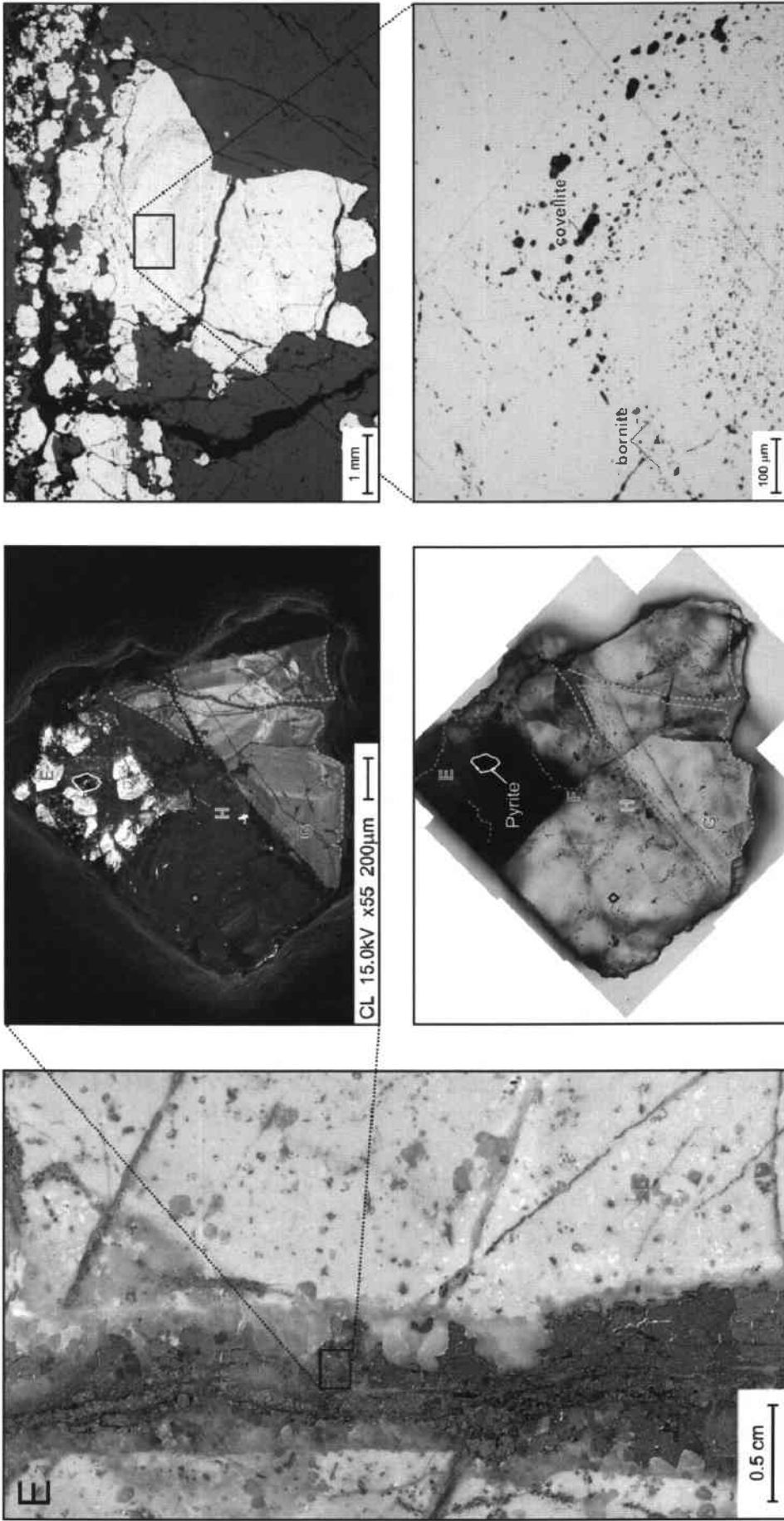
Figure 3 E: Sample FM-DH4-352.1: Paragenetic sequence of a straight QSP vein hosted by a porphyritic dacite of the Mogote Formation. Note the small sericitic alteration envelope related to this mineralization stage. The SEM-CL image reveals four successive quartz generations, E-H, with the youngest containing fragments of previously deposited pyrite. This dull-luminescent quartz fills fractures and open spaces, thereby truncating and partly replacing the older quartz generations. Solid inclusions, such as bornite and covellite, occur along growth zones in pyrite, as revealed by reflected-light microscopy (right). By contrast, high-sulfidation epithermal mineral assemblages, such as tennantite/tetrahedrite, are restricted to microfractures that cut the pyrite.
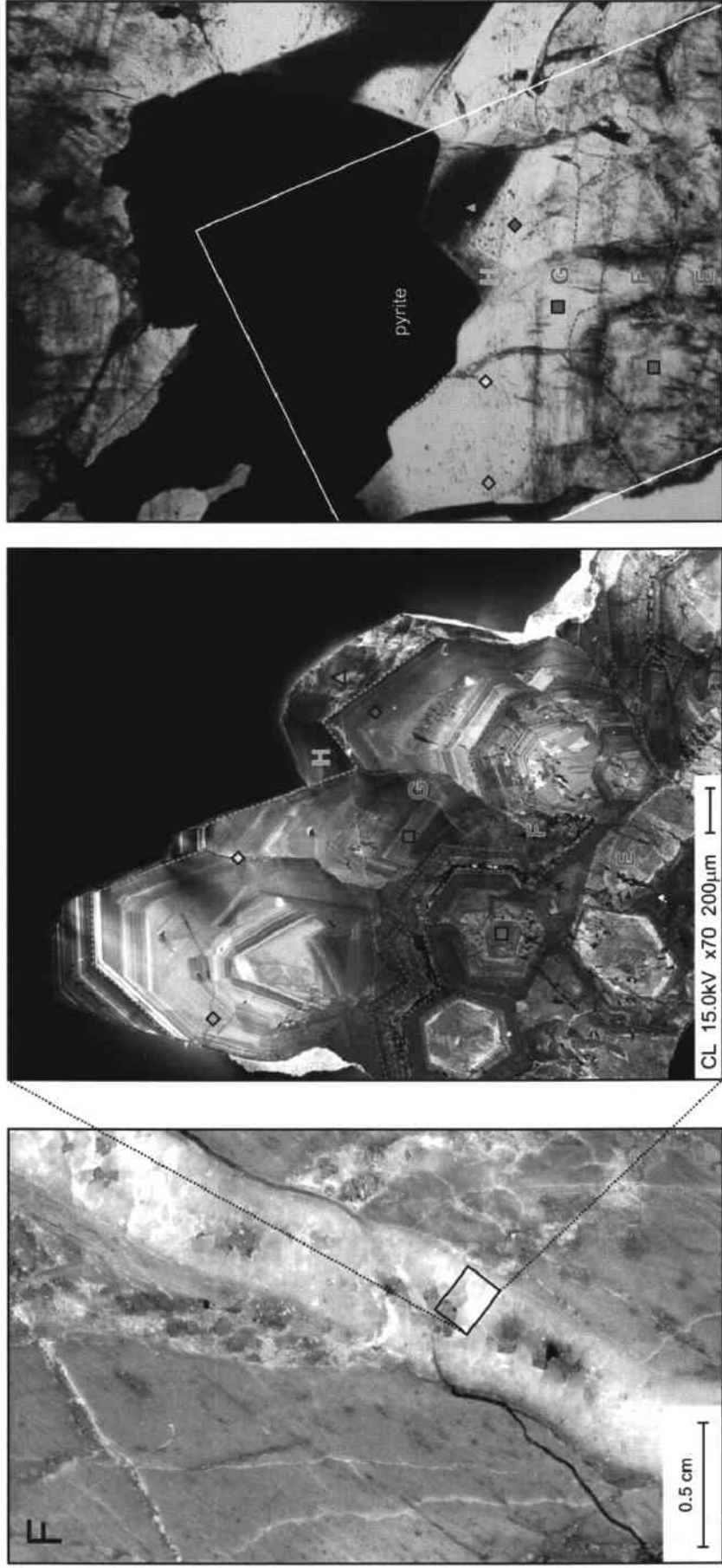
Figure 3 F: Sample FM-DH4-427.3: Petrography of a slightly irregular QSP vein hosted by strongly altered metasediments of the Negro Peinado Formation. The SEM-CL image reveals the (laterally reversed) succession of four different quartz generations from the rim towards the vein center. Pyrite either occurs as subhedral crystals filling open spaces or as anhedral grains along the vein margin. Quartz is the most abundant mineral phase and contains numerous fluid inclusion assemblages.

Appendix figure 4: Petrography of quartz-rich samples from the high-sulfidation epithermal stage
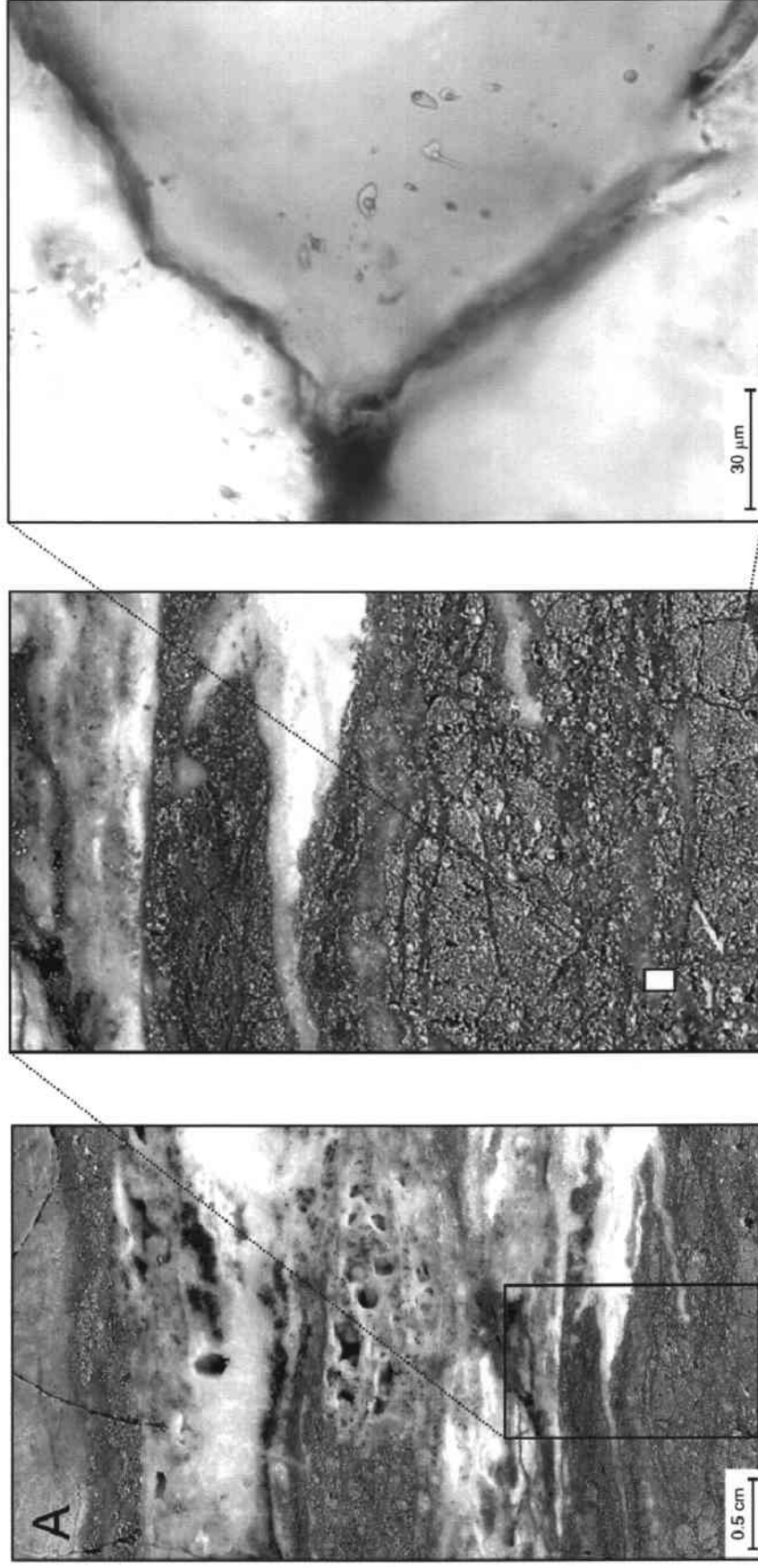
Figure 4 A: Sample FM-CP05-28: Petrography of an epithermal replacement vein representing the alunitic assemblage, including alunite, enargite, covellite, pyrite, and quartz. The fine-grained host rock consists of strongly altered metapelites of the Negro Peinado Formation. Quartz is commonly microcrystalline and lines open vugs. Euhedral quartz crystals are subordinate and contain aqueous inclusions of type L2$_J$, which may reach 10 µm in size and are sufficiently large to allow microthermometric investigations. SEM-CL on quartz was impossible to conduct due to the bright luminescence of the associated alunite.
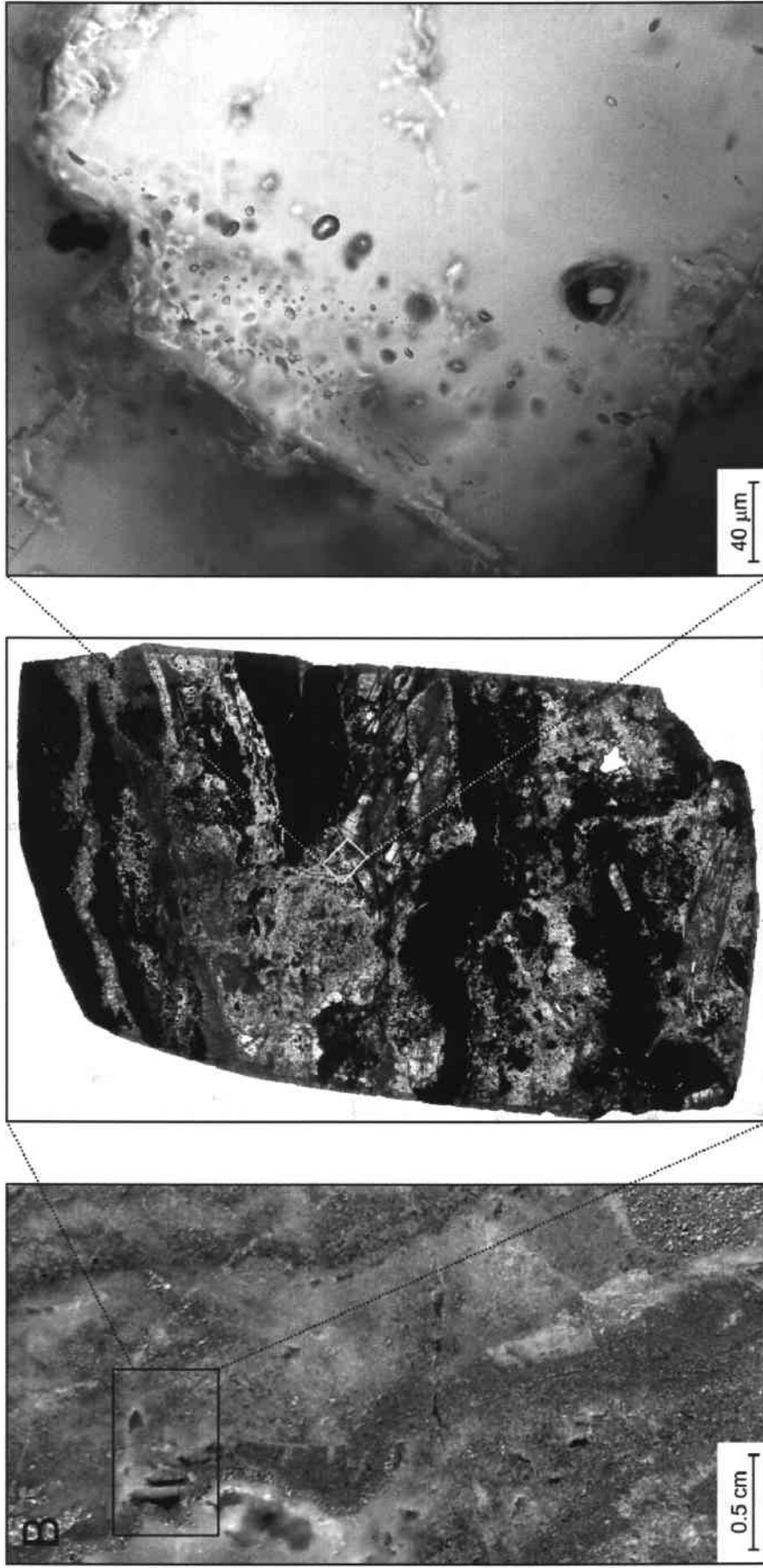
Figure 4 B: Sample FM-CP05-47: Petrography of an epithermal replacement vein representing the alunitic assemblage, including alunite, enargite, covellite, pyrite, and quartz. The fine-grained host rock consists of strongly altered metapelites of the Negro Peinado Formation. Quartz is commonly microcrystalline and lines open vugs. Minor barite forms euhedral crystals and is host for numerous vapor-rich inclusions, which occur along late growth zones or in fractures that cut through the mineral. Locally, they coexist with aqueous inclusions indicating phase separation at shallow levels. Microthermometry was impossible to conduct due to the poor visibility of the liquid phase, which occupies less than 5% of the inclusion volume.

Appendix table 2: Microthermometry of individual fluid inclusions from inclusion assemblages of the porphyry stage

sample	chip	Qtz	FI type	FI size	boil	Tm_{ice}	$Tm_{sylvite}$	Tm_{halite}	Th_{H2O}	Th_{total}	salinity	ph	ph-basis
FM-CP05-37	1	P	ID	20		-5.2				>600	8.1		
FM-CP05-37	1	P	ID	80		-0.9			462	462	1.6		
FM-CP05-37	1	P	ID	60		-6.2				>600	9.5		
FM-CP05-37	1	P	ID	70		-2.9				>600	4.8		
FM-CP05-37	1	P	ID	50		-2.5				>600	4.2		
FM-CP05-37	1	P	ID	80		-12.5				>600	16.4		
FM-CP05-37	1	P	ID	60		-3.3				>600	5.4		
FM-CP05-37	1	P	ID	50		-0.6			529	529	1.1		
FM-CP05-37	1	P	ID	32		-3.9				>600	6.3		
FM-CP05-37	1	P	ID	40		-1.4				>600	2.4		
FM-CP05-37	1	P	ID	50		-3.3				>600	5.4		
FM-CP05-37	1	P	ID	40		-2.8				>600	4.7		
average						**-3.8**			**496**	**496**	**5.8**	549	LV curve
stdev						*3.2*			*47*	*47*	*4.1*		
N						*12*			*2*	*2*	*12*		
FM-CP05-37	1	P	ID	8		-3.7				>600	6.0		
FM-CP05-37	1	P	ID	20		-3.4				>600	5.6		
FM-CP05-37	1	P	ID	20		-4.9				>600	7.7		
FM-CP05-37	1	P	ID	10		-4.2				>600	6.7		
FM-CP05-37	1	P	ID	8		-5.4				>600	8.4		
FM-CP05-37	1	P	ID	4		-4.3				>600	6.9		
FM-CP05-37	1	P	ID	8		-2.9				>600	4.8		
FM-CP05-37	1	P	ID	10		-3.8				>600	6.2		
FM-CP05-37	1	P	ID	20		-4.7				>600	7.5		
FM-CP05-37	1	P	ID	23		-2.8				>600	4.7		
average						**-4.0**				**>600**	**6.4**	>864	LV curve
stdev						*0.9*					*1.2*		
N						*10*				*10*	*10*		
FM-CP05-37	1	P	ID	30		-8.2				>600	11.9		
FM-CP05-37	1	P	ID	30		-16.6				>600	19.9		
FM-CP05-37	1	P	ID	32		-12.5				>600	16.4		
FM-CP05-37	1	P	ID	35		-14.5				>600	18.2		
FM-CP05-37	1	P	ID	30		-3.9				>600	5.7		
average						**-11.1**				**>600**	**14.4**	>912	LV curve
stdev						*5.1*					*5.7*		
N						*5*				*5*	*5*		
FM-CP05-37	2	P	ID	20		-10.3				>600	14.3		
FM-CP05-37	2	P	ID	22		-15.1				>600	18.7		
FM-CP05-37	2	P	ID	10		-20.0				>600	22.4		
average						**-15.1**				**>600**	**18.5**	>915	LV curve
stdev						*4.9*					*4.1*		
N						*3*				*3*	*3*		

sample	chip	Qtz	FI type	FI size	boil	Tm_{ice}	$Tm_{sylvite}$	Tm_{halite}	Th_{H2O}	Th_{total}	salinity	ph	ph-basis
FM-CP05-34	1	P	ID	12					539	539			
FM-CP05-34	1	P	ID	15		-6.8			418	418	10.2		
FM-CP05-34	1	P	ID	25		-7.9			424	424	11.6		
FM-CP05-34	1	P	ID	18		-8.0			463	463	11.7		
average						**-7.6**			**461**	**461**	**11.2**	451	LV curve
stdev						*0.7*			*56*	*56*	*0.8*		
N						*3*			*4*	*4*	*3*		
FM-CP05-21	1	A	ID	15		-9.7			412	412	13.6		
FM-CP05-21	1	A	ID	15		-21.3			400	400	23.2		
FM-CP05-21	1	A	ID	25		-6.3			419	419	9.6		
FM-CP05-21	1	A	ID	15		-13.2			384	384	17.1		
FM-CP05-21	1	A	ID	20		-6.7			424	424	10.1		
average						**-11.4**			**408**	**408**	**14.7**	278	LV curve
stdev						*6.2*			*16*	*16*	*5.6*		
N						*5*			*5*	*5*	*5*		
FM-CP05-21	2	A	ID	10		-6.1			423	423	9.3		
FM-CP05-21	2	A	ID	10		-8.7			385	385	12.5		
FM-CP05-21	2	A	ID	15		-9.9			392	392	13.8		
FM-CP05-21	2	A	ID	20		-8.3			486	486	12.1		
FM-CP05-21	2	A	ID	30		-9.5			408	408	13.4		
FM-CP05-21	2	A	ID	40		-12.2			456	456	16.2		
FM-CP05-21	2	A	ID	10		-7.4			421	421	11.0		
FM-CP05-21	2	A	ID	15		-7.3			382	382	10.9		
average						**-8.7**			**419**	**419**	**12.4**	314	LV curve
stdev						*1.9*			*36*	*36*	*2.1*		
N						*8*			*8*	*8*	*8*		
FM-CP05-21	2	A	ID	15		-7.9				>600	11.6		
FM-CP05-21	2	A	ID	15		-8.0				>600	11.7		
average						**-8.0**				**>600**	**11.6**	>901	LV curve
stdev						*0.1*					*0.1*		
N						*2*				*2*	*2*		
FM-CP05-21	2	A	ID	40		-13.4			571	571	17.3		
FM-CP05-21	2	A	ID	30		-11.3				>600	15.3		
average						**-12.4**			**571**	**571**	**16.3**	820	LV curve
stdev						*1.5*					*1.4*		
N						*2*			*1*	*1*	*2*		
FM-CH04-02	1	A	ID	15					574	574			
FM-CH04-02	1	A	ID	20		-20.3				>600	22.6		
FM-CH04-02	1	A	ID	32		-6.7				>600	10.1		
FM-CH04-02	1	A	ID	15		-10.3				>600	14.3		
FM-CH04-02	1	A	ID	20		-4.9				>600	7.7		
FM-CH04-02	1	A	ID	18		-1.2			485	485	2.1		
FM-CH04-02	1	A	ID	15		-14.3			449	449	18.0		
FM-CH04-02	1	A	ID	25		-19.8				>600	22.2		
FM-CH04-02	1	A	ID	22		-14.8				>600	18.5		
average						**-11.5**			**503**	**503**	**14.4**	588	LV curve
stdev						*7.0*			*65*	*65*	*7.3*		
N						*8*			*3*	*3*	*8*		

sample	chip	Qtz	Fl type	Fl size	boil	Tm_{ice}	$Tm_{sylvite}$	Tm_{halite}	Th_{H2O}	Th_{total}	salinity	ph	ph-basis
FM-CP05-37	1	A	ID	15		-2.0				>600	3.4		
FM-CP05-37	1	A	ID	22		-1.6				>600	2.7		
FM-CP05-37	1	A	ID	25		-2.0				>600	3.4		
FM-CP05-37	1	A	ID	22		-2.5				>600	4.2		
FM-CP05-37	1	A	ID	10		-0.7				>600	1.2		
average						**-1.8**				**>600**	**3.0**	>805	LV curve
stdev						*0.7*					*1.1*		
N						*5*				*5*	*5*		
FM-CP05-37	2	A	ID	20		-2.6			487	487	4.3		
FM-CP05-37	2	A	ID	17		-4.4			473	473	7.0		
FM-CP05-37	2	A	ID	20		-3.9			463	463	6.3		
FM-CP05-37	2	A	ID	22		-3.8			508	508	6.2		
FM-CP05-37	2	A	ID	30		-3.2			497	497	5.3		
FM-CP05-37	2	A	ID	30		-3.8			513	513	6.2		
FM-CP05-37	2	A	ID	15		-4.1			543	543	6.6		
average						**-3.7**			**498**	**498**	**6.0**	556	LV curve
stdev						*0.6*			*27*	*27*	*0.9*		
N						*7*			*7*	*7*	*7*		
FM-CP05-37	2	A	ID	60		-3.2			508	508	5.3		
FM-CP05-37	2	A	ID	90		-1.8			529	529	3.1		
FM-CP05-37	2	A	ID	80		-1.6			529	529	2.7		
FM-CP05-37	2	A	ID	45		-5.3			558	558	8.3		
average						**-3.0**			**531**	**531**	**4.8**	645	LV curve
stdev						*1.7*			*21*	*21*	*2.6*		
N						*4*			*4*	*4*	*4*		
FM-DB99-15	1	A	B	25			125	534		>600	64.5		
FM-DB99-15	1	A	B	30			110	542		>600	65.6		
FM-DB99-15	1	A	B	35			123	528		>600	63.6		
FM-DB99-15	1	A	B	25			105	533		>600	64.3		
FM-DB99-15	1	A	B	30			112	531		>600	64.0		
average							**115**	**534**		**>600**	**64.4**	>512	LV curve
stdev							*8.6*	*5*			*0.7*		
N							*5*	*5*		*5*	*5*		
FM-CP05-27	1	B	B	20			126	381	593	593	45.4		
FM-CP05-27	1	B	B	25				451			53.4		
FM-CP05-27	1	B	B	10				448			53.0		
FM-CP05-27	1	B	B	30				453	485	485	53.6		
FM-CP05-27	1	B	B	15				488			58.1		
FM-CP05-27	1	B	B	25				420			49.7		
FM-CP05-27	1	B	B	20			281	350			42.4		
FM-CP05-27	1	B	B	20				445			52.7		
FM-CP05-27	1	B	B	18			201	456			54.0		
FM-CP05-27	1	B	B	40			184	492	549	549	58.7		
FM-CP05-27	1	B	B	50				498	510	510	59.5		
FM-CP05-27	1	B	B	25			264	445			52.7		
FM-CP05-27	1	B	B	40				351	460	460	42.5		
FM-CP05-27	1	B	B	20			172	499	468	499	59.6		
FM-CP05-27	1	B	B	20			201	502	459	502	60.0		
FM-CP05-27	1	B	B	35			245	482	471	482	57.4		

sample	chip	Qtz	FI type	FI size	boil	Tm$_{ice}$	Tm$_{sylvite}$	Tm$_{halite}$	Th$_{H2O}$	Th$_{total}$	salinity	ph	ph-basis
FM-CP05-27	1	B	B	25			168	513	471	513	61.5		
FM-CP05-27	1	B	B	30			230	478	459	478	56.8		
FM-CP05-27	1	B	B	25			201		461	461			
average							**207**	**453**	**490**	**503**	**53.8**	342	LV curve
stdev							*46*	*50*	*44*	*39*	*6.5*		
N							*11*	*18*	*11*	*11*	*14*		
FM-CP05-27	1	B	B	15				495	436	495	59.1		
FM-CP05-27	1	B	B	15				499	448	499	59.6		
FM-CP05-27	1	B	B	15				487	409	487	58.0		
FM-CP05-27	1	B	B	30				492	487	492	58.7		
FM-CP05-27	1	B	B	35				488	491	491	58.1		
FM-CP05-27	1	B	B	25				492	458	492	58.7		
FM-CP05-27	1	B	B	30				488	443	488	58.1		
FM-CP05-27	1	B	B	20				470			55.8		
FM-CP05-27	1	B	B	25				489	460	489	58.3		
FM-CP05-27	1	B	B	20				487	443	487	58.0		
FM-CP05-27	1	B	B	20				487	437	487	58.0		
FM-CP05-27	1	B	B	25			170	·450	469	469	53.3		
FM-CP05-27	1	B	B	25				487			58.0		
FM-CP05-27	1	B	B	18				495	520	520	59.1		
FM-CP05-27	1	B	B	25				470	455	470	55.8		
FM-CP05-27	1	B	B	30				501	450	501	59.9		
average							**170**	**486**	**458**	**491**	**57.9**	303	LV curve
stdev								*13*	*28*	*12*	*1.7*		
N							*1*	*16*	*14*	*14*	*16*		
FM-DB99-15	2	C	B	18									
FM-DB99-15	2	C	B	15									
FM-DB99-15	2	C	B	30				383	461	461	45.6		
FM-DB99-15	2	C	B	30				394	470	470	46.8		
FM-DB99-15	2	C	B	15				380	468	468	45.3		
FM-DB99-15	2	C	B	45				387	464	464	46.1		
FM-DB99-15	2	C	B	20				382	421	421	45.5		
FM-DB99-15	2	C	B	53				369	473	473	44.2		
FM-DB99-15	2	C	B	25				382	428	428	45.5		
FM-DB99-15	2	C	B	18				391	449	449	46.5		
FM-DB99-15	2	C	B	15				385	447	447	45.9		
FM-DB99-15	2	C	B	20				377	460	460	45.0		
FM-DB99-15	2	C	B	15				377	440	440	45.0		
FM-DB99-15	2	C	B	25				374	476	476	44.7		
FM-DB99-15	2	C	B	30				382	489	489	45.5		
FM-DB99-15	2	C	B	20				398	426	426	47.2		
average								**383**	**455**	**455**	**45.6**	300	LV curve
stdev								*8*	*21*	*21*	*0.8*		
N								*14*	*14*	*14*	*14*		

sample	chip	Qtz	FI type	FI size	boil	Tm_{ice}	$Tm_{sylvite}$	Tm_{halite}	Th_{H2O}	Th_{total}	salinity	ph	ph-basis
FM-DB99-15	1	C	B	10				403	588	588	47.8		
FM-DB99-15	1	C	B	10				425	556	556	50.3		
FM-DB99-15	1	C	B	8				383			45.6		
FM-DB99-15	1	C	B	10				385	513	513	45.9		
FM-DB99-15	1	C	B	8				385			45.9		
average								**396**	**552**	**552**	**47.1**	570	LV curve
stdev								*18*	*38*	*38*	*2.0*		
N								*5*	*3*	*3*	*5*		
FM-DB99-15	2	C	B	15	X			311	488	488	39.0		
FM-DB99-15	2	C	B	18	X			158	457	457	30.0		
FM-DB99-15	2	C	B	18	X				586	586			
FM-DB99-15	2	C	B	20	X				588	588			
FM-DB99-15	2	C	B	25	X			178	502	502	30.8		
FM-DB99-15	2	C	B	15	X			374	475	475	44.7		
FM-DB99-15	2	C	B	15	X			394	463	463	46.8		
FM-DB99-15	2	C	B	20	X			244	564	564	34.3		
average								**277**	**515**	**515**	**37.6**	531	LV curve
stdev								*99*	*55*	*55*	*7.1*		
N								*6*	*8*	*8*	*6*		
FM-CP05-21	1	A	V	10		-2.0				>600	3.4		
FM-CP05-21	1	A	V	10						>600			
FM-CP05-21	1	A	V	15						>600			
FM-CP05-21	1	A	V	13						>600			
FM-CP05-21	1	A	V	10						>600			
FM-CP05-21	1	A	V	12						>600			
FM-CP05-21	1	A	V	13						>600			
FM-CP05-21	1	A	V	12						>600			
FM-CP05-21	1	A	V	8						>600			
FM-CP05-21	1	A	V	10						>600			
average						**-2.0**				**>600**	**3.4**	>816	LV curve
stdev													
N						*1.0*				*10*	*1*		
FM-CP05-34	1	A	V	15						>600			
FM-CP05-34	1	A	V	35						>600			
FM-CP05-34	1	A	V	25						>600			
FM-CP05-34	1	A	V	30						>600			
FM-CP05-34	1	A	V	20		-1.2				>600	2.1		
FM-CP05-34	1	A	V	20		-1.1				>600	1.9		
FM-CP05-34	1	A	V	15		-1.2				>600	2.1		
FM-CP05-34	1	A	V	30		-0.9				>600	1.6		
average						**-1.1**				**>600**	**1.9**	>762	LV curve
stdev						*0.1*					*0.2*		
N						*4*				*8*	*4*		

sample	chip	Qtz	FI type	FI size	boil	Tm_{ice}	$Tm_{sylvite}$	Tm_{halite}	Th_{H2O}	Th_{total}	salinity	ph	ph-basis
FM-CP05-37	2	A	V	40		-2.3				>600	3.9		
FM-CP05-37	2	A	V	15		-2.2				>600	3.7		
FM-CP05-37	2	A	V	30		-3.2					5.3		
FM-CP05-37	2	A	V	40		-1.8					3.1		
FM-CP05-37	2	A	V	35		-1.6					2.7		
average						**-2.2**				**>600**	**3.7**	>824	LV curve
stdev						*0.6*					*1.0*		
N						*5*				*2*	*5*		
FM-CP05-37	1	A	V	20		-1.2				>600	2.1		
FM-CP05-37	1	A	V	30		-0.9				>600	1.6		
average						**-1.1**				**>600**	**1.8**	>757	LV curve
stdev						*0.2*					*0.4*		
N						*2*				*2*	*2*		
FM-CP05-27	1	B	V	30		-9.7					13.6		
FM-CP05-27	1	B	V	40		-12.5					16.4		
FM-CP05-27	1	B	V	30		-7.6					11.2		
FM-CP05-27	1	B	V	22		-5.8					9.0		
FM-CP05-27	1	B	V	45		-9.8					13.7		
FM-CP05-27	1	B	V	18		-4.0					6.5		
average						**-8.2**					**11.7**		
stdev						*3.1*					*3.6*		
N						*6*					*6*		
FM-CP05-27	1	B	V	25		-11.3					15.3		
FM-CP05-27	1	B	V	15		-12.6					16.5		
FM-CP05-27	1	B	V	25		-11.0					15.0		
FM-CP05-27	1	B	V	15		-7.0					10.5		
FM-CP05-27	1	B	V	40		-7.4					11.0		
FM-CP05-27	1	B	V	50		-5.8					9.0		
FM-CP05-27	1	B	V	25		-5.1					8.0		
FM-CP05-27	1	B	V	10		-10.6					14.6		
FM-CP05-27	1	B	V	30		-11.8					15.8		
average						**-9.2**					**12.8**		
stdev						*2.8*					*3.2*		
N						*9*					*9*		
FM-DB99-15	1	C	V	15		-3.0					5.0		
FM-DB99-15	1	C	V	18		-3.2					5.3		
FM-DB99-15	1	C	V	12		-2.9					4.8		
FM-DB99-15	1	C	V	18		-3.0					5.0		
FM-DB99-15	1	C	V	15		-2.9					4.8		
average						**-3.0**					**5.0**		
stdev						*0.1*					*0.2*		
N						*5*					*5*		
FM-DB99-15	2	C	V	15		-1.9					3.2		
FM-DB99-15	2	C	V	10		-1.9					3.2		
FM-DB99-15	2	C	V	10		-1.8					3.1		
average						**-1.9**					**3.2**		
stdev						*0.1*					*0.1*		
N						*3*					*3*		

sample	chip	Qtz	Fl type	Fl size	boil	Tm$_{ice}$	Tm$_{sylvite}$	Tm$_{halite}$	Th$_{H2O}$	Th$_{total}$	salinity	ph	ph-basis
FM-DB99-15	2	C	V	30	X	-1.8					3.1		
FM-DB99-15	2	C	V	20	X	-1.8					3.1		
FM-DB99-15	2	C	V	30	X	-1.9					3.2		
average						**-1.8**					**3.1**		
stdev						*0.1*					*0.1*		
N						*3*					*3*		
FM-DB99-15	2	D	V	15					329	329			
FM-DB99-15	2	D	V	10					334	334			
FM-DB99-15	2	D	V	20					341	341			
average									**335**	**335**			
stdev									*6*	*6*			
N									*3*	*3*			
FM-DB99-15	1	D	V	12		-1.8			350	350	3.1		
FM-DB99-15	1	D	V	10		-2.2			348	348	3.7		
FM-DB99-15	1	D	V	7					365	365			
FM-DB99-15	1	D	V	5		-1.8			373	373	3.1		
FM-DB99-15	1	D	V	12		-1.5			350	350	2.6		
average						**-1.8**			**357**	**357**	**3.1**	176	LV curve
stdev						*0.3*			*11*	*11*	*0.5*		
N						*4*			*5*	*5*	*4*		
FM-CP05-27	1	D	L	15		-1.0			238	238	1.7		
FM-CP05-27	1	D	L	20		-1.1			231	231	1.9		
FM-CP05-27	1	D	L	30		-0.6			210	210	1.1		
FM-CP05-27	1	D	L	40		-0.9			229	229	1.6		
FM-CP05-27	1	D	L	30		-1.3			243	243	2.2		
FM-CP05-27	1	D	L	40		-1.3			239	239	2.2		
average						**-1.0**			**232**	**232**	**1.8**	28	LV curve
stdev						*0.3*			*12*	*12*	*0.5*		
N						*6*			*6*	*6*	*6*		
FM-CP05-27	1	D	L	10		-4.1			383	383	6.6		
FM-CP05-27	1	D	L	15		-10.6			232	232	14.6		
FM-CP05-27	1	D	L	70		-1.9			238	238	3.2		
FM-CP05-27	1	D	L	50		-1.2			245	245	2.1		
FM-CP05-27	1	D	L	30		-2.2			241	241	3.7		
FM-CP05-27	1	D	L	40		-10.8			425	425	14.8		
FM-CP05-27	1	D	L	30		-10.6					14.6		
FM-CP05-27	1	D	L	20		-8.9					12.7		
FM-CP05-27	1	D	L	25		-0.9					1.6		
FM-CP05-27	1	D	L	20		-2.5					4.2		
FM-CP05-27	1	D	L	10		-4.5					7.2		
average						**-5.3**			**294**	**294**	**7.7**	75	LV curve
stdev						*4.1*			*86*	*86*	*5.4*		
N						*11*			*6*	*6*	*11*		

sample	chip	Qtz	Fl type	Fl size	boil	Tm_{ice}	$Tm_{sylvite}$	Tm_{halite}	Th_{H2O}	Th_{total}	salinity	ph	ph-basis
FM-CP05-27	1	D	L	40		-13.9			238	238	17.7		
FM-CP05-27	1	D	L	35		-7.9			235	235	11.6		
FM-CP05-27	1	D	L	25		-3.5					5.7		
FM-CP05-27	1	D	L	12		-2.5			259	259	4.2		
FM-CP05-27	1	D	L	10		-6.5			244	244	9.9		
FM-CP05-27	1	D	L	20		-3.7			228	228	6.0		
FM-CP05-27	1	D	L	15		-3.8			232	232	6.2		
average						**-6.0**			**239**	**239**	**8.7**	31	LV curve
stdev						*4.0*			*11*	*11*	*4.7*		
N						*7*			*6*	*6*	*7*		
FM-CP05-27	1	D	L	15		-0.9			236	236	1.6		
FM-CP05-27	1	D	L	20		-1.0			231	231	1.7		
FM-CP05-27	1	D	L	40		-1.9			218	218	3.2		
FM-CP05-27	1	D	L	15		-1.0			224	224	1.7		
average						**-1.2**			**227**	**227**	**2.1**	26	LV curve
stdev						*0.5*			*8*	*8*	*0.8*		
N						*4*			*4*	*4*	*4*		
FM-CP05-27	1	D	L	35		-10.5					14.5		
FM-CP05-27	1	D	L	10		-3.3					5.4		
FM-CP05-27	1	D	L	40		-21.4					23.3		
FM-CP05-27	1	D	L	10		-4.5					7.2		
average						**-9.9**					**12.6**		
stdev						*8.3*					*8.2*		
N						*4*					*4*		
FM-CP05-21	1	D	L	30		-2.0			217	217	3.4		
FM-CP05-21	1	D	L	15		-1.6			217	217	2.7		
FM-CP05-21	1	D	L	15		-1.9			224	224	3.2		
FM-CP05-21	1	D	L	35		-4.6			214	214	7.3		
FM-CP05-21	1	D	L	30					212	212			
FM-CP05-21	1	D	L	40					215	215			
FM-CP05-21	1	D	L	25					234	234			
average						**-2.5**			**219**	**219**	**4.2**	22	LV curve
stdev						*1.4*			*8*	*8*	*2.1*		
N						*4*			*7*	*7*	*4*		
FM-CP05-34	1	D	L	33		-3.5			274	274	5.7		
FM-CP05-34	1	D	L	30		-6.1			256	256	9.3		
average						**-4.8**			**265**	**265**	**7.5**	48	LV curve
stdev						*1.8*			*12*	*12*	*2.6*		
N						*2*			*2*	*2*	*2*		
FM-CP05-37	1	D	L	15		-6.5			269	269	9.9		
FM-CP05-37	1	D	L	15		-6.6			276	276	10.0		
FM-CP05-37	1	D	L	17		-3.6			291	291	5.9		
FM-CP05-37	1	D	L	10		-3.4			308	308	5.6		
FM-CP05-37	1	D	L	17		-3.3			282	282	5.4		
FM-CP05-37	1	D	L	10		-4.0			241	241	6.5		
average						**-4.6**			**278**	**278**	**7.2**	59	LV curve
stdev						*1.6*			*23*	*23*	*2.1*		
N						*6*			*6*	*6*	*6*		

Appendix table 3: Microthermometry of individual fluid inclusions from inclusion assemblages of the QSP stage

sample	chip	Qtz	Fl type	Fl size	boil	Tm$_{ice}$	Tm$_{clathrate}$	Tm$_{halite}$	Th$_{H2O}$	salinity	ph	ph-basis
FM-DH4-427.3	2-11	H	L2	20		-0.9			226	1.6		
FM-DH4-427.3	2-11	H	L2	9		-0.9			237	1.6		
FM-DH4-427.3	2-11	H	L2	6		-0.9			237	1.6		
FM-DH4-427.3	2-11	H	L2	7		-0.9				1.6		
FM-DH4-427.3	2-11	H	L2	14		-0.9			261	1.6		
FM-DH4-427.3	2-11	H	L2	14		-0.5				0.9		
average						-0.8			240	1.5	33	LV curve
stdev						0.2			15	0.3		
N						6			4	6		
FM-DH4-427.3	2-7	H	L2	25		-0.9				1.6		
FM-DH4-427.3	2-7	H	L2	10		-0.9				1.6		
FM-DH4-427.3	2-7	H	L2	35		-0.9			224	1.6		
FM-DH4-427.3	2-7	H	L2	25		-0.9			225	1.6		
FM-DH4-427.3	2-7	H	L2	25		-0.9			235	1.6		
FM-DH4-427.3	2-7	H	L2	7		-0.9				1.6		
FM-DH4-427.3	2-7	H	L2	40		-0.5			219	0.9		
FM-DH4-427.3	2-7	H	L2	20		-0.7				1.2		
FM-DH4-427.3	2-7	H	L2	20		-0.9				1.6		
FM-DH4-427.3	2-7	H	L2	20		-0.6				1.1		
average						-0.8			225	1.4	25	LV curve
stdev						0.2			7	0.3		
N						10			4	10		
FM-DH4-427.3	3-2	H	L2	20		-0.3			322	0.5		
FM-DH4-427.3	3-2	H	L2	12		-0.4			344	0.7		
average						-0.4			333	0.6	133	LV curve
stdev						0.1			15	0.1		
N						2			2	2		
FM-DH4-427.3	2-2	H	L2	7		-0.9			225	1.6		
FM-DH4-427.3	2-2	H	L2	9		-0.8			219	1.4		
FM-DH4-427.3	2-2	H	L2	17		-0.7			210	1.2		
FM-DH4-427.3	2-2	H	L2	9		-0.5			210	0.9		
FM-DH4-427.3	2-2	H	L2	14		-0.9			211	1.6		
FM-DH4-427.3	2-2	H	L2	17		-0.9			222	1.6		
FM-DH4-427.3	2-2	H	L2	22		-0.9			215	1.6		
FM-DH4-427.3	2-2	H	L2	17		-0.9			229	1.6		
FM-DH4-427.3	2-2	H	L2	8		-0.8			215	1.4		
FM-DH4-427.3	2-2	H	L2	15		-0.5			212	0.9		
FM-DH4-427.3	2-2	H	L2	14		-0.9			229	1.6		
average						-0.8			218	1.4	22	LV curve
stdev						0.2			7	0.3		
N						11			11	11		

sample	chip	Qtz	Fl type	Fl size	boil	Tm_{ice}	$Tm_{clathrate}$	Tm_{halite}	Th_{H2O}	salinity	ph	ph-basis
FM-DH4-427.3	2-2	H	L2	20		-0.9			219	1.6		
FM-DH4-427.3	2-2	H	L2	20		-0.9			210	1.6		
FM-DH4-427.3	2-2	H	L2	20		-0.9			215	1.6		
FM-DH4-427.3	2-2	H	L2	20		-0.9			224	1.6		
average						**-0.9**			**217**	**1.6**	21	LV curve
stdev									*6*			
N						*4*			*4*	*4*		
FM-DH4-427.3	2-2	H	L2	15		-0.9				1.6		
FM-DH4-427.3	2-2	H	L2	40		-0.9				1.6		
FM-DH4-427.3	2-2	H	L2	20		-0.9				1.6		
average						**-0.9**				**1.6**		
stdev						*0.0*				*0.0*		
N						*3*				*3*		
FM-DH4-427.3	2-3	H	L2	12		-1.2			235	2.1		
FM-DH4-427.3	2-3	H	L2	10		-1.1			228	1.9		
FM-DH4-427.3	2-3	H	L2	8		-1.0			232	1.7		
FM-DH4-427.3	2-3	H	L2	10		-0.9				1.6		
average						**-1.1**			**232**	**1.8**	28	LV curve
stdev						*0.1*			*3*	*0.2*		
N						*4*			*3*	*4*		
FM-DH4-427.3	2-5	H	L2	12		-1.2				2.1		
FM-DH4-427.3	2-5	H	L2	20		-1.1				1.9		
FM-DH4-427.3	2-5	H	L2	15		-1.1				1.9		
FM-DH4-427.3	2-5	H	L2	13		-1.3				2.2		
FM-DH4-427.3	2-5	H	L2	8		-1.2				2.1		
average						**-1.2**				**2.0**		
stdev						*0.1*				*0.1*		
N						*5*				*5*		
FM-DH4-427.3	2-18	H	L2	50		-0.6			215	1.1		
FM-DH4-427.3	2-18	H	L2	25		-0.4				0.7		
FM-DH4-427.3	2-18	H	L2	15		-0.4			213	0.7		
FM-DH4-427.3	2-18	H	L2	20		-1.0				1.7		
FM-DH4-427.3	2-18	H	L2	15		-1.0				1.7		
FM-DH4-427.3	2-18	H	L2	15		-0.9			234	1.6		
FM-DH4-427.3	2-18	H	L2	15		-0.5			211	0.9		
FM-DH4-427.3	2-18	H	L2	13		-0.5			220	0.9		
FM-DH4-427.3	2-18	H	L2	12		-0.5			221	0.9		
FM-DH4-427.3	2-18	H	L2	12		-0.5			208	0.9		
FM-DH4-427.3	2-18	H	L2	5		-0.5			217	0.9		
FM-DH4-427.3	2-18	H	L2	10		-0.5				0.9		
average						**-0.6**			**217**	**1.1**	21	LV curve
stdev						*0.2*			*8*	*0.4*		
N						*12*			*8*	*12*		

sample	chip	Qtz	Fl type	Fl size	boil	Tm_{ice}	$Tm_{clathrate}$	Tm_{halite}	Th_{H2O}	salinity	ph	ph-basis
FM-DH4-427.3	2-18	H	L2	20		-1.5				2.6		
FM-DH4-427.3	2-18	H	L2	30		-1.5				2.6		
FM-DH4-427.3	2-18	H	L2	20		-0.5				0.9		
FM-DH4-427.3	2-18	H	L2	10		-0.5				0.9		
FM-DH4-427.3	2-18	H	L2	12		-0.5				0.9		
FM-DH4-427.3	2-18	H	L2	40		-1.0				1.7		
average						**-0.9**				**1.6**		
stdev						*0.5*				*0.8*		
N						*6*				*6*		
FM-DH4-350.5	1	H	L2	25		-1.1			210	1.9		
FM-DH4-350.5	1	H	L2	30		-0.9			208	1.6		
FM-DH4-350.5	1	H	L2	30		-0.4			226	0.7		
average						**-0.8**			**215**	**1.4**	20	LV curve
stdev						*0.4*			*10*	*0.6*		
N						*3*			*3*	*3*		
FM-DH4-277.6	4	H	L2	15		-1.2				2.1		
FM-DH4-277.6	4	H	L2	15		-1.3			278	2.2		
FM-DH4-277.6	4	H	L2	10		-1.2				2.1		
FM-DH4-277.6	4	H	L2	12		-1.3				2.2		
average						**-1.3**			**278**	**2.2**	61	LV curve
stdev						*0.1*				*0.1*		
N						*4*			*1*	*4*		
FM-CP05-06	1	H	L1	20		-2.6				4.3		
FM-CP05-06	1	H	L1	60		-8.1				11.8		
FM-CP05-06	1	H	L1	20		-1.9				3.2		
FM-CP05-06	1	H	L1	20		-2.8				4.7		
FM-CP05-06	1	H	L1	20		-2.1				3.6		
FM-CP05-06	1	H	L1	30		-4.8				7.6		
FM-CP05-06	1	H	L1	40		-4.8				7.6		
FM-CP05-06	1	H	L1	40		-4.6				7.3		
FM-CP05-06	1	H	L1	15		-8.2				11.9		
FM-CP05-06	1	H	L1	12		-4.7				7.5		
FM-CP05-06	1	H	L1	15		-2.7				4.5		
FM-CP05-06	1	H	L1	15		-1.1				1.9		
FM-CP05-06	1	H	L1	8		-1.1				1.9		
average						**-3.8**				**6.0**		
stdev						*2.3*				*3.3*		
N						*13*				*13*		
FM-DH4-352.1	1	H	L1	25		-4.7				7.5		
FM-DH4-352.1	1	H	L1	12		-3.9				6.3		
FM-DH4-352.1	1	H	L1	15		-3.8				6.2		
FM-DH4-352.1	1	H	L1	12		-3.5				5.7		
FM-DH4-352.1	1	H	L1	15		-3.7				6.0		
average						**-3.9**				**6.3**		
stdev						*0.5*				*0.7*		
N						*5*				*5*		

sample	chip	Qtz	FI type	FI size	boil	Tm_{ice}	$Tm_{clathrate}$	Tm_{halite}	Th_{H2O}	salinity	ph	ph-basis
FM-DH4-277.6	2	H	L1	16		-4.2			301	6.7		
FM-DH4-277.6	2	H	L1	20		-3.7			259	6.0		
FM-DH4-277.6	2	H	L1	15		-3.3			266	5.4		
FM-DH4-277.6	2	H	L1	15		-3.8			265	6.2		
FM-DH4-277.6	2	H	L1	10					262			
FM-DH4-277.6	2	H	L1	12		-2.5			245	4.2		
average						**-3.5**			**266**	**5.7**	50	LV curve
stdev						*0.6*			*19*	*1.0*		
N						*5*			*6*	*5*		
FM-DH4-427.3	3-2	H	L1	15		-3.4			363	5.6		
FM-DH4-427.3	3-2	H	L1	15		-3.7			364	6.0		
FM-DH4-427.3	3-2	H	L1	40		-3.9			359	6.3		
FM-DH4-427.3	3-2	H	L1	43		-5.5			391	8.6		
FM-DH4-427.3	3-2	H	L1	15		-5.0			385	7.9		
average						**-4.3**			**372**	**6.9**	205	LV curve
stdev						*0.9*			*15*	*1.3*		
N						*5*			*5*	*5*		
FM-DH4-427.3	3-2	H	L1	20		-3.4			367	5.6		
FM-DH4-427.3	3-2	H	L1	23		-3.8			385	6.2		
average						**-3.6**			**376**	**5.9**	215	LV curve
stdev						*0.3*			*13*	*0.4*		
N						*2*			*2*	*2*		
FM-DH4-427.3	2-18	H	L1	24		-3.0				5.0		
FM-DH4-427.3	2-18	H	L1	50		-2.7				4.5		
FM-DH4-427.3	2-18	H	L1	35		-2.7			372	4.5		
FM-DH4-427.3	2-18	H	L1	30		-3.0			359	5.0		
FM-DH4-427.3	2-18	H	L1	10		-2.6			363	4.3		
average						**-2.8**			**364**	**4.6**	190	LV curve
stdev						*0.2*			*7*	*0.3*		
N						*5*			*3*	*5*		
FM-DH4-427.3	2-18	H	L1	20		-2.4			365	4.0		
FM-DH4-427.3	2-18	H	L1	30		-2.3			358	3.9		
FM-DH4-427.3	2-18	H	L1	20		-2.3			361	3.9		
FM-DH4-427.3	2-18	H	L1	20		-2.7			369	4.5		
FM-DH4-427.3	2-18	H	L1	20		-2.2			343	3.7		
average						**-2.4**			**359**	**4.0**	180	LV curve
stdev						*0.2*			*10*	*0.3*		
N						*5*			*5*	*5*		

sample	chip	Qtz	FI type	FI size	boil	Tm_{ice}	$Tm_{clathrate}$	Tm_{halite}	Th_{H2O}	salinity	ph	ph-basis
FM-DH4-427.3	2b	H	L1	20		-3.8			358	6.2		
FM-DH4-427.3	2b	H	L1	20		-6.5				9.9		
FM-DH4-427.3	2b	H	L1	25		-4.1				6.6		
FM-DH4-427.3	2b	H	L1	12		-3.5			364	5.7		
FM-DH4-427.3	2b	H	L1	10		-3.3				5.4		
FM-DH4-427.3	2b	H	L1	15		-1.4				2.4		
FM-DH4-427.3	2b	H	L1	12		-5.4				8.4		
FM-DH4-427.3	2b	H	L1	10		-5.2				8.1		
average						**-4.2**			**361**	**6.6**	180	LV curve
stdev						*1.6*			*4*	*2.3*		
N						*8*			*2*	*8*		
FM-DH4-350.5	1	H	L1	20		-2.3				3.9		
FM-DH4-350.5	1	H	L1	20		-2.2				3.7		
FM-DH4-350.5	1	H	L1	15		-2.3				3.9		
FM-DH4-350.5	1	H	L1	10		-1.8				3.1		
FM-DH4-350.5	1	H	L1	5		-1.9				3.2		
FM-DH4-350.5	1	H	L1	8		-2.3				3.9		
FM-DH4-350.5	1	H	L1	10		-2.4				4.0		
FM-DH4-350.5	1	H	L1	15		-2.4				4.0		
FM-DH4-350.5	1	H	L1	10		-2.2				3.7		
average						**-2.2**				**3.7**		
stdev						*0.2*				*0.3*		
N						*9*				*9*		
FM-DH4-277.6	4	H	L1	14		-2.0				3.4		
FM-DH4-277.6	4	H	L1	15		-5.9				9.1		
FM-DH4-277.6	4	H	L1	8		-4.6				7.3		
FM-DH4-277.6	4	H	L1	12		-3.6				5.9		
FM-DH4-277.6	4	H	L1	20		-7.9				11.6		
average						**-4.8**				**7.4**		
stdev						*2.2*				*3.1*		
N						*5*				*5*		
FM-DH4-277.6	4	H	L1	12		-5.0				7.9		
FM-DH4-277.6	4	H	L1	15		-2.4			280	4.0		
FM-DH4-277.6	4	H	L1	5		-5.7			225	8.8		
FM-DH4-277.6	4	H	L1	35		-7.6			274	11.2		
FM-DH4-277.6	4	H	L1	10		-1.7			282	2.9		
FM-DH4-277.6	4	H	L1	15					276			
average						**-4.5**			**268**	**7.0**	51	LV curve
stdev						*2.4*			*24*	*3.4*		
N						*5*			*5*	*5*		
FM-DH4-277.6	1	H	L1	30		-2.1				3.6		
FM-DH4-277.6	1	H	L1	12		-2.2				3.7		
FM-DH4-277.6	1	H	L1	15		-2.3				3.9		
FM-DH4-277.6	1	H	L1	15		-1.6				2.7		
FM-DH4-277.6	1	H	L1	10		-1.9				3.2		
FM-DH4-277.6	1	H	L1	10		-1.9				3.2		
average						**-2.0**				**3.4**		
stdev						*0.3*				*0.4*		
N						*6*				*6*		

sample	chip	Qtz	FI type	FI size	boil	Tm_{ice}	$Tm_{clathrate}$	Tm_{halite}	Th_{H2O}	salinity	ph	ph-basis
FM-DH4-277.6	2	G	L1	20			5.7		278	7.9		
FM-DH4-277.6	2	G	L1	25			5.7		247	7.9		
FM-DH4-277.6	2	G	L1	20		-5.0			282	7.9		
FM-DH4-277.6	2	G	L1	15					243			
FM-DH4-277.6	2	G	L1	12			5.6		244	8.1		
FM-DH4-277.6	2	G	L1	20		-5.0			269	7.9		
FM-DH4-277.6	2	G	L1	12					236			
FM-DH4-277.6	2	G	L1	18					271			
average						**-5.0**	**5.7**		**259**	**7.9**	44	LV curve
stdev							*0.1*		*18*	*0.1*		
N						*2*	*3*		*8*	*5*		
FM-DH4-427.3	2-14	G	L1	7		-3.0			357	5.0		
FM-DH4-427.3	2-14	G	L1	10		-2.9				4.8		
FM-DH4-427.3	2-14	G	L1	12		-3.0				5.0		
FM-DH4-427.3	2-14	G	L1	12		-3.2			363	5.3		
FM-DH4-427.3	2-14	G	L1	15		-3.0			350	5.0		
FM-DH4-427.3	2-14	G	L1	7		-2.8			352	4.6		
FM-DH4-427.3	2-14	G	L1	15		-2.7				4.5		
FM-DH4-427.3	2-14	G	L1	12		-3.0			348	5.0		
FM-DH4-427.3	2-14	G	L1	12		-2.9				4.8		
FM-DH4-427.3	2-14	G	L1	20		-3.0				5.0		
FM-DH4-427.3	2-14	G	L1	15		-3.0			367	5.0		
average						**-3.0**			**356**	**4.9**	172	LV curve
stdev						*0.1*			*7*	*0.2*		
N						*11*			*6*	*11*		
FM-DH4-427.3	2-2	G	L1	20		-2.7			362	4.5		
FM-DH4-427.3	2-2	G	L1	12		-2.5				4.2		
FM-DH4-427.3	2-2	G	L1	8		-2.4			371	4.0		
FM-DH4-427.3	2-2	G	L1	10		-2.2				3.7		
FM-DH4-427.3	2-2	G	L1	6		-2.3				3.9		
FM-DH4-427.3	2-2	G	L1	18		-2.3				3.9		
FM-DH4-427.3	2-2	G	L1	10		-2.4				4.0		
FM-DH4-427.3	2-2	G	L1	5		-2.5				4.2		
FM-DH4-427.3	2-2	G	L1	10		-2.5			364	4.2		
FM-DH4-427.3	2-2	G	L1	18		-2.1				3.6		
FM-DH4-427.3	2-2	G	L1	7		-2.3				3.9		
FM-DH4-427.3	2-2	G	L1	6		-2.9			382	4.8		
FM-DH4-427.3	2-2	G	L1	8		-2.5				4.2		
average						**-2.4**			**370**	**4.1**	204	LV curve
stdev						*0.2*			*9*	*0.3*		
N						*13*			*4*	*13*		

sample	chip	Qtz	Fl type	Fl size	boil	Tm_{ice}	$Tm_{clathrate}$	Tm_{halite}	Th_{H2O}	salinity	ph	ph-basis
FM-DH4-427.3	2-5	G	L1	5		-2.7				4.5		
FM-DH4-427.3	2-5	G	L1	7		-2.9				4.8		
FM-DH4-427.3	2-5	G	L1	8		-3.0				5.0		
FM-DH4-427.3	2-5	G	L1	10		-2.9				4.8		
FM-DH4-427.3	2-5	G	L1	8		-2.7				5.0		
FM-DH4-427.3	2-5	G	L1	8		-2.9				4.8		
FM-DH4-427.3	2-5	G	L1	5		-3.0				5.0		
FM-DH4-427.3	2-5	G	L1	8		-2.9				4.8		
average						-2.9				4.8		
stdev						0.1				0.2		
N						8				8		
FM-DH4-427.3	2-11	G	L1	35		-4.7			367	7.5		
FM-DH4-427.3	2-11	G	L1	35		-4.6			362	7.3		
FM-DH4-427.3	2-11	G	L1	25		-7.6			354	11.2		
FM-DH4-427.3	2-11	G	L1	15		-7.4			380	11.0		
FM-DH4-427.3	2-11	G	L1	15		-9.3			367	13.2		
average						-6.7			366	10.0	186	LV curve
stdev						2.0			10	2.6		
N						5			5	5		
FM-DH4-427.3	2-3	G	L1	25		-2.6			348	4.3		
FM-DH4-427.3	2-3	G	L1	22		-1.5			361	2.6		
FM-DH4-427.3	2-3	G	L1	40		-1.0			359	1.7		
FM-DH4-427.3	2-3	G	L1	20		-2.4			357	4.0		
FM-DH4-427.3	2-3	G	L1	20		-2.8			372	4.7		
FM-DH4-427.3	2-3	G	L1	12		-2.0			354	3.4		
FM-DH4-427.3	2-3	G	L1	15		-2.4			372	4.0		
average						-2.1			360	3.5	182	LV curve
stdev						0.6			9	1.0		
N						7			7	7		
FM-DH4-427.3	2-5	G	B	20				324		40.1		
FM-DH4-427.3	2-5	G	B	13				320		39.8		
FM-DH4-427.3	2-5	G	B	15				318		39.6		
FM-DH4-427.3	2-5	G	B	20				343		41.8		
FM-DH4-427.3	2-5	G	B	15				344		41.9		
FM-DH4-427.3	2-5	G	B	12				325		40.2		
FM-DH4-427.3	2-5	G	B	13				328		40.4		
FM-DH4-427.3	2-5	G	B	10				305	356	38.6		
FM-DH4-427.3	2-5	G	B	15				315	360	39.4		
FM-DH4-427.3	2-5	G	B	15				330	363	40.6		
average								325	360	40.2	127	LV curve
stdev								12	4	1.0		
N								10	3	10		

sample	chip	Qtz	Fl type	Fl size	boil	Tm_{ice}	$Tm_{clathrate}$	Tm_{halite}	Th_{H2O}	salinity	ph	ph-basis
FM-DH4-427.3	2-14	G	B	15				305	344	38.6		
FM-DH4-427.3	2-14	G	B	25				329		40.5		
FM-DH4-427.3	2-14	G	B	25				344	344	41.9		
FM-DH4-427.3	2-14	G	B	30				328	343	40.4		
FM-DH4-427.3	2-14	G	B	15				324	340	40.1		
FM-DH4-427.3	2-14	G	B	40				323		40.0		
FM-DH4-427.3	2-14	G	B	15				323		40.0		
FM-DH4-427.3	2-14	G	B	25				330		40.6		
average								**326**	**343**	**40.3**	103	LV curve
stdev								*11*	*2*	*0.9*		
N								*8*	*4*	*8*		
FM-DH4-277.6	1	F	V	15		-1.2				2.1		
FM-DH4-277.6	1	F	V	12		-1.1				1.9		
FM-DH4-277.6	1	F	V	15		-0.9				1.6		
FM-DH4-277.6	1	F	V	15		-0.9				1.6		
FM-DH4-277.6	1	F	V	12		-1.2				2.1		
FM-DH4-277.6	1	F	V	10		-1.2				2.1		
FM-DH4-277.6	1	F	V	20		-1.5				2.6		
FM-DH4-277.6	1	F	V	15		-1.2				2.1		
FM-DH4-277.6	1	F	V	18		-1.3				2.2		
FM-DH4-277.6	1	F	V	20		-1.2				2.1		
FM-DH4-277.6	1	F	V	12		-1.3				2.2		
FM-DH4-277.6	1	F	V	15		-1.5				2.6		
FM-DH4-277.6	1	F	V	15		-1.5				2.6		
FM-DH4-277.6	1	F	V	15		-1.4				2.4		
average						**-1.2**				**2.1**		
stdev						*0.2*				*0.3*		
N						*15*				*15*		
FM-DH4-276.6	1	F	V	30	X	-2.4				4.0		
FM-DH4-276.6	1	F	V	20	X	-2.2				3.7		
FM-DH4-276.6	1	F	V	20	X					3.9		
average						**-2.3**				**3.9**		
stdev						*0.1*				*0.2*		
N						*2*				*3*		
FM-DH4-276.6	1	F	B	40	X			324		40.1		
FM-DH4-276.6	1	F	B	30	X			300		38.2		
FM-DH4-276.6	1	F	B	18	X			282		36.8		
FM-DH4-276.6	1	F	B	30	X			310		39.0		
FM-DH4-276.6	1	F	B	35	X			280		36.7		
FM-DH4-276.6	1	F	B	15	X			280		36.7		
FM-DH4-276.6	1	F	B	25	X			320		39.8		
FM-DH4-276.6	1	F	B	18	X			285		37.0		
FM-DH4-276.6	1	F	B	10	X			322	335	39.9		
FM-DH4-276.6	1	F	B	10	X			328	363	40.4		
FM-DH4-276.6	1	F	B	12	X			329		40.5		
FM-DH4-276.6	1	F	B	15	X			328		40.4		
FM-DH4-276.6	1	F	B	10	X			332	337	40.8		
average								**309**	**345**	**38.9**	108	LV curve
stdev								*21*	*16*	*1.6*		
N								*13*	*3*	*13*		

Appendix table 4: Microthermometry of individual fluid inclusions from an inclusion assemblage of the high-sulfidation epithermal stage

sample	chip	Qtz	Fl type	Fl size	boil	Tm_{ice}	$Tm_{clathrate}$	Tm_{halite}	Th_{H2O}	salinity	ph	ph-basis
FM-CP05-28	1	J	L2	6		-1.5			178	2.6		
FM-CP05-28	1	J	L2	8		-1.3			172	2.2		
FM-CP05-28	1	J	L2	10		-1.7			153	2.9		
FM-CP05-28	1	J	L2	8		-1.6			183	2.7		
FM-CP05-28	1	J	L2	10		-1.6			187	2.7		
average						**-1.5**			**175**	**2.6**	9	LV curve
stdev						*0.2*			*13*	*0.3*		
N						*5*			*5*	*5*		

Headings and abbreviations: sample, sample ID; chip, number of fluid inclusion wafer; Qtz, quartz crystallization stage; Fl type, fluid inclusion type; Fl size, fluid inclusion size in μm; boil, boiling assemblage (i.e., cogenetic vapor and liquid inclusions); Tm_{ice}, final melting temperature of ice in °C; $Tm_{clathrate}$, final melting temperature of clathrates in °C; $Tm_{sylvite}$, final dissolution temperature of sylvite in °C; Tm_{halite}, final dissolution temperature of halite in °C; Th_{H2O}, homogenization temperature of the H_2O phases in °C; Th_{total}, bulk inclusion homogenization temperature in °C; salinity, apparent salinity in wt% NaCl equivalent; ph, pressure estimate in bar; ph-basis, basis for pressure estimate.

Appendix table 5: LA-ICP-MS data of individual fluid inclusions from inclusion assemblages of the porphyry stage

sample	chip	stage	Fl type	boil	shot	ablation	Na	K	Fe	Cu	As	Mo	Ag	Sb	Te	Cs	Au	Pb
FM-CP05-34	1	P	ID		dc21b03	**(*)	31542	18486	17114	4086	<298	<114	<42	<99	<340	<12	<26	196.2
FM-CP05-34	1	P	ID		dc21b04	***	25380	10195	29867	5683	<547	<220	<115	<163	<826	<28	<38	277.1
FM-CP05-34	1	P	ID		dc21b05	***	37215	19453	<15589	665	<508	<206	<76	<124	<501	<15	<49	<185
FM-CP05-34	1	P	ID		dc21b06	**(*)	22428	22907	19436	1385	<437	<178	<66	<63	<308	<19	<32	<168
FM-CP05-34	1	P	ID		dc21b07	**(*)	30199	17773	17292	2216	<149	117.2	<19	<33	<126	7.7	<9	291.4
FM-CP05-37	1	P	ID		mr22b03	***	27626	11724	<2147	<37	<48	<23	<13	<11	<80	<3	<2	204.0
FM-CP05-37	1	P	ID		mr22b04	**	15854	9736	9273	28	<19	<14	<9	<5	<49	4.6	<1	161.0
FM-CP05-37	1	P	ID		mr22b05	***	15141	7335	8307	686	<18	27.1	<5	<5	<32	1.3	<1	68.7
FM-CP05-37	1	P	ID		mr22b06	*(*)	20165	11698	12874	311	<24	24.5	<6	<6	<39	4.5	<2	204.6
FM-CP05-37	1	P	ID		mr22b07	**(*)	17950	7637	11016	1926	<129	<82	<58	<51	<190	16.2	<10	193.6
FM-CP05-37	1	P	ID		mr22b08	**	23924	11260	10983	122	<37	27.4	<10	<13	<72	6.3	<1	159.9
FM-CP05-37	1	P	ID		mr22b09	**	18500	11391	9540	119	<56	<29	<16	<19	<108	8.2	<4	197.3
FM-CP05-37	1	P	ID		mr22b10	**(*)	15287	<5322	<21056	3663	<506	<490	<114	<117	<660	<18	<27	109.9
FM-CP05-37	1	P	ID		mr22b11	**	19447	10011	<8966	262	<182	170.7	<47	<79	<241	<7	<12	41.5
FM-CP05-37	1	P	ID		mr22b12	**(*)	20116	11184	10924	330	<24	<23	<12	<8	<57	4.0	<1	197.2
FM-CP05-37	1	P	ID		mr22c09	***	37478	17075	6386	65	<45	<31	<19	<12	93.0	5.0	<2	792.3
FM-CP05-37	1	P	ID		mr22c10	**	64678	23225	10915	144	40.0	<4	<2	<2	<12	10.8	<1	454.7
FM-CP05-37	1	P	ID		mr22c14	**	57231	15452	7440	178	29.6	<4	2.0	<2	<8	15.5	<1	411.7
FM-CP05-37	1	P	ID		mr22c15	**(*)	17368	7933	9875	209	<19	50.0	<6	<7	<22	2.6	<1	177.1
FM-CP05-37	2	P	ID		mr22d12	**(*)	40108	16460	21975	<35	<19	<19	<8	<3	<32	7.9	<1	264.1
FM-CP05-37	2	P	ID		mr22d13	***	57621	26387	13479	233	<33	<32	<7	<8	<45	15.4	<2	489.3
FM-CP05-37	2	P	ID		mr22d15	**(*)	76102	25545	5065	328	<19	<19	<5	<5	<47	14.1	<1	403.8

sample	chip	stage	Fl type	boil	shot	ablation	Na	K	Fe	Cu	As	Mo	Ag	Sb	Te	Cs	Au	Pb
FM-CP05-21	1	A		ID	nv15a14	**	31821	34380	19629	<466	<490	<340	<138	<175	<1170	<31	<42	<257
FM-CP05-21	1	A		ID	nv15a15	***	28990	30385	38797	721	<128	<103	<21	<30	<261	14.4	<12	397.3
FM-CP05-21	1	A		ID	nv15a16	**	31134	28540	33473	2929	<52	<37	<23	<16	<92	2.4	<6	211.5
FM-CP05-21	1	A		ID	nv15a17	**	44767	54514	56561	2523	<171	<63	29.5	<38	<384	22.3	<10	406.9
FM-CP05-21	2	A		ID	nv15b05	**(*)	25523	16422	36553	1915	<301	<143	<54	<91	<433	<12	<21	495.4
FM-CP05-21	2	A		ID	nv15b06	**	34850	30356	4315	1418	<59	49.2	<11	23.5	<55	9.1	<5	390.4
FM-CP05-21	2	A		ID	nv15b07	**(*)	43251	20213	3345	954	<18	<10	<5	<6	<43	4.7	<1	542.1
FM-CP05-21	2	A		ID	nv15b08	**	29413	35470	12624	989	<25	<17	<8	<6	<37	4.7	<2	365.6
FM-CP05-21	2	A		ID	nv15b09	***	38131	23789	3484	338	<63	<29	<11	<19	<51	<4	<5	630.0
FM-CP05-21	2	A		ID	nv15b10	***	38173	<20859	<80970	<1233	<1823	<912	<346	<546	<2285	<133	<197	<915
FM-CP05-21	2	A		ID	nv15b11	**(*)	24650	17653	23615	2276	<120	<59	<22	<22	<149	<7	<8	209.4
FM-CP05-21	2	A		ID	nv15b12	**(*)	16836	29475	18380	1627	<122	<61	<32	<25	<277	6.2	<13	332.5
FM-CP05-21	2	A		ID	nv15b13	***	28844	19404	21566	4066	<263	<146	<55	<65	<511	<17	<21	227.9
FM-CP05-21	2	A		ID	nv15b14	***	33859	22129	<19791	558	<496	<276	<105	<152	<695	<23	<44	<315
FM-CP05-21	2	A		ID	nv15b15	**	35661	19026	6216	1124	32.5	<14	<8	<8	<51	3.0	<3	174.0
FM-CP05-21	2	A		ID	nv15b16	**	43677	4707	<7903	273	<239	<169	<46	<44	<368	<10	<15	<106
FM-CP05-21	2	A		ID	nv15b17	**(*)	15275	59671	57126	2250	<181	<148	73.6	<54	<189	<15	<16	191.9
FM-CP05-21	2	A		ID	nv15b18	**	35367	30720	36386	2235	<281	<312	<69	<111	<638	<15	<38	200.1
FM-CH04-02	1	A		ID	dc21a03	**(*)	43365	34376	29179	2226	<72	<57	<15	<24	<81	8.2	<5	289.8
FM-CH04-02	1	A		ID	dc21a04	**	42558	37689	72033	2955	<482	<203	<97	<127	<758	<25	<45	317.8
FM-CH04-02	1	A		ID	dc21a05	**(*)	17843	18039	12956	832	<95	<33	<16	<13	<157	<3	<8	139.2
FM-CH04-02	1	A		ID	dc21a06	***	31975	25193	32786	497	<94	<39	22.8	<23	<88	7.6	<10	178.6
FM-CH04-02	1	A		ID	dc21a07	**	54348	25708	15632	436	<34	<16	<6	<8	<36	9.0	<4	93.3
FM-CH04-02	1	A		ID	dc21a09	**(*)	26091	39324	63738	4598	<198	<104	<50	<34	<300	<5	<17	437.6
FM-CH04-02	1	A		ID	dc21a10	**	21166	124882	43657	2509	<28	21.1	<3	<7	<36	9.9	<2	257.2
FM-CH04-02	1	A		ID	dc21a11	**(*)	48240	42806	18715	711	(31.9)	<29	<12	<7	<78	5.7	<4	152.1
FM-CH04-02	1	A		ID	dc21a12	**(*)	36812	36397	42173	7524	<44	21.7	9.3	<11	<40	10.1	<3	338.1
FM-CH04-02	1	A		ID	dc21a13	*(*)	16101	18642	37385	1412	<49	175.5	<10	<13	<58	2.3	<5	166.7

sample	chip	stage	Fl type	boil	shot	ablation	Na	K	Fe	Cu	As	Mo	Ag	Sb	Te	Cs	Au	Pb
FM-CP05-37	1	A	ID		mr22b14	**	8253	7652	<6818	842	<148	<87	<28	<54	<255	<6	<9	206.4
FM-CP05-37	1	A	ID		mr22b15	**(*)	7324	6313	<4832	<159	<90	<75	<17	<35	<72	<3	<5	23.2
FM-CP05-37	1	A	ID		mr22b16	**	10032	5829	<2169	390	<50	<64	<13	<14	<91	<2	<3	89.4
FM-CP05-37	1	A	ID		mr22b17	**	10176	5884	8739	416	<35	<25	<8	<10	<33	3.2	<2	118.0
FM-CP05-37	2	A	ID		mr22d04	**	14514	5438	1171	<20	<17	16.7	<3	<5	<32	2.1	<1	37.6
FM-CP05-37	2	A	ID		mr22d05	**(*)	24720	7725	<791	24	<16	<10	<4	<5	<35	2.5	<1	<5
FM-CP05-37	2	A	ID		mr22d06	**	16814	5830	10264	2930	<121	428.0	<23	<33	<165	<7	<7	84.0
FM-CP05-37	2	A	ID		mr22d07	**	23374	5221	<1737	<44	<37	38.7	<19	<19	<81	6.4	<4	<14
FM-CP05-37	2	A	ID		mr22d08	**	14165	7030	8744	521	19.6	<13	<3	<5	<33	1.4	<1	107.7
FM-CP05-37	2	A	ID		mr22d09	**(*)	20462	8851	1015	<25	<21	<17	4.3	4.2	<40	2.6	<1	<7
FM-CP05-37	1	A	B		mr22c16	**	226043	51625	16893	409	42.5	<12	<3	<3	<29	26.9	<2	977.3
FM-CP05-37	1	A	B		mr22c17	**	196567	77053	61388	2269	142.1	96.9	<9	<8	<68	58.3	<2	2151.9
FM-CP05-37	1	A	B		mr22d17	**(*)	189981	93636	62381	1718	31.5	51.2	24.8	4.6	<13	65.0	<1	1871.8
FM-CP05-37	1	A	B		dc21b14	***	170830	101647	97123	1776	25.0	424.3	<9	<5	<31	41.7	<1	1678.9
FM-CP05-27	1	B	B		oc21b03	**	119065	79073	66854	341	<12	44.4	<40	<3	<12	33.1	<1	960.2
FM-CP05-27	1	B	B		oc21b04	***	142852	85048	78608	87	<9	<6	9.9	<3	<7	29.2	<1	1026.3
FM-CP05-27	1	B	B		oc21b05	**(*)	144702	67550	65904	1164	<107	97.1	<47	<30	94.7	14.7	<8	1053.8
FM-CP05-27	1	B	B		oc21b06	**	144573	79024	81466	655	<8	39.9	4.0	<1	<13	23.2	<1	942.6
FM-CP05-27	1	B	B		oc21b07	**	63742	132721	192915	1078	<91	<38	<32	<17	<71	116.1	<8	1192.8
FM-CP05-27	1	B	B		oc21b08	**	150778	48374	59255	181	<10	11.5	7.5	<2	<11	38.6	<1	582.1
FM-CP05-27	1	B	B		oc21b09	**	106976	55802	83279	3224	<441	<232	<62	<99	<309	25.3	<30	1896.7
FM-CP05-27	1	B	B		oc21b10	**(*)	121288	89886	100553	176	<38	<16	<6	<9	<30	46.1	<3	1436.7
FM-CP05-27	1	B	B		oc21b11	***	133535	86686	75855	175	<10	16.6	7.6	<2	11.9	24.1	<1	1224.6
FM-CP05-27	1	B	B		oc21b12	***	123196	89717	96625	30	<6	63.0	8.1	1.9	<15	28.7	<1	1073.3
FM-CP05-27	1	B	B		oc21b13	**(*)	153773	49513	59603	2565	<106	<77	<33	<19	<241	9.9	<8	734.6
FM-CP05-27	1	B	B		oc21b14	**	169799	57617	91726	<11	<23	<9	6.9	<4	<16	27.1	<2	744.1
FM-CP05-27	1	B	B		oc21b15	**	183575	54813	43327	13	6.7	8.4	6.2	<1	<5	48.2	<1	1043.7
FM-CP05-27	1	B	B		oc21b17	***	162702	76184	82444	<22	<31	<10	<9	<5	<38	24.5	<2	951.4
FM-CP05-27	1	B	B		oc21b18	**	159665	88717	84606	81	4.6	66.7	9.0	<1	<2	21.5	<1	994.5

sample	chip	stage	Fl type	boil	shot	ablation	Na	K	Fe	Cu	As	Mo	Ag	Sb	Te	Cs	Au	Pb
FM-DB99-15	1	C	B		oc20c03	***	100270	97998	95570	209	18.1	64.3	<8	<4	<37	27.7	1.3	1320.2
FM-DB99-15	1	C	B		oc20c04	**(*)	114791	85437	73523	170	<38	9.0	10.5	<10	<42	20.7	<3	882.7
FM-DB99-15	1	C	B		oc20c05	**	109928	96224	75361	350	5.8	115.3	8.9	0.5	<5	54.1	0.2	1278.5
FM-DB99-15	1	C	B		oc20c06	**	111930	97804	79696	421	5.7	221.8	7.1	<1	<7	40.1	<1	1386.5
FM-DB99-15	1	C	B		oc20c07	***	108751	95599	75793	426	<19	127.1	<4	<5	<19	31.3	<1	1432.0
FM-DB99-15	1	C	B		oc20c08	**	109885	107191	69841	139	5.5	153.9	7.5	<1	<6	44.7	0.4	1323.7
FM-DB99-15	1	C	B		oc20c09	***	106095	95435	83667	166	(4.6)	2711.7	10.5	<3	<13	29.7	<1	1166.4
FM-DB99-15	1	C	B		oc20c10	**(*)	107010	89136	75339	85	5.4	64.4	9.8	0.9	<4	18.6	0.3	1148.8
FM-DB99-15	1	C	B		oc20c11	***	108317	92615	81051	237	<9	8.8	8.6	<2	<19	20.2	<1	1037.8
FM-DB99-15	1	C	B		oc20c12	***	111102	97369	71758	267	<11	70.7	<4	<2	26.6	27.0	<1	1135.4
FM-DB99-15	1	C	B		oc20c13	**	119929	96757	59863	272	<11	64.3	10.9	<2	<13	22.4	<1	1234.1
FM-DB99-15	1	C	B		oc20c14	**(*)	108729	95636	80406	163	<22	736.1	<7	<4	<29	30.1	<2	1051.3
FM-DB99-15	1	C	B	X	oc20b07	***	63364	87529	126473	1585	<903	<379	<307	<230	<1816	37.7	<79	1578.3
FM-DB99-15	1	C	B	X	oc20b08	***	69875	59965	55737	1413	<57	57.5	11.9	14.0	<48	16.8	<4	714.8
FM-DB99-15	1	C	B	X	oc20b09	*(*)	61824	76750	133077	1364	<924	<23	<239	<207	<1637	46.7	<76	617.7
FM-DB99-15	1	C	B	X	oc20b10	**	96638	40264	86915	<308	<288	<156	<78	<51	<232	26.6	<25	527.9
FM-DB99-15	1	C	B	X	oc20b12	**	71086	59566	62139	213	(13.0)	8.7	<8	<5	<45	15.7	<2	793.9
FM-DB99-15	1	C	B	X	oc20b13	***	112766	87229	67694	213	(18.5)	58.7	<6	<8	<42	25.9	(1.2)	1238.9
FM-DB99-15	1	C	B	X	oc20b14	***	121916	92366	61154	340	25.6	36.1	6.2	<6	<54	19.8	<2	1152.0
FM-DB99-15	1	C	B	X	oc20b15	**	82654	70105	57362	642	<28	10.8	11.9	<4	<18	17.0	<2	905.8
FM-CP05-21	1	A	V		nv15a04	**(*)	7635	8502	5434	228	<23	<12	<6	<7	<28	6.4	<2	97.5
FM-CP05-21	1	A	V		nv15a05	**(*)	4107	8490	12464	1202	<61	<31	<15	<18	<76	6.5	<4	136.0
FM-CP05-21	1	A	V		nv15a06	***	5826	8409	8534	1346	<60	49.1	12.7	<11	<81	<4	<6	100.7
FM-CP05-21	1	A	V		nv15a07	**(*)	8523	5553	5395	794	<41	<18	<10	<9	64.1	<3	<4	83.1
FM-CP05-21	1	A	V		nv15a08	**	8587	9042	<12419	1277	<280	<140	<110	<78	<480	<12	<26	<164
FM-CP05-21	1	A	V		nv15a09	***	7667	6569	6711	530	<35	27.0	<12	<13	<116	<2	<5	57.3
FM-CP05-21	1	A	V		nv15a10	**	8987	7796	<3675	376	<97	<70	<28	<33	<171	<4	<10	78.4
FM-CP05-21	1	A	V		nv15a11	***	6608	13820	3357	126	<53	55.4	<10	<19	<92	<4	<6	<33
FM-CP05-21	1	A	V		nv15a12	**(*)	9639	9351	<9419	458	<263	<171	<49	<73	<629	<15	<27	<130
FM-CP05-21	1	A	V		nv15a13	***	7574	6876	6824	354	<8	<7	<4	<3	<17	1.0	<12	68.1

sample	chip	stage	Fl type	boil	shot	ablation	Na	K	Fe	Cu	As	Mo	Ag	Sb	Te	Cs	Au	Pb
FM-CP05-34	1	A		>	dc21b09	**	5330	5296	<5279	476	<235	<85	<61	<30	<315	<6	<18	<72
FM-CP05-34	1	A		>	dc21b10	***	4929	2952	2999	310	<12	7.3	<2	<3	<9	0.7	<1	55.3
FM-CP05-34	1	A		>	dc21b11	**(*)	4578	3178	3575	334	<15	<9	<2	<3	<19	1.2	(0.9)	53.9
FM-CP05-34	1	A		>	dc21b12	**	6355	2376	539	59	1.7	4.1	<1	<1	<2	1.3	<1	13.1
FM-CP05-34	1	A		>	dc21b13	**	4168	5580	4013	169	<11	<8	<3	<3	<19	1.6	<1	101.3
FM-CP05-37	1	A		>	mr22c12	**	3023	3892	14450	198	<79	<45	<25	<24	<60	<3	3.7	76.1
FM-CP05-37	1	A		>	mr22c13	**	4060	2031	<5199	2055	<121	<168	<43	<40	<315	<5	<7	51.1
FM-CP05-37	2	A		>	mr22d14	**	7747	10147	8252	<26	<14	<13	<3	<4	39.3	4.6	<1	63.1
FM-CP05-37	2	A		>	mr22d16	***	9581	4566	6877	582	<125	<77	<37	<22	<281	<5	<9	85.0
FM-CP05-27	1	B		>	oc21a05	***	32243	16674	17192	<41	<58	<27	<17	<11	<82	6.0	<4	206.4
FM-CP05-27	1	B		>	oc21a06	*	41638	16356	13055	41	<35	88.5	<8	<9	<48	2.6	<2	242.3
FM-CP05-27	1	B		>	oc21a07	**	43765	21892	28451	<17	<21	<7	<13	<9	<19	8.2	<1	312.5
FM-CP05-27	1	B		>	oc21a08	*	34576	16635	11981	44	<54	<17	<15	<11	<46	5.4	<3	161.0
FM-CP05-27	1	B		>	oc21a09	**	35210	18334	4616	<17	<24	<14	<6	<3	<34	2.7	<2	207.8
FM-CP05-27	1	B		>	oc21a10	**	32818	20629	<21742	<473	<884	<270	<177	<108	<722	<25	<50	<302
FM-CP05-27	1	B		>	oc21a11	***	33861	18230	12243	<38	<111	53.7	<25	<18	<138	19.5	<6	223.8
FM-CP05-27	1	B		>	oc21a12	***	32934	14250	17681	<263	<245	<76	<41	<41	<342	<7	<13	110.4
FM-CP05-27	1	B		>	oc21a13	***	31163	12799	9093	14787	<223	<99	<53	<51	<367	<9	<16	115.2
FM-CP05-27	1	B		>	oc21a14	*(*)	27137	12600	7521	121	<27	<11	<6	<7	<21	5.1	<2	119.0
FM-CP05-27	1	B		>	oc21a15	**(*)	31925	15173	14679	4817	<146	<51	<27	<22	<97	15.7	<9	255.8
FM-CP05-27	1	B		>	oc21a16	***	32713	18097	9772	5537	<42	<12	<5	<6	<39	6.5	<2	229.1
FM-CP05-27	1	B		>	oc21a17	**	36774	16259	7358	418	<76	<27	<10	<8	<88	<3	<5	192.8
FM-CP05-27	1	B		>	oc21a18	*	32388	6203	24915	830	<228	<138	<37	<53	<259	14.6	<16	222.2
FM-DB99-15	1	C		>	oc20a04	*	9399	5526	2247	348	<55	<22	<12	<13	<60	<2	<5	145.2
FM-DB99-15	1	C		>	oc20a05	**	7422	5473	5996	791	<11	<6	<2	1.0	17.3	1.4	(0.3)	88.1
FM-DB99-15	1	C		>	oc20a06	**	7229	6458	6336	124	<8	<2	<1	2.8	<9	2.5	<1	102.5
FM-DB99-15	1	C		>	oc20a07	*(*)	6352	8670	6444	271	<20	<10	16.5	4.0	<23	2.5	<1	74.1
FM-DB99-15	1	C		>	oc20a08	*(*)	8514	4990	4686	495	<69	<35	<16	<10	<82	<2	<5	78.8
FM-DB99-15	1	C		>	oc20a09	***	7858	5543	6226	160	<81	36.3	<25	<19	<99	5.3	<6	78.3

sample	chip	stage	Fl type	boil	shot	ablation	Na	K	Fe	Cu	As	Mo	Ag	Sb	Te	Cs	Au	Pb
FM-DB99-15	1	C	V		oc20a10	***	4515	<1851	<3097	14964	<127	<48	<26	<25	<92	<6	<11	<48
FM-DB99-15	1	C	V		oc20a11	*(*)	7219	6774	6094	587	<18	11.1	<5	<4	<23	2.2	<2	182.0
FM-DB99-15	1	C	V		oc20a13	*(*)	8536	4218	5818	773	<153	<51	<19	<25	<204	<6	<10	<47
FM-DB99-15	1	C	V		oc20a14	**	8101	<2327	4448	2819	<166	<76	<40	<40	<195	<6	<12	<62
FM-DB99-15	1	C	V		mr22a04	**	11185	<28656	<90898	<3063	<1978	<1437	<674	<730	<3434	<78	<123	<685
FM-DB99-15	1	C	V		mr22a05	**	6834	<5531	14872	5650	<398	<196	<111	<115	<787	<25	<18	<121
FM-DB99-15	1	C	V		mr22a06	***(*)	10352	6763	<6252	7762	<218	<86	<48	<44	<265	<6	<7	<65
FM-DB99-15	1	C	V		mr22a07	**(*)	9235	5160	6696	5718	<60	<47	26.9	<17	<54	2.6	3.5	68.9
FM-DB99-15	1	C	V		mr22a08	**(*)	11446	7087	<4845	1778	<118	<110	<26	<35	<260	<4	<7	75.0
FM-DB99-15	1	C	V		mr22a09	***	7447	7037	8327	6582	<244	<164	<91	<57	<320	<12	<13	73.3
FM-DB99-15	1	C	V	X	oc20b03	**	7689	5985	4730	197	<4	8.7	<2	<1	<6	1.7	<1	75.8
FM-DB99-15	1	C	V	X	oc20b06	**	5220	9927	6875	<65	<81	<25	<18	<16	<73	<3	<6	134.0
FM-DB99-15	1	C	V	X	oc20b16	*(*)	7562	5619	5323	154	<16	<5	<3	<3	<20	4.1	1.1	88.3
FM-DB99-15	1	C	V	X	oc20b17	**	7111	5717	6499	592	<24	12.0	<5	<7	<30	2.1	<2	89.3
FM-DB99-15	1	C	V	X	oc20b18	*	7602	6101	5759	612	<19	20.3	<7	<4	<33	1.9	<2	83.9
FM-DB99-15	1	D	V		oc20a15	**	8134	6409	4294	1133	<10	<7	<3	<3	<15	3.3	<1	86.6
FM-DB99-15	1	D	V		oc20a16	***	7447	5336	5148	1764	<24	<14	<7	<6	<31	<1	<2	69.2
FM-DB99-15	1	D	V		oc20a17	*	6299	4809	8219	1714	<38	<17	<12	<6	<60	<1	<3	120.4
FM-CP05-27	1	D	L		oc21a03	*(*)	7333	9047	30354	<130	<167	<62	<40	<43	<201	<8	<11	176.2
FM-CP05-21	1	D	L		nv15a18	***	6087	5217	5620	567	<60	<36	<10	<13	<106	<4	<4	60.8
FM-CP05-37	2	D	L		mr22d10	**	20413	<3759	<11579	<501	<274	164.4	<114	<83	668.6	<19	<13	231.9
FM-CP05-37	1	D	L		mr22c03	**(*)	26949	24827	<5533	<187	<105	<64	<46	<27	<202	<8	<7	429.5
FM-CP05-37	1	D	L		mr22c04	**(*)	29795	24813	<12548	<286	<231	<146	<94	<67	<495	24.8	<15	610.7
FM-CP05-37	1	D	L		mr22c05	**	14928	11152	<11058	<281	<329	<174	<57	<79	501.0	<12	<17	81.9
FM-CP05-37	1	D	L		mr22c06	***	17856	10698	<7974	380	<236	<125	<41	<56	<285	<9	<12	<55
FM-CP05-37	1	D	L		mr22c07	**	16029	11264	2245	<71	<46	<48	<22	<14	<82	2.9	3.2	118.0

Appendix table 6: LA-ICP-MS data of individual fluid inclusions from inclusion assemblages of the QSP stage

sample	chip stage	Fl type	boil	shot	ablation	Na	K	Mn	Fe	Cu	Zn	As	Sr	Ag	Sb	Te	Cs	Au	Pb
FM-DH4-427.3	2-3	H	V	ap13g11	***	859	457	<31	<925	775	<56	<63	<3	17.9	<6	n.a.	<1	3.5	5.1
FM-DH4-427.3	2-3	H	V	ap13g12	***	877	558	51	<658	644	<29	<38	2.2	<5	<3	n.a.	<1	<2	5.0
FM-DH4-427.3	2-3	H	V	ap13g13	***	840	564	45	<557	1	<28	<36	1.6	<5	34.9	n.a.	2.1	<2	<2
FM-DH4-427.3	2-3	H	V	ap13g14	**	927	456	80	<2119	611	<79	<125	<4	<10	<14	n.a.	<2	<6	<9
FM-DH4-427.3	2-3	H	V	mm16b10	***	1016	438	<27	<824	48	<43	<56	<2	<7	<6	n.a.	<33	<3	8.6
FM-DH4-427.3	2-3	H	V	mm16b11	**(*)	750	1148	91	<1346	103	84	<67	<4	<10	10.9	n.a.	<52	<5	14.6
FM-DH4-427.3	2-11	H	L2	mm16b15	**(*)	3539	7032	<211	42129	1076	675	<256	60.9	<31	138.2	<201	n.a.	<18	135.9
FM-DH4-427.3	2-11	H	L2	mm16b16	*(*)	4443	4621	<85	<1917	274	1635	<113	<5	14.8	24.0	<77	n.a.	<7	20.8
FM-DH4-427.3	2-11	H	L2	mm16b17	***	4814	3633	338	<808	60	131	<52	<3	<6	<5	<32	n.a.	<4	21.8
FM-DH4-427.3	2-7	H	L2	jl08b11	***	5690	1298	<127	<2852	2173	<160	<88	<5	<16	<32	<99	n.a.	<13	<36
FM-DH4-427.3	2-7	H	L2	jl08b12	***	5342	2225	161	<910	2766	111	39.6	<3	<6	<9	<40	n.a.	<5	21.7
FM-DH4-427.3	2-7	H	L2	jl08b14	**	5322	2277	179	390	2879	180	51.2	<1	25.9	5.4	16.7	n.a.	<1	10.6
FM-DH4-427.3	2-7	H	L2	jl08b15	***	4099	5539	<86	<1773	2949	<106	(26.8)	<6	<9	39.0	<94	n.a.	<9	<18
FM-DH4-427.3	2-7	H	L2	jl08b16	***	4379	1120	<120	<2546	4171	<135	85.1	6.8	<14	<31	<119	n.a.	<13	<28
FM-DH4-427.3	2-7	H	L2	jl08b17	***	3159	2591	55	<956	2561	<60	71.6	<3	<7	<10	(29.7)	n.a.	<4	14.2
FM-DH4-427.3	2-2	H	L2	ap13g05	***	4691	3962	<926	<31747	<1974	<1611	<2304	<69	<196	<144	n.a.	<49	<114	<123
FM-DH4-427.3	2-2	H	L2	ap13g06	***	3390	2743	540	<4692	<274	<324	<360	<13	<44	<31	n.a.	21.1	<15	<24
FM-DH4-427.3	2-2	H	L2	ap13g07	***	3800	2140	137	<3210	<207	<186	<267	<9	<31	<27	n.a.	<5	<13	<18
FM-DH4-427.3	2-2	H	L2	ap13g10	***	4544	2520	229	<2882	<242	206	<205	<7	<19	<16	n.a.	<5	<9	<18
FM-DH4-427.3	2-2	H	L2	mi04a06	***	5508	1756	306	<1826	210	122.9	<78	<4	<15	<9	<116	n.a.	<7	35.8
FM-DH4-427.3	2-2	H	L2	mi04a07	**	5224	2515	306	<2305	174	<117	<97	<6	<19	<14	<148	n.a.	<11	33.1
FM-DH4-427.3	2-2	H	L2	mi04a08	**	4642	4066	<233	<7568	<385	<363	<420	<27	<66	<52	<477	n.a.	<32	34.7

sample	chip	stage	FI type	boil	shot	ablation	Na	K	Mn	Fe	Cu	Zn	As	Sr	Ag	Sb	Te	Cs	Au	Pb
FM-DH4-427.3	2-3	H	L2		jl08a05	**(*)	5817	6204	217	<2110	<70	136	<54	<5	<9	<21	<79	n.a.	<8	<25
FM-DH4-427.3	2-3	H	L2		jl08a06	**(*)	7005	1358	241	<3950	<128	376	<86	<11	<23	<41	<132	n.a.	<20	60.5
FM-DH4-427.3	2-3	H	L2		jl08a07	***	5997	2262	473	<1008	<371	<470	<306	<25	<48	<116	<480	n.a.	<42	114.9
FM-DH4-427.3	2-18	H	L2		jl08a11	***	4558	6099	<195	<4678	<177	<239	<124	<14	<35	<64	<218	n.a.	<21	<58
FM-DH4-427.3	2-18	H	L2		jl08a12	***	3059	10095	71	<1019	<30	<65	<28	<2	<5	<10	<33	n.a.	<4	<9
FM-DH4-427.3	2-18	H	L2		jl08a13	**(*)	2137	1644	<43	<1060	472	<65	50.3	<2	<5	<12	<53	n.a.	<4	76.9
FM-DH4-427.3	2-18	H	L2		jl08a15	*(*)	2872	1574	98	519	177	<7	21.1	1.1	<1	<1	9.2	n.a.	4.2	29.2
FM-DH4-277.6	4	H	L2		mr28a10	***	6488	3829	n.a.	493	36	n.a.	5.9	n.a.	<1	<1	<7	2.3	<1	35.4
FM-DH4-277.6	4	H	L2		mr28a11	***	6536	3049	n.a.	1042	32	n.a.	12.5	n.a.	<4	<2	<19	1.9	<1	45.7
FM-DH4-277.6	4	H	L2		mr28a12	***	6800	3034	n.a.	463	34	n.a.	4.0	n.a.	<1	1.0	<5	1.5	<1	36.7
FM-CP05-06	1	H	L1		mr28c10	*(*)	12245	5651	n.a.	6089	250	n.a.	36.7	n.a.	<17	124.3	<69	<2	<2	103.1
FM-CP05-06	1	H	L1		mr28c11	*	33395	14542	n.a.	17107	153	n.a.	189.9	n.a.	13.8	697.0	147.4	15.7	2.0	397.6
FM-CP05-06	1	H	L1		mr28c12	**	9577	8345	n.a.	<2084	<72	n.a.	42.3	n.a.	<17	43.4	<45	6.9	<4	27.2
FM-CP05-06	1	H	L1		mr28c13	**(*)	15263	7791	n.a.	<1695	97	n.a.	103.9	n.a.	<14	149.9	70.7	9.3	2.3	21.6
FM-CP05-06	1	H	L1		mr28c14	***	6684	19417	n.a.	<2888	46	n.a.	<64	n.a.	<26	124.4	170.4	5.8	<3	284.3
FM-CP05-06	1	H	L1		mr28c15	***	16661	17277	n.a.	15099	147	n.a.	503.8	n.a.	<22	584.2	101.9	4.9	<4	598.8
FM-CP05-06	1	H	L1		mr28c16	***	17757	18364	n.a.	11721	119	n.a.	322.7	n.a.	<6	385.2	59.2	4.7	<1	627.3
FM-CP05-06	1	H	L1		mr28c17	***	17686	14892	n.a.	12332	74	n.a.	61.2	n.a.	13.8	236.1	58.1	5.6	<1	524.3
FM-DH4-352.1	1	H	L1		mr28d04	**(*)	25451	7639	n.a.	2232	265	n.a.	115.4	n.a.	<10	15.0	<32	8.6	<2	73.2
FM-DH4-352.1	1	H	L1		mr28d05	**	19128	8043	n.a.	5932	780	n.a.	37.7	n.a.	<9	27.2	<37	5.6	<1	81.6
FM-DH4-352.1	1	H	L1		mr28d06	**	18379	10390	n.a.	4400	920	n.a.	45.6	n.a.	<9	100.0	23.2	3.9	<1	99.7
FM-DH4-352.1	1	H	L1		mr28d07	*(*)	18299	6315	n.a.	4035	530	n.a.	44.8	n.a.	<11	<5	<31	<2	<2	68.7
FM-DH4-352.1	1	H	L1		mr28d08	*(*)	17182	9046	n.a.	6896	497	n.a.	39.2	n.a.	<14	53.8	<68	4.7	<2	92.3
FM-DH4-277.6	2	H	L1		mr28a15	***	23037	6500	n.a.	<4555	<208	n.a.	<112	n.a.	<32	<35	<146	<5	<5	101.1
FM-DH4-277.6	2	H	L1		mr28a16	***	17851	15447	n.a.	<6240	<159	n.a.	<135	n.a.	<50	<26	<162	14.3	<7	54.0
FM-DH4-277.6	2	H	L1		mr28a17	***	16349	13157	n.a.	<8132	<198	n.a.	<128	n.a.	<85	<43	<201	7.8	<13	<59
FM-DH4-277.6	2	H	L1		mr28a18	***	16662	20192	n.a.	<9718	<233	n.a.	<268	n.a.	<102	<49	<401	13.4	<17	157.0

sample	chip	stage	Fl type	boil	shot	ablation	Na	K	Mn	Fe	Cu	Zn	As	Sr	Ag	Sb	Te	Cs	Au	Pb
FM-DH4-427.3	3-2	H	L1		mr23a07	*(*)	20399	3931	n.a.	<3783	<123	n.a.	<109	n.a.	<34	<25	<140	<5	<7	30.1
FM-DH4-427.3	3-2	H	L1		mr23a08	**(*)	20605	11145	n.a.	<827	2532	n.a.	218.6	n.a.	<7	<5	<43	8.4	2.3	392.0
FM-DH4-427.3	3-2	H	L1		mr23a09	*	27662	15930	n.a.	<1692	2202	n.a.	57.4	n.a.	<11	<10	87.7	11.1	<2	1597.8
FM-DH4-427.3	3-2	H	L1		mr23a10	***	15287	7702	n.a.	8309	228	n.a.	<5	n.a.	1.5	<1	13.5	6.3	<1	117.2
FM-DH4-427.3	3-2	H	L1		mr23a11	***	15980	8253	n.a.	11592	179	n.a.	<4	n.a.	<2	<1	(5.9)	6.8	<1	107.5
FM-DH4-427.3	2-18	H	L1		je17a07	**(*)	12465	9038	n.a.	n.a.	<82	n.a.	<209	n.a.	n.a.	<36	122.7	6.6	<6	<47
FM-DH4-427.3	2-18	H	L1		je17a08	***	8540	17825	n.a.	n.a.	345	n.a.	(11.1)	n.a.	n.a.	15.3	<16	9.1	<1	86.7
FM-DH4-427.3	2-18	H	L1		je17a10	***	12994	5948	n.a.	n.a.	<116	n.a.	<433	n.a.	n.a.	144.4	342.9	<12	<9	<93
FM-DH4-427.3	2-18	H	L1		je17a11	**	11120	12204	n.a.	n.a.	1331	n.a.	(89.7)	n.a.	n.a.	50.5	<102	8.6	<4	62.9
FM-DH4-427.3	2-18	H	L1		je17a12	***	15573	5576	n.a.	n.a.	469	n.a.	43.8	n.a.	n.a.	3.8	<18	92.8	<1	78.5
FM-DH4-427.3	2-18	H	L1		je17a13	***	12851	7588	n.a.	n.a.	50	n.a.	(48.9)	n.a.	n.a.	<14	<62	4.6	<2	44.7
FM-DH4-427.3	2-18	H	L1		je17a14	***	9729	12975	n.a.	n.a.	502	n.a.	(58.0)	n.a.	n.a.	<22	<114	8.8	<4	<39
FM-DH4-427.3	2-18	H	L1		je17a15	***	11268	11810	n.a.	n.a.	94	n.a.	<125	n.a.	n.a.	<36	<127	21.1	<5	61.7
FM-DH4-427.3	2-18	H	L1		je17a16	**	12954	7315	n.a.	n.a.	40	n.a.	12.8	n.a.	n.a.	<1	<5	4.6	<1	24.5
FM-DH4-427.3	2-18	H	L1		je17a17	***	13657	5438	n.a.	n.a.	712	n.a.	19.0	n.a.	n.a.	3.6	22.4	5.2	<1	56.9
FM-DH4-427.3	2b	H	L1		mr28c04	**	13670	23539	n.a.	3902	917	n.a.	13.8	n.a.	<4	3.4	<12	3.7	0.4	56.3
FM-DH4-427.3	2b	H	L1		mr28c05	**(*)	28178	18312	n.a.	8414	522	n.a.	25.1	n.a.	<8	3.4	<30	7.2	<1	141.0
FM-DH4-427.3	2b	H	L1		mr28c08	**	16958	8927	n.a.	4848	436	n.a.	(21.3)	n.a.	<9	<6	26.9	2.6	<2	82.4
FM-DH4-427.3	2b	H	L1		mr28c09	**	15647	9481	n.a.	4674	446	n.a.	<119	n.a.	<42	<13	<222	<6	<6	96.1
FM-DH4-350.5	2	H	L1		jl08c03	***	4079	1472	396	3073	187	309.8	<93	<6	<12	<31	<103	n.a.	<13	<39
FM-DH4-350.5	2	H	L1		jl08c04	***	3965	2554	541	3774	315	207.3	<3	<1	<1	<1	<4	n.a.	<1	22.1
FM-DH4-350.5	2	H	L1		jl08c05	**(*)	3563	2661	551	3073	232	172.4	<2	1.4	<1	<1	<2	n.a.	<1	13.3
FM-DH4-350.5	2	H	L1		jl08c06	**	4203	2828	502	3046	116	109.0	<2	0.8	<1	0.8	<2	n.a.	<1	22.7
FM-DH4-277.6	4	H	L1		mr23b04	**	9974	5395	n.a.	<3318	<132	n.a.	104.6	n.a.	<33	<32	<133	7.4	(1.8)	<26
FM-DH4-277.6	4	H	L1		mr23b05	**	18479	39798	n.a.	<9558	<301	n.a.	<221	n.a.	<50	<99	<431	<15	<11	<90
FM-DH4-277.6	4	H	L1		mr23b07	**(*)	19572	7175	n.a.	<3456	<67	n.a.	126.8	n.a.	<13	<17	<90	3.3	<3	93.7
FM-DH4-277.6	4	H	L1		mr23b08	***	32839	29054	n.a.	4092	216	n.a.	108.2	n.a.	<11	<29	<116	9.9	<3	102.7
FM-DH4-277.6	4	H	L1		mr23b09	***	19131	6924	n.a.	4304	<108	n.a.	<86	n.a.	<24	<27	<178	6.6	<5	87.5

sample	chip	stage	Fl type	boil	shot	ablation	Na	K	Mn	Fe	Cu	Zn	As	Sr	Ag	Sb	Te	Cs	Au	Pb
FM-DH4-277.6	4	H	L1		mr23b13	***	22430	8203	n.a.	12170	314	n.a.	<15	n.a.	<3	<5	<27	8.2	<1	99.3
FM-DH4-277.6	4	H	L1		mr23b14	**	10108	3910	n.a.	9618	195	n.a.	<77	n.a.	<20	<29	<175	5.6	<7	79.1
FM-DH4-277.6	4	H	L1		mr23b16	*(*)	25063	12515	n.a.	11018	408	n.a.	<25	n.a.	<7	<7	<35	5.8	<1	136.3
FM-DH4-277.6	4	H	L1		mr23b17	**	34562	17707	n.a.	6600	467	n.a.	<46	n.a.	<30	<21	<121	4.2	<4	264.9
FM-DH4-427.3	2-14	G	L1		dd10b06	***	16446	8179	483	<2408	3329	<143	(35.4)	n.a.	<15	<35	<120	n.a.	8.5	52.0
FM-DH4-427.3	2-14	G	L1		dd10b07	***	14911	9226	389	<3121	5642	<212	159.8	n.a.	<29	<44	(106.0)	n.a.	17.4	(36.1)
FM-DH4-427.3	2-14	G	L1		dd10b08	**	13939	6078	675	3248	2964	<188	(28.3)	n.a.	<17	<24	<186	n.a.	<15	(21.3)
FM-DH4-427.3	2-14	G	L1		dd10b09	***	16508	8011	635	<9212	7248	<698	<219	n.a.	<63	79.1	<576	n.a.	<40	<124
FM-DH4-427.3	2-14	G	L1		dd10b10	***	13181	15205	532	<2696	8390	562	317.7	n.a.	<22	<26	(146.2)	n.a.	<16	76.9
FM-DH4-427.3	2-2	G	L1		je17a03	***	12190	4734	n.a.	n.a.	<250	n.a.	627.1	n.a.	n.a.	<327	<487	<21	<20	<138
FM-DH4-427.3	2-2	G	L1		je17a04	***	14687	3532	n.a.	n.a.	<116	n.a.	(163.8)	n.a.	n.a.	256.9	<370	<12	<11	<114
FM-DH4-427.3	2-2	G	L1		je17a05	***	13819	5847	n.a.	n.a.	<67	n.a.	(140.0)	n.a.	n.a.	<42	<215	11.5	<6	307.1
FM-DH4-427.3	2-2	G	L1		je17a06	***	13646	6309	n.a.	n.a.	<120	n.a.	<303	n.a.	n.a.	103.7	<166	11.2	<7	<54
FM-DH4-277.6	2	G	L1		mr28a04	**(*)	24901	8416	n.a.	7144	380	n.a.	92.8	n.a.	<2	8.7	<8	10.3	<1	98.5
FM-DH4-277.6	2	G	L1		mr28a05	**(*)	23815	9731	n.a.	8475	438	n.a.	151.9	n.a.	<2	37.9	<20	8.2	<1	108.6
FM-DH4-277.6	2	G	L1		mr28a06	**	24635	8557	n.a.	6915	402	n.a.	85.8	n.a.	<7	17.5	<22	10.1	<1	148.8
FM-DH4-277.6	2	G	L1		mr28a07	***	24834	8006	n.a.	7639	418	n.a.	69.0	n.a.	<4	10.8	<23	6.8	<1	93.7
FM-DH4-277.6	2	G	L1		mr28a08	***	25000	8312	n.a.	7009	432	n.a.	124.9	n.a.	<16	<16	<76	7.1	<3	135.2
FM-DH4-277.6	2	G	L1		mr28a09	**(*)	24096	6623	n.a.	9756	240	n.a.	367.5	n.a.	8.0	95.4	<67	4.4	<3	164.5
FM-DH4-427.3	2-5	G	B		jl08b04	***	114557	45547	7608	45950	6823	2214	<41	18.2	14.5	<16	<57	n.a.	<6	487.2
FM-DH4-427.3	2-5	G	B		jl08b05	***	116740	60234	7367	47531	1385	2058	(18.8)	52.7	11.5	(3.7)	<25	n.a.	<2	563.6
FM-DH4-427.3	2-5	G	B		jl08b06	**(*)	110728	58972	7082	42591	2990	1960	(15.6)	31.2	8.9	(4.2)	<30	n.a.	<2	528.8
FM-DH4-427.3	2-5	G	B		jl08b07	***	109041	64064	9310	58284	1232	2665	24.9	12.4	8.3	<7	<24	n.a.	<2	609.5
FM-DH4-427.3	2-5	G	B		jl08b08	***	105999	64484	8022	54542	6520	2512	<28	29.7	<5	<13	<50	n.a.	<4	545.0
FM-DH4-427.3	2-5	G	B		jl08b09	***	125955	43674	5711	28067	3567	1646	<56	13.2	<14	<22	<104	n.a.	<10	479.9

sample	chip	stage	Fl type	boil	shot ablation		Na	K	Mn	Fe	Cu	Zn	As	Sr	Ag	Sb	Te	Cs	Au	Pb
FM-DH4-427.3	2-14	G	B		dd10b05	**	107717	62455	7448	50286	2439	1394	25.2	n.a.	6.1	2.6	<2	n.a.	0.9	443.0
FM-DH4-427.3	2-14	G	B		dd10b11	*(*)	102156	64331	8888	61233	1471	2180	(10.0)	n.a.	32.9	<4	<27	n.a.	<2	486.4
FM-DH4-427.3	2-14	G	B		dd10b12	***	80825	91884	12458	78684	5078	3280	(10.8)	n.a.	<6	<9	<55	n.a.	<6	723.6
FM-DH4-276.6	1	F	B	X	jl08c07	***(*)	105377	57982	13321	49925	5107	2645	69.5	256.7	66.8	47.5	<58	n.a.	17.3†	514.0
FM-DH4-276.6	1	F	B	X	jl08c10	***	102992	61675	9089	49131	3852	2820	41.1	102.4	<2	6.5	<12	n.a.	<2	500.5
FM-DH4-276.6	1	F	B	X	jl08c11	***	98899	89994	5896	18475	<130	1896	279.8	10.3	<18	<39	<142	n.a.	<14	282.7
FM-DH4-276.6	1	F	B	X	jl08c12	***	79081	86652	11905	59151	3337	3467	(13.4)	34.3	<4	<8	<27	n.a.	<4	803.3
FM-DH4-276.6	1	F	B	X	jl08c14	**	95139	73755	10698	63852	7244	3707	62.6	93.8	8.6	23.3	16.9	n.a.	3.6	785.6
FM-DH4-276.6	1	F	B	X	jl08c15	**	97473	56328	13061	70131	3421	4569	63.6	47.9	21.0	29.5	<17	n.a.	3.5	747.7
FM-DH4-277.6	1	F	V		mr28b04	***	5271	<1514	n.a.	<4136	5014	n.a.	<90	n.a.	<42	14.9	<204	<4	<7	200.9
FM-DH4-277.6	1	F	V		mr28b05	***	4025	6527	n.a.	<7465	5637	n.a.	219.0	n.a.	<45	70.6	<249	<9	<11	141.4
FM-DH4-277.6	1	F	V		mr28b06	***	4600	<1985	n.a.	<6183	5329	n.a.	909.6	n.a.	<43	90.4	<114	<8	<8	111.3
FM-DH4-277.6	1	F	V		mr28b07	***	7562	8145	n.a.	<10945	5132	n.a.	1245.9	n.a.	<46	63.1	<506	<10	<14	<95
FM-DH4-277.6	1	F	V		mr28b08	**(*)	2345	7705	n.a.	<9872	6077	n.a.	2309.4	n.a.	<61	288.9	<319	<8	<9	<76
FM-DH4-276.6	1	F	V	X	jl08c08	**(*)	11574	10343	1067	5445	967	580	(4.9)	1.7	1.1	<2	<6	n.a.	<1	134.5
FM-DH4-276.6	1	F	V	X	jl08c09	***	9883	12460	1932	8761	1612	700	(18.0)	10.1	<6	<10	<32	n.a.	<4	96.3
FM-DH4-276.6	1	F	V	X	jl08c16	**(*)	9846	11360	1568	8552	1177	692	61.4	11.4	<4	12.0	(22.4)	n.a.	<4	88.0

Headings and abbreviations: sample, sample ID; chip, number of fluid inclusion wafer; stage, quartz crystallization stage; Fl type, fluid inclusion type; boil, boiling assemblage; shot, number of individual laser ablation shot; ablation, ablation quality (* = bad, ** = good, *** = excellent). Element concentrations for major, minor, and trace elements are given in µg/g. <VALUE represents values below the limit of detection using the 3σ criterion after Longerich et al. (1996). † denotes accidentally trapped Au-particles as indicated by the consistently lower LOD's of the other inclusions of the same assemblage.

Data treatment for certain trace elements, such as Au, which are often below the limit of detection:
(VALUE) value above the limit of detection using the 1σ criterion
VALUE value above the limit of detection using the 2σ criterion
VALUE value above the limit of detection using the 3σ criterion
VALUE signal can be optically recognized as detected

Appendix table 7: Stable isotope data from the magmatic-hydrothermal system at Famatina, NW Argentina

sample	altitude	vein type*	stage*	alteration*	analyte	$\delta^{18}O_{analyte}$	$\delta D_{analyte}$	T_{est}	$\delta^{18}O_{H2O}$	δD_{H2O}
37-20	3200	A-veinlet	A	potassic	dacite	9.8	-61.4	550		
37-20	3200	A-veinlet	A	potassic	vein quartz	10.2	-48.8	550	8.0	
10-20	4300	A-veinlet	A	potassic	vein quartz	9.8	-59.1	550	7.6	
28-15	3635	B-vein	B	potassic	vein quartz	10.3	-56.8	500	7.5	
11-40	4200	B-vein	B	potassic	vein quartz	10.1	-59.0	500	7.3	
29-11	3720	B-vein	B	potassic	vein quartz	10.7	-40.8	450	7.1	
25-11	3585	B-vein	C	sericitic	vein quartz	10.1	-32.7	500	7.3	
37-12	3420	B-vein	C	sericitic	vein quartz	10.1	-30.6	450	6.5	
37-52	3700	B-vein	C	sericitic	vein quartz	10.5	-28.2	450	6.9	
32-16	3740	B-vein	C	sericitic	vein quartz	10.5	-24.1	450	6.9	
37-15	3300	QSP vein	G	sericitic	sericite	10.2	-53.0	350	7.7	-19.0
30-61	3725	QSP vein	G	sericitic	vein quartz	10.9	-37.8	350	5.1	
21-40	4380	QSP vein	G	sericitic	vein quartz	10.2	-65.7	350	4.4	
1106	4335	QSP vein	I	sericitic	sericite	11.6	-50.1	350	9.1	-15.1
0209	4335	QSP vein	I	sericitic	quartz	12.5	-40.1	250	3.1	
0506	4335	epithermal vein	J	alunitic	quartz	12.0	-50.3	350	4.8	
2107	4410	epithermal vein	J	alunitic	quartz	10.6	-26.4	300	3.2	
0906	4335	epithermal vein	J	alunitic	quartz	12.0	-47.1	250	2.6	
0806	4335	epithermal vein	J	alunitic	quartz	10.8	-52.3	250	1.4	
2407	4410	epithermal vein	J	alunitic	quartz	11.0	-34.3	250	1.6	
1007	4410	epithermal vein	J	alunitic	quartz	12.2	-49.9	250	2.8	
0807	4410	epithermal vein	J	alunitic	quartz	11.1	-48.1	250	1.7	
0507	4410	epithermal vein	J	alunitic	quartz	11.1	-43.6	250	1.7	
C					meteoric water				-5.2	-29.0
F					meteoric water				-5.2	-32.6
RA					meteoric water				-5.1	-30.1
LM					meteoric water				-5.2	-32.3

*All data presented in this table are re-interpreted from Losada-Calderón (1992) according to the petrographic distinction criteria used in this study. Temperature estimates (T_{est}) are either from homogenization temperatures of fluid inclusions or interpolated from data outlined in Losada-Calderón (1992). Water samples originate from the mining district and were collected in February 1991. For more detailed information the reader is referred to this reference and references therein. Units: altitude in m, $\delta^{18}O$ in ‰, δD in ‰, T_{est} in °C.

CURRICULUM VITAE

Name: Claudia Pudack

Date of birth: October 29, 1973

Place of birth: Rathenow, Germany

Nationality: German

Marital status: Married (1 child)

Education:

2002 – 2007	Doctoral studies at the Institute of Isotope Geochemistry and Mineral Resources, ETH Zürich, Switzerland
	PhD thesis: Evolution of ore-forming fluids at the porphyry to epithermal transition: the Famatina Cu-Mo-Au district (NW Argentina)
	Supervisor: Prof. Dr. C. A. Heinrich
1993 – 2001	Graduate and undergraduate studies in geology at the University of Mining and Technology, Freiberg, Germany
	MSc thesis: Lead isotopic composition of Silurian and Devonian volcanic-hosted massive sulfide deposits from the southern Urals
	Supervisor: Prof. Dr. P. M. Herzig
1992 – 1993	Undergraduate studies in geophysics at the University of Mining and Technology, Freiberg, Germany
1990 – 1992	High School: Erweiterte Oberschule Rathenow, Germany